UNIVERSITY OF
BIRMINGHAM

FABRICATION OF CERAMIC AND CERAMIC COMPOSITE MICROCOMPONENTS USING SOFT LITHOGRAPHY

By

Hany Salama Sayed Ali Hassanin

A thesis submitted to
The University of Birmingham
for the degree of

DOCTOR OF PHILOSOPHY

School of Mechanical Engineering
College of Engineering and Physical Sciences
The University of Birmingham
December 2010

ABSTRACT

This PhD project is set out to develop a high precision ceramic fabrication approach suitable for mass production, and to meet the needs of microengine application. A group of new processes have been developed and the results are characterized for fabrication of high precision ceramic oxides and composite microcomponents using soft lithography and colloidal powder processing. The materials chosen in the research are alumina, yttria stabilised zirconia and their composite for their excellent properties at high temperature.

The research can be divided into four main sections. In the first section fabrication processes high precision hard and soft moulds were studied. The process for producing SU-8 hard moulds and PDMS soft moulds were optimized. In particular, much attention was paid to obtain vertical and straight sidewalls, dimensional accuracy, and smooth surfaces of the moulds. BPR100, DRIE silicon, reinforced PDMS and Dragon Skin were experimented as alternatives to fabricate hard and soft moulds.

In the second section, water, solvent and paraffin wax slurry systems were tested to fill PDMS soft moulds. A comparison study was carried out to choose the best slurry system based on their outputs. Damage free microcomponents with different sintered properties were successfully produced using the proposed slurry systems. It was found that microcomponents fabricated using the water-based slurry show distinctive advantages over solvent and paraffin wax-based slurries in its high density and low shrinkage properties.

In the third section, different ceramic powder sizes of both alumina and zirconia were used in experiments. The work includes detailed characterisation of slurries, green and sintered

microcomponents. Characterization of the slurries was performed in terms of zeta potential and sedimentation measurements, while characterization of the green parts was performed in terms of shape retention, density and shrinkage. It was found that using pH = 7 and the optimum dispersant and binder concentrations not only improve suspension stability but also improve green density and drying shrinkage significantly. In addition, characterization of the sintered parts was performed in terms of shape retention, density, shrinkage, surface morphology, roughness, micro hardness, flexural strength. It was concluded that, alumina microcomponents fabricated using particle size of 0.7 μm and sintered at 1600 °C has sintered density of 98.3%, linear shrinkage of 17.6%, Vickers hardness of 23.05 GPa, flexural strength of 366 MPa and surface roughness Ra= 54.77 nm. On the other hand, 8 mole% yttria stabilized zirconia microcomponents fabricated using particle size of 2.0 μm and sintered at 1550 °C produced sintered density of 98.5%, linear shrinkage of 20.9%, Vickers hardness of 14.65 GPa, flexural strength of 508 MPa and surface roughness Ra= 54.38 nm.

In the fourth section, the proposed techniques were extended to fabricated homogenous and gradient profiles zirconia/alumina composite microcomponents with tailored properties. Two different types of composites were proposed. The first is zirconia matrix alumina nanocomposite microcomponents, where alumina nano particles are homogenously dispersed into YSZ8 matrix. The sintered YSZ8/Al_2O_3 nanocomposite microcomponents can achieve sintered density 0.4% and micro hardness 17% superior to the pure YSZ8 sintered microcomponents. The second is functionally graded zirconia alumina composite microcomponents with alumina shell and YSZ8 composite core. It was found that altering the colloidal powder processing and changing layers compositions is an effective approach to solve the observed cracks problems.

Dedicated to my Family

ACKNOWLEDGEMENTS

Above all, I would like to express my great appreciation to my research supervisor, Professor Kyle Jiang for his guidance, feedback, and support during my graduate study. He has challenged me to push beyond what I thought was possible in my research.

I would also like to thank the members of Microengineering and Nanotechnology group, for being kind and supportive and my colleges Mohamed, Sean, Sam, Majid, Ali and Haseena for sharing the knowledge and expertise and for their helpful suggestions and support throughout the completion of my PhD thesis. I would also thank my colleague Hossein Ostadi for his help in the surface roughness measurements. I owe my sincere thanks to Dr Moataz Atalah and Dr Sattar AzZubaydi for their helpful discussions regarding the XRD analysis.

Most of all I would like to thank my family, my father, my mother, my brother Ahmed and my sister Nadia, for their support throughout my graduate student journey. They have always been there as a sounding board during my hard times. I would not have been able to do it without them. I would like also to thank my fiancée Rania for her encouragement and patience throughout the course of this research work.

TABLE OF CONTENTS

LIST OF FIGURES

LIST OF TABLES

ABBREVIATIONS

µCP	Microcontact printing
µIM	Microinjection moulding
µTM	Microtransfer moulding
3DP	Three-dimensional printing
BSE	Back-scattered electrons
CAD	Computer-aided design
DRIE	Deep reactive ion etching
EDS	Energy dispersive X-ray spectroscopy
EPD	Electrophoretic deposition
FDM	Fused deposition modelling
FGM	Functionally graded composite materials
FIB	Focus Ion Beam
IJP	Ink jet printing
IPA	Isopropanol
LMS	Laser micro sintering
LOM	Laminated Object Manufacturing
LPIM	Low-pressure injection moulding
MEMS	Micro electromechanical system
MIMIC	Micromoulding in capillaries
MWCNT	Multi-wall carbon nanotube
PCR	Preceramic coating
PDMS	Polydimethylsiloxane
pHIEP	Isoelectrostatic point
PZT	Lead zirconium titanate

REM	Replica moulding
RP	Rapid prototyping
SAMIM	Solvent-assisted micromoulding
SEM	Scanning electron microscope
SFF	Solid free form
SLA	Stereolithography
UV	Ultraviolet
XRD	X-ray diffraction
YSZ	Yttria stabilized zirconia
YSZ8	8 mole% yttria stabilized zirconia

LIST OF PUBLICATIONS

The thesis is based on the experimental work presented in details in the following papers.

Journal papers:

[1] H. Hassanin and K. Jiang, "Fabrication of AI_2O_3/SiC composite microcomponents using non-aqueous suspension," Advanced Engineering Materials, vol. 11, pp. 101-105, 2009.

[2] Zhigang Zhu, Hany Hassanin and Kyle Jiang, "A soft moulding process for manufacture of net-shape ceramic microcomponents," International Journal of Advanced Manufacturing Technology 47, 147-152, 2010.

[3] H. Hassanin and K. Jiang, "Functionally graded microceramic components," Microelectronic Engineering, vol. 87, pp. 1610-1613, 2010.

[4] H. Hassanin and K. Jiang, "Optimized process for the fabrication of zirconia microcomponents," Microelectronic Engineering, vol. 87, pp. 1617-1619, 2010.

[5] H. Hassanin and K. Jiang, "Alumina composite suspension preparation for softlithography microfabrication," Microelectronic Engineering, vol. 86, pp. 929-932, 2009.

[6] H. Hassanin and K. Jiang, "Surface and geometry characterization of soft lithography thick moulds for net shape ceramic micro fabrication," Microelectronic Engineering, 2010.

[7] H. Hassanin and K. Jiang, "Self replication of thick PDMS micro pattern using surfactants as release agents," Microelectronic Engineering, 2010.

Conference papers:

[1] H. Hassanin and K. Jiang, "Infiltration-processed, functionally graded Materials for microceramic components," The 23rd IEEE International Conference on Micro Electro Mechanical Systems (MEMS 2010).

[2] H. Hassanin and K. Jiang, "Fabrication of zirconia/alumina nanocomposite microcomponents using colloidal powder processing and soft lithography," The 36th International Conference on Micro & Nano Engineering (MNE 2010), Genoa, Italy, 19 September to 22 September 2010.

[3] H. Hassanin and K. Jiang, “Fabrication of free standing alumina micro components by pressurless slip casting in PDMS moulds," The 36th International Conference on Micro & Nano Engineering (MNE 2010), Genoa, Italy, 19 September to 22 September 2010.

[4] H. Hassanin and K. Jiang, “Functionally graded microceramic components," The 35th International Conference on Micro & Nano Engineering (MNE 09), Ghent, Belgium, 28 September to 1 October 2009.

[5] H. Hassanin and K. Jiang, “Optimized process for the fabrication of zirconia microcomponents," the 35th International Conference on Micro & Nano Engineering (MNE 09), Athens, Greece, 28 September to 1 October 2009.

[6] H. Hassanin and K. Jiang, "Fabrication of near net shape alumina nickel composite micro parts using aqueous suspension," The 22nd IEEE International Conference on Micro Electro Mechanical Systems (MEMS 2009), pp. 721-724, 2009.

[7] H. Hassanin and K. Jiang, “Alumina composite suspension preparation for softlithography microfabrication," the 34th International Conference on Micro & Nano Engineering (MNE 09), Ghent, Belgium, 15 September to 18 September 2008.

[8] Hany Hassanin and Kyle Jiang, "Fabrication of Alumina Composite Microengine Parts using Softlithography," SAE international, 2009-01-0118, 2009.

CHAPTER 1: INTRODUCTION

1.1 Introduction

This thesis presents an investigation into fabrication of micro ceramic and ceramic composite components. The project was driven by the need to fabricate high temperature resistant and high strength microcomponents to meet the design requirements of microcombustion engines. It is part of the microengines project developed at the University of Birmingham, initiated by Kyle Jiang [1-4]. Most MEMS technology based micro heat engines are constructed using single crystal silicon components fabricated using deep reactive ion etching (DRIE) process [5-7], but silicon has a softening temperature of 600 °C, which poses one of the biggest technical challenges in microengine development. Ceramics have outstanding properties in high temperature resistance, high wear resistance, and high compression strength. It is a not much explored area to fabricate microceramic components with engine component complexity and high accuracy. Typical conventional ceramic component fabrication methods cannot be applied, such as injection moulding. New processes need to be developed.

The proposed approach combines soft lithography and colloidal powder process. With soft lithography, high precision soft moulds are obtained from mirroring hard master moulds fabricated using MEMS lithography techniques. With colloidal powder process, microceramic components are formed from the soft moulds and sintered in furnaces. Extensive characterizations of the ceramic components are conducted to investigate the properties of the components.

1.2 Aims and Objectives

The aims of this PhD project are to fill the technical gap in precision fabrication by developing a high precision ceramic fabrication approach suitable for mass production, and to meet the particular needs of microengine development. The significance of the research is not limited to microengine development, but also to expand ceramic fabrication capability, enabling ceramic components to be made much smaller with high accuracy to meet a wide range of applications.

The project poses various new challenges. It is planned to tackle the challenges by introducing the latest micro and nanotechnology into ceramic fabrication. The research will start based on the existing micro/nanotechnology developed in the research group and progress further to develop complete microceramic fabrication processes. The microcomponents used in this research are micro reciprocating engine parts, which have characteristics of a 1000 μm thick, minimum feature dimension of 75 μm and aspect ratio of 10. The major challenges in the project originate from the complexity of the devices and they fall into three categories. First, precision dimension control for the master and soft moulds which are strongly influenced by the complexity of the micro features and the processing parameters. Second, finding a productive colloidal powder process which is compatible with the used soft mould, and yielding to desirable properties. Third, Integrate of the complete microengine, which require uniform shrinkage of all parts during fabrication process.

In order to achieve the research aims mentioned above, the project objectives are set out below.

1. Review the status of ceramic microfabrication techniques and the recent progress of alumina, zirconia and ceramic composite microcomponents.

2. Fabricate the optimum master moulds among SU-8, BPR100, DRIE silicon and reinforced PDMS, and produce the negative replica soft moulds between PDMS and Dragon Skin in terms of accuracy and surface roughness.

3. Develop an appropriate slurry system to fabricate alumina and zirconia microcomponents. The systems to be tested include water, solvent and paraffin wax based slurries to identify the best system in terms of processing and sintered properties.

4. Perform slurry and green parts characterization for optimization of alumina and zirconia slurry composition to achieve well-dispersed slurry and dense green microcomponents.

5. Sinter green microcomponents, which satisfy net shape requirements needed for the microengine.

6. Perform characterisation on the microcomponents produced in terms of sintered density, linear shrinkage, surface morphology and porosity, micro hardness, flexural strength and surface roughness.

7. Extend proposed fabrication technique to zirconia/alumina composite with homogenous and gradient profiles microcomponents.

1.3 Thesis Outline

This thesis consists of eight chapters. Chapter One introduces the project research topic covered by this thesis. It includes the project aims, objectives and thesis outline.

Chapter Two reviews the current research progress on ceramic and ceramic composite microcomponents development. It starts with the main ceramic microfabrication techniques relevant to the contents presented in this thesis, and is followed by a review of alumina and zirconia properties, the main materials used in this project. Afterwards, a literature survey covering ceramic composite microcomponents is presented.

Chapters Three to Eight describe research work carried out by the PhD candidate. Chapter Three introduces fabrication of SU-8 and PDMS moulds. High precision moulds are the foundation to the fabrication of the required microcomponents. Therefore, the optimisation process is explained. The optimisation includes geometry control, sidewall profile and surface roughness characterization. Also discussed are the use of BPR100, DRIE silicon, reinforced PDMS as master moulds and Dragon Skin as soft mould aiming to achieve better quality alternatives.

After realisation of the master and soft moulds, Chapter Four identifies experimentally the appropriate ceramic slurry system and its processing rout for fabrication of alumina and yttria stabilized zirconia microengine parts using soft lithography. Water, solvent and paraffin wax based slurries are proposed and their composition is optimized. The challenges in each process are discussed and solutions are subsequently provided. The results from the slurries are compared and the best is selected.

Chapter Five presents characterisation of alumina and zirconia slurries and green parts. The experimental details of preparing well-dispersed slurries using different alumina and zirconia powder with different sizes are first explained. The effects of powder, pH and dispersant concentration on suspension zeta potential, suspension stability, green density and drying shrinkage are analysed and discussed.

Chapter Six describes characterisation of the resultant sintered microcomponents. Physical, mechanical and structural properties are characterised in this study. Following this, results of shape retention, sintered density, linear shrinkage, micro hardness, flexural strength, surface morphology and porosity in the sintered microcomponents are presented and discussed. Finally, assemblies of complete alumina and zirconia microengines are illustrated.

Chapter Seven explains the detailed fabrication process of zirconia/alumina composite microcomponents. Two types of ceramic composite microcomponents are presented. Fabrication of zirconia matrix alumina nanocomposite and functionally graded zirconia/alumina composite is introduced to achieve microcomponents with tailored properties. The effects of the fabrication processes and the material composition on the properties of the sintered composite microcomponents are studied and discussed.

The study of ceramic and ceramic composite microcomponents is finally concluded in Chapter Eight. The major findings obtained from the study are summarised. Possible future research topics are suggested.

CHAPTER 2: LITERATURE REVIEW

2.1 Introduction

This chapter presents a literature review of different ceramic microfabrication techniques as the first step towards selecting an appropriate approach. Several microfabrication techniques are possible candidates for application within the microengine. However, there are advantages and drawbacks of each technique. The candidate techniques are evaluated according to their characteristics and resultant microparts properties and outlined in Section 2.2. Ceramic sintering review is presented in Section 2.3. Ceramic materials adopted in this research are reviewed in Section 2.4, where properties of both alumina and zirconia are listed and discussed. In addition, microfabrication processes of both materials and properties of the developed microcomponents are also investigated. The recent progress of ceramic matrix nanocomposite and functionally graded composite for microsystem applications are reviewed in Section 2.5. Finally, the literature review is summarised in Section 2.6.

2.2 Ceramic Microfabrication Techniques

In this section, the main ceramic microfabrication techniques are reviewed to determine their feasibility as potential candidates for fabrication of the microengine.

2.2.1 Solid Freeform Fabrication (SFF)

Solid free form (SFF) is a group of fabrication processes where three-dimensional parts are constructed by adding or subtracting layers of materials on point, line or planar surfaces. The structure formation of this technique is computer controlled. It is the result of the

advanced progress in both the hardware and software of computers. Solid free forming is a direct writing technique, which does not required moulds. A moving device such as laser, light or ink jet performs the shaping of the designed pattern. Objects in this technique are created incrementally [8]. Solid free forming processes include stereolithography (SLA), laser micro sintering (LMS), three-dimensional printing (3DP), fused deposition modelling (FDM), laminated Object Manufacturing (LOM) and ink jet printing (IJP) [9-12]. There are two main drawbacks of the technique. First, the resultant parts normally exhibit unfavourable surface roughness on all inclined surface, which is a typical consequence of the stair stepping effect due to the formation of the build up layers. The rough surface can be diminished by reducing layer thickness or by post machining (grinding or polishing). However, this can be a time consuming process. Second, the final components from of the free solid forming usually suffer from relatively low density and large shrinkage. This is because the used ceramic suspension has a very low solid loading. In addition, it also affects the dimensional tolerance and the utility of the designed microcomponents.

2.2.1.1 Stereolithography (SLA)

Stereolithography (SLA) is a process developed from rapid prototyping technology. It allows the manufacture of three-dimensional complex shapes components. Objects are made by building up many sequential layers defined by a CAD design. Forming of these layers are achieved using space scanning mirror and a light induced polymerization of a photosensitive ceramic suspension or a liquid resin into a solid polymer, as shown in Figure 2.1 [12-14].

The term microstereolithography process for composite and ceramic microcomponent fabrication is very much related to the work performed at the macroscale. The difference is

that in microstereolithography ceramic mixture composed of ceramic powder embedded in a photo initiator polymer matrix is used to create micro prototype parts. The resulting ceramic parts have been used either as working components or as moulds for later casting process. After forming of the green parts using microstereolithography, microcomponents undergo debinding process to burn out the polymer content. Next, the moulded parts are placed in a high temperature sintering furnace to obtain the final structure.

Direct fabrication of polymer/ceramic composite components by SLA requires the use of a photo curable resin loaded with ceramic powder in the manufacturing process. Sintered ceramic parts are obtained after a debinding and sintering step. In order to obtain satisfying physical and mechanical properties of the ceramic structure, the ceramic powder content of the resins should be as those used in conventional ceramic processing. Solid volume loadings of 50% or more are thus required. Indirect ceramic SLA was developed to overcome the limitation of direct SLA and ability to form fine and dense structures. In this process, a casting mould (permanent or lost) is fabricated using SLA instead of forming the ceramic part as in the direct method, into which the ceramic slurry is poured and cured. Afterwards, the green parts can be obtained from the SLA mould either by demoulding (permanent mould) or thermally (lost mould) and finally the green parts are sintered to obtain the final microcomponents [15].

SLA offers a unique opportunity to fabricate complex 3D ceramic parts. However, the stair stepping caused by the build up layers is one of the main reasons of rough surface in SLA and other rapid prototyping (RP) systems. More potential problems include delamination and poor mechanical properties limit the use of this technique. The poor mechanical

properties obtained from SLA techniques can be attributed to poor adhesion between layers and to the low density of the ceramic microcomponents [12-15].

Surface roughness is mainly depends on formed layers thickness, the designed draft angle and the light penetration depth. To improve the surface finish quality, layer thickness and draft angle should keep as low as possible. In addition, light penetration depth should be correctly controlled to achieve accurate polymerization depth [16-17].

Further development has been achieved to reduce SLA stair stepping. These efforts include vector-by-vector microsterolithography, integral microsterolithography and slant beam rotation. These improvements can decrease the resolution to 5 µm and the surface finish to about 1.1 µm. In addition, By debinding the ceramic/resin objects with a heating rate of 0.1 to 1 °C/min and keeping temperature at 600 °C, ceramic oxides green parts were obtained and then sintered at 1600 °C [18-20].

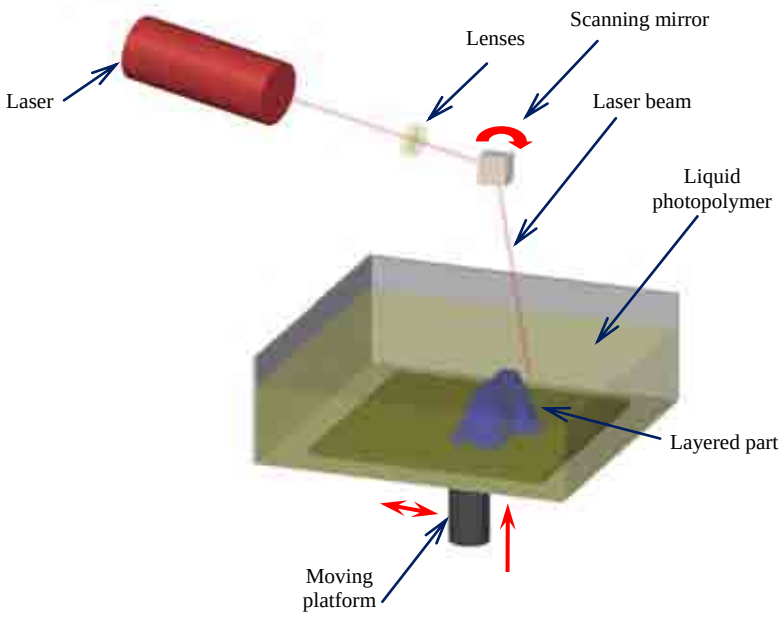

Figure 2.1. Schematic representation of Stereolithography setup.

2.2.1.2 Fused Deposition Modelling (FDM)

In fused deposition modelling (FDM), thermoplastic ceramic polymer is extruded through a nozzle using solid polymer strand as the extrusion ram. Filament is fed into a die between driving wheels as a solid rod. Liquefier is heated to melt the filament material and can be moved in both horizontal and vertical directions by a programme-controlled system to build a range of multi microcomponents. The technique is shown schematically in Figure 2.2 [8-9].

Many parameters affect the FDM technique and its resultant microcomponents. These variables include material, geometry properties, machine and operation specifications. Of these variables, the material properties must be optimized first in preparation of a new material feedstock. After development of material feedstock, other variables should be also optimized to determine the internal and external quality of FDM parts. Other variables are affecting each other and hence need to be optimized together. A variety of ceramic materials has been used in FDM, including silica, alumina, silicon nitride and lead zirconium titanate (PZT). The main problem with FDM is the formation of internal and surface defects due to possible poor bonding between the contiguous layers, or defective filling. Several improvements have been preformed to reduce surface defects, including green, partial sintering, and final machining. Internal defects are formed by voids, flaws, pores, delaminations and cracks in the green ceramic parts, which are unacceptable for structural and functional applications. The causes for the defect formation are easily traceable. Therefore, through optimization of the process variables and achievement of satisfactory process techniques to address the complications, it is likely to fabricate better quality green ceramic parts. In addition, elimination of the surface and internal defects can improve the sintered density from 95% to 98% [21-24].

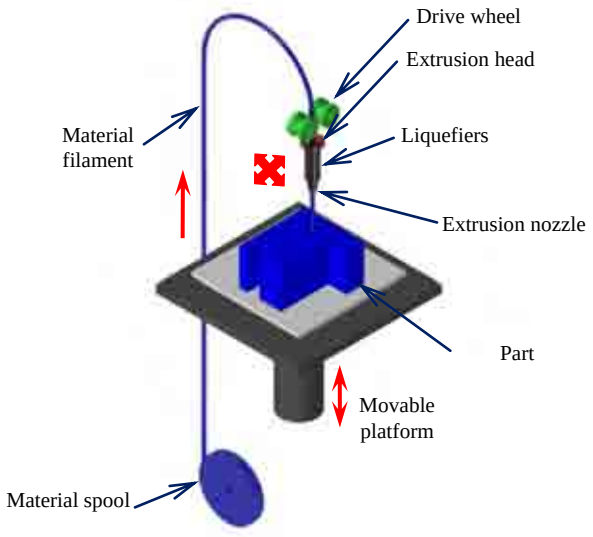

Figure 2.2. Schematic diagram of the fused deposition process.

2.2.1.3 Laser Micro Sintering (LMS)

Laser micro sintering (LMS) is a direct fabrication technique developed based on laser selective sintering. It uses a high power laser to sinter ceramic powder into three-dimensional microcomponents. A laser beam selectively scans over a thin powder bed and sinters the powder particles. Afterwards, another layer of the powder is applied for subsequent forming. The non-formed parts of the powder bed provide enough support for the forming process. Once the microcomponents are formed, the shaped part can be lifted from the powder bed, as shown in Figure 2.3. For ceramic materials, it is difficult to obtain complete shape compared to metals and polymers due to large thermal expansion difference, thermal shock and the transparency of oxide ceramics. Moreover, the powder size should be in sub micrometer range to reach the required resolution. Additionally, the absorption coefficient of a high intensity near infrared laser wavelength has to be sufficient to transfer the energy into the material. The powder is usually mixed with a lower melting

point second phase binder either as by particle coating, or as a mixture of ceramic powder and binder particles. The organic binders are burnt out in the firing process, while inorganic binders in some cases can act as a second phase. LMS technique was able to fabricate alumina microcomponents with a resolution up to 50 µm. In addition, the average density of the measured alumina specimens was 98.5% of the theoretical density using CO_2-laser irradiation. The laser scanning velocity was varied between 95 and 400 mm/s [25-28].

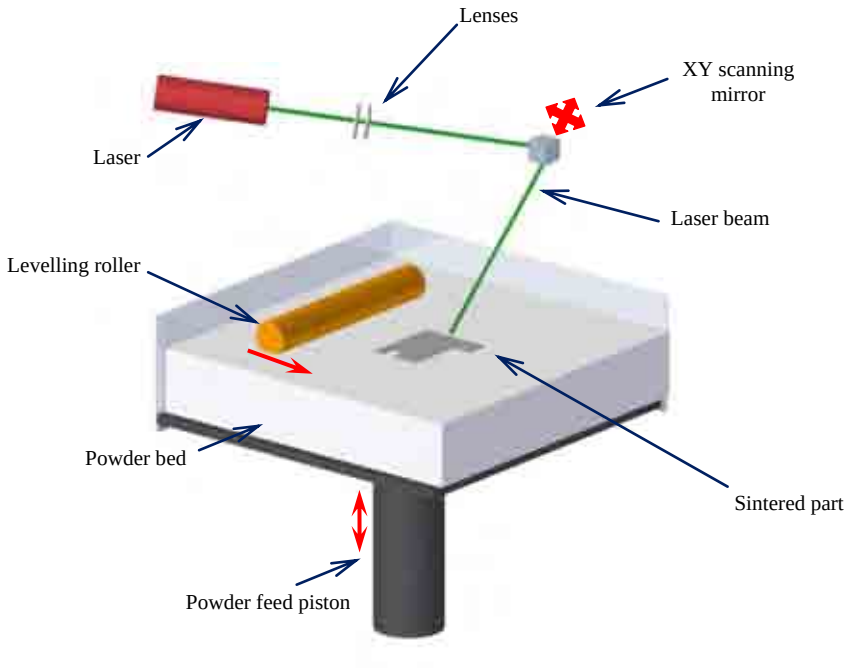

Figure 2.3. Schematic diagram of selective laser melting process.

2.2.1.4 Laminated Object Manufacturing (LOM)

Laminated object manufacturing (LOM) was first developed in 1991 by Helisys of Torrance. Parts are built up by bonding stacks of contoured thin adhesive coated ceramic layers on the top of the previous layer. As schematically shown in Figure 2.4, the outline of the first layer is cut by means of laser beam according to the CAD design. Next, the

platform goes up slightly and the heated roller applies pressure to bond the fresh layer on the top surface of the previous deposited layer. The laser cutting and bonding are repeated until the part is completely constructed. After a layer outline is cut, the remaining extra material supports the cut part during the construction [8-9]. As explained in the fabrication technique, LOM is partly considered a subtracted process when compared to other solid free forming processes, because it tracks the contours of the parts and discards the rest of the roll during layer fabrication. Therefore, it is considered the fastest method among the SFF for building ceramic parts [8-9]. LOM has been used to fabricate ceramic parts using thin ceramic sheets (100 µm). Since each layer is formed previously (tapes), microstructural defects inside each layer is minimised. However, it is difficult to prevent forming of flaws in the interfaces of successive layers. This technique is very useful for fabricating multi layers of functionally graded materials or multilayered composites as different materials tapes can be added onto designed supply rolls [29-34].

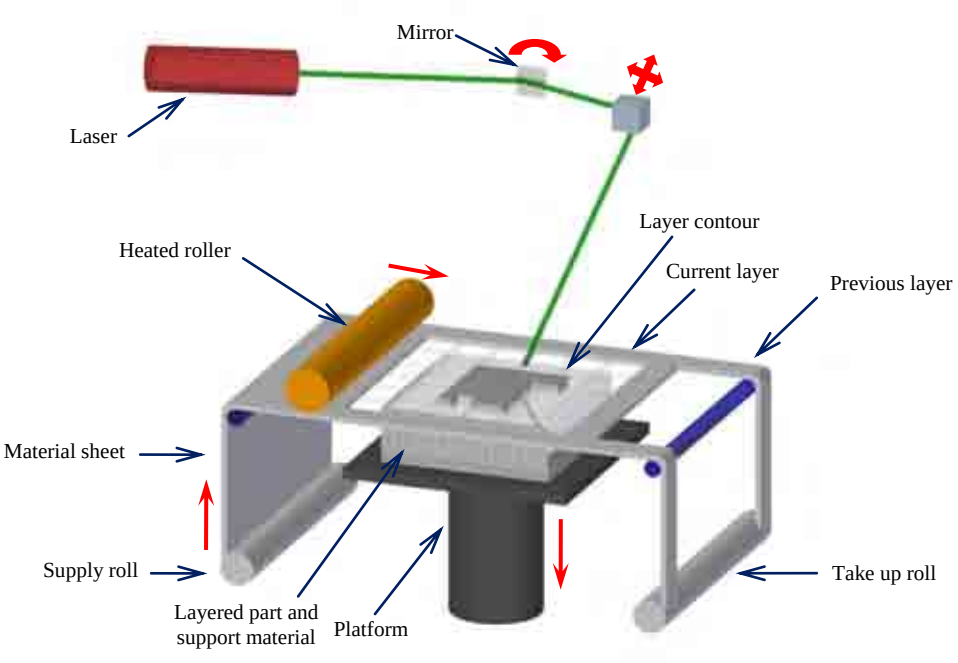

Figure 2.4. Schematic diagram of laminated object manufacturing process.

2.2.1.5 Three-Dimensional Printing (3DP)

Three dimensional-printing (3DP) was originally developed by Massachusetts Institute of Technology (MIT) in 1990. The process is similar to selective laser sintering, but an ink jet printing head prints a polymeric binder according to the CAD design to bind powder, rather than a laser to sinter the material, as shown in Figure 2.5. Therefore, it is considered a simple and low cost process. The deposited binder bonds the printed areas together, while the imprinted areas works to support the printed areas from deformation during the forming process. Afterwards, the part is lift from the powder bed and goes under debinding and sintering process. To improve the microcomponents quality in density and surface finish, finer, dispersed and homogenous ceramic powder is recommended. Therefore, slurry based ceramic mixture was developed. A layer of the slurry is sprayed over the platform. After drying, the ink jet head selectively prints a layer in the desired areas to pattern the structure. The slurry process avoids internal microstructural inhomogeneities and flaws. In addition, it improves green density and shrinkage significantly [35-38].

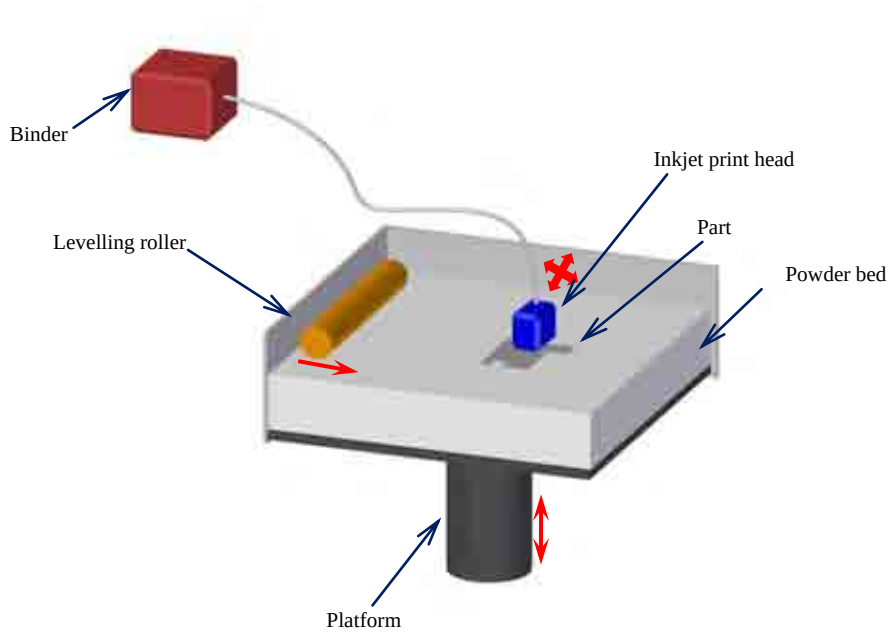

Figure 2.5. Schematic diagram of three-dimensional printing process.

2.2.1.6 Ink Jet Printing (IJP)

Ink jet printing (IJP) is an additive fabrication process that uses ink jet printers to print the required model. Here, the ink is replaced with ceramic mixture and kept in a slurry state. Unlike the 3DP, the ceramic powder is prepared in suspension to form colloidal mixture and deposited through the jet head instead of the binder systems. After printing, the patterned areas are left to dry and solidify instantly to form microcomponents. After completion of the layer building up, a milling head smoothes the surface. The particle collector takes the particles coming out from the smoothing process away. Then an elevator moves the platform down so that the fresh layer can be added. This process is repeated until the component is built, Figure 2.6. Rheological properties of the ceramic mixture and viscoelastic properties play the key roles for making optimized ceramic ink. Inkjet printing produces very good accuracy and acceptable surface finish. However, it is considered as a very slow building process, and the produced parts are fragile. There are two groups of ink jet printing system according to the printer used. The first one is called continuous ink jet printing and the second one is drop on demand ink jet printing. Ceramic suspension with a 40% vol. solid loading can be obtained [39-40]. Al_2O_3 suspension was prepared using n-alkane at low temperature of temperatures of 50-60 °C. Freestanding ceramic parts such as a rotation wheel with green wall thickness of 100 μm were successfully obtained by using drop-on-demand technique. After sintering, the final linear shrinkage achieved was 18% and the final sintered relative density was 80% [41-42].

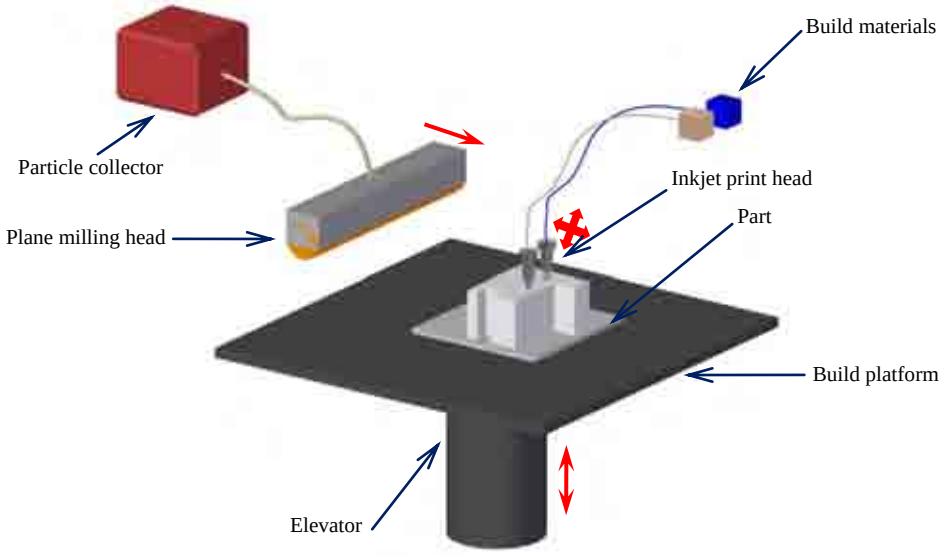

Figure 2.6. Schematic diagram of ink jet printing process.

2.2.2 Indirect Fabrication Processes

Conventional ceramic forming techniques are well established for shaping fine features in the millimetre scale using moulding techniques. However, it is challenging to get net shape ceramic parts when they have micrometer size features. In this section, indirect ceramic microfabrication techniques will be reviewed. The literature will include injection moulding, electrophoretic deposition, co-extrusion and soft lithography.

2.2.2.1 Microinjection Moulding (μIM)

Microinjection moulding is a popular forming technique for ceramic microfabrication. The technique is much similar to plastic injection moulding. It can fabricate a wide variety of sizes, complexity and materials. In the process, polymer or wax is melted and put together with ceramic powder to form a composite slurry and to be used by a microinjection moulding machine to fill moulds under heat and pressure, Figure 2.7. Afterwards, the moulds are left to cool and solidify and the green parts then can be demoulded. For small

features and high aspect ratio microcomponents, demoulding becomes a problem because of the increased surface area. A photoresist fabricated by UV or X-ray lithography is normally utilized as a lost mould to overcome the demoulding problems. After forming a component, the mould is removed by plasma etching to avoid the microcomponents damage caused by the conventional melting or dissolving methods. Low melting temperature materials are used as binders in a low-pressure injection moulding technique (LPIM). These methods allows the use of low temperature of 60-100 °C and pressures at 0.2 MPa, which offer the opportunity to use soft moulds instead of photoresist moulds. Slow thermal debinding processes at a rate of 0.1 °C/min and sintered at 1500 °C for 1 h were used to sinter zirconia microparts. After sintering, microcomponents showed 98% theoretical density and 12% linear shrinkage [43-46].

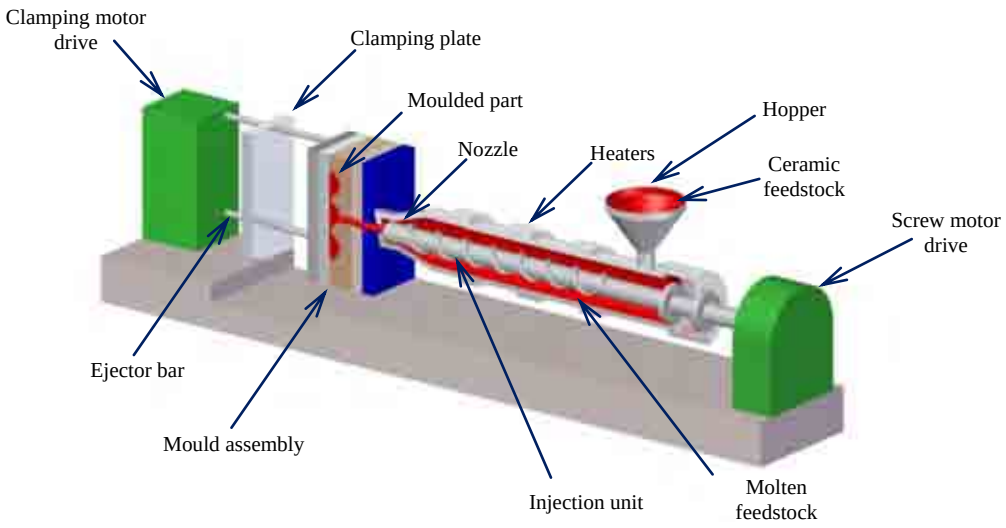

Figure 2.7. Schematic diagram of injection moulding setup.

2.2.2.2 Electrophoretic Deposition (EPD)

Electrophoretic deposition (EPD) is defined as a group of processes, which includes electrocoating, cathodic electrodeposition, and electrophoretic coating, or electrophoretic painting. In these processes, electric current is applied to a well-dispersed colloidal suspension, which results in migration of the suspended particles and forming a consistent deposition on the electrode surface, Figure 2.8. The mould is then being demoulded and sintered in order to intensify the powder compact. EPD has been successfully used to shape ceramic microcomponents by the means of micro moulds, coated or plated with a conductive layer. To produce parts with high mechanical properties and low surface roughness, well-dispersed suspensions should be employed. One of the disadvantages of this technique is the resultant low sintered density and the necessity to burnout the mould, which can easily damage the microcomponents due to high organic content in the mould. Apart from fabrication of ceramic microcomponents, EPD is also used to form thin films or coatings on different materials [47-51].

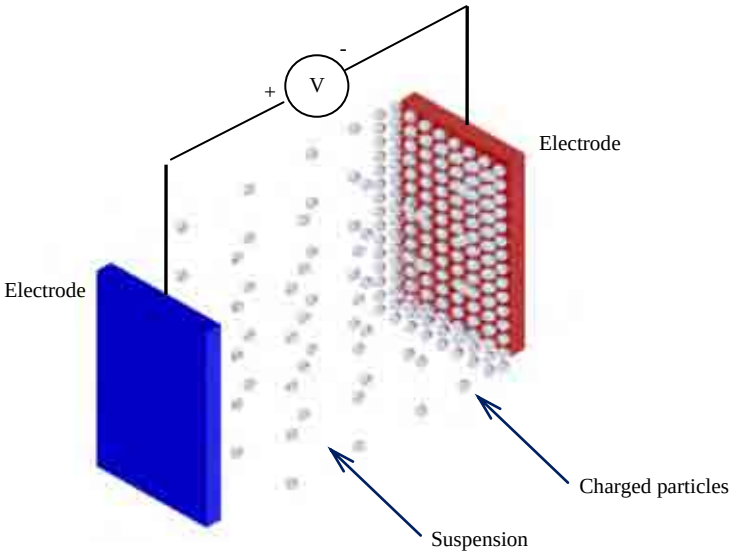

Figure 2.8. Schematic diagram of electrophoretic deposition principal.

2.2.2.3 Co-Extrusion

Extrusion is a very powerful technique for producing parts with uniform cross section such as cylinders, plates and honeycombs. Extrusion has been used to fabricate different materials includes plastic, metals and ceramics. In ceramic extrusion, the process is the same as plastic and metals extrusion except it uses plasticizers and binders to provide enough plasticity when forcing the feedstock through the die. The micro extrusion processing is based on the general extrusion processing but the size is in micrometer scale. Parts cross section shape is outlined by the extrusion die cross section, Figure 2.9. In co-extrusion, two different materials are involved. One is a primary material while the other is a support material. In simple shapes process, forming is carried out by using round or square dies, and performs the size reduction while the pattern in which the various compounds are assembled is maintained. Complex parts have been performed by using co-extrusion with carbon black as the support material in the extrusion and the sacrificial material in the sintering step. 10 μm feature size was successfully achieved using co-extrusion. Alumina objects were by buried in powder for support during sintering. The binder was removed with the following heating schedule in air: 5 °C/min to 100 °C; 1 °C/min to 250 °C; hold 1 h; heat 1 °C/min to 500 °C; hold 1 h. Sintering was done by heating at 5 °C/min to 1600 °C [52].

In the co-extrusion process, no expensive micromachining tools are required. In addition, it has the ability to achieve very fine micro-features with high aspect ratios. However, the extruded parts have to be post machined with cutting and grinding, which is complicated for such fine microcomponents [53-54].

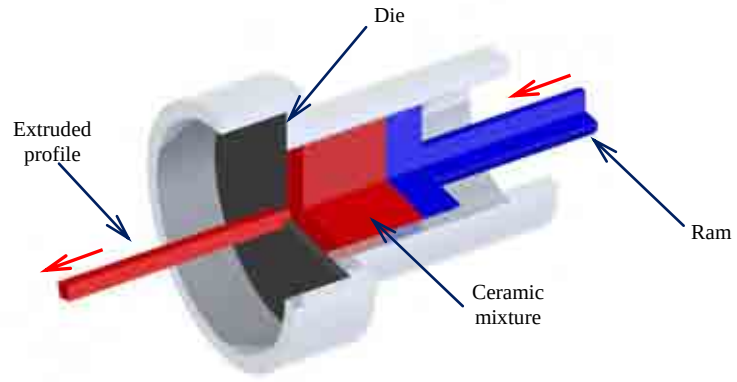

Figure 2.9. Schematic diagram of co-extrusion process.

2.2.2.4 Soft Lithography

Soft lithography is a non-photolithographic fabrication technique, which established on replica moulding and self-assembly for fabrication of micro and nanostructures from non-photosensitive materials. Soft lithography is an increasingly popular technique for its low cost template replication feature for a wide variety of applications. In soft lithography, a soft mould is used as a stamp with patterned relief microstructures on its surface to generate components with micro and nano features. The elastomeric stamp or mould with patterned relief structures is the key element in soft lithography. There are several materials that have been used for the elastomeric stamps, for example, poly (dimethylsiloxane) (PDMS) elastomers (or silicone rubbers) is used in most applications; some groups have used polyurethanes, cross-linked Novolac resins and polyimides. Five sub techniques have been developed, and they are microcontact printing (μCP), replica

moulding (REM), microtransfer moulding (μTM), micromoulding in capillaries (MIMIC), and solvent-assisted micromoulding (SAMIM) [55-58].

2.2.2.4.1 Microcontact Printing (μCP)

Microcontact printing (μCP) is a flexible technique that forms patterns in submicron lateral dimensions. A PDMS soft mould is used to transfer ceramic suspension of the ink to the top surface of a substrate by direct contact, which is shown in Figure 2.10. Additionally, it is also possible to use it with planar surface with planar stamp, planar surface with a rolling stamp and rolling surface with planar stamp. The technique is an attractive process because it is simple, inexpensive, flexible, and very efficient [59-61].

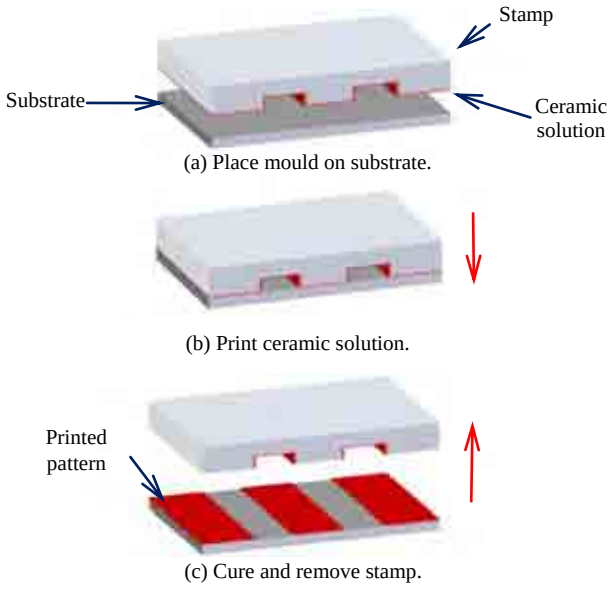

Figure 2.10. Schematic illustration of the general process of microcontact printing.

2.2.2.4.2 Replica Moulding (REM)

Replica moulding is considered an efficient technique for replication of pattern in the surface of a mould, Figure 2.11. Various kinds of ceramic suspensions and curable pre-

polymers have been patterned using replica moulding. Elastomeric moulds offer the chance to control the shape and size of micro features of the moulds by mechanical deformation. The capability and versatility of this procedure has been demonstrated for nanomanufacturing [62]. High-resolution nanolithographic processes are used to fabricate the moulds, and these nanostructures would then be duplicated into multiple copies by replica moulding with organic polymers. This process has also been tuned for the fabrication of topologically complex, optically functional surfaces that would be difficult to fabricate with other techniques [63].

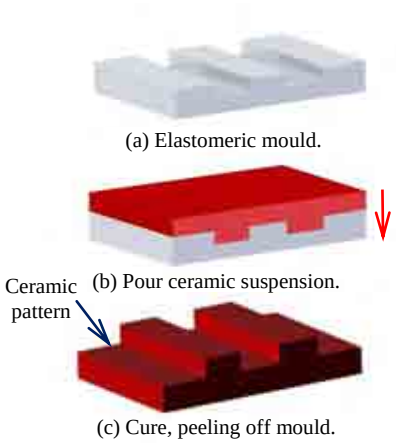

Figure 2.11. Schematic illustration of replica moulding process.

2.2.2.4.3 Microtransfer Moulding (μTM)

In microtransfer moulding (μTM), a drop of ceramic suspension or liquid precursor is casted to the surface of a patterned PDMS mould and the excess suspension is cleared away by cleaning with a flat razor blade or by blowing off with a nitrogen gun. The filled mould is then placed on a substrate and irradiated or heated. After the suspension is dried or cured to a solid, the soft mould is peeled away gently to leave a replica pattern on the

top surface of the substrate, Figure 2.12. Microtransfer moulding can fabricate microstructures of a wide variety of materials apart from organic polymers such as sol-gels, glassy carbon, and ceramics. In addition, it allows generating both interconnected and freestanding microstructures. The most significant advantage of μTM over other microlithographic methods is its simplicity and suitability to manufacture micro patterns on non-planar surfaces, a property that is crucial for building three-dimensional microstructures [64-66].

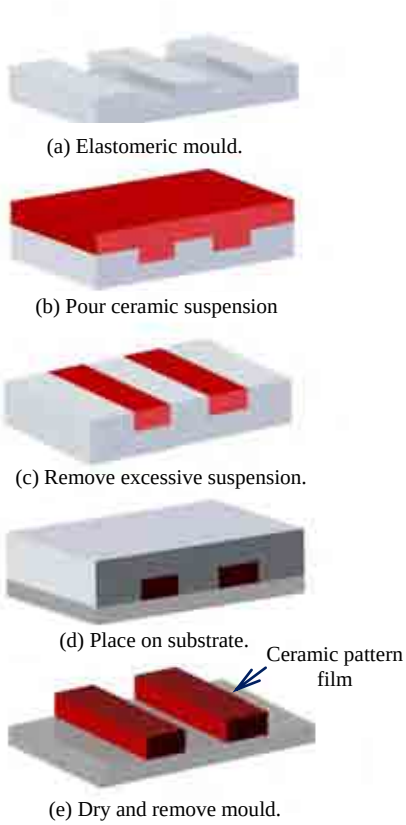

Figure 2.12. Schematic illustration microtransfer moulding process.

2.2.2.4.4 Micromoulding in Capillaries (MIMIC)

In micromoulding in capillaries, the PDMS mould is adhered on top of a substrate and creates conformal contact to that surface. Next, the relief micro pattern in the mould builds a connection of empty micro channels. When a low-viscosity ceramic suspension or pre-polymer is dropped at the opening of the network channels, the suspension freely fills the micro channels by capillary forces. After filling the channels, the suspension is left to cure into a solid. Afterwards, the PDMS mould is peeled off and a residual solid micro pattern remains on the surface of the substrate, as shown as in Figure 2.13. MIMIC represents another non-photolithographic technique that forms microstructures on planar and curved surfaces. MIMIC is also capable to pattern a wide range of materials such as UV-curable prepolymers, suspensions or solutions of functional or structural polymers, precursor polymers to glassy carbon, sol-gel materials. Ceramic microfabrication based on MIMIC technique is considered remarkable for its simplicity and its accuracy in transferring the patterns from the soft mould to the ceramic structures that it forms [67-69].

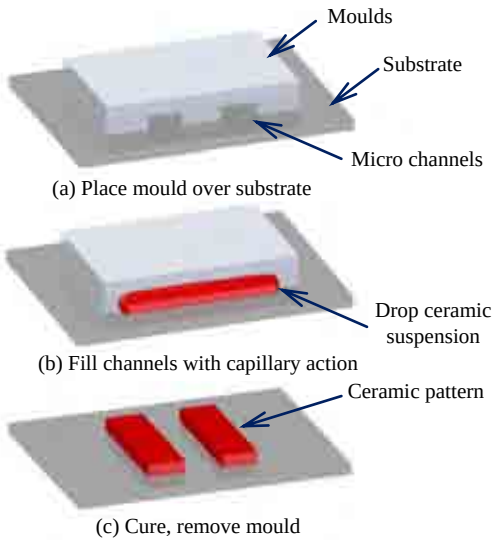

Figure 2.13. Schematic illustration micromoulding in capillaries process.

2.2.2.4.5 Solvent-Assisted Micromoulding (SAMIM)

Solvent-assisted micromoulding (SAMIM) is a process that offers fabrication of microcomponents on the surfaces of polymeric substrates. It is also used to alter the surface structures of polymers. The general principle of this process combines the methodology of both replica moulding and embossing as shown in Figure 2.14. In this technique, a preceramic polymer is spread over a substrate. On the other hand, a PDMS soft mould is covered with a wetting solvent. Next, the PDMS mould is placed to the surface of the coated substrate. The solvent dissolves the polymer in contact, forming the resulting pattern of the surface of the soft mould. Afterwards, the solvent is evaporates and the polymer solidifies to form the desired patterns attached to that on the surface of the mould [70-71].

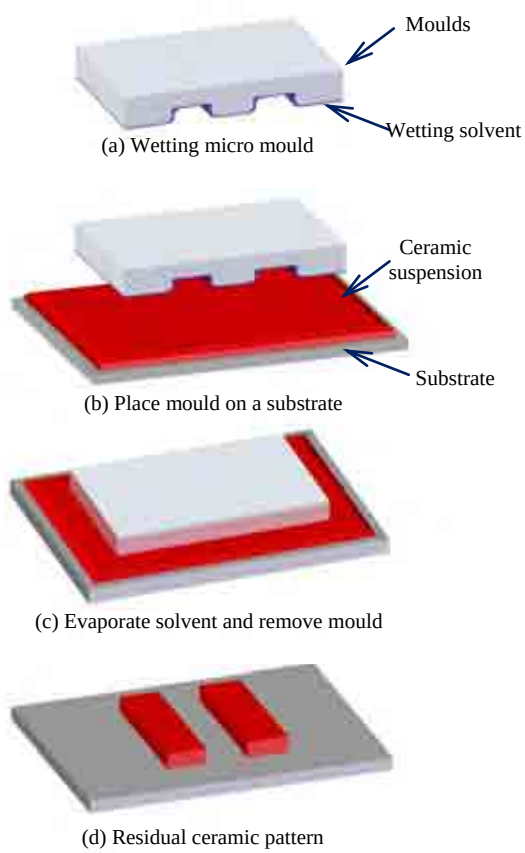

Figure 2.14. Schematic illustration solvent-assisted micromoulding process.

2.3 Ceramic Sintering

Ceramic sintering is a processing technique used to produce density-controlled components from ceramic powders by applying thermal energy. Figure 2.15 shows the general fabrication pattern of sintered ceramic parts [72]. To obtain dense ceramic components, it requires a number of stages, including mixing, incorporating additives, shape forming, drying and sintering.

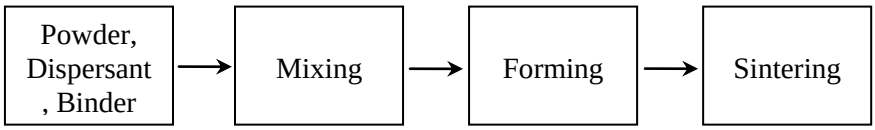

Figure 2.15. General fabrication pattern of sintered ceramic parts.

2.3.1 Categories of Sintering

Sintering can be divided into two main categories: solid state sintering and liquid phase sintering. Solid state sintering occurs when the powder compact is totally densified in a solid state at the sintering temperature, while liquid phase sintering occurs when a liquid phase is formed during processing. Other types of sintering such as viscous flow sintering and transient liquid phase sintering can be also utilized. Figure 2.16 shows the different categories in a schematic phase diagram [73].

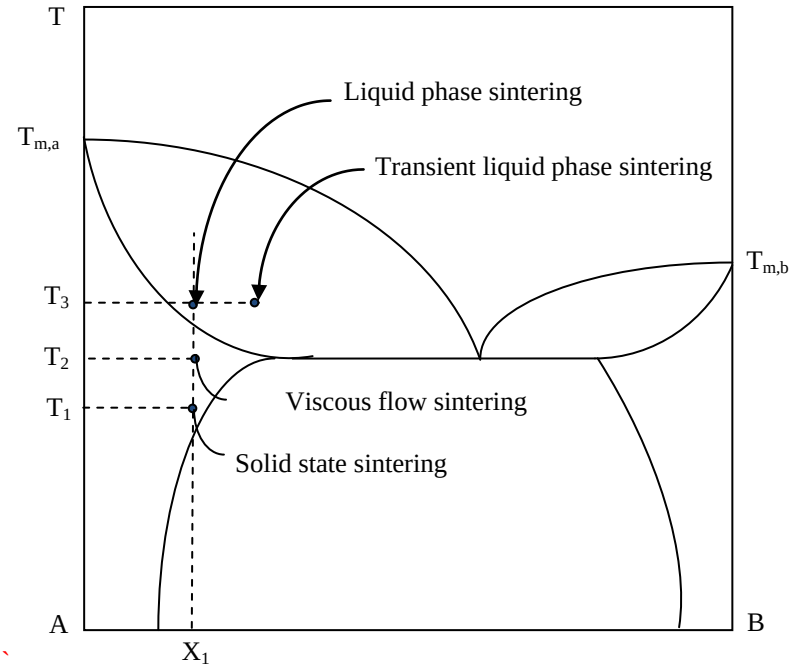

Figure 2.16. Illustration of various types of sintering [73].

2.3.2 Sintering Mechanism

The driving force influential to sintering process is the reduction of the total interfacial energy. This can occur by (1) reducing of the total surface area by increasing the average particles size, which leads to coarsening, and/or (2) eliminating solid/vapour interfaces and creation of grain boundary followed by grain growth, which leads to densification. Solid-state sintering mechanism can be divided into three main stages, i.e. an initial, an intermediate, and a final stage, as shown in Figure 2.17. In the initial stage, the interparticle contact area increases by neck growth, and the relative density increases from about 60 to 65 percent. The intermediate stage is characterized by continuous pore channels and formation of grain boundaries. During this stage, the relative density increases from 65 to about 90 percent, and pores are still connected with each other and form a continuous pore network. The final stage begins when the pore phase eventually diminishes and is

characterized by the absence of a continuous pore channel. In addition, the isolated pores are located at grain boundaries (interfaces), or linear junctures of three grains or point junctures of four grains, and/or entrapped in grains. Density increases slightly but the microstructure develops (grains grow) very rapidly in this stage of sintering [72-74].

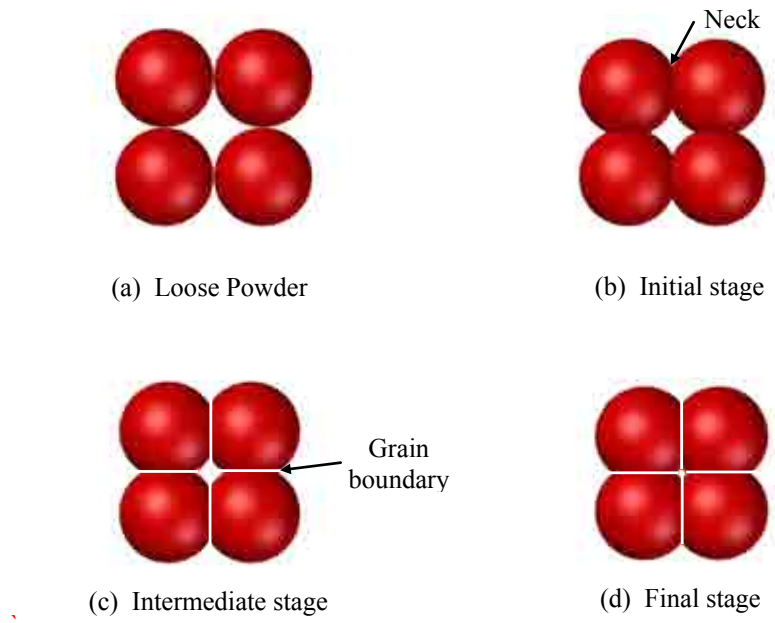

Figure 2.17. Solid-state sintering stages.

2.3.3 Effect of Powder Packing on Sintering Properties

In real ceramic green parts, the sizes of the particles are different, and pore size and distribution are nonuniform. Therefore, differential densification happens and particles may move, which can cause the production of larger pores. Grain growth at the initial stage of sintering may also cause the formation of large pores. This means that the particle packing and distribution are an important parameter, which determines the sintering kinetics of real green bodies. Particles size in the green compact plays an important role during sintering. As the average particle size in green compact is reduced, the specific

surface area is increased and the diffusion distance is reduced. The finer the particle, the faster the sintering rate [75-78]. Sintering behaviour depends also on the green compacts density. It is found that the maximum sintered density is higher and the temperature for the maximum densification rate is lower for the higher green density. It is suggested that the population of the pores is drastically reduced for green densities larger than 58% and giving higher amount of sinterable pores [79-80]. Non-uniform green density may also form large flaws. When green parts have large agglomerates, the compact density is locally non-uniform and full densification is hard to obtain because of differential densification during sintering. When differential densification occurs, internal stresses build up in and large flaws can form. Therefore, the formation of large pores during formation of the green parts must be avoided in order to achieve full densification [81].

2.4 Monolithic Ceramic Microcomponents

The word ceramic came from the Greek word keramos, which means pottery and porcelain. The description includes inorganic and non-metallic materials whose structure is formed by either heat or heat and pressure, producing at least one metal and a non-metallic element, or a structure combined of at least two non-metallic elements, or a structure combined of at least two non-metallic and a non metallic elements [82].

Ceramics can be divided according to their chemical bonding structure into two main categories, the ionic and the covalent ceramics. The ionic ceramics, such as alumina and zirconia, basically consists of metallic and non-metallic compounds. While, the covalent ceramics, such as silica, usually consists of two non-metallic elements. Ionic and covalent bonds are very strong and present high lattice resistance to the motion of dislocations. Therefore, ceramics usually have high Young's modulus, high flexural strength, and low

fracture toughness. The need for enhanced mechanical properties under demanding conditions was the motivation to develop structural ceramics where they are subject to mechanical loading and serve as structural members and, therefore, they are named as structural ceramics [83]. Compared to metals, ceramics have a higher strength, lower density, lower thermal expansion coefficient and very high melting temperature. High strength and low density implies the potential for high load environment. High melting temperature and low expansion coefficient implies the high operating temperature and dimensional stability during operation. All of these attributes are desirable for micro devices that operate in sever conditions of high temperature and high stress. Although structural ceramics have extraordinary properties, their toughness is still lower than metals. In addition, their flexural strength is affected by the surface roughness properties [84].

2.4.1 Alumina

Alumina is regarded as one of the most popularly used advanced ceramic materials. its availability as low cost material makes it commercially used in many applications. In addition, the availability in highly purified grades makes it very popular in materials research studies [82]. Alumina represents about 25% of the earth's crust, but often occurs in forms of hydrous aluminium oxide phases or combined oxides in a wide variety of minerals. α-Al_2O_3 is the most thermally stable phase among the aluminium oxides. The major properties of sintered α-Al_2O_3 are listed in Table 2.1. The purity of listed α-Al_2O_3 is at least 99.5% and its average grain size is about 5 μm. Alumina has an excellent thermal shock resistance owning to its high thermal conductivity, low thermal expansion coefficient and extraordinary strength. Therefore, they are suitable for high temperature furnace products, such as crucibles, tubes and thermocouple cases. High purity alumina can be operated up to 1700 °C and is able to seal gases up to 1300 °C. Alumina is

chemically stable because of its melting point of 2050 °C. In addition, alumina shows extraordinary hardness, wear resistance, and electrical insulation properties, making it very popular for mechanical elements such as piston pumps and deep drawing tools. Its wide availability in purity ranges from 94% to 99.9% can satisfy a variety of most demanding high temperature applications. Moreover, alumina exhibits very good dielectric properties, making it popular in electronic components [86-88].

Table 2.1. Selected properties of sintered α-Al_2O_3 [86-88].

Properties	**Unit**
Density (g/cc)	3.97-3.99
Shear modulus (GPa)	161-164
Elastic modulus (GPa)	380-405
Flexural strength (MPa)	150-450
Hardness Vickers (GPa)	15-19
Fracture toughness ($MPa.m^{1/2}$)	3.5-6
Tensile strength (MPa)	267
Thermal conductivity ($W.m^{-1}.K^{-1}$)	30-40

Soft lithography has been used previously in manufacturing alumina microcomponents. Schonholzer et al. firstly described the process to fabricate ceramic structure with features in the range of several micrometers [89-90]. They used PDMS moulds to pattern alumina structure. Alumina suspension was used to fill the micro mould. Next, peeling off the mould and sintering, as shown in Figures 2.18(a)-(b). The authors then further replaced the PDMS mould with a photoresist mould, use it as a lost mould and dissolve it prior sintering process. The SEM results are shown in Figures 2.18(c). The samples have reached to nearly the full density with shrinkage of nearly 15%. They also studied the effect of

different particle sizes on the features resolution of ceramic component, but their work was limited to cavities only.

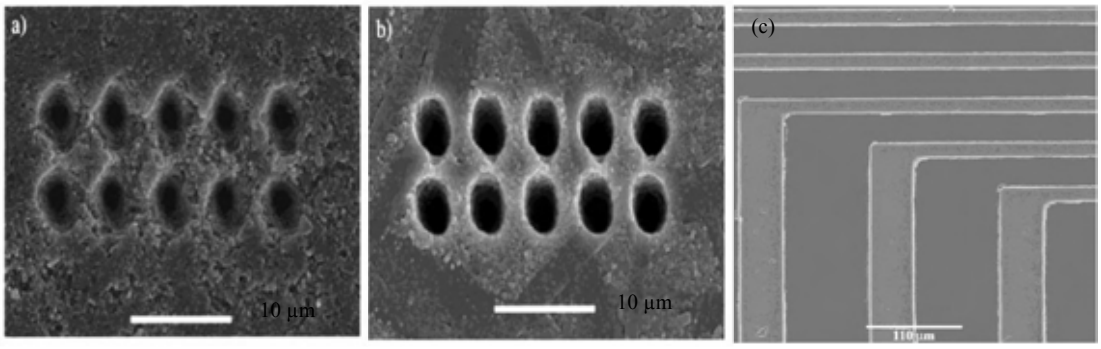

Figure 2.18. Alumina cavities fabricated with an average diameter of (a) 0.5 µm, (b) 0.2 µm, (c) alumina structure fabricated using photoresist lost mould.

Jin et al. used also PDMS soft mould for the development of alumina microcomponents [91]. They used high solid loading alumina suspension of 84% wt. to fill the PDMS moulds and successfully fabricated sintered microcomponents with aspect ratio of 10 and linear shrinkage 17 %.

Zhu et al. also used PDMS as elastomeric mould and succeeded in fabricating near net shape alumina microcomponents [92]. Alumina rheological properties have been characterised with varying pH value and amount of dispersant. The optimal composition of the suspension for mould filling was obtained. After pressurized filling, complete, dense and freestanding microgears were manufactured by applying alumina slurry and optimum fabrication technique, and the overall shrinkage was 22 %. In the characterisation process, the authors optimized pH and dispersant of the slurry independently. Zhang et al. also used both solid mould embossing and soft mould centrifugal casting to fabricate three-dimensional alumina micro components [93-94]. They used highly concentrated alumina

with a solid loading of 84% wt. to fill the mould. The structure was patterned on thin photo resist layers coated on an alumina substrate by the use of soft polymer moulds. The freestanding components were realized by dissolving the sacrificial layer in acetone to realise the green ceramic structures. Low shrinkage of about 15%, dense and freestanding components were obtained after sintering, Figure 2.19.

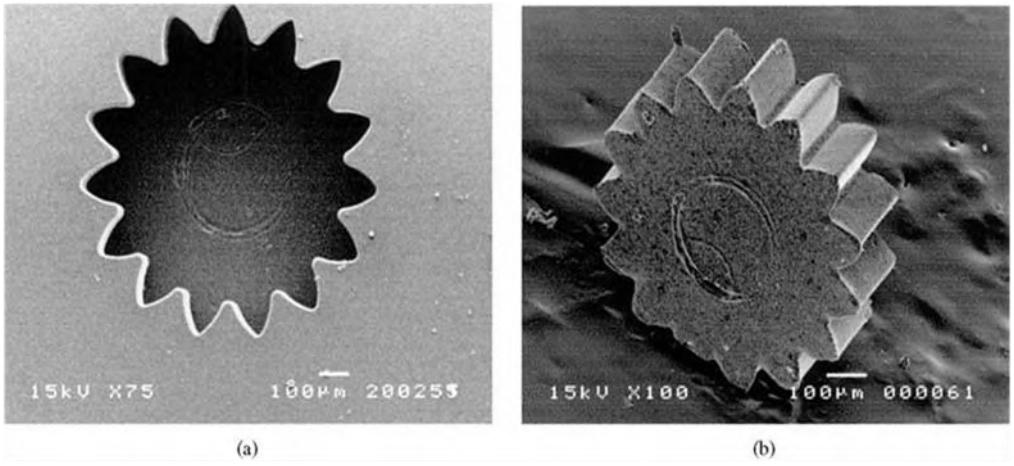

Figure 2.19. SEM micrographs of (a) silicone rubber mould (b) Alumina ceramic microgear.

2.4.2 Yttria Stabilised Zirconia

Pure zirconia has different crystal structures along with different temperatures. It has monoclinic crystal structure at room temperature and pressure. The material transforms to tetragonal structure at approximately 1170 °C and then transforms to a cubic fluorite structure at about 2370 °C. It melts at 2716 °C. These crystal transformations are martensitic and involve a shape and volume deformation during cooling. These changes limit the use of pure zirconia in applications where temperature changes. The family of zirconia was employed as structural material only during the 1970s when the transformation toughening of zirconia enhanced its mechanical strength for use in harsh

applications. Because of this feature, zirconia ceramics have since been called (ceramic steel). Several oxides were successfully used to stabilise zirconia. These oxides dissolve in the zirconia crystal structure and slow down or eliminate the associated crystal structure transformations. The most popular oxide effective additives are Y_2O_3, CaO and MgO [95].

Yttria stabilized zirconia (YSZ) has very good mechanical and electrochemical properties. The addition of yttria to pure zirconia provides sufficient vacant site mobility, which improves the ionic conductivity, and makes it suitable for solid oxide fuel cells. YSZ has a good corrosion resistance, good optical properties and low thermal conductivity, which makes it attractive for a range of high temperature applications such as microengine [96-98]. Therefore, it is expected to increase engine thermal efficiency through more complete combustion of fuel at high working temperatures.

Table 2.2. Selected properties of sintered 8YSZ [96-98].

Properties	Units
Density (g/cc)	5.953
Elastic modulus (GPa)	200
Flexural strength (MPa)	250-416
Hardness Vickers (GPa)	13.8
Fracture toughness ($MPa.m^{1/2}$)	1.6
Tensile strength (MPa)	276
Thermal conductivity ($W.m^{-1}.K^{-1}$)	2

Literature found in the fabrication of zirconia microcomponents has been based on microinjection moulding, the primary reason being that microinjection moulding technology has become well established in powder processing and polymer industry due to

the ability to produce complex shape parts that are achievable at a reasonable quality cost. Piotter et al. managed to fabricate zirconia microparts using microinjection moulding [99]. They explored the potential of microinjection moulding for large-scale manufacturing of microcomponents. Muller and co workers fabricated and tested the bending strength of zirconia micro beams for the optimization of the fabrication process using microinjection moulding [100-101], Figure 2.20. They found that the strength of micro bending samples is increasing with the increase in density and increasing edge radius, and decrease in roughness. In addition, they did not find considerable effect of the grain size on the bending properties.

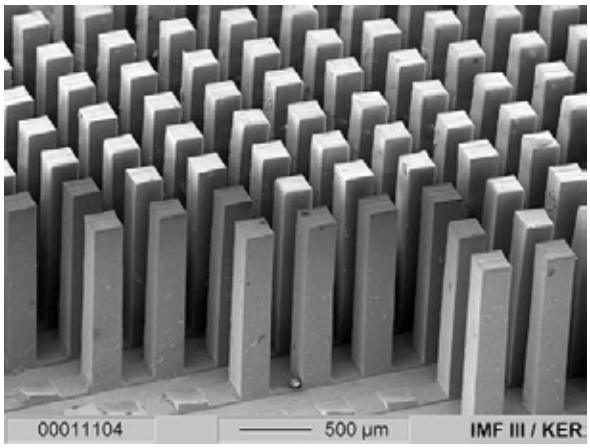

Figure 2.20. SEM image of sintered ZrO_2 column array.

Yu et al. successfully produced yttria stabilized zirconia tensile bars and 3 mm microgears using microinjection moulding [102]. They studied the solid loading effects on the sintered density, weight loss and Vicker hardness. Agglomeration problems were addressed using optimum process. They managed to obtain microcomponents with high density, Figure 2.21.

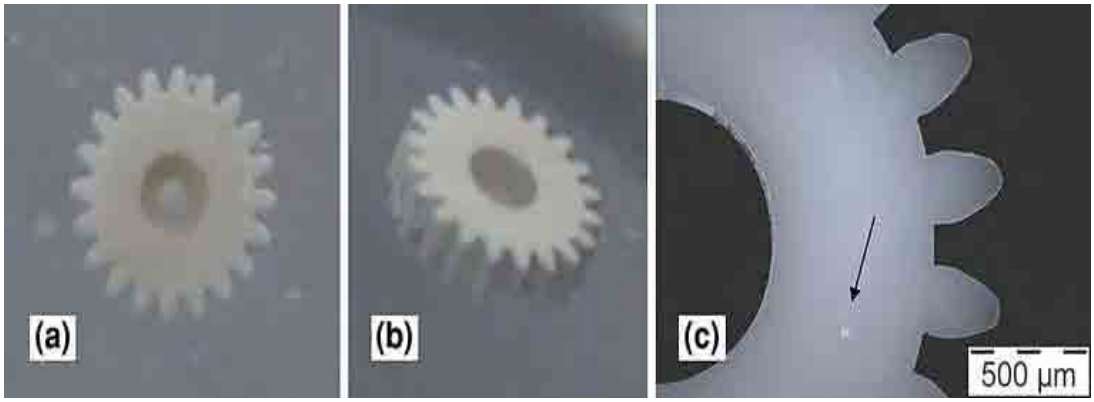

Figure 2.21. Optical microscopic photographs showing (a) the top and (b) isometric views of a sintered micro gear (c) well defined gear teeth.

2.5 Ceramic Composite Microcomponents

Monolithic ceramics holding promise for use in many MEMS applications. These materials perform satisfactorily in their pure state. However, in special applications, structural ceramics are required to be more resistant to harsh environments. Composite ceramics provide the ability to create a huge number of new ceramic systems having tailored and functional properties that cannot be obtained using the monolithic ceramic material [103]. A review of ceramic composite microcomponents is given, along with composite microcomponents processing information. The review is divided into two main sections. The first section is ceramic matrix nanocomposite microcomponents and the second one is functionally graded ceramic composite microcomponents. In the following, the most reported literature involved in the processing of composite matrix microcomponents will be analysed in detail, arising from fabrication processes to characteristic properties of resultant microcomponents.

2.5.1 Ceramic Matrix Nanocomposite Microcomponents

Ceramic matrix nanocomposites combine embedded phases with a ceramic matrix to form materials with tailored and superior properties. The embedded phases could be metallic, ceramic or polymers, exist in the form of particles, fibres or textile, and are dispersed homogenously in the matrix. This approach to construction holds great promise for future bulk and microcomponents. Their composition can be designed to meet the property requirements, rather than selecting monolithic ceramics to do so [104].

In reviewing the current literature in ceramic matrix nanocomposite microcomponents, it is important to note that most of the research work has been invested to produce metallic matrix nanocomposite microcomponents [105-113]. Apart from rapid prototyping techniques, a very few reports were found in fabrication of ceramic matrix nanocomposite matrix microcomponents.

Electrophoretic deposition (EPD) has been used, as all stable colloidal suspensions can carry a charge, including ceramics and carbon nanotubes CNTs. Zaman et al. [114] have fabricated Boehmite/multi-wall carbon nanotube (MWCNT) nanocomposite 3D microcomponents using electrophoretic deposition. They used aluminium acetate powders ($2Al(OH)(C_2H_3O_2)_2$) and MWCNT through hydrothermal process for preparation of Boehmite/multi-wall carbon nanotube (MWCNT) nanocomposite powders. The results show that kinetically stable suspensions of MWCNT– boehmite composite powders were obtained. Later, electrophoretic deposition (EPD) was applied to prepare suspension for fabrication of 3D microgear as shown in Figure 2.22. Small components such as microgear were successfully fabricated using EPD technique in short time. In the characterisation of the EPD Boehmite/CNT nanocomposite microgear microstructures, SEM images shows a

quite dense and free of large voids and pores. Pullout and bridging mechanisms of CNT in the Boehmite matrix are clearly shown in Figure 2.23.

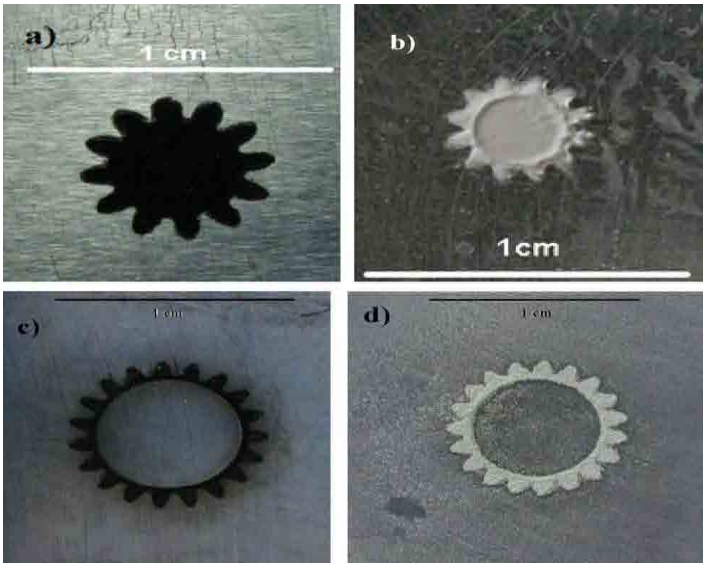

Figure 2.22. Electrophoretically formed 1% wt. CNT-reinforced boehmite (a,c) and alpha alumina (b,d) microgears before sintering.

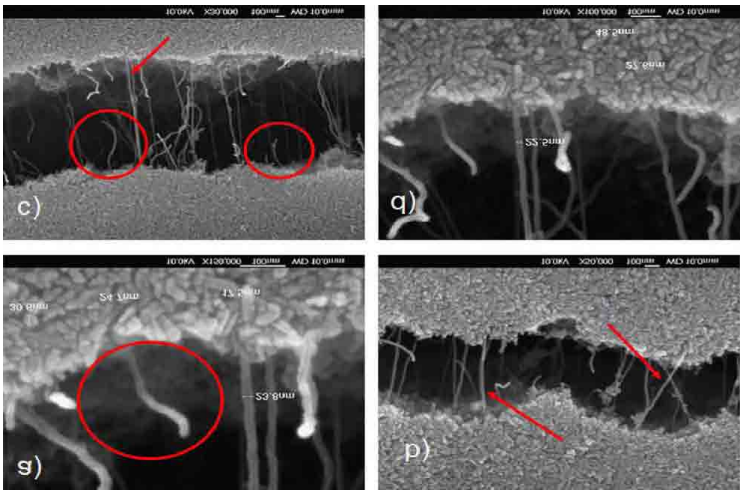

Figure 2.23. SEM images of CNT-reinforced boehmite microgear shape.

Gadow et al. managed to fabricate zirconia toughened alumina for microcomponents applications using injection moulding process and modified pressureless sintering process [115]. The smallest sample dimension fabricated was 0.65×5.7×2.8 mm^3. They managed to sinter the samples to nearly their theoretical density with very fine grains by modifying the feedstock recipe at only about 1500 ^oC. The sintered grains were in the range of 0.4 to 1.4 µm, which is believed to enhance the mechanical properties, Figure 2.24. However, the fabricated samples were small components in irregular shapes.

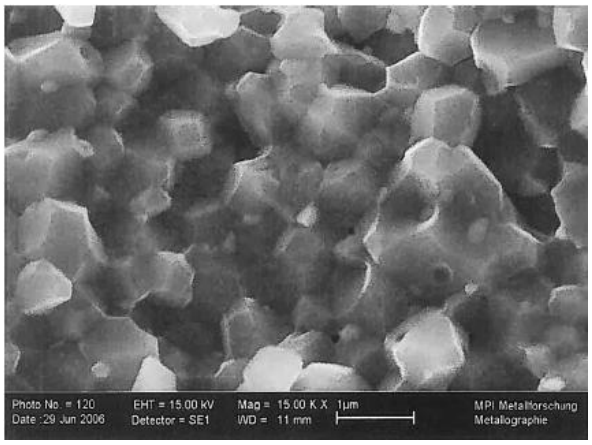

Figure 2.24. SEM image of alumina/3YSZ sample sintered at 1450 for 6 h.

Chan et al. fabricated silica titania composite microgears using sol-gel casting technique [116]. Near net shape silica microcomponents were obtained with dispersed titania. They studied the permeability of the moulds and surface properties for sol gel casting optimization. The resultant ceramic composite microgears have dense sidewalls due to the high quality PMMA mould and good wetability, but bottom surfaces were porous because of the impermeable bottom surface of the mould and restricted shrinkage, Figure 2.25.

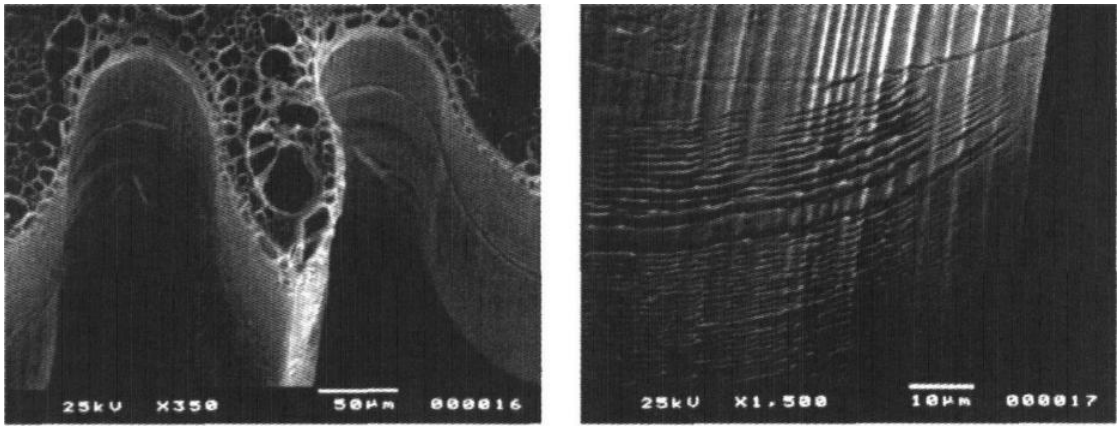

Figure 2.25. SEM images of the (a) bottom surface and (b) sidewalls of the ceramic microgear made by sol-gel casting.

As reviewed, there were few attempts to fabricate ceramic matrix nanocomposites microcomponents. The obtained microcomponents are far from the net shape quality. In addition, authors did not perform mechanical characterization to the resultant samples.

2.5.2 Functionally Graded Ceramic Composite Microcomponents

Functionally graded composite materials (FGM) are composite materials where both the composition and the structure of each material in the composite gradually vary over the volume, resulting in tailored or functional properties at each structure in the material [117]. Similarly to ceramic matrix nanocomposite microcomponents, there are few literature reported on functionally graded composite small components and are reviewed here. No reports were found in the fabrication of functionally graded components in micro scale size.

Takagi et al. studied the properties of the PZT/Pt composites with the aim to fabricate a PZT/Pt FGM actuator with gradient microstructure for enhanced mechanical reliability [118]. They found that, adding Pt particles into the PZT matrix enhances the mechanical

properties of the composite parts. Although they did not fabricate the actuator but they concluded that, a bending-type actuator with graded microstructure from PZT to PZT/Pt composites can be manufactured by powder processing.

Imgrund et al. used microinjection moulding technique to fabricate combination of magnetic and non-magnetic bimetals made of 316L/17-4PH and 316L/Fe parts in millimetres scale [119-120], Figure 2.26. They used fine powders of 3-7 μm mixed with wax polymer binder system to prepare the feedstock. In addition, they evaluated the isothermal and non-isothermal sintering properties of the moulded parts under hydrogen atmosphere.

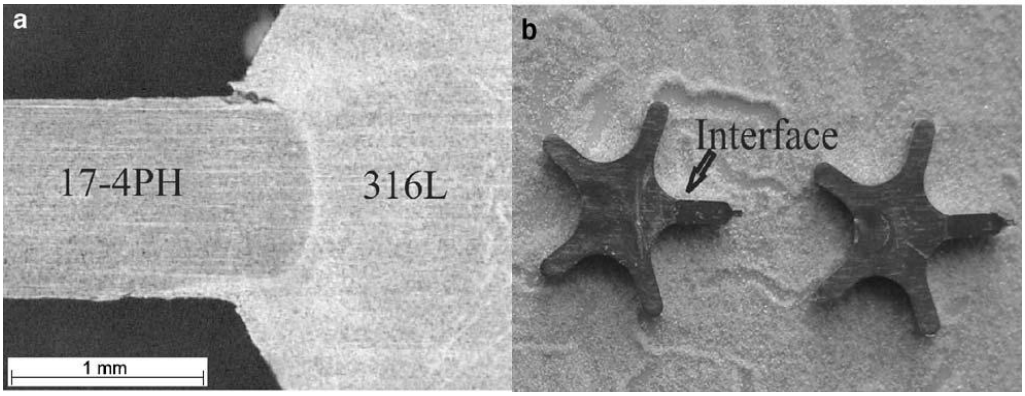

Figure 2.26. Interface of sintered miniature tachometer.

2.6 Summary

Main techniques for producing ceramic microcomponents have been reviewed in Section 2.2, including direct solid freeform and indirect fabrication techniques. In each technique the main advantages, disadvantages and comments are reported. Solid free forming techniques presented in the literature include stereolithography, laser micro sintering, three dimensional printing, fused deposition modelling, laminated object manufacturing and ink

jet printing. On the other hand, indirect fabrication techniques reviewed here include, injection moulding, electrophoretic deposition, co-extrusion and soft lithography. Based on the analysis of the mentioned ceramic microfabrication techniques it can be concluded that, soft lithography is regarded the most suitable technique for the microengine. When compared to the reported techniques, micro parts fabricated using soft lithography does not suffer from low resolution, poor surface finish and low density, which are the main limitations when using the reported fabrication techniques. In addition, Soft lithography is considered productive and low cost fabrication method where the mould can include many micro moulds. The main fabrication techniques is followed by a review of ceramic sintering and has been presented in Section 2.3. Afterwards, a detailed review of the candidate ceramic materials used for the microengine has been presented in Section 2.4. Alumina and zirconia were selected as candidate ceramic materials for the microengine owing to their reported excellent properties. Work in ceramic composite microcomponents is reported in Section 2.5. It has been shown that work in this area is very limited. As reviewed, fabrication of ceramic composite microcomponents is needed for improved, tuneable and functional properties of the microengine different parts.

The review reported in this chapter has a considerable influence on the direction of this research. The possible material and fabrication technology for the microengine components are selected. The main challenges faced in this research are identified to be the fabrication of high quality moulds and to choose the appropriate powder processing approach suitable to fill the mould and to obtain the defects free green and sintered monolithic and composite parts with high accuracy, physical and mechanical properties using soft lithography.

CHAPTER 3: FABRICATION OF MASTER AND SOFT MOULDS

3.1 Introduction

This chapter describes the use of a soft lithography technique for the fabrication of ceramic microcomponents. Master and soft moulds are crucial parts in the soft lithography technique and affect the quality of each subsequent step in the process. The master carries a micro-pattern design on the surface that serves as a template for the production of soft mould replicas. In this chapter, fabrication and examination of master and soft moulds are studied. The chapter begins by presenting the micro reciprocating engine design in Section 3.2. Section 3.3 describes the general fabrication process of ceramic reciprocating engine parts. Section 3.4 explains the characterisation methodology used for the examination of the master and soft moulds. Fabrication process details and results of the SU-8 master and PDMS soft moulds are discussed in Section 3.5 and Section 3.6, respectively. Alternative methods and materials for both SU-8 and PDMS are introduced and discussed in Section 3.7. Finally, the chapter is summarized in Section 3-8.

3.2 Micro Reciprocating Engine Parts

Research into the fabrication of a micro reciprocating engine was started by Kyle Jiang in the Micro/Nano technology group at the University of Birmingham in 2001. A representation of the micro reciprocating engine, assembled from parts designed by Jin et al. [1] is shown in Figure 3.1. The engine has dimensions of 10.6×3.3×3 mm^3, rotational speed of 5000 rpm and power output of 7.3 mW. The microengine parts have a thickness

of 1000 µm, minimum feature size of 75 µm, and high aspect ratio of 10. As shown in Figure 3.1, the high precision microgear teeth and its involute profile make the gear the most complex part within the microengine. Therefore, it was extensively used for fabrication, examination and characterization throughout the PhD thesis.

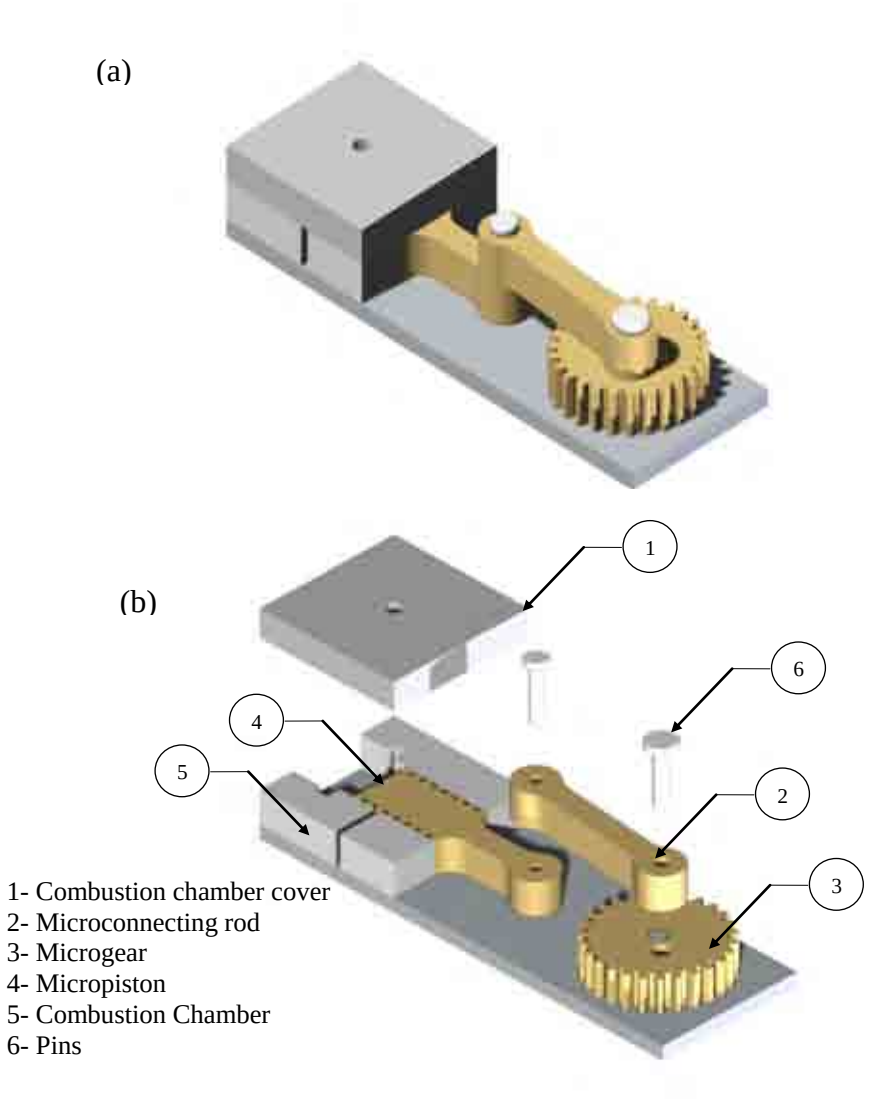

Figure 3.1 (a) Microengine assembly, (b) exploded views of the microengine parts

3.3 Fabrication Process of Micro Reciprocating Engine Parts

The general process chosen for the fabrication of the ceramic microengine components consisted of the following steps.

1. Fabrication of ultra thick master moulds using UV photolithography.
2. Fabrication of soft moulds replicas from the master moulds.
3. Preparation of ceramic slurry to fill micro features of the soft moulds.
4. Filling the soft mould cavities with the ceramic suspension.
5. Drying, demoulding and sintering.

A schematic diagram of the process is shown in Figure 3.2. As will be explained in the following sections, modifications were applied to this process according to mould materials, filling of the moulds and the micro part design. Since this chapter focuses on the fabrication of master and soft moulds, only steps from 1 to 6 were required. Materials proposed as suitable for forming into master moulds were SU-8, BPR100, reinforced PDMS and deep reactive ion etched substrates. In addition, PDMS and Dragon Skin were proposed as soft moulds. For each of the proposed master and soft moulds, optimization of the fabrication process was required, as indicated by high resolution, accurate dimensions and smooth surface moulds.

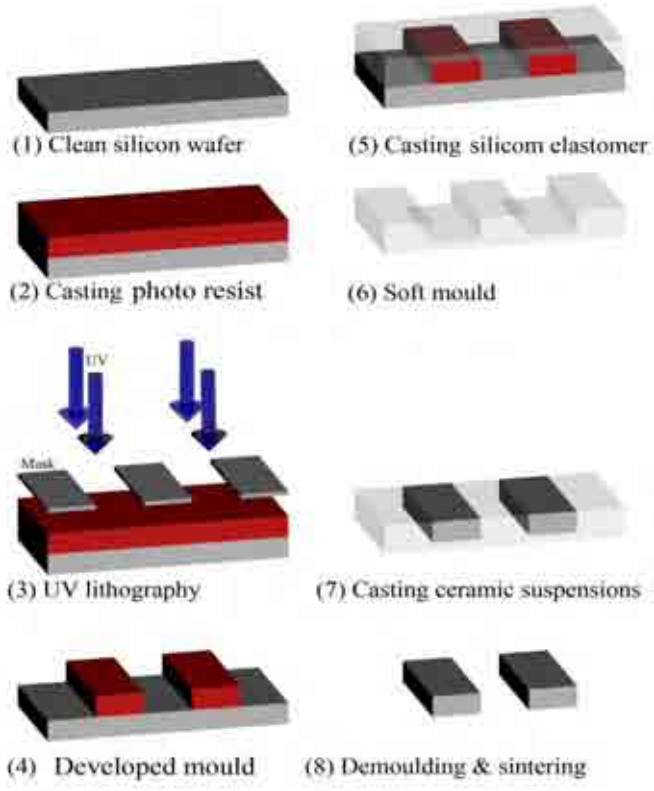

Figure 3.2. Schematic diagram of the fabrication process.

3.4 Characterisation Methodology

Examination of the master and soft moulds was performed using scanning electron microscopy (SEM) micrographs. Surface topography and roughness were obtained using a stereo imaging technique.

3.4.1 Scanning Electron Microscopy Graphs (SEM)

As both the master and soft moulds define the shapes of the final ceramic microcomponents, moulds were examined to check the strict geometric requirements given in the design of the microengine components. Vertical sidewalls of the moulds throughout the depth are important aspects to ensure parallel sidewall surfaces between the

microengine moving parts, thus avoiding leakage. Jeol 7000, Philips XL-30 and Focus Ion Beam (FIB) SEM machines were used throughout the study. The electron beam was ranging from 5 keV to 20 keV depending on the resolution requirement. In addition, the SEM micrographs were used to construct 3D surfaces using stereo imaging. The SEM samples were prepared by attaching the part to an aluminium stub using conductive adhesive tape. To prevent a build-up of surface charge during image acquisition the samples were then sputtered with a gold layer prior to SEM examination.

3.4.2 Surface Roughness Measurements

Surface roughness is an important parameter in the characterization study for both moulds and ceramic parts. Surface roughness affects device performance during operation, especially for moving parts.

Surfaces are defined using amplitude parameters such as average roughness (R_a), root mean square roughness (R_q), peak roughness (R_p), valley roughness (R_v), skewness (R_{sk}) and kurtosis (R_{ku}):

Average roughness (R_a) is average height of all the maximum peaks and minimum valleys from the mean line over the measured distance, L.

$$R_a = \frac{1}{L}\int_0^L |r(x)|dx \qquad \text{Eq. 3.1}$$

Root mean square surface roughness (R_q) is calculated as the root mean value of the average height.

$$R_q = \sqrt{\frac{1}{L}\int_0^L r^2(x)dx} \qquad \text{Eq. 3.2}$$

Peak roughness (R_p) is the maximum height of peak over the measured distance.

$$R_p = \left|\max[r(x)]\right| \quad \text{Eq. 3.3}$$

Valley roughness (R_v) is the maximum valley depth value over the measured distance.

$$R_v = \left|\min[r(x)]\right| \quad \text{Eq. 3.4}$$

Skewness (R_{sk}) measures the asymmetry of the surface profile. Positive skewness indicates a surface dominated by peak. On the other hand, negative skewness indicates a surface dominated by valleys.

$$R_{sk} = \frac{1}{LR_q^3}\int_0^L r^3(x)dx \quad \text{Eq. 3.5}$$

Kurtosis (R_{ku}) shows the value of spikiness or bluntness of the surface profile.

$$R_{ku} = \frac{1}{LR_q^4}\int_0^L r^4(x)dx \quad \text{Eq. 3.6}$$

Throughout this thesis, measurements of surface roughness were obtained by producing a 3D reconstruction of the surface using stereo imaging. In this technique, two SEM images were taken for a surface with a normal tilting angle between 5^o and 8^o. The third dimension (Z) can be concluded as follow:

$$Z = \frac{x_2 - x_1 + x_1(1-\cos\alpha)}{\sin\alpha} \quad \text{Eq. 3.7}$$

where x_1 and x_2 are the projections coordinate of the two points on the reference plan, and α is the tilting angle.

This calculation can be performed for each of the pixels associated with the two SEM images, and from the profile of the structure may be constructed. Reducing the image noise is necessary to obtain the optimal result, and maximum 3D reconstruction volume. Several parameters should be included in the process to reduce noise; (i) a conductive surface is necessary; (ii) the reconstructed feature must be clearly visible; (iii) the images should be oriented eccentrically. To obtain 3D construction three tilted SEM images were analyzed using the commercial software package Mex (Alicona) [121].

3.5 Fabrication of SU-8 Master Mould

SU-8 is a negative tone, epoxy type photoresist developed by IBM Research. It has a low UV absorbance in the wavelength range 360 to 420 nm, which allows a uniform exposure. The main structure contains eight epoxy groups constituting the SU-8 monomer. Different concentrations are available that alter the viscosity of the polymer. The cross-linking of SU-8 starts upon exposure to UV radiation. The UV light generates an acid due to the presence of triarylium sulphonium salts in its chemical structure, which acts as a photo initiator that begins cross-linking of the epoxy group, and acts as a catalyst in the subsequent post baking process. The post bake is used to supply additional heat energy to complete the cross linking reaction. The complete cross-linked solid SU-8 becomes strong, tough and highly resistant to chemicals [122].

The UV lithography of SU-8 allows high quality products in terms of high contrast, high aspect ratio and vertical sidewalls [123]. SU-8 thickness can be varied from several micrometers to millimetres depending on the SU-8 type and the process parameters, such as coating, soft baking, exposure and post baking.

The SU-8 2000 series is an improved version of the original SU-8 formula; the type used in these experiments is SU-8 2050 (MicroChem, USA) [124]. Presented in Table 3.1 are the material properties of SU-8 2050.

There are two approaches developed to fabricate 1000 μm thick SU-8 master moulds, as proposed by Jin et al [1 & 125]. For both approaches, SU-8 50 was employed in the fabrication of SU-8 micro engine components. In the first approach, they used a UV exposure dose without filters for a short time soft bake process. In the second approach, they used a filtered UV exposure dose with longer soft bake process. In the experiments detailed within this thesis, both approaches were employed for SU-8 2050 thick photoresist. Details of the fabrication steps are explained in the next section.

Table 3.1. Selected properties of SU-8 2050 as supplied [124].

Properties	**Unit**
Density (g/cc)	1.233
Viscosity (cST)	12900
Solids content (%)	71.65
Thermal conductivity (W/mK)	0.3
Coefficient of thermal expansion (μm/m^{-}°C)	52
Tensile strength (MPa)	60
Young's modulus (GPa)	2

3.5.1 SU-8 Fabrication Process

The SU-8 fabrication process for a 1000 μm thick mould is illustrated in Figure 3.3. In the UV lithography process, a clean wafer was coated by SU-8 followed by a soft baking process. Afterwards the exposure was performed by applying UV radiation onto the silicon substrate through a chrome mask. The mask was placed in a hard contact mode, without

any gaps between the mask and the substrate to ensure optimum resolution. Care should be taken during this step since damage to the mask can be caused. In negative photoresists such as SU-8, the parts exposed to UV radiation become insoluble while the unexposed parts remain soluble in the resist developer. After development, the design was formed from the remaining solid resist on the wafer. Finally, a hard baking step was performed to ensure that mould properties did not change during the use of the mould, especially at higher temperature, and to anneal any surface cracks. Due to the grade difference between the SU-8 50 which was used in the two SU-8 ultra thick fabrication approaches and SU-8 2050 used in this study, the soft bake and exposure process was optimized accordingly.

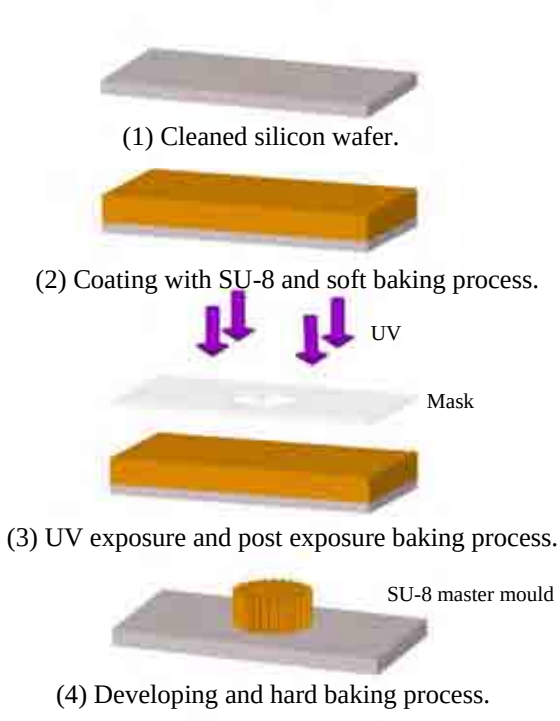

Figure 3.3. A schematic diagram of the SU-8 master mould fabrication process.

3.5.2 SU-8 Experiments

This section explains the detailed experiments for the fabrication of 1000 μm thick SU-8 microcomponents and discusses the quality of the fabricated SU-8 structures. Facilities located in the class 100 clean room (Microengineering and Nanotechnology Research Centre- University of Birmingham) were used to perform the SU-8 fabrication experiments.

3.5.2.1 Coating Process

Substrates used in the experiments were standard silicon wafer discs 4 inches in diameter and 500 μm in thickness. The supplied wafers are cleaned to remove any chemicals or molecules on the top surface of the wafers that may cause photoresists to bond weakly to the substrates or cross-link prior to UV exposure. First, the substrates were immersed in acetone, Isopropanol (IPA), and deionised water (DI). The wafers were then dried by a stream of nitrogen gas before being baked at 150 °C for 5 minutes to remove any remaining solvents. The resists were poured directly onto the wafers without the use of any adhesion promoter.

The preferred technique for coating wafers with polymer layers is the spin coating technique. However, according to the SU-8 2050 datasheet [124], the maximum thickness that can be achieved when using spin coating is 175 μm, obtained with a spin speed of 1000 rpm. To achieve the 1000 μm thickness, three methods were attempted can be followed. Since a higher spin speed results in a thinner layer the most obvious of these methods is to spin at lower speed. However, SU-8 2050 is a viscous grade, which led to an irregular thickness when spinning was performed at speeds lower than 1000 rpm. The second method was to coat the wafer with six SU-8 layers each with a thickness of 166.6

μm at a spin speed of 1060 rpm. After each coat, the wafer was soft baked at 65 °C for 7 minutes and 95 °C for 45 minutes. However, by observation, it was difficult to maintain a flat surface for coating after three layers had been deposited, due to the resist high viscosity. The third method was to directly cast onto the wafer the amount required to produce the desired thickness. The mass required to coat the wafer was calculated using the following equation.

$$m = \frac{\pi . d^2 . t . \rho}{4 . \varphi} \qquad \text{Eq. 3.8}$$

where m is the SU-8 coated mass (g), d is the wafer diameter (4 inch wafer= 10.2 cm), t is the desired SU-8 thickness (0.1 cm), ρ is the SU-8 resist density (1.233 g/cc) and φ is the SU-8 solid content (0.7165). It is assumed that the solvent content in the resist will be completely evaporated during the soft baking process.

Applying the desired thickness into equation 3.8 together with the resist parameters, the required mass was calculated to be 14.06 g of SU-8 2050. However, because of residual solvent content in the SU-8 after baking, and the inability to completely coat to the wafer edges, it was found that between 13.5 and 13.7 g was the required amount of SU-8 2050 to obtain the desired thickness.

The direct coating method was usually accompanied by bubbles forming on the resist. Reducing the number of bubbles was simply achieved by bursting them with a metallic needle before the soft baking process. After casting the required amount of the resist and removal of any developed air bubbles, the wafer was placed on a levelled hotplate for few minutes to allow planarization of the resist.

3.5.2.2 Fabrication without UV Filters

After coating the wafer with the desired SU-8 thickness, the wafer was then soft baked to evaporate the resist solvent. According to Jin et al. [1], the optimized soft bake process was to first heat up the wafer to 65 °C for 2 hours, and then to increase the temperature to 95 °C for 24 hours. After soft baking of the sample, the hotplate was turned off and the coated wafer left on the hotplate to naturally cool down for 45-60 minutes. By then the sample is ready for the UV lithography process. Slow heating up and cooling down is helpful in reducing the internal stresses developed due to the difference in thermal expansion between SU-8 and the silicon wafer. This process was performed with the aid of a levelled hotplate inside the clean room fume cabinet.

A mask aligner (Canon PLA-501FA) equipped with UV light (Hg-lamp, 12.6 mW/cm^2) was used in the UV exposure process. The mask containing the microengine components design was placed over the baked wafer to pattern the structure using UV light. Several experiments were conducted with different exposure times and the resulting structures investigated to optimize the exposure dose. Table 3.2 summarizes some representative experiments from the investigation of different exposure doses.

After performing UV exposure of the SU-8 coated wafers, the samples were placed on a hotplate for a post-exposure baking process. The samples were heated to 65 °C for 15 minutes and then to 95 °C for 25 minutes. Subsequently, the hotplate was turned off to cool down the samples. After cooling down, the sample was immersed in a beaker filled with the SU-8 developer and placed in an ultrasonic bath to agitate the developing process. In the developing process, the developer dissolves the unexposed areas of the sample. Fresh SU-8 developer was repeatedly introduced to accelerate the process and to remove

the dissolved SU-8 from the sample. The developing time is approximately 1 hour, but this varies according to the agitation conditions. To ensure a complete developing process, Isopropanol (IPA) spray was applied to the sample. If a white film appeared on the sample, this indicated that undeveloped parts were still in the sample and the sample was then immersed again in the SU-8 developer to complete the process. Otherwise, the sample was dried with a stream nitrogen gun. Finally, the sample was hard baked by heating up the sample to 150 °C for 5 minutes followed by a slow cool down to room temperature.

Table 3.2. SU-8 2050 experimental parameters.

Sample	**Soft Bake**	**Exposure Energy (mJ/cm^2)**	**Development**
A1	65 °C / 2 hours 95 °C / 24 hours	5000	1 hour
A2	65 °C / 2 hours 95 °C / 24 hours	6500	1 hour
A3	65 °C / 2 hours 95 °C / 24 hours	10000	1 hour
A4	65 °C / 2 hours 95 °C / 24 hours	12000	1 hour
A5	65 °C / 2 hours 95 °C / 24 hours	20000	1 hour

The experiment samples are grouped into five sets according to the exposure dose. In the first set A1, sample exposure dose was 5000 mJ/cm^2. In the second set A2, sample exposure dose was 6500 mJ/cm^2. In the third set A3, sample exposure dose was 9000 mJ/cm^2. In the fourth set A4, sample exposure dose was 12000 mJ/cm^2. In the fifth set A5, sample exposure dose was 20000 mJ/cm^2. All samples were coated using the direct single coating process described in Section 3.4.2.1 and soft baked at 95 °C for 24 hours. The post exposure bake, development and hard bake processes were as previously described.

Figures 3.4 and 3.5 show SEM images of perspective views of SU-8 gears for different exposure doses. For Figure 3.4(a), the upper part of the microgear is much wider than the lower part. The narrow lower part could not stand internal stresses resulted from heating up during post exposure bake and/ or hard bake process causing cracks at the weakest sections. In addition, sidewalls were clearly not vertical, and the cross linking at the bottom of the part was not sufficient. In the second set A2, increasing of the exposure energy to 6500 mJ/cm^2 slightly improves the geometry. Specifically, the difference in width between the upper and the lower portions was decreased. In addition, the sidewalls appear nearly vertical, however, cracks still appear at the base. In the third set A3, increasing the exposure energy to 9000 mJ/cm^2 results in crack-free samples. In the fourth and fifth sets (A4 and A5), with increasing exposure energy both upper and lower widths increased, but not equally. In addition, vertical line traces appear at the base of the micro gears.

To explain these effects, it is important to discuss the absorption properties of SU-8 50 mentioned in the literature [125]. The soft bake process has a strong influence on the resist polymerization during exposure. When the soft bake process is long, SU-8 absorbs more UV light. Therefore, it decreases the penetration of UV light into the SU-8 layer. Conversely, a short soft bake time can be used for obtaining a low UV light absorption. The results from samples (A1 to A5) clearly show that the upper regions absorb more energy than the lower regions. This may be because SU-8 2050 has a lower transparency for a 1000 µm thick layer than the SU-8 50 used in the first approach. Therefore, the short soft baking process that was successful for SU-8 50 is not efficient for SU-8 2050 due to the grade difference between them.

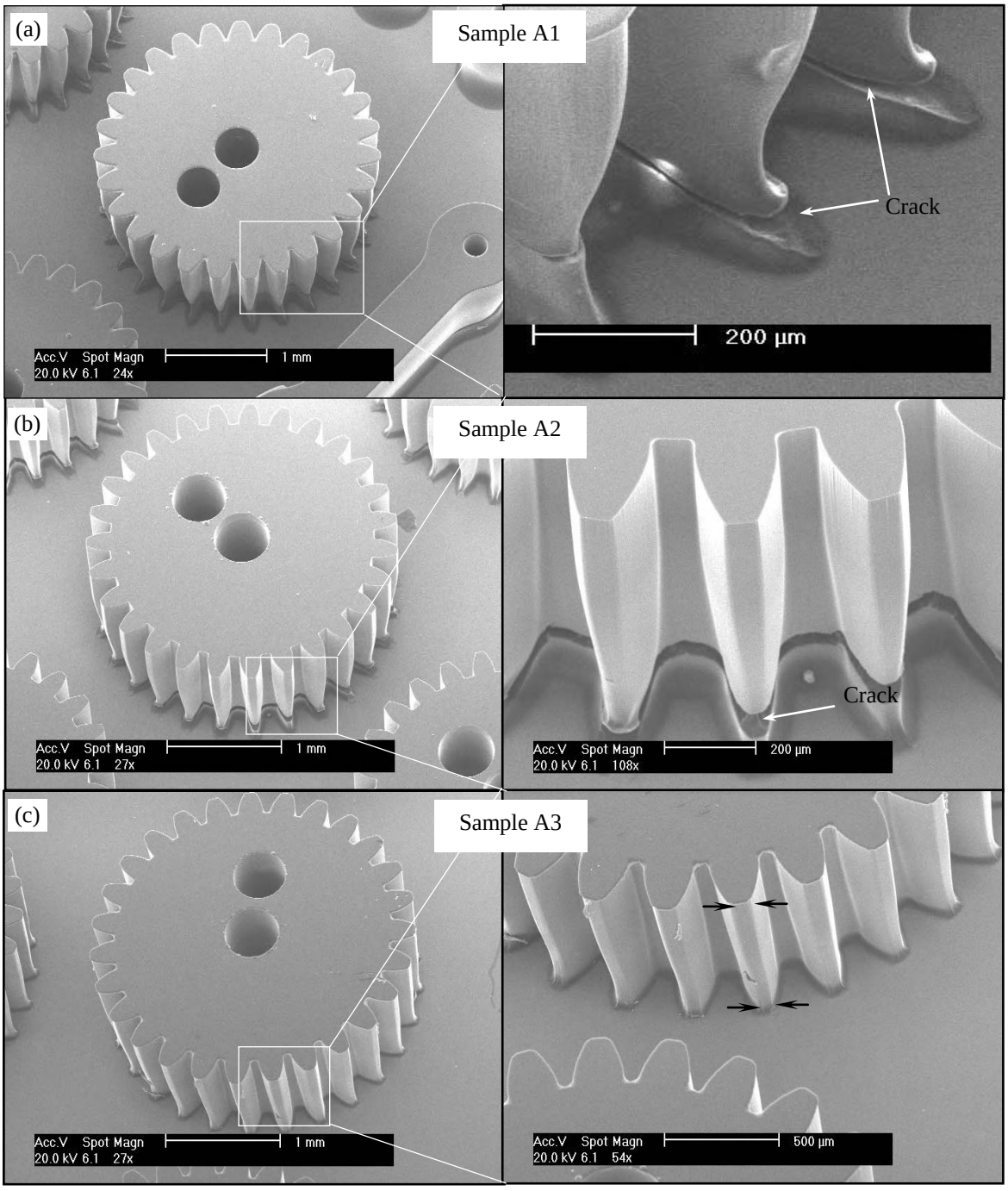

Figure 3.4. SEM images of perspective view of SU-8 2050 microgears for samples A1, A2 and A3.

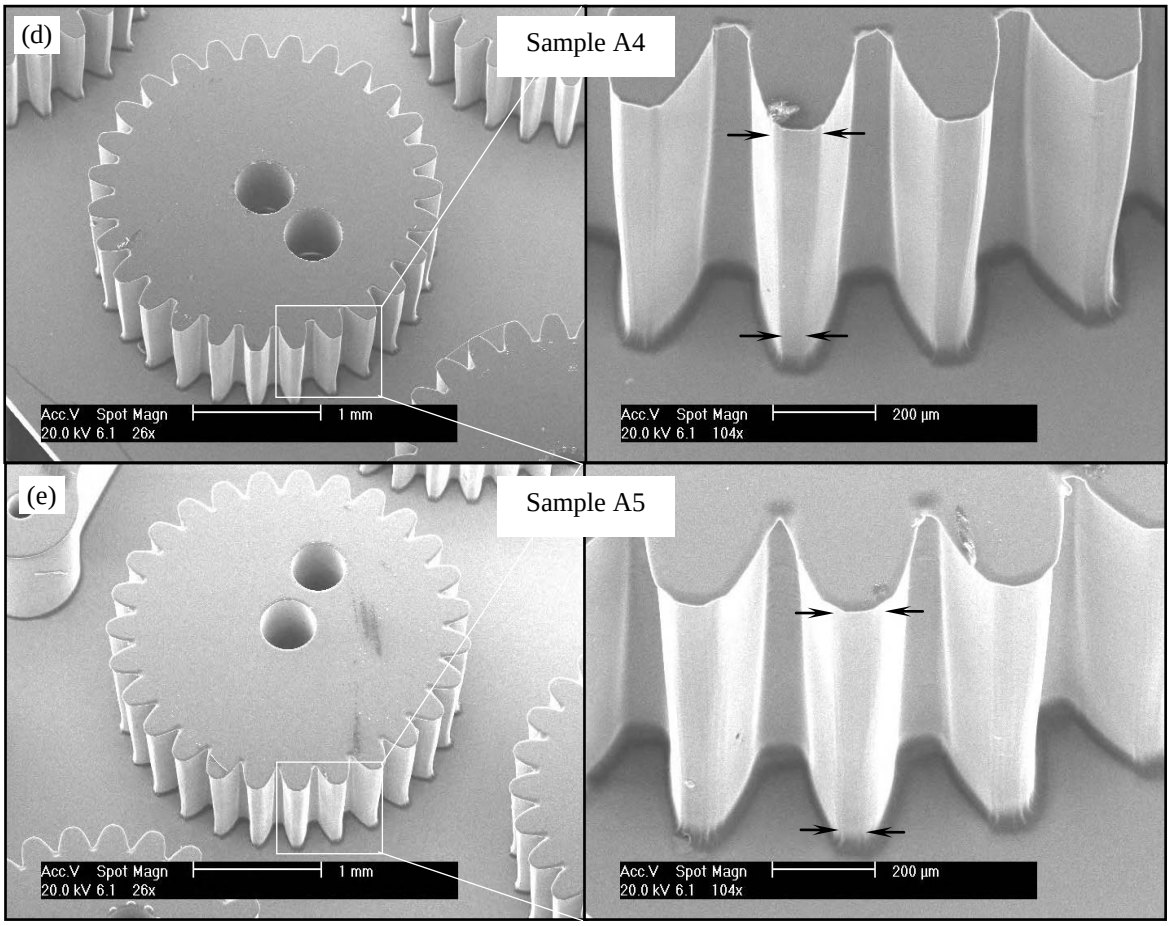

Figure 3.5. SEM images of perspective view of SU-8 2050 microgears for samples A4 and A5.

3.5.2.3 Fabrication with UV Filters

Jin et al. [125] optimized the soft baking process by heating the samples at 65 °C for 2 hours, followed by an increase to 95 °C for 30 hours. After cooling down, exposure was performed with the aid of mask aligner filters. Post exposure baking, development and hard baking remained the same as in the fabrication without filters, Section 3.4.2.2. For thick SU-8 photoresist, UV absorption is low at wavelengths greater than 360 nm while it has a high absorption at wavelengths below 360 nm [126]. In addition, the illumination from the mask aligner used in the exposure process has a spectral range from 320 to 500

nm. Therefore, exposure to wavelengths lower than 360 nm will cause the upper parts of the layer to absorb more energy than the lower parts, which was clearly observed when no filters were used in the exposure process. Briefly, for longer wavelengths (> 360 nm), SU-8 transparency increased and absorbance decreased significantly.

The mask aligner (Canon PLA-501FA) was equipped with three filters, UC-20, UC-10, and LG-39. These filters prevent some UV wavelength radiation provided by the mask aligner lamp. As a result, the ratio between the i-line (365 nm) and g-line (436 nm) was reduced by a controlled amount with the aid of these filters [2]. Table 3.3 summarizes the parameters used in a representative experiment.

Table 3.3. SU-8 2050 experimental parameters.

Sample	**Soft bake**	**Filtered exposure energy (mJ/cm^2)**	**Development**
B1	65 °C / 2 hours 95 °C /30:34 hours	24000:26000	1 hour

Initial samples B1 were fabricated according to the following instructions. The samples were first soft baked at 65 °C for 2 hours and 95 °C for 30-34 hours. Afterwards, the samples were UV exposed with the aid of UV filters as described previously with a total energy density of 24000-26000 mJ/cm^2. The samples were examined using SEM images as shown in Figure 3.6. The results obtained from initial samples were within tolerance; consequently, there was no need for further experimentation to determine exposure parameters.

As shown in Figure 3.6, the candidate samples for the selected exposure parameters show high quality results. Looking at the upper and lower regions of the SU-8 microcomponents,

both have nearly the same geometry. In addition, the samples demonstrate vertical and straight sidewall profiles. As explained previously, the UV filters cuts off low UV radiation wavelengths, which allows higher wavelengths to penetrate homogeneously through the whole thickness.

A SU-8 micro mould surface fabricated by UV lithography was investigated using stereo imaging. Figure 3.7 shows the constructed top surface of the mould and the computed surface roughness parameters are listed in Table 3.4. As shown from both Figure 3.7 and Table 3.4, it can be concluded that, the top surface of the SU-8 structure has a relatively smooth surface.

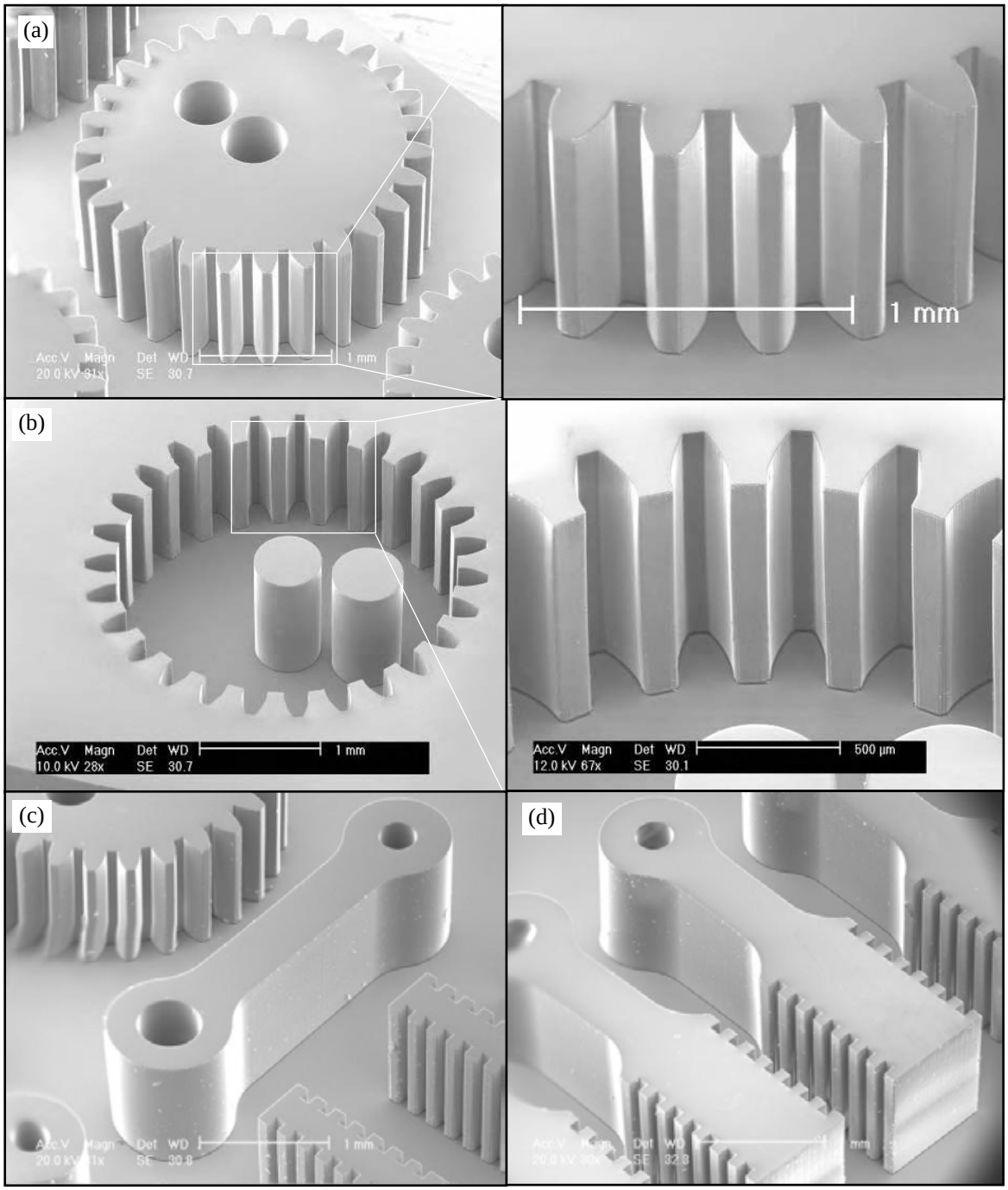

Figure 3.6. SEM images of perspective view of SU-8 2050 microengine parts fabricated with the aid of UV filters.

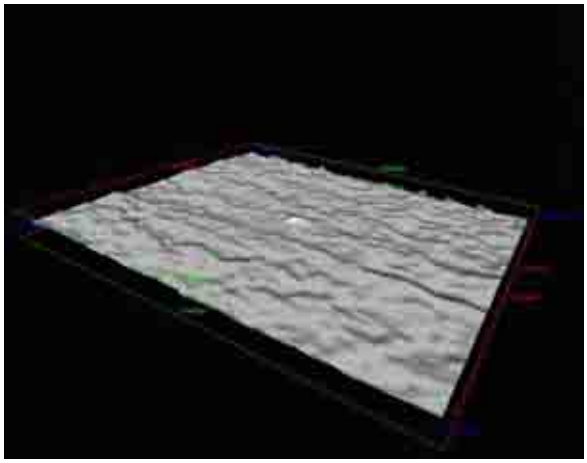

Figure 3.7. 3D constructed surface texture at the top surface of SU-8 mould using stereo imaging.

Table 3.4. Top surface parameters of the fabricated SU-8 micro gear.

Roughness parameter	**Unit**
$\mathbf{R_a}$	17.9 nm
$\mathbf{R_q}$	24.3 nm
$\mathbf{R_p}$	229.7 nm
$\mathbf{R_v}$	317.3 nm
$\mathbf{R_{sk}}$	-1.3319
$\mathbf{R_{ku}}$	11.44

3.6 Fabrication of Soft Mould

A soft mould is an elastomeric mould that produces the inverse of the master mould. In this work, the soft mould was employed to define the ceramic structure, in effect duplicating the master mould. It is often used to manipulate suspensions or slurries that are dried or cured as part of the soft lithography process. Once the soft mould is fabricated, the master can be replicated many times independently from the clean room facilities and expensive equipment. The process for fabrication of an elastomeric mould is presented in Figure 3.8.

The process starts by casting a pre-polymer mixture into the fabricated master mould. The mould is then cured and transformed to a solid, and then peeled from the master.

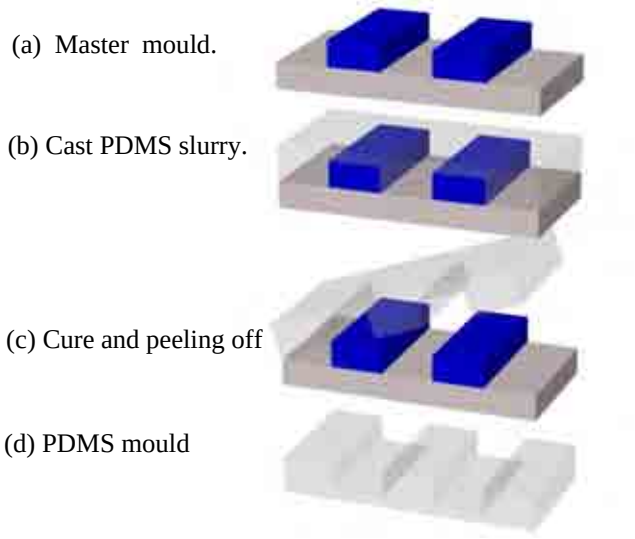

Figure 3.8. Schematic of soft mould fabrication steps.

3.6.1 PDMS Experiments

PDMS is a popular elastomer material for soft lithography. Chemically, it is composed of an inorganic siloxane attached to organic methyl groups. PDMS has many advantages over other soft lithographic materials. It is a flexible elastomer that can be used in temperatures range up to 200 °C. It is a thermally and electrically insulating material. In addition, PDMS is optically transparent, inert, non-flammable and gas permeable. Its low surface energy allows an easy release from master moulds and templates [122]. PDMS (Sylgard 184-Dow Corning Corp.) commercial kit consists of two parts, a base material and a curing agent. In its initial state, PDMS pre-polymer is a liquid with a viscosity of 4575 cSt. When cured, it turns into a solid elastomer. Sylgard 184 properties are listed in Table 3.5.

Table 3.5. Selected properties of Sylgard 184 as supplied [120].

Properties	**Unit**
Specific gravity	1.03
Viscosity (cST)	4575
Thermal conductivity (W/mK)	0.16
Coefficient of thermal expansion (μm/m-°C)	325

To fabricate a PDMS soft mould, the silicon wafer holding the SU-8 microcomponents was placed into an aluminium foil container. The two PDMS parts were mixed in the weight ratio of 10:1 base to curing agent, and thoroughly stirred and degassed to remove air bubbles formed during the stirring. After degassing, a layer of the PDMS slurry approximately 2 mm thick was cast onto the master mould and degassed in vacuum until all residual bubbles were removed. The typical curing durations recommended by the manufacturer are 24 hours at normal room temperature or 4 hours at 65 °C. In this experiment, the mould was cured in temperature ranging from 65 °C for 4 hours. After cooling, the cured PDMS layer was carefully peeled off from the master mould. Successful release of the PDMS soft mould was achieved without the use of any release agent. PDMS layers thinner than 1 mm were difficult to produce as they tended to tear when released from the master mould. Finally, the mould was cut into pieces with an area of 2×2 cm^2 using a stainless steel blade. PDMS micro moulds were examined using SEM images as shown in Figure 3.9.

Figure 3.9 shows that the geometry of the structures was complete due to the highly conformal contact between PDMS and the SU-8 pattern, and the ability to remove bubbles after casting. In addition, the low surface energy of PDMS meant that there was no adhesion to the patterns, allowing an easy release from the master mould, resulting in an

undistorted stamp. It is clearly seen that the PDMS moulds have the same high quality as the SU-8 mould.

(a) Optical micrograph of PDMS mould.

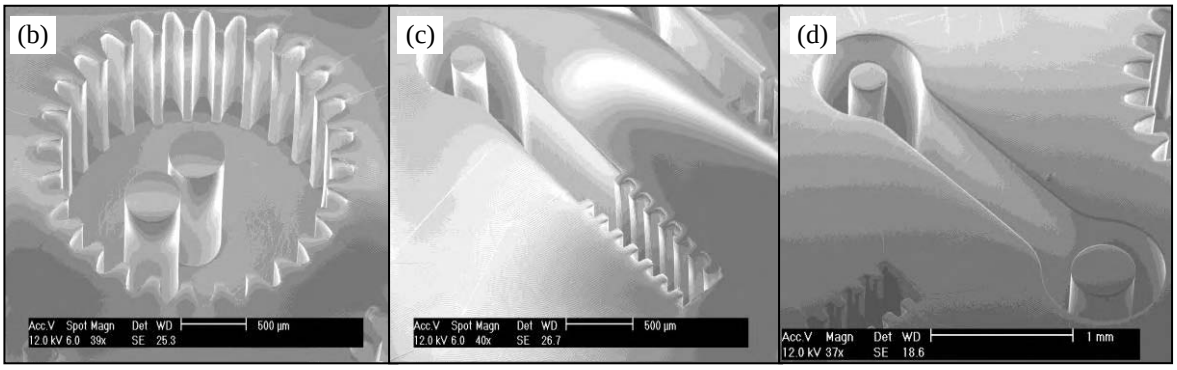

(b) SEM image of PDMS microgear. (c) SEM image of PDMS micropiston. (d) SEM image of PDMS microconnecting rod.

Figure 3.9. Optical and SEM images of a PDMS soft mould for producing different microengine parts.

Surface topography of the PDMS replica micro mould was constructed using stereo imaging. Figure 3.10 shows constructed top surface of the mould with the computed surface roughness parameters listed in Table 3.6. Figure 3.10 and Table 3.6 indicate that, the surface of the PDMS structure has a relatively a smooth surface.

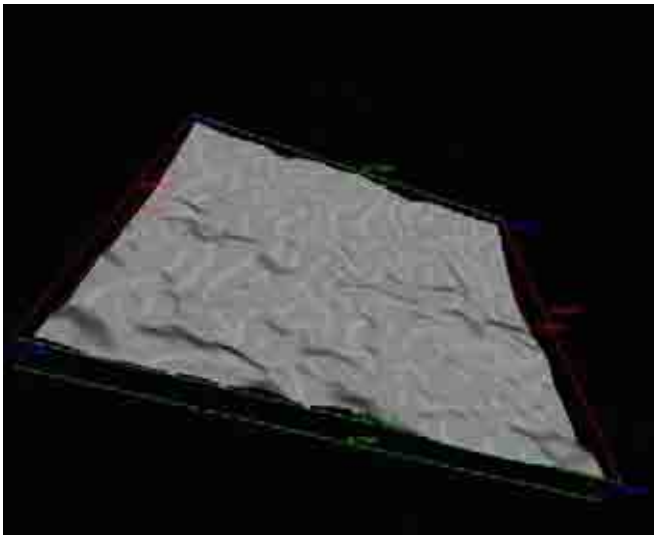

Figure 3.10. 3D constructed surface texture of PDMS mould using stereo imaging.

Table 3.6. Top surface parameters of the fabricated PDMS mould.

Roughness parameters	**Unit**
$\mathbf{R_a}$	54.1 nm
$\mathbf{R_q}$	69.7 nm
$\mathbf{R_p}$	364.5 nm
$\mathbf{R_v}$	476.6 nm
Rsk	0.2743
$\mathbf{R_{ku}}$	3.7665

3.7 Alternatives for SU-8 Master and PDMS Moulds

Although SU-8 and PDMS moulds have several favourable properties, some problems exist during experimentation of the moulds mentioned above. After repeated use of the master mould, the SU-8 structures tend to become damaged, particularly during the peeling of the PDMS layer. This may be because of thermal stresses that develop during heating and cooling of the PDMS in the curing process. In addition, the PDMS mould also may be damaged with the moulding and demoulding repeatability during fabrication of ceramic

microcomponents. Here, experiments are described that investigate alternative methods and materials.

3.7.1 Alternatives for SU-8 Master Mould

In this section, alternatives to SU-8 master moulds for the fabrication of microengine parts are proposed and discussed. Three materials were trialled: a thick BPR100 micromould, a silicon mould fabricated by deep reactive ion etching (DRIE - Bosch process) and reinforced PDMS.

3.7.1.1 Fabrication of BPR100 Master Mould

BPR100 (Rohm and Haas) photoresist has a wide variety of applications including electroforming, etching and wafer level packing processes [128]. BPR100 is a liquid negative tone type with a solid content of 58-62 % and is typically used to form layers with a thickness ranging from 40 to 130 µm. In this study, attempts were made to increase this upper limit to 1000 µm [129].

3.7.1.1.1 BPR100 Experiments

In the fabrication of BPR100 moulds, direct casting process was used for coating the substrate with BPR100. Experiments revealed that about 13, 5.2 and 3.25 ml of BPR100 resist were the required amounts to produce uniform layers with a thickness of 1000, 400 and 250 µm respectively. The fabrication steps were slightly different from those used in the SU-8 process. Table 3.7 summarizes the process parameters for producing thick BPR100 micro moulds.

Table 3.7. Experimental parameters for BPR100 moulds.

Sample	**Thickness**	**Soft bake**	**Exposure energy (mJ/cm^2)**	**Development**
C1	1000 µm	65 °C / 10 minutes 90 °C /10 hours	1000:30000	4 hours
C2	400 µm	65 °C / 10 minutes 90 °C /5 hours	1000:15000	1.5 hours
C3	250 µm	65 °C / 10 minutes 90 °C /3 hours	1000:10000	1 hours

After the exact amount of BPR100 had been applied to a cleaned silicon wafer, the soft baking process was performed with a slow ramp to prevent formation of bubbles during the solvent evaporation. This treatment was different to the standard baking process, as supplied by the manufacturer (30 minutes at 90 °C). For resists with a thickness of 1000 µm, 400 µm and 250 µm, the following procedure was used to determine the soft bake parameters. First, the sample was placed on a hotplate and heated up to 65 °C for 5 minutes. Next, the sample was heated up to 90 °C for 3-10 hours, see Table 3.7. After heating, the hotplate was turned off and left to cool down naturally. After cooling to room temperature, the hotplate was reheated to 90 °C. Completion of the soft bake was determined by observing the form of the layer surface during heating. A wrinkled surface meant that the solvent content was still excessive; if the surface remained flat, it meant that the solvent content had reduced to acceptable levels and the soft bake was completed. The soft bake time was then recorded and the experiment repeated for each thickness. It was found that the soft bake time at 90 °C were 10 hours, 5 hours and 3 hours for 1000 µm, 400 µm and 250 µm respectively.

UV lithography was performed on the baked samples using various exposure doses. After exposure, the samples were directly developed using BPR100 developer. Afterwards, the BPR100 samples were rinsed in deionised water and dried using a nitrogen stream.

The obtained samples were examined using SEM images, shown in Figures 3.11(a)-(c). For different exposure doses, samples within set C1 were almost all removed from the silicon wafer during the development process. Structures that did remain on the wafer are shown in the Figure 3.11(a). It is obviously clear that for a high thickness of 1000 µm, UV light could not penetrate deeply to the lower parts of the BPR100 layer, and only the upper parts of the sample were cross-linked. As a result, the BPR100 developer dissolved the lower regions of the samples, leaving the upper parts of the samples on the silicon wafer. Thickness of the cross-linked parts was measured to be between 400 and 600 µm.

Thickness of the BPR100 was then decreased to 400 µm (set C2) using the experimental parameters listed in Table 3.7. It was found that, there was no significant difference between structures when changing the exposure dose across the range 1000 to 15000 mJ/c^2. Results obtained from one of the samples are shown in Figure 3.11(b) illustrating that the microgear profile is not well defined. It seems that BPR100 absorbs more energy for 400 µm, which results in poorly defined structures.

For a BPR100 thickness of 250 µm (set C3) UV light could penetrate throughout the BPR100 layer resulting in a more even dose. Shown in Figure 3.11(c), the microgear profile is now well defined and the upper and lower parts of the layer have similar dimensions.

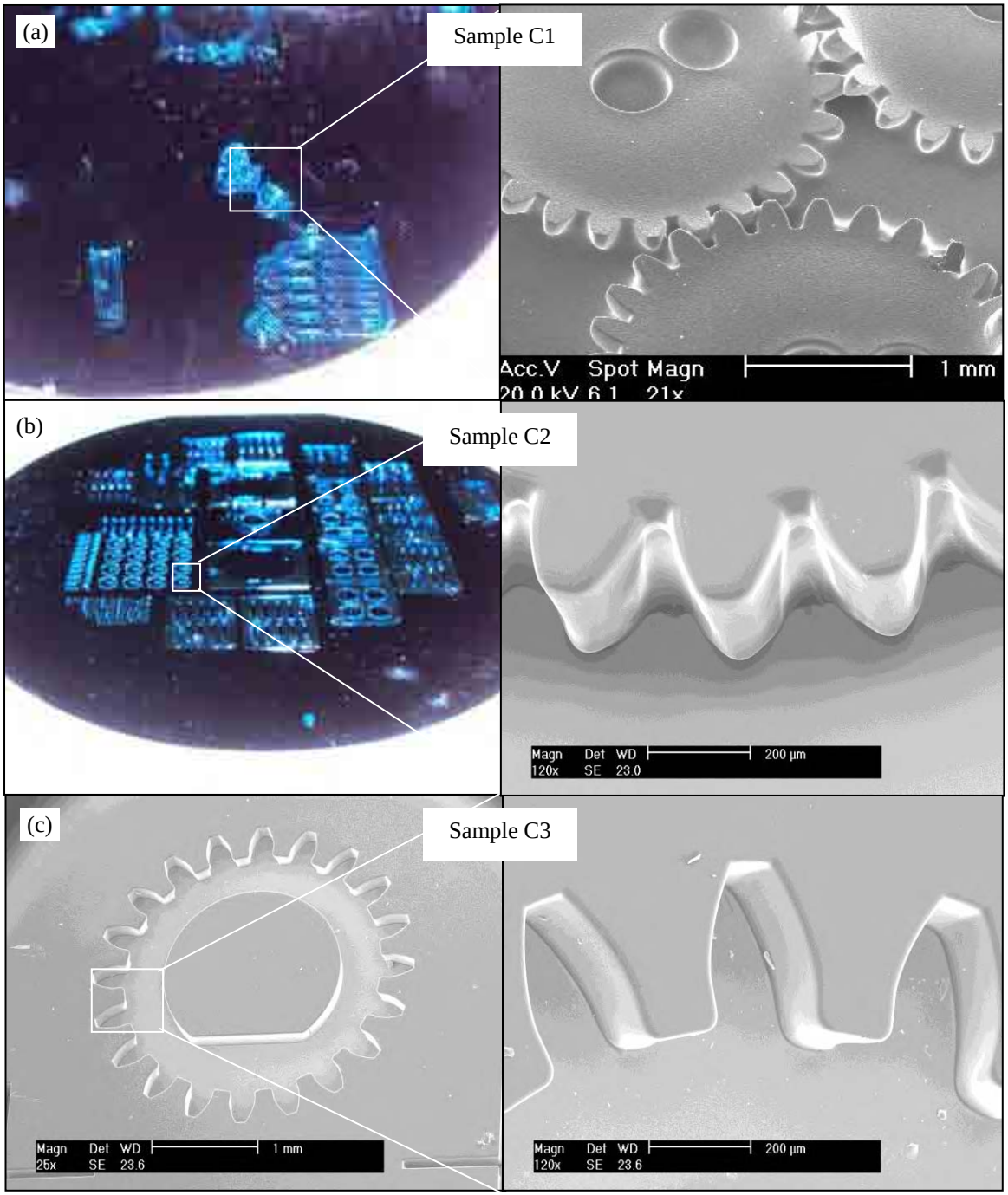

Figure 3.11. Optical and SEM images of BPR100 moulds.

3D constructed surface was obtained and shown in Figure 3.12. In addition, the surface roughness parameters are listed in Table 3.8. As shown from both Figure 3.12 and Table

3.8, it was found that the top surface of the BPR100 structure has a rougher surface than the SU-8 mould.

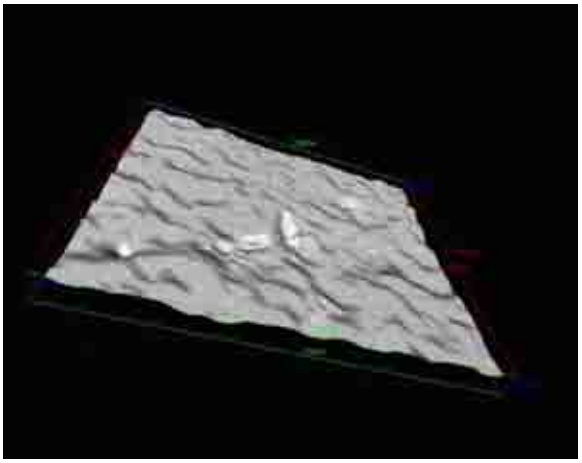

Figure 3.12. 3D constructed surface texture at the top surface of BPR100 mould obtained using stereo imaging.

Table 3.8. Top surface parameters of the fabricated BPR100 mould.

Roughness parameters	**Unit**
$\mathbf{R_a}$	30.8 nm
$\mathbf{R_q}$	40.2 nm
$\mathbf{R_p}$	142.5 nm
$\mathbf{R_v}$	223.5 nm
$\mathbf{R_{sk}}$	-0.3717
$\mathbf{R_{ku}}$	4.675

From experimental work carried out on BPR100, it can be concluded that BPR100 is not a suitable resist for ultathick micromoulds. This was mainly due to the high absorption of UV energy that prevents UV radiation from penetrating sufficiently into the BPR100 layer.

This was particularly noticeable for layers with a thickness of 1000 µm, even with a high exposure dose.

3.7.1.2 Fabrication of DRIE Master Mould

Deep reactive ion etching using the Bosch process is one of the most important silicon microfabrication techniques available. The main advantages of the Bosch process are that it provides a means for deep etching of high aspect ratio patterns with almost vertical sidewalls and high etching rates. The process consists of many repetitions of alternating etch and passivation cycles, as shown in Figure 3.13. The first cycle is to etch the silicon using an etching gas (SF_6) and the second cycle is to protect the sidewalls using a polymer gas (C_4F_8), which coats the sidewalls with a polymer that prevents lateral etching. Repeating the etching and passivation loop results in a high rate and selective etching. Photoresist with a low etching rate is necessary for optimal results [130].

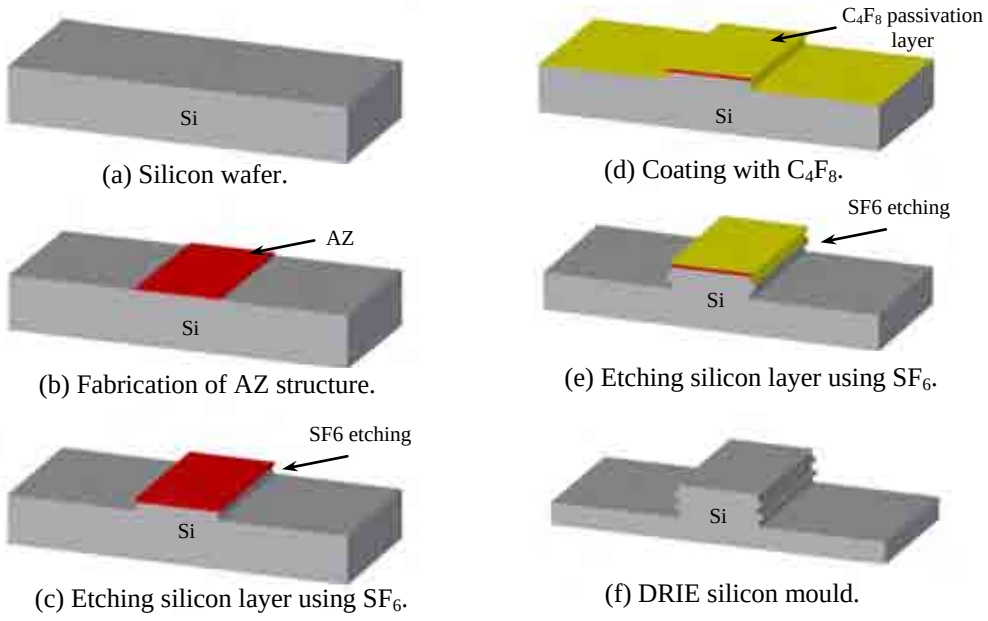

Figure 3.13. Schematic diagram of deep reactive ion etching (DRIE-Bosch) process.

3.7.1.2.1 DRIE Experiments

In the Bosch process, a resist mask is fabricated using conventional UV lithography. An AZ-5214 with a thickness of 2 µm was patterned using the parameters shown in Table 3.9.

Table 3.9. Experimental parameters of 2 µm thick AZ-5214 mask fabrication.

Spinning speed (rpm)	**Soft bake**	**Exposure energy (mJ/cm^2)**	**Development**
2000	110 °C / 2 minute	200	2 minutes

The patterned sample was then etched using a reactive ion etcher (Multiplex ICP DRIE etcher from STS Plc., UK). The recipe typically etches at a rate of 4 µm/min. Based on that rate, an estimated total etch time was calculated that should allow the desired etch depth to be reached. The process parameters for the DRIE Bosch process outlined in Table 3.10 are the basis from which the mould was fabricated.

Table 3.10. Etching parameters of DRIE using the STS Multiplex ICP DRIE etcher.

Parameter	**Etch cycle**	**Passivate cycle**
SF_6 Flow Rate	100 sccm	0 sccm
C_4F_8 Flow Rate	0 sccm	85 sccm
Duration	8s	5s
13.56MHz Platen Power	800W	600W

The experiment samples are grouped into 2 sets according to the etching time. In the first set D1, etching time was 50 minutes to achieve a thickness of 200 µm. In the second set

D2, sample etching time was 100 minutes to achieve a thickness of 400 µm. Samples were characterised by SEM examination and are shown in Figure 3.14.

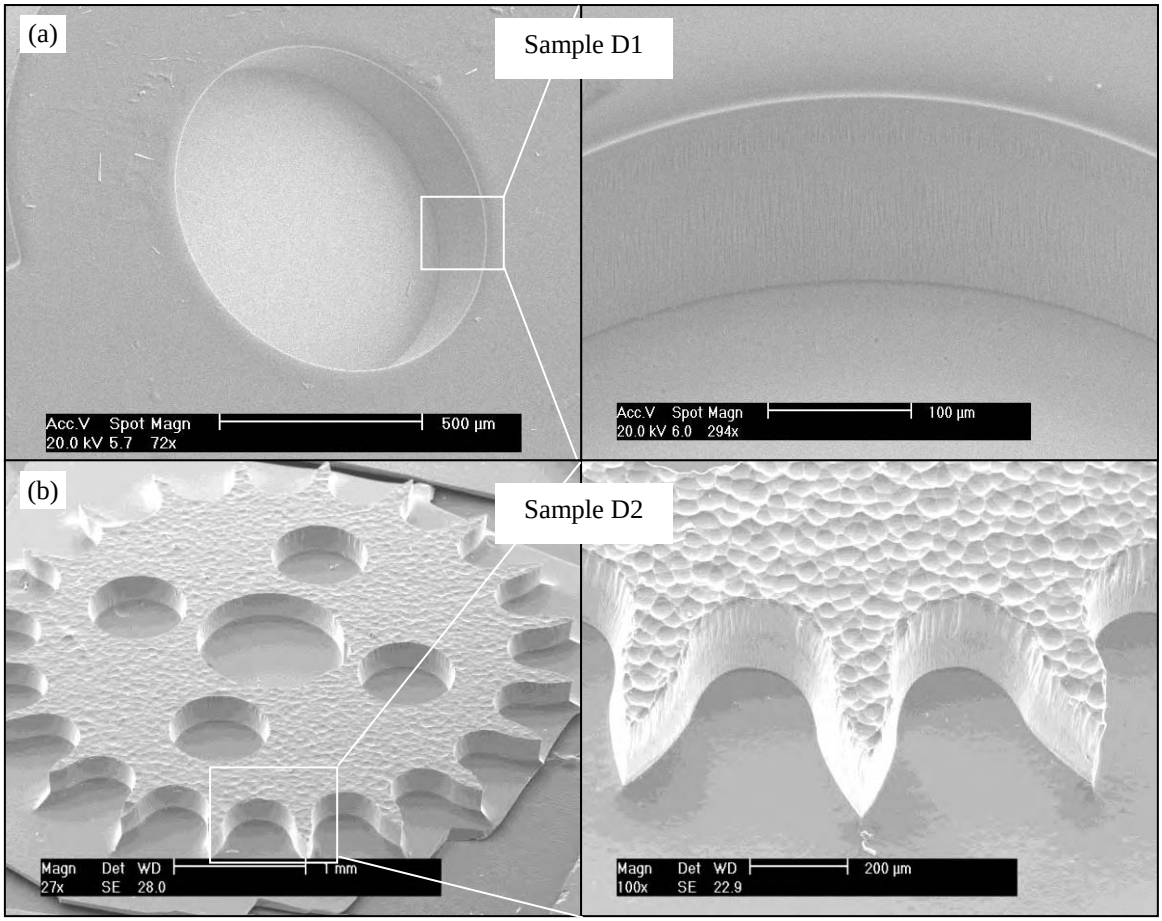

Figure 3.14. SEM image of silicon moulds fabricated using DRIE.

As shown in Figure 3.14, the pattern profiles are well defined with nearly vertical sidewalls. The images clearly show the effect of the repeating gas cycle on the mould, especially on the mould sidewalls. This effect is more distinct in the second sample set, D2, implying that longer etching times result in rougher sidewall surfaces. Moreover, it is clear that the regions around the top of the sidewalls look rougher than the bottom of the mould sidewall. To quantify the roughness the surfaces of the sidewalls were examined

using the stereo imaging technique. Figures 3.15(a)-(c) show the constructed surface at the upper, middle and the lower parts of the mould sidewall. Surface roughness parameters are listed in Table 3.11. These results show that, the top parts of the sidewalls have a relatively rough surface when compared to the middle and bottom parts of the sidewalls.

High values of sidewall surface roughness are the major drawback of this fabrication technique. In summary, silicon moulds fabricated using DRIE are not suitable for manufacturing high quality master moulds due to significantly higher sidewall roughness compared to the SU-8 moulds.

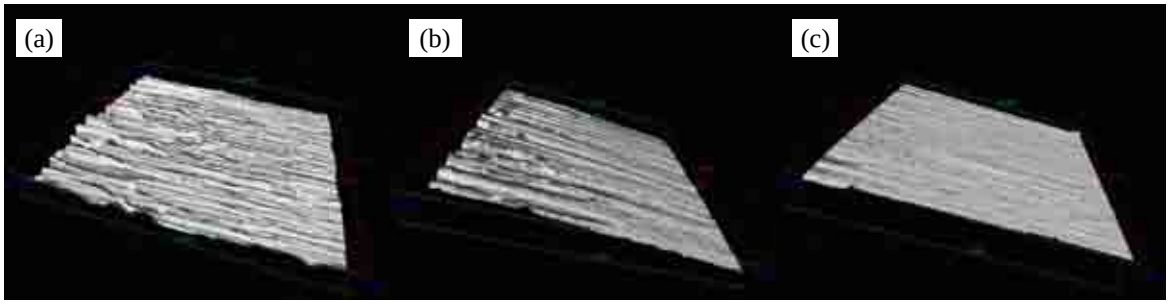

(a) Top part of the sidewall. (b) Middle part of the sidewall. (b) Bottom part of the sidewall.

Figure 3.15. 3D constructed surface texture at the top, middle and the bottom parts of the silicon mould using stereo imaging fabricated using DRIE Bosch process.

Table 3.11. Top, middle and bottom parts of the mould sidewalls surface parameters of the fabricated silicon mould.

Roughness parameters	**Top**	**Middle**	**Bottom**
R_a nm	164.1	145.03	32.5
R_q nm	227.26	225.37	47.8
R_p nm	1351.8	999.24	673.2
R_v nm	1333.5	1227.6	1049.5
R_{sk}	0.6974	-0.9714	-2.2802
R_{ku}	5.4322	6.5928	31.67

3.7.1.3 Reinforced PDMS Master Mould

As previously explained, polydimethylsiloxane (PDMS) is considered an attractive and simple approach for micro/nano systems. It is a low cost material when compared to the traditional micro/nano materials such as SU-8, silicon and glass. In addition, the fabrication tools are simple when compared to those required in the fabrication of the SU-8 mould. The PDMS casting technique is principally dependent upon the master mould. Accordingly, several approaches to replicate soft elastomeric structures without the need for the SU-8 structures have been introduced [131].

Using a PDMS mould to create PDMS structures was recognized as having potential as a technique for improving the lifetime of the cast. However, the main challenge to overcome in using PDMS in this way was the adhesion between the two PDMS layers. A second drawback when using PDMS is that the surface is hydrophobic. The poor wettability is an issue for many applications such as microcontact printing and microfluidics. For this reason, surface treatments using an oxygen plasma, silanization, polymers, proteins, lipid coating and Triton X-100 have been investigated as a means to improve the wettability of the PDMS surface [132-133].

A surfactant is a wetting agent that reduces the surface tension of a liquid, allowing better dispersal of fluid across a surface by generating a hydrophilic dynamic coating on the surface. Here, a PDMS replica was used as a master mould for fabrication of high quality PDMS structure after treating the surface with low concentrations of commercial ceramic surfactants to provide easy demoulding. The process details for using PDMS as a master mould are listed below and are illustrated schematically in Figure 3.16.

1. The PDMS soft mould is reinforced with by the adhesion of a glass or plastic plate into PDMS mould to increase the durability of the master.

2. The reinforced PDMS mould is surface treated by immersing the PDMS mould for 15 minutes in the surfactant solution to increase the wettability.

3. The master is rinsed in deionised water to remove excess surfactant from the mould.

4. PDMS slurry is poured into the PDMS master, degassed and cured at 90 ^{o}C for 30 minutes.

5. The PDMS replica is demoulded from the PDMS master by peeling off the replica with the aid of razor blade.

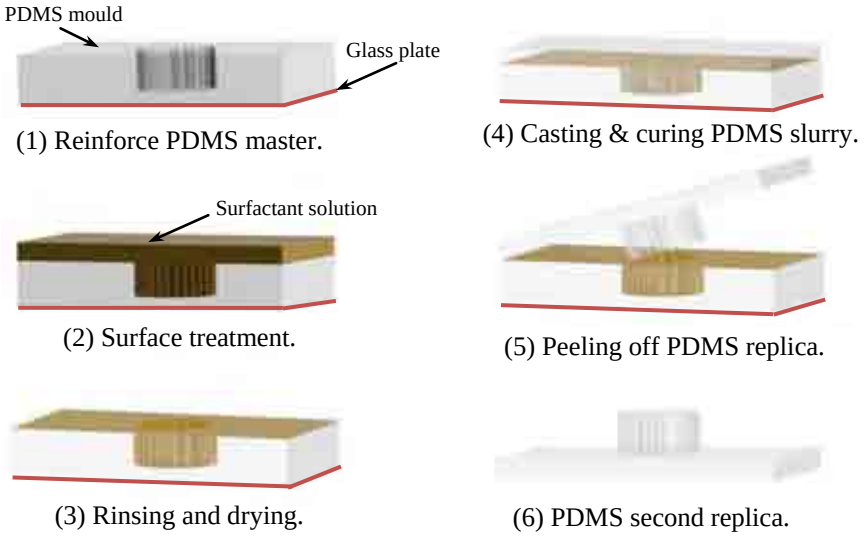

Figure 3.16. Schematic steps of multiple replication of PDMS mould.

3.7.1.3.1 PDMS Multiple Replication Experiments

The PDMS master mould was treated with diluted surfactants. These were D-3005 (Rohm & Haas, USA) and Brij52 (Sigma Aldrich, UK) diluted in deionised water and acetone respectively, to reach a concentration of 5-10 wt%. Experiments were carried out using each surfactant individually.

Preliminary experiments were performed using the PDMS master as fabricated and described in Section 3.5.1 without the reinforcement plate. It was found that the master mould was cut and damaged during demoulding. This was mainly because of the flexible nature of the PDMS material. To counter this problem, a rigid support plate was needed to reinforce the mould, after which the experiments could be carried out with the proposed surfactant treatments. Results are shown in Figure 3.17. Figures 3.17(a)-(b) show SEM images of multiple replication PDMS moulds obtained using reinforced PDMS master mould surface treated with D-3005 and Brij52 solutions respectively. The results show that the PDMS replicas obtained from PDMS masters treated with D-3005 and Brij52 were successful. Both, the first and the second copies were successfully obtained undamaged by careful demoulding. Sidewalls, surface topography and micro features of the teeth associated with the original master have been transferred to the replicas because of the clean separation and the conformal contact between the PDMS slurry and the PDMS reinforced master mould. The high quality PDMS replica geometry indicates that the surfactant layer thickness is very low due to the low concentration of surfactant in solution. In summary, multiple PDMS replicas were successfully obtained using reinforced PDMS treated with surfactant solutions as the master mould. The master structure remained unharmed. As a result, a PDMS mould was used as an alternative to the SU-8 master mould for repeatable replication processes.

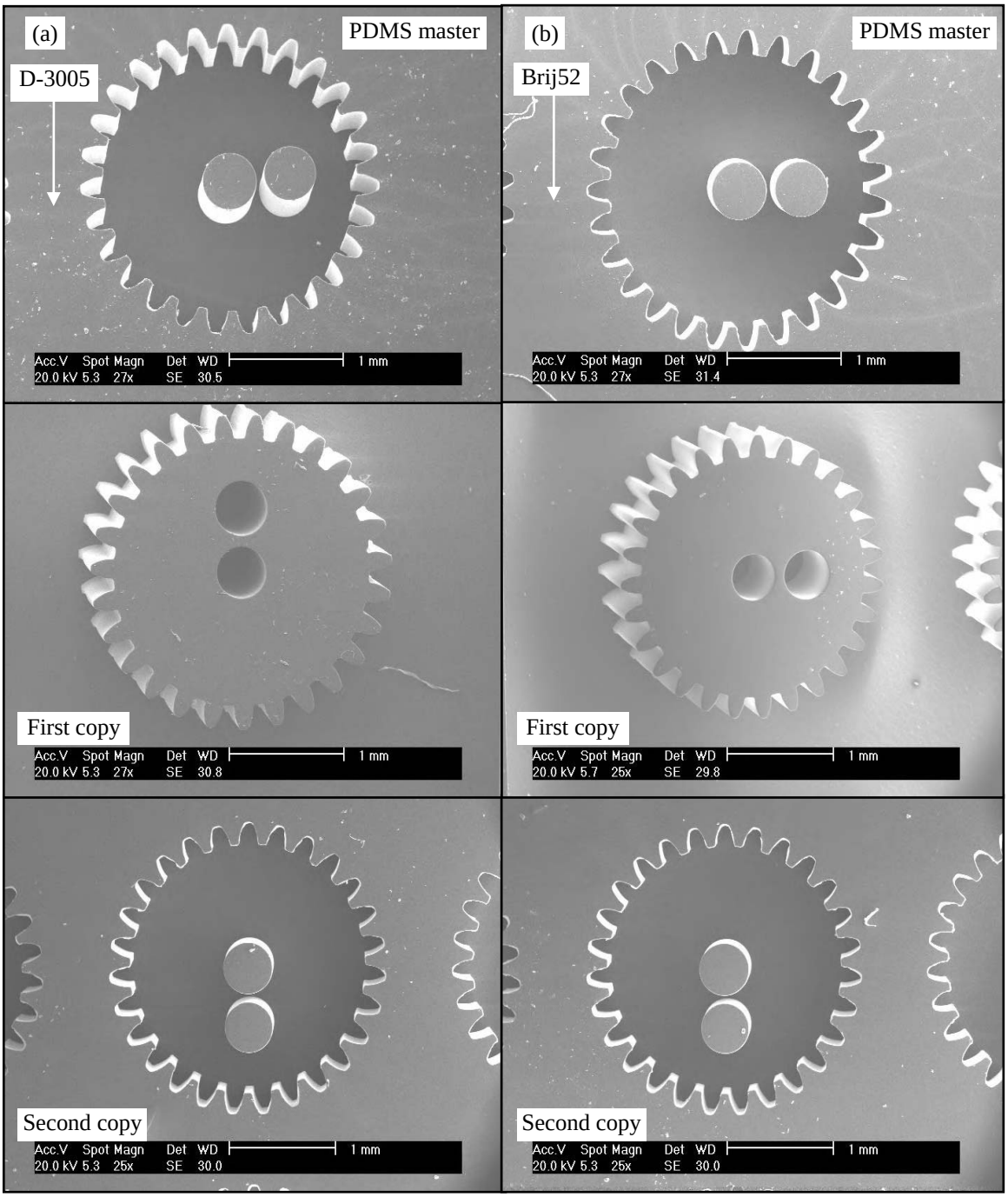

Figure 3.17. SEM images of multiple replication PDMS moulds fabricated using reinforced PDMS master mould treated with (a) D-3005, (b) Brij52.

3.7.2 Alternatives for PDMS Soft Mould

3.7.2.1 Dragon Skin

Another material that was proposed for soft mould fabrication was Dragon Skin. Dragon Skin series are very efficient platinum cure silicon elastomers. It can be cured at room temperature with negligible shrinkage. Cured Dragon Skin is a water white semi transparent material, strong and flexible elastomer [134]. Dragon Skin (Dragon Skin 10-Smooth-on) commercial kit is supplied in two parts (A, B). The process is slightly different to that used for PDMS moulds. In the Dragon Skin process, the two parts are mixed thoroughly (1:1 ratio by weight or volume) in a glass beaker for 5 minutes. The mixed slurry was then degassed in an attempt to remove bubbles that had formed within the slurry. This proved to be a difficult process due to its high viscosity. Afterwards, the mixture was immediately cast onto the master mould to avoid curing initiation, and again placed under vacuum to remove trapped air. The mould was allowed to cure at room temperature for 10 hours and then cut with a stainless steel blade.

During demoulding, it was observed that a strong adhesion exists between the Dragon Skin and the SU-8 master structures, making the release of the Dragon Skin mould difficult when compared to PDMS. The Dragon Skin mould could not be released completely from the SU-8 master, and was cut, resulting in distortion of protruding features of the soft mould. In addition, many of the SU-8 master features were also destroyed during the release step, as shown in Figure 3.18(a)-(b). Cured Dragon skin moulds were further characterised using SEM examination with the results shown in Figure 3.18(c)-(d). The cuts and distorted regions described previously are clearly visible in the mould. However, micro features were replicated without any problems. This means a good conformal

contact between the Dragon Skin slurry and the SU-8 master mould and the damage occurs during the demoulding step.

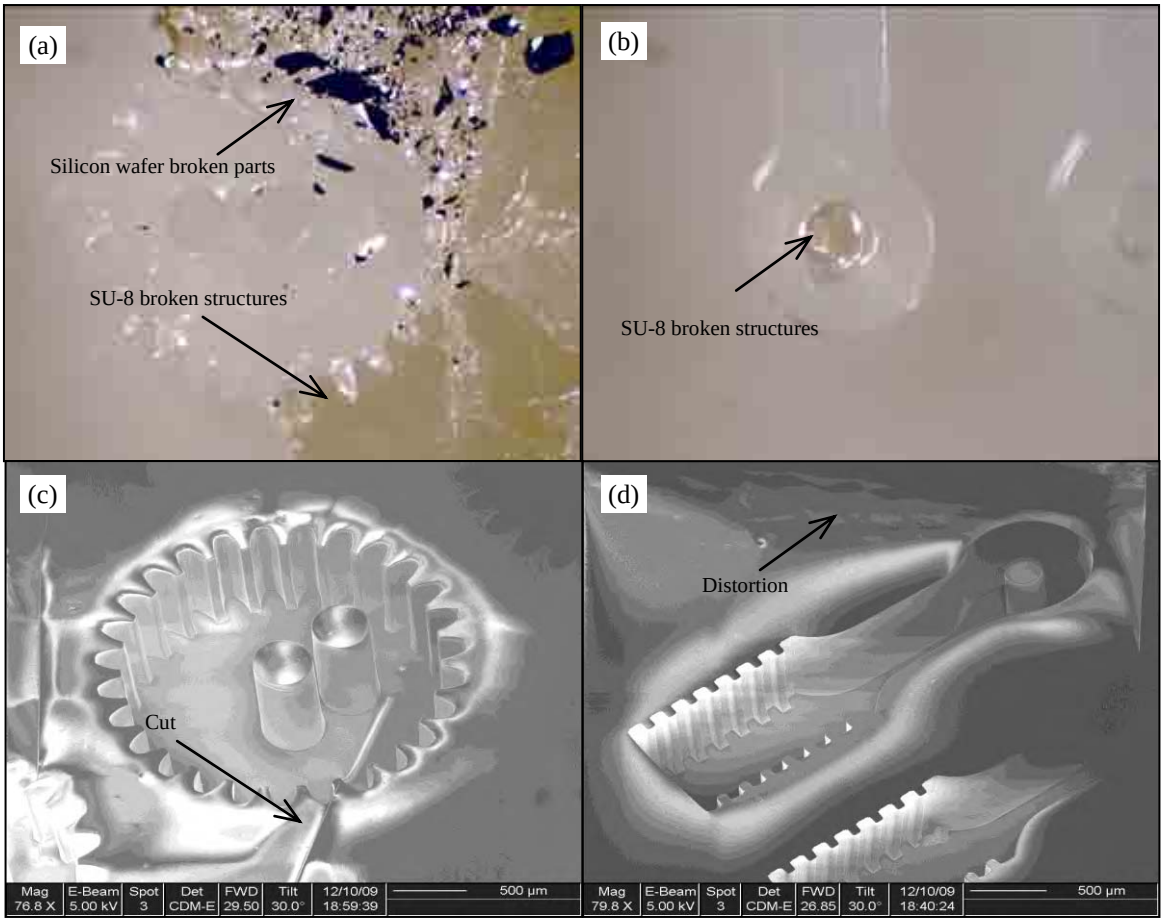

Figure 3.18. Optical and SEM images of Dragon Skin elastomer released from the SU-8 master moulds.

Further examination of the mould was performed using surface roughness characterisation as shown in Figure 3.19 and Table 3.12. It can be concluded that, the top surface of the Dragon Skin mould has a relatively smoother surface when compared to the PDMS surface. Despite the surface improvements, Dragon skin is considered less favourable than PDMS mould since many of the soft and SU-8 moulds were distorted during demoulding.

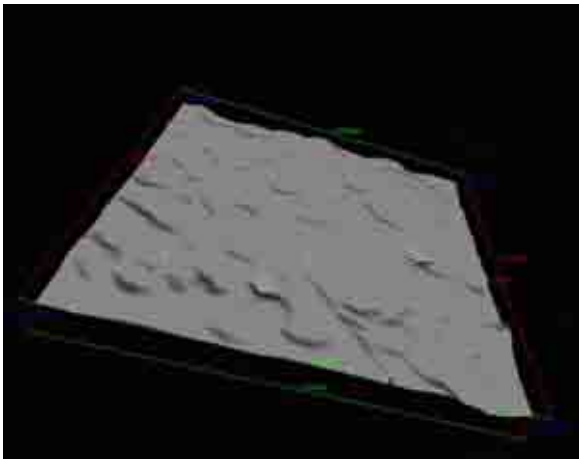

Figure 3.19. 3D constructed surface texture of a Dragon Skin mould surface.

Table 3.13. Top surface parameters of the fabricated Dragon Skin mould.

Roughness parameters	**Unit**
$\mathbf{R_a}$	35.7 nm
$\mathbf{R_q}$	45.1 nm
$\mathbf{R_p}$	231.74 nm
$\mathbf{R_v}$	266.97 nm
$\mathbf{R_{sk}}$	0.0493
$\mathbf{R_{ku}}$	3.5864

3.8 Summary

In this chapter, high quality ultra thick SU-8 master moulds were successfully fabricated and characterised. It was found that a filtered UV exposure was the dominant influence on mould quality when optimizing the soft bake process. PDMS soft moulds were successfully fabricated with the same quality as the master mould. SU-8 and PDMS alternatives such as BPR100, DRIE silicon, reinforced PDMS master and Dragon Skin

moulds were fabricated and characterised. When comparing with the SU-8 and PDMS it can be concluded that:

1. The quality of the SU-8 and PDMS satisfies the requirements for master and soft moulds, and contributes to the objective of fabricating ceramic microcomponents to high quality geometry and roughness tolerances.

2. BPR100 and DRIE silicon moulds are not suitable for 1000 μm thick moulds. In addition, their surface roughness values were higher than those found for the SU-8 mould.

3. A reinforced PDMS master with a surfactant-treated surface was studied; experiments succeeded in producing an alternative mould for use as a master in conjunction with SU-8 moulds.

4. Dragon Skin soft moulds were shown to have demoulding problems due to strong adhesion with the SU-8 master mould. Therefore, it was not suitable for use as a soft mould despite having a slightly smoother surface than PDMS.

CHAPTER 4: OPTIMIZATION OF CERAMIC SLURRY SYSTEM

4.1 Introduction

In this chapter, different ceramic slurries are proposed and their compositions are optimised for fabrication of ceramic microengine parts. The aim is to fabricate dense net shape alumina (Al_2O_3) and 8 mole% yttria stabilized zirconia (YSZ8) microengine parts using soft lithography. Based on experimental work, a comparison between the proposed processes was studied to decide the optimum slurry technique. The fabricated ceramic microengine parts were inspected under high magnification electron microscopes and their densities and shrinkages have been measured for the optimization of each slurry parameters. The chapter starts by introducing properties of ceramic powders used through the project, detailed in Section 4.2. Optimization methodology of both the binder and dispersant are described in Section 4.3. The chapter introduces the proposed slurry systems in Section 4.4. Composition, fabrication procedure, green and sintered results are discussed in Sections 4.4.1, 4.4.2 and 4.4.3 respectively. Fabrication results presented in this chapter include the ability to mirror PDMS mould and to fabricate high aspect ratio ceramic structures. In addition, the optimum binders and dispersants concentration of each proposed slurry results for achieving high green density and low green shrinkage are concluded. Challenges in each slurry system, including moulding, demoulding and sintering processes, are also discussed and solutions are proposed. A comparative study of these processes is discussed in Section 4.5. Finally, the chapter summary is presented in Section 4.6.

4.2 Ceramic Powder

Properties of ceramic powders play important role in the fabrication of ceramic microcomponents. In the experiments, Al_2O_3 and YSZ8 powders were selected as they differ from each other in the mean particle diameters. The selected Al_2O_3 powders have average sizes of 0.4, 0.7, 1.0 and 12.0 µm respectively, and YSZ8 powders have average sizes of 2.0, 5.0 and 10.0 µm respectively. For the comparison between different slurry systems, the focus in this chapter is on 0.7 µm Al_2O_3 and 2 µm YSZ8 powders. 0.7 µm, 1.0 µm, and 12.0 µm alumina powders and 2.0 µm, 5.0 µm and 10.0 µm YSZ8 powders were used in further experimentations to study the influence of the powder size on the prepared ceramic slurry, the green and sintered properties, and are presented in Chapter 5 and Chapter 6. In addition, alumina powder with an average size of 0.4 µm and YSZ8 powder with an average size of 2 µm powder were used to fabricate zirconia matrix alumina nanocomposite microcomponents and are presented in Chapter 7. Finally, 0.7 µm Al_2O_3 powder and 2 µm YSZ8 powders were employed in the fabrication of functionally graded ceramic composite microcomponents and are presented in Chapter 7. The characteristics of Al_2O_3 and YSZ8 powders, as supplied by the manufacturers, are given in Table 4.1 and Table 4.2, respectively. The powders were heated at 110 °C for 24 hours to remove humidity adsorbed on the particles surface before being used in the experiments.

Table 4.1. Properties of Al_2O_3 powders.

Powder	**Manufacturer**	**Structure**	**d_{50}**	**Tap density**
A0.4	ABSCO Materials-UK	α-Al_2O_3	0.4 µm	0.4 g/cc
A0.7	PI-KEM -UK	α-Al_2O_3	0.7 µm	1.28 g/cc
A1.0	Sigma Aldrich-UK	α-Al_2O_3	1.0 µm	0.67 g/cc
A12.0	PI-KEM -UK	α-Al_2O_3	12.0 µm	1.52 g/cc

Table 4.2. Properties of YSZ8 powders.

Powder	**Manufacturer**	**Structure**	**d_{50}**	**Tap density**
2YSZ8	UCM -Germany	8 mol.% yttria	2.0 µm	1.52 g/cc
5YSZ8	UCM -Germany	8 mol.% yttria	5.0 µm	1.62 g/cc
10YSZ8	UCM -Germany	8 mol.% yttria	10.0 µm	1.81 g/cc

SEM examinations were preformed on the used powder by spreading the powder on an adhesive carbon pad. The samples were coated by a gold sputtering device to enhance the conductivity and the contrast of the SEM images. Figure 4.1 and Figure 4.2 show the SEM images of the Al_2O_3 and YSZ8 powders, respectively.

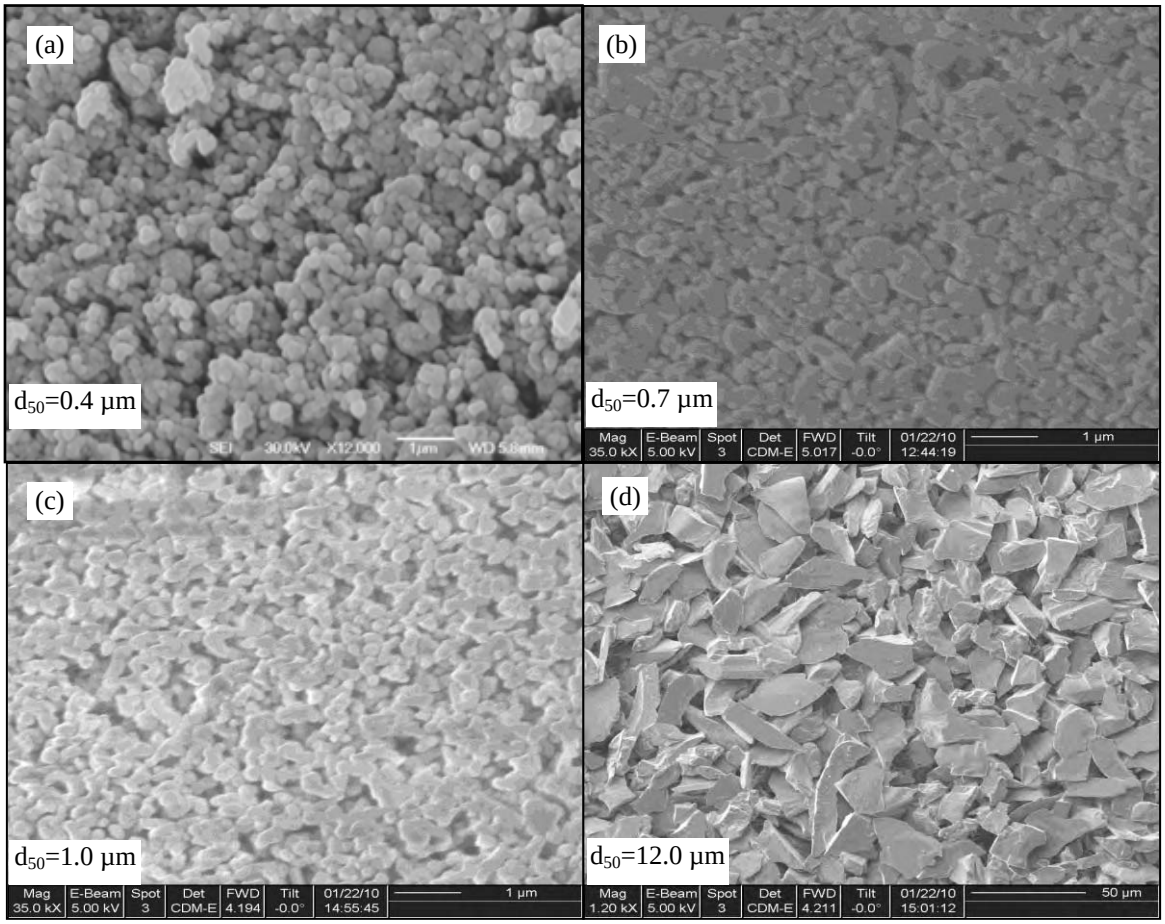

Figure 4.1. SEM images of Al_2O_3 powders of different powder sizes (a) A0.4, (b) A0.7, (c) A1.0, and (d) A12.0.

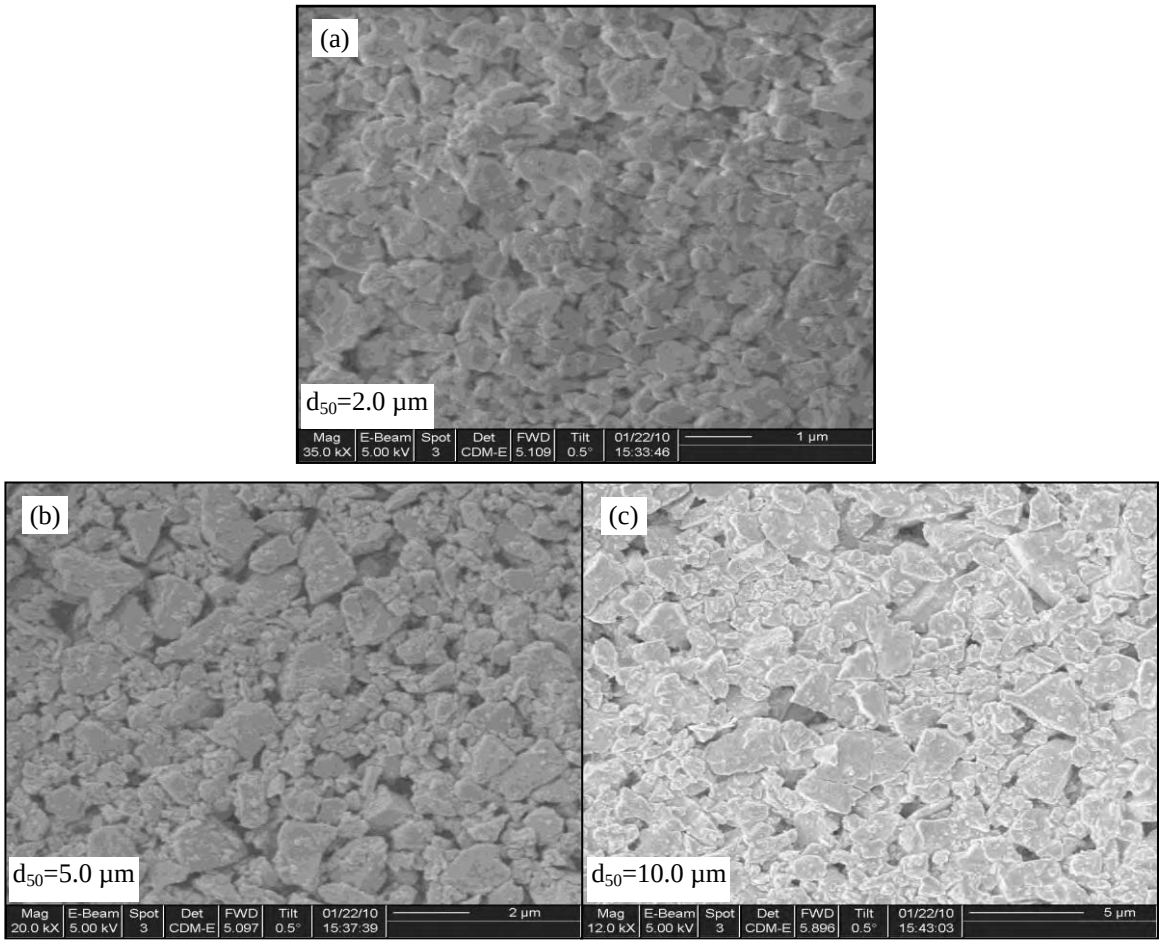

Figure 4.2. SEM images of YSZ8 powders of different powder sizes (a) 2YSZ8, (b) 5YSZ8, and (c) 10YSZ8.

4.3 Optimization Methodology

Ceramic slurry is obtained by mixing ceramic powder, carrying vehicle, binder, and dispersant to produce uniformly dispersed ceramic slurry. In this section, optimization methodology of both dispersant and binder is presented for net shaping of ceramic microcomponents, high green density, low green shrinkage and sufficient green strength to produce defect free demoulding.

4.3.1 Dispersant Optimization

Dispersant is used to separate the agglomerated particles in the slurry by controlling the inter particle forces affecting the colloidal stability of the system. Dispersion of ceramic powder processing is very important to obtain a high reliability in the final sintered structure. Any inhomogeneity is a potential flaw in the sintered parts. Hence, the agglomerates, which exist in most commercially supplied powders, either have to be broken down or removed [135]. Slurry dispersion conditions have a direct impact to the green density. Well-dispersed slurry is required to produce green bodies with high packing densities and uniform microstructures. Therefore, density and shrinkage measurements of the green parts have been carried out for the optimization of dispersant concentration.

The aim here is to maximize the relative density and minimize the shrinkage of the green parts. Therefore, the optimum dispersant amount is decided as the minimum amount that produces the highest green density and the minimum green shrinkage.

Green density indicates how tightly the ceramic particles are packed in the green part. In addition, it is the key for achieving low sintered shrinkage, high dimensional resolution and less distortion on resultant sintered part. Therefore, it is considered as a dominant parameter in forming of the microcomponents.

Density measurements of the fabricated microcomponents (green and sintered) throughout the research were carried out using the Archimedes principal with ethanol as the emersion medium, and were calculated using Equation 4.1.

$$\rho = \frac{m_a \times \rho_L}{(m_a - m_L)} \qquad \text{Eq. 4.1}$$

where:

m_a is the mass of the object in air.

m_L is the mass of the object in the emersion medium.

ρ_L is the density of the emersion medium (Ethanol).

The method was valid for all the sintered and green microcomponents in this research except for green parts fabricated using water-based slurry. It was found that green parts fabricated using the above-mentioned slurry were dissolvable in many solvents, such as ethanol, water, toluene, etc. Therefore, it was calculated from the mass divide by volume. Microcomponents in regular geometries, such as rectangular, are easy to measure and to calculate their volume. Moreover, rectangular already exist in the microengine design parts shown in Figure 3.1. The combustion chamber cover is a rectangular shape with a dimension of 4×3×1 mm^3, and was chosen for the calculation of the green density.

Dimensions of the microcomponents were measured using optical microscope or digital vernier caliper with a 0.01 mm resolution, as shown in Figure 4.3. Masses of the green parts were measured using high sensitivity balance, which has a resolution of 0.0001 g.

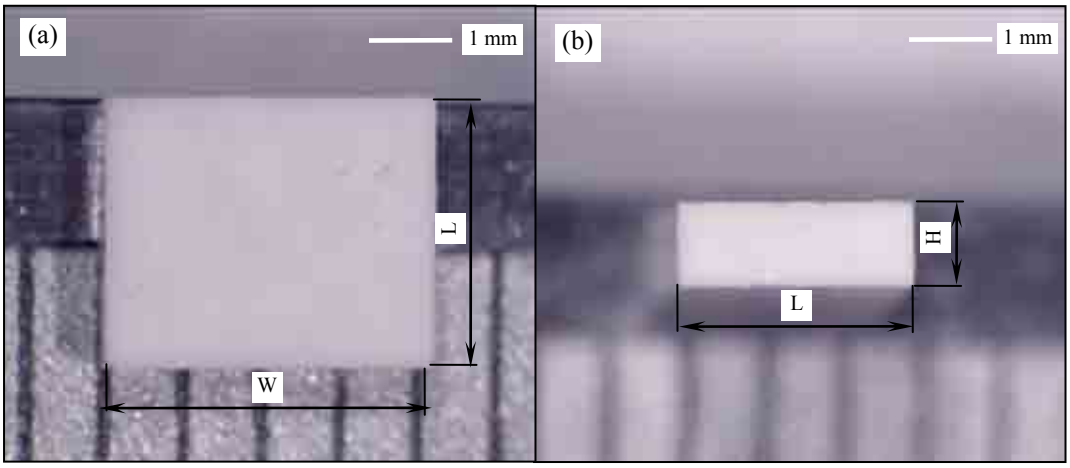

Figure 4.3. Rectangular shape green part ready for density measurement.

As for shrinkage of the fabricated green and sintered microcomponents, it was referred throughout the research to the axial linear shrinkage obtained from the outer diameter of green and sintered microgears with respect to the SU-8 master mould, as shown in Figure 4.4, and was calculated from Equation 4.2, as follows.

$$\text{Relative shrinkage } \% = \frac{OD_{su8} - OD_{g,s}}{OD_{su8}} \times 100 \qquad \text{Eq. 4.2}$$

where:

OD_{su8} is the SU-8 microgear outer diameter.

$OD_{g,s}$ is the green or sintered microgear outer diameter.

Five samples were measured and the average was recorded at each dispersant value for both the density and shrinkage measurements.

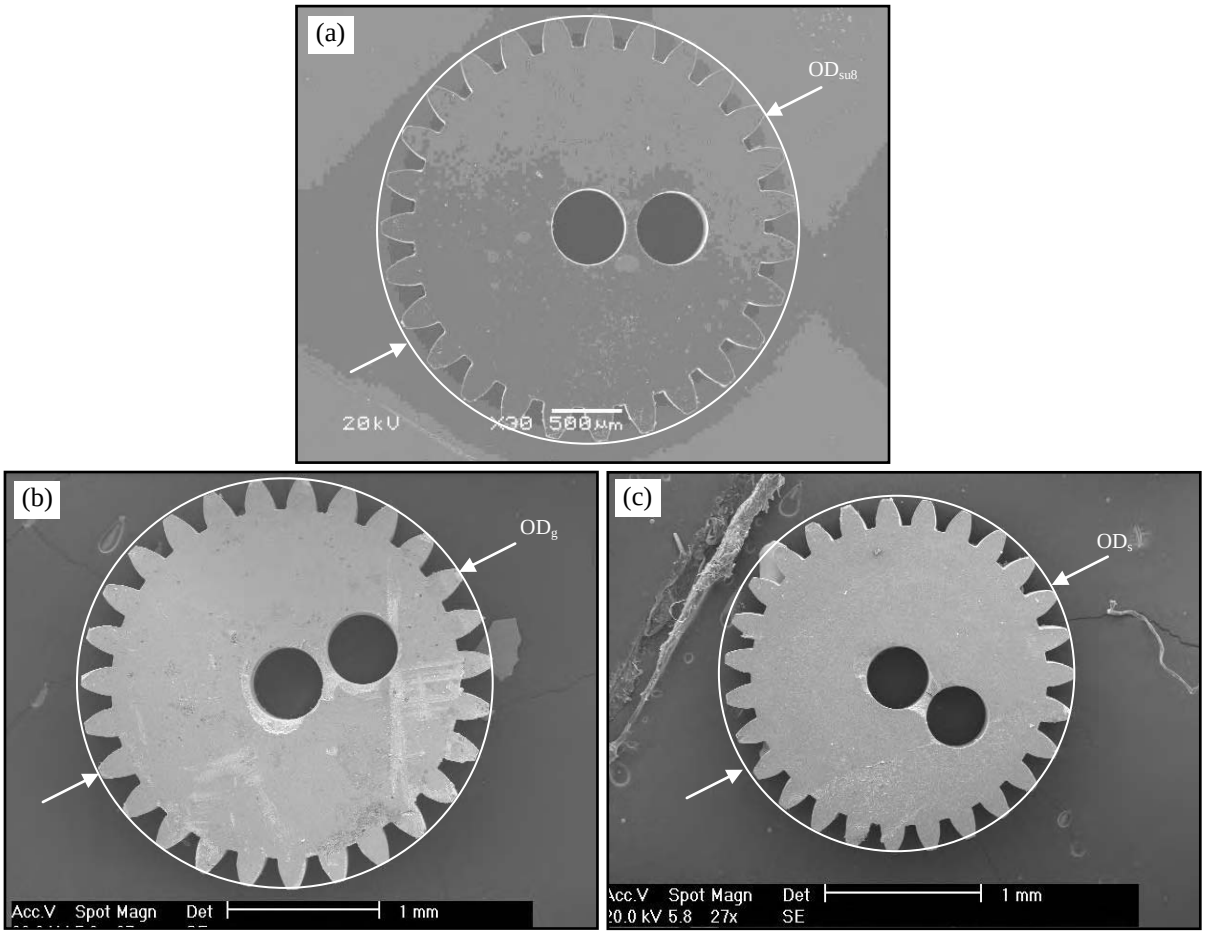

Figure 4.4. SEM images of (a) SU-8, (b) green, (c) sintered microgears for shrinkage measurements.

4.3.2 Binder Optimization

Ceramic binder is a substance that is used to bind ceramic particles into the desired shape in the mould. In addition, it enhances green strength and improves flexibility of the ceramic parts. Polymers and waxes are the two major ingredients that are mainly present equally in a typical ceramic binder [136-137]. In slurry systems, binders play a crucial part in preparing optimum ceramic slurry. The more binder added, the stronger the green body is expected. Additionally, binders must be taken off from green parts before sintering. The more added binder, the more difficult the debinding process will be. As a consequence of

large amount of binder, more gas will be formed during the binder burnout step, which causes internal stress, possible part damage and geometry distortion. In balancing between the green strength and the debinding requirements, binder content in the proposed slurry systems was decided as the minimum added amount for damage free green parts fabricated using water and solvent based slurry systems. As for paraffin wax based slurry, which resulted in high green strength, binder content was decided as the minimum amount for convenient mixing and moulding which is a demanding requirement for high solid loading paraffin wax slurry.

4.4 Slurry Systems

Slurry based techniques are considered to be an effective approach to fill small micro features of the microengine parts in the PDMS mould and to obtain high precision green parts and hence the sintered microcomponents [138]. To achieve this purpose, characterisation of the raw ceramic powder and the chemical additives of well-dispersed ceramic slurry are essential, as it is difficult to obtain the optimum properties of the resultant ceramic structures if the powders, dispersant, binder and any other additives do not have the right characteristics. The aim of this experimental work is to investigate different Al_2O_3 and YSZ8 ceramic slurry systems and their optimum composition for fabrication of net shape ceramic microengine parts. The optimum slurry system was selected to achieve net shape green and sintered ceramic microcomponents with the highest density and the lowest shrinkage.

Three different slurry systems were employed and optimized in the fabrication of Al_2O_3 and YSZ8 microcomponents. In the selection process, first, the candidate binders and dispersants were decided based on their compatibility with both PDMS mould and the

carrying vehicle. Next, the amount of the binders and dispersants were optimized based on their effects on the green parts. Afterwards, the green parts were sintered and the sintered density and shrinkage were measured for both Al_2O_3 and YSZ8 using the proposed slurry system. In these experiments, water, solvent, and paraffin wax based slurries were tested and optimized for the manufacturing of Al_2O_3 and YSZ8 microengine parts.

4.4.1 Water-Based Slurry

Water-based slurry process has been employed extensively in many ceramic forming techniques, such as tape casting and slip casting [137]. The use of water as the dispersing liquid is attractive because of cost, environmental and health benefits. Aqueous binders, such as Duramax B-1000 (Rohm & Haas, USA) and Duramax B-1007 (Rohm & Haas, USA), were used together in the experiments. They are commercially available low foaming binders. In addition, their high dispersion in water enables an effective adsorption on the powder in water, reducing possible cracks on the green body during drying. The high solid loading of the binders increases the particle binding in the green body, which improves its flexibility. During the drying of the slurry, the polymer particles bind the particles together and increase the green strength [139-141]. On the other hand, Duramax D-3005 (Rohm & Haas, USA) was used as a dispersant. D-3005 is an ammonium salt of a polyelectrolyte, commercially available for dispersing different ceramic powders in aqueous suspensions. D-3005 has a low molecular weight, which makes it effective at low use levels. The dispersant is supplied as a 35% solution in water. The physical properties of B-1000 and D-3005 as supplied by the manufacturer are given in Table 4.3.

Table 4.3. Selected properties of B-1000, B-1007 and D-3005 [140-142].

Properties	**B-1000**	**B-1007**	**D-3005**
Density (g/cc)	1.00-1.20	1.00-1.20	1.16
Total Solids (%)	55	37	35
pH	8.0-9.0	6.0-7.0	6.0-7.0

4.4.1.1 Fabrication Process

Fabrication of ceramic microcomponents using water-based slurry was performed in the following steps.

1. Dispersant D-3005 is added to deionised water and mixed with the aid of magnetic stirrer for 5 minutes.

2. Ceramic powder is added to the mixture to achieve a constant solid loading for all powders of 80% vol. The deagglomeration of the powder is achieved using mechanical stirring for 1 hour followed by ultrasonic processing for 8 minutes.

3. Polymer based binders B-1000 and B-1007 are then added at a ratio of 1:4 and mixed for 30 minutes using a low speed stirring to reduce the foaming.

4. The prepared slurry is degassed and then casted onto the PDMS to fill the mould cavities with the aid of stainless steel spatula and vacuum casting. Vacuum casting is performed by placing the PDMS mould covered with ceramic slurry inside a vacuum chamber at 0.3 bar.

5. The excess slurry on the top of the mould is removed using a razor blade, and the mould is left to dry slowly for 24 hours.

6. Once the mould is dried, the green parts are achieved by carefully bending the soft PDMS mould and then are pulled out with the aid of a thin tweezer.

7. The PDMS mould is cleaned by an ultrasonic bath with acetone and are ready for the next use.

8. The green parts are placed in a high temperature chamber furnace (Elite Thermal Systems- UK). Temperature of the furnace is ramped from room temperature to 600 °C at a rate of 1 °C/min and then from 600 °C to the final temperature at a rate of 4 °C/min. The temperature is remained at final temperature for 2 hours before the furnace is cooled naturally down to room temperature. The final temperatures are 1600 °C and 1550 °C for alumina and YSZ8, respectively.

4.4.1.2 Results

4.4.1.2.1 Green Microcomponents

In the fabrication of Al_2O_3 and YSZ8 green parts using water-based slurry. It was found that, the minimum binder concentration used in the slurry without damaging the resultant green parts during both drying and demoulding processes was about 20-25 mg/g powder for both A0.7 and 2YSZ8 powders. Less binder concentration increased the possibility to break the green parts. Using the optimum binder concentration resulted in complete and crack free green parts as shown in Figure 4.5.

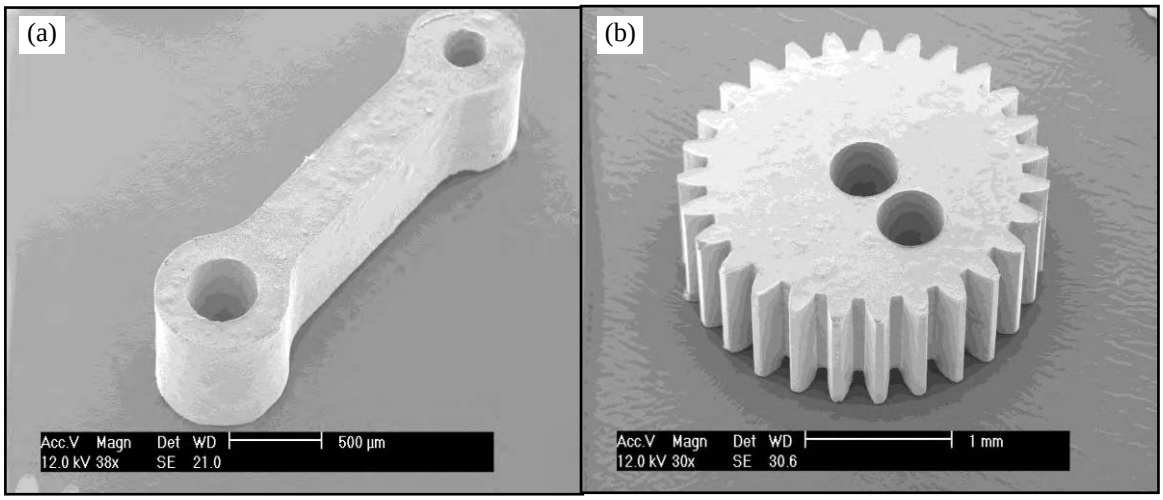

Figure 4.5. SEM images of green ceramic microcomponents fabricated using water-based slurry.

In the optimization of D-3005 concentration in water based slurry, the green densities and drying shrinkages of A0.7 and 2YSZ8 powders were measured with respect to D-3005 concentration. It was found that, the highest green densities were 61.2% and 55.9% when D-3005 concentration was 11.8 mg/g and 20.6 mg/g for both A0.7 and 2YSZ8 powders respectively. In addition, the linear shrinkages were 2.5% and 3.1% for both A0.7 and 2YSZ8 powders respectively at the same optimum D-3005 concentrations.

4.4.1.2.2 Sintered Microcomponents

Sintered samples obtained using the optimum water-based slurry and the above mentioned heating cycle are shown in Figure 4.6. The samples include a net shape, complete and crack free sintered microcomponents. The maximum sintered densities obtained using A0.7 and 2YSZ8 are 98.3% and 98.5% with a linear shrinkage of 17.6% and 21.9% respectively. More details and characterisation of the concerning water-based slurry, green and sintered microcomponents properties are explained in Chapter 5 and Chapter 6.

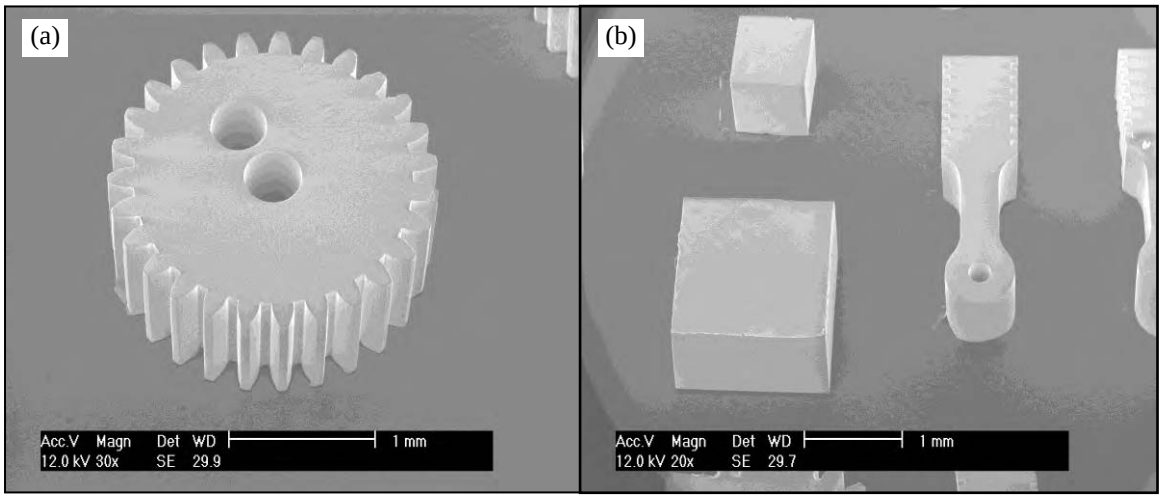

Figure 4.6. Sintered ceramic microcomponents fabricated using water-based slurry.

4.4.2 Solvent-Based Slurry

Polymer-derived ceramics are fabricated through pyrolysis of preceramic polymers. They offer a great variety of chemical and microstructure modifications, allowing molecular tailoring of ceramic materials with improved properties compared to conventional ceramic materials. They gain in importance with the increase of advanced precursor materials, such as polycarbosilane, polysilazane, polysiloxane and polyborosilazan. They have been used to fabricate net shape monolithic ceramic MEMS by either microcasting a liquid ceramic precursor into a mould that has been prepared by conventional lithographic methods or by microforged moulds [143]. Recently, polymer ceramics have been successfully used to fabricate alumina composites by hot pressing of poly allyl carbosilane coated alumina powder into green pattern shapes, with subsequent pyrolysis and pressureless sintering [144]. Here, polysiloxazane preceramic coatings resin (PCR) was used as a binder in this slurry system. The commercial product of preceramic coating resin used in the experiments was (HTA 1500 Slow Cure, KiON Speciality Polymers, Germany). It is a clear and low viscosity coating resin designed to cure at room temperature curable with 100% solids

within 1 hour. The polymer pyrolysis after curing results in conversion of the cured polymer to amorphous and crystalline ceramic phases. Therefore, using PCR over organic binders is expected to be better than conventional polymeric binders as it works both as the binder and as the additive of ceramic inclusion within the sintered ceramic matrix. In addition, no debinding process is required. Properties of the PCR polymer are listed in Table 4.4.

Table 4.4. Properties of HTA 1500 Slow Cure [145].

Properties	**Unit**
Density (g/cc)	0.9897
Viscosity (cps)	40
Yield Solids (%)	100%

PCR is hydrolytically sensitive and will slowly generate ammonia upon contact with water or moist surfaces. In addition, it is miscible with aromatic hydrocarbons, alkanes, ethers, ketones [145]. On the other hand, PDMS is not compatible with certain hydrocarbons such as toluene, alkanes such as hexanes and ethers such as tetrahydrofuran [146]. As a result, acetone and acetonitrile are considered appropriate candidates as carrying vehicle. Both are compatible with the introduced PCR and with the PDMS soft mould. However, acetone was excluded from the experiments due to its high evaporation rate during processing of the slurry.

The choice of the dispersant in the preparation of solvent-based slurry is also governed by its compatibility with PCR, PDMS and acetonitrile. For the introduced solvent slurry, Brij52 was used as a dispersant. Brij52 (Polyethylene glycol hexadecyl ether) is a non-

ionic surfactant of the polyethylene glycol family and was used as a dispersant with different materials [147]. For both Al_2O_3 and YSZ8 solvent-based slurry, green measurements were performed for the optimization of the slurry optimum composition.

4.4.2.1 Fabrication Process

Preparation of ceramic slurry based on solvent-based slurry was performed using the following steps.

1. Brij52 is added to the acetonitrile and mixed with the aid of magnetic stirrer for 5 minutes.
2. Ceramic powder is then added to the mixture and mixed by using mechanical stirring for 1 hour followed by ultrasonic processing for 8 min.
3. Preceramic polymer (PCR) is then added and mixed for 30 minutes using mechanical stirrer.
4. Ceramic slurry is degassed using vacuum and then was casted on the PDMS to fill the mould cavities with the aid of stainless steel spatula and vacuum casting.
5. The excess slurry on the top is removed using a blade, and the mould is left to cure.
6. Once the mould is cured, the green parts are achieved as previously explained.
7. As there is no information about the conversion conditions of the cured PCR to ceramic, two types of heating cycles are proposed for the sintering process. The first cycle is started by placing the green samples in a high temperature tube furnace (Elite Thermal Systems-UK) in flowing nitrogen. Temperature of the furnace is ramped to 1500 °C at a rate of 2 °C/min. The temperature remained unchanged for 2 hours before the furnace is cooled down to room temperature. The second cycle is by heating up the samples to 1600 °C for 2 hours with a heating rate of 2 °C/min in air.

4.4.2.2 Results

4.4.2.2.1 Green Microcomponents

Preceramic polymers are not originally designed as binders and their curing or binding conditions are different from conventional organic binders. Therefore, several factors affect the use of PCR as a binder in colloidal systems. By observation, they can be listed as follows.

1. Moulded parts shrinkage due to evaporation of acetonitrile content is faster than curing of PCR. A slow drying rate is required to reduce acetonitrile evaporation rate and hence to reduce drying cracks and this was achieved by keeping mould in a closed container.

2. Moisture contents in powder reacted with the PCR and generated ammonia bubbles in the slurry, and sub consequently in the green parts as shown in Figure 4.7(a). Therefore, heating up the powder first is necessary to remove moisture before processing.

3. Insufficient PCR content in the slurry (less than 200 mg/g powder), caused visible cracks in the green body even before the completion of the curing process. As a result, the green parts were broken during the demoulding step, as shown in Figure 4.7(b).

4. Curing time is another important parameter. According to PCR properties, the preceramic polymer will be dry to touch after 1 hour [145]. However, it was observed that when the curing time of the slurry was longer than 10 hours, the green parts tend to adhere strongly to the PDMS mould. Even after demoulding, part of the PDMS mould clung to the green part, as shown in Figure 4.7(c).

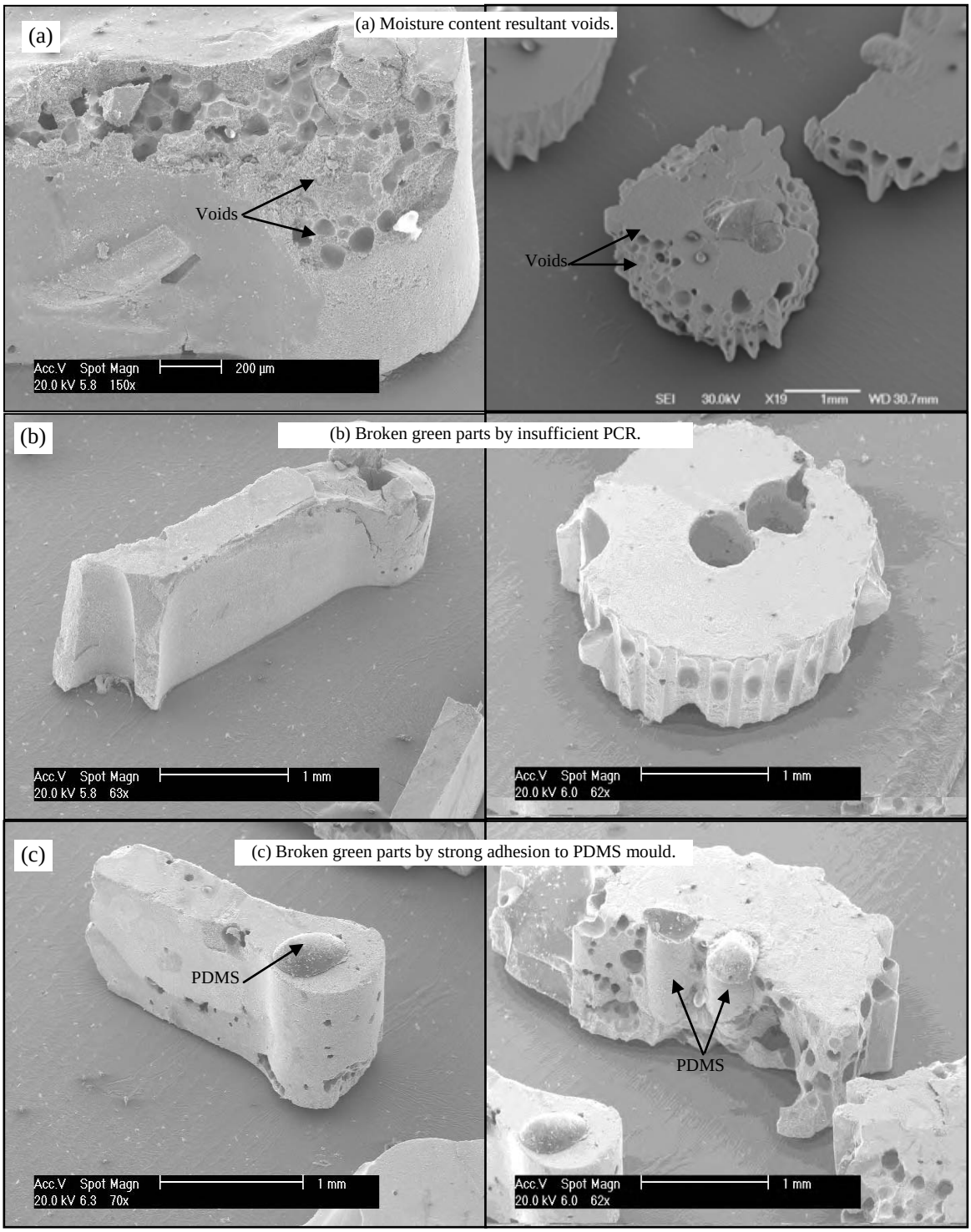

Figure 4.7. SEM images of defected green parts fabricated using solvent-based slurry.

By adjusting the slurry composition with PCR content of a minimum amount of 200 mg/g powder and curing time to about 5-8 hours, a few undamaged near net shape green micropistons were produced. However, other microengine parts could not be successfully demoulded, especially the microgears. The resultant freestanding green alumina micropistons without cracks are shown in Figure 4.8.

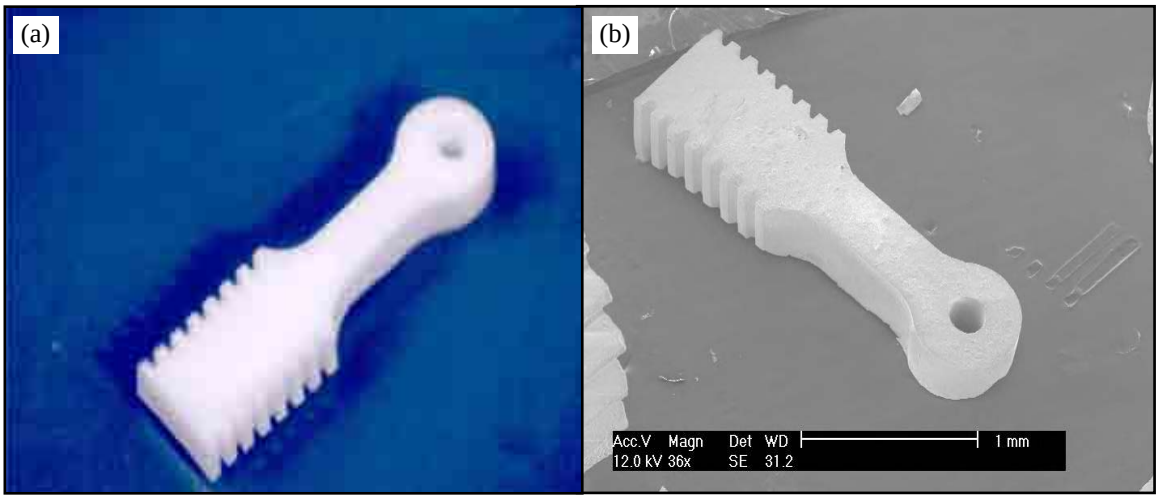

Figure 4.8. Optical and SEM images of ceramic green micropistons fabricated using solvent-based slurry.

In optimization of Brij52 concentration in the solvent-based slurry, Al_2O_3, YSZ8 green density and drying shrinkage using A0.7 and 2YSZ8 powders with respect to the Brij52 concentration were measured. It was found that, the highest green densities were 53.4% and 52.1% when Brij52 concentration was 1.1 mg/g and 0.8 mg/g for both A0.7 and 2YSZ8 powders respectively. In addition, the linear shrinkages were 4.1% and 4.3% for both A0.7 and 2YSZ8 powders respectively at the optimum Brij52 concentrations.

From both the green density and drying shrinkage for both Al_2O_3 and 2YSZ8, it can be clearly concluded that Brij52 has a negligible effect on the green properties of the proposed

solvent-based slurry. This is may be because of high PCR content in the slurry, which has the dominant concentration of 200 mg/g when compared to the Brij52 concentration.

4.4.2.2.2 Sintered Microcomponents

Sintered alumina micropistons were obtained using the optimum solvent-based slurry composition and are shown in Figure 4.9. The results show net shape, complete and crack free microcomponents. The maximum sintered density obtained using A0.7 was about 72.2% with a linear shrinkage of 15.2% when sintered in nitrogen and was 57.6% with a linear shrinkage of 10.5% when sintered in air. On the other hand, the maximum sintered density obtained using 2YSZ8 was about 69.9% with a linear shrinkage of 18.4% when sintered in nitrogen and was 55.3% with a linear shrinkage of 11.4% when sintered in air.

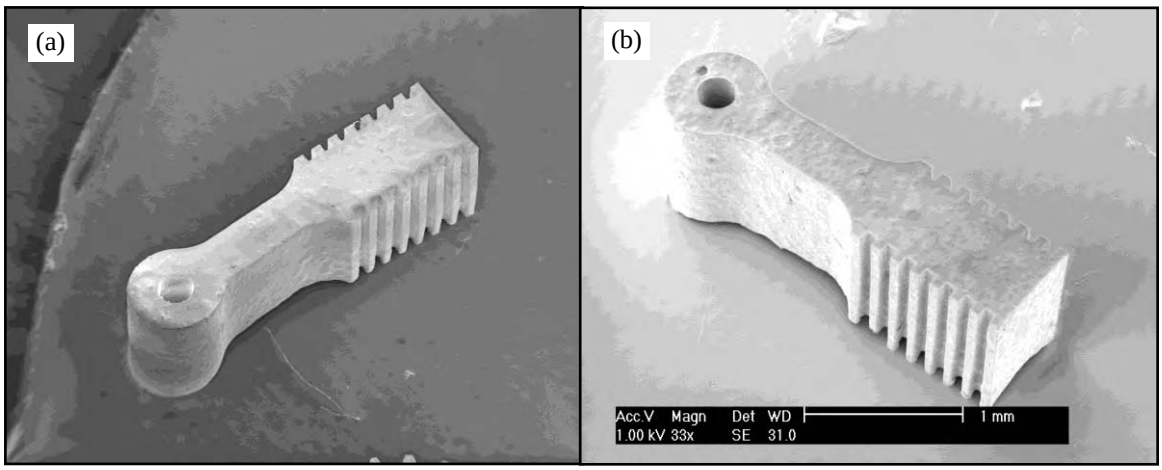

Figure 4.9. SEM image of sintered micropiston fabricated using solvent-based slurry and sintered in (a) nitrogen, and (b) air.

4.4.3 Paraffin Wax-Based Slurry

Paraffin wax is a mixture of alkane hydrocarbons having C_nH_{n+2} formula where $20 \leq n \leq 40$. They are solid in room temperature and start to melt in temperature starting from 37°C. Paraffin wax is a very popular binder in low-pressure injection moulding for its low cost

and versatile working temperatures. In addition, the resultant high strength green parts make it effective binder for complex shape ceramics [138]. A low temperature paraffin wax was used in the slurry in the research for the convenience of the thermal working temperature of the PDMS mould. Paraffin wax (Sigma Aldrich-UK) has the melting point of 53-57 °C. Ceramic slurry based on paraffin wax could be improved with the addition of dispersants, which improves ceramic particle dispersion and enhances wetting of the binder on the ceramic particles [148]. Stearic acid $C_{18}H_{36}O_2$ supplied by (Sigma Aldrich-UK) with a melting point of 69-71 °C was used as a dispersant in the paraffin wax-based slurry. In the proposed paraffin wax based-slurry, green body measurements and SEM examination are discussed for the optimization of stearic acid concentration composition in the Al_2O_3 and YSZ8 slurry for the production of net shape ceramic microcomponents.

4.4.3.1 Fabrication Process

The fabrication procedure using paraffin wax-based slurry was performed using the following steps.

1. Paraffin wax is added to a glass beaker and placed on a hotplate at a temperature of 100-120 °C in order to melt the wax.

2. Stearic acid is then added to the wax, melted and mixed using a mechanical stirrer for 5 minutes on the hotplate.

3. Ceramic powder is added to the mixture and continued stirring the mixture using mechanical stirrer for 5 minutes on the hotplate.

4. PDMS mould is adhered on a glass petri dish and placed on the hotplate for 2 minutes to heat up the mould before the moulding process.

5. The hot PDMS mould is filled with the slurry on the hotplate with the aid of stainless steel spatula.

6. To ensure complete filling of the bottom parts of the PDMS mould, the mould is placed in a vacuum chamber for few seconds. Afterwards, the mould is quickly placed again on the hotplate to continue filling of the mould before the slurry cools down. After the filling is completed, the excess slurry on the surface is removed using a razor blade.

7. The mould is removed from the hotplate to cool down for about 15 minutes.

8. Green parts were achieved by peeling off the cooled soft mould.

9. The obtained green parts are placed in a high temperature chamber furnace (Elite Thermal Systems- UK). The following heating cycle is introduced. From room temperature to 600 °C a slow heating rate of 0.5 °C /min was performed and held at that temperature for 30 min to prevent defects during melting and burning of the binder system. Next, it was heated from 600 °C to 800 °C at a ramping rate of 1 °C /min. Afterwards, from 800 °C to 1600 °C the heating rate was increased to 4 °C/min and kept for 2 hours.

4.4.3.2 Results

4.4.3.2.1 Green Microcomponents

Paraffin wax is played the role of both the binder and the carrying medium. In the mixing step, the minimum amount of binder, which provides the necessary convenient moulding process, was decided as the optimization criteria. For binder concentration less than 50 mg/g powder, it was difficult to mix the ceramic slurry using the mechanical stirrer. By increasing the binder concentration to about 200 mg/g and 100 mg/g for A0.7 and 2YSZ8

powder respectively, it was easier to get homogenous slurry using mechanical stirring. However, the slurry flows less easily and freezes faster before complete filling, especially in thin microfeatures, due to its high viscosity. As a result, incomplete microengine parts were obtained and are shown in Figure 4.10. Further increasing of the binder content to about 260 mg/g and 130 mg/g for A0.7 and 2YSZ8 respectively, the filling process was improved and a complete filling was achieved, as shown in Figure 4.11.

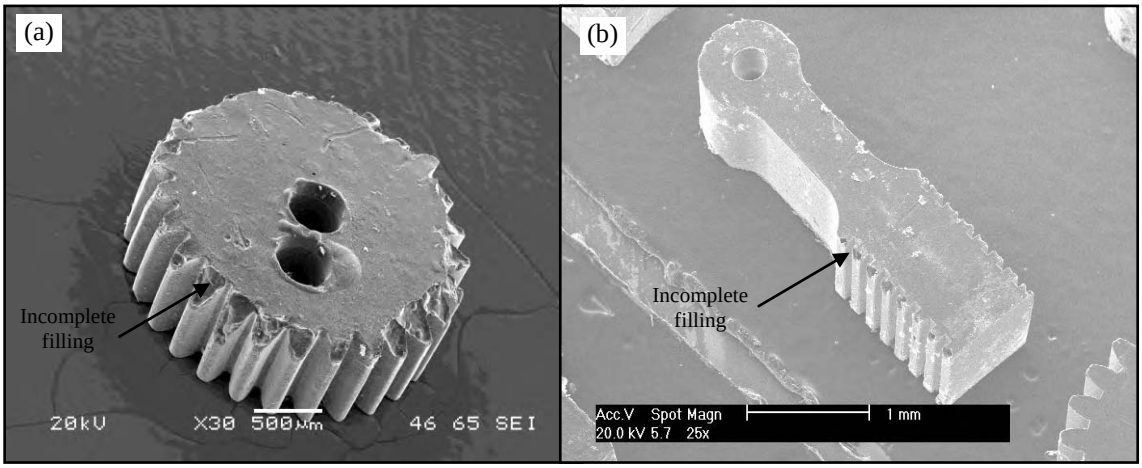

Figure 4.10. SEM image of incomplete green microcomponents fabricated using paraffin wax-based slurry.

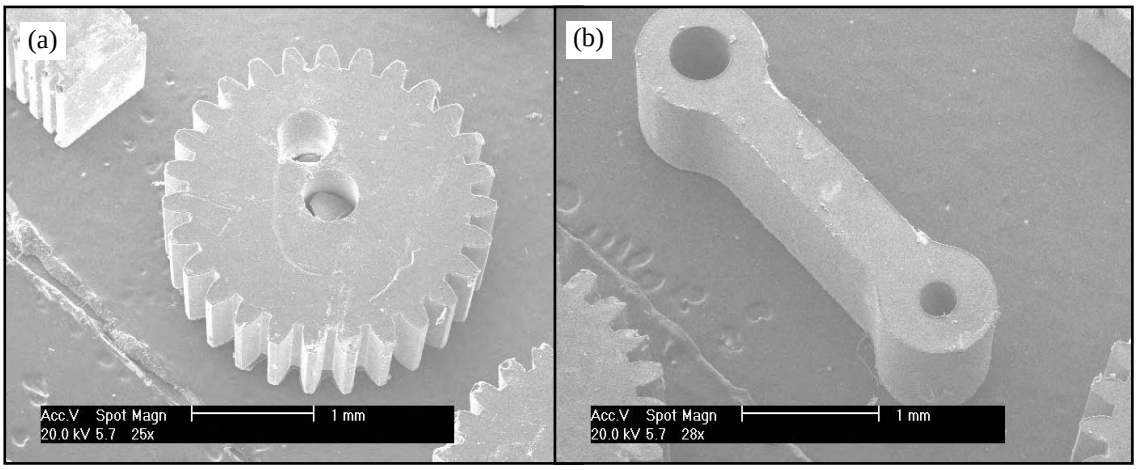

Figure 4.11. SEM image of complete green microcomponents fabricated using paraffin wax-based slurry.

In optimization of stearic acid as a dispersant in the paraffin wax-based A0.7 and 2YSZ8 powder slurries, green density and drying shrinkage with respect to the stearic acid concentration were recorded. It was found that, the highest green densities were 56.5% and 50.9% when stearic acid concentration was 14.2 mg/g and 24.5 mg/g for A0.7 and 2YSZ8 powders respectively. In addition, the linear shrinkages were 3.8% and 4.1% for both A0.7 and 2YSZ8 powders respectively at the optimum stearic acid concentrations.

4.4.3.2.2 Sintered Microcomponents

After obtaining complete green parts and due to the high binder content in the paraffin wax-based slurry when compared with water-based slurry, the binder must be removed properly before sintering process. The main contents in the paraffin wax are normally removed below 600 °C [148]. Therefore, thermal debinding technique has been performed for this purpose. Four techniques have been introduced in the proposed thermal cycle, and they are as follows.

1. The samples were placed on flat a alumina substrate during sintering. The resultant samples are shown in Figure 4.12(a). Sintered microgears were significantly deformed and broken during debinding process. This is mainly happened due to a poor debinding process. Paraffin wax destroyed the green parts during either their melting or burning out.

2. To support green body and to infiltrate the molten wax during debinding, the green microcomponents were completely embedded in the same ceramic powder as the samples during the heating cycle. The resultant sintered microgear is shown in Figure 4.12(b). As shown, the sintered microgear obtained using embedding process did not deformed due to the support of the powder. Furthermore, the microgear teeth look

complete. However, the surface of the sintered microgear was completely distorted due to adhesion of the supporting powder to the microgears surface and resulting in rough surface.

3. To reduce effect of the supporting powder on the shape retention and the surface quality, the green microcomponents were placed on a powder bed during heating process. The resultant sintered microgear is shown in Figure 4.12(c). As shown in the figure, the top surface of the sintered microgear obtained using powder bed was significantly improved. However, minor defects can still be observed on the top surface of the microgears due to deformation during debinding. In addition, there are adhesion of the supporting powder located at the bottom surface.

4. To eliminate the effects of the supporting powder, the green samples were placed on a porous substrate to provide an infiltration of the molten wax. In addition, the samples were covered with a ceramic crucible to reduce sudden heat effect resulting from the heating elements of the sintering furnace. The resultant sintered microcomponents are shown in Figure 4.13. The samples include a net shape, complete and defect free sintered microcomponents

As for the density and shrinkage measurements, the sintered densities obtained using A0.7 and 2YSZ8 were 97.1% and 96.4% with a linear shrinkage of 21.5% and 23.4% respectively.

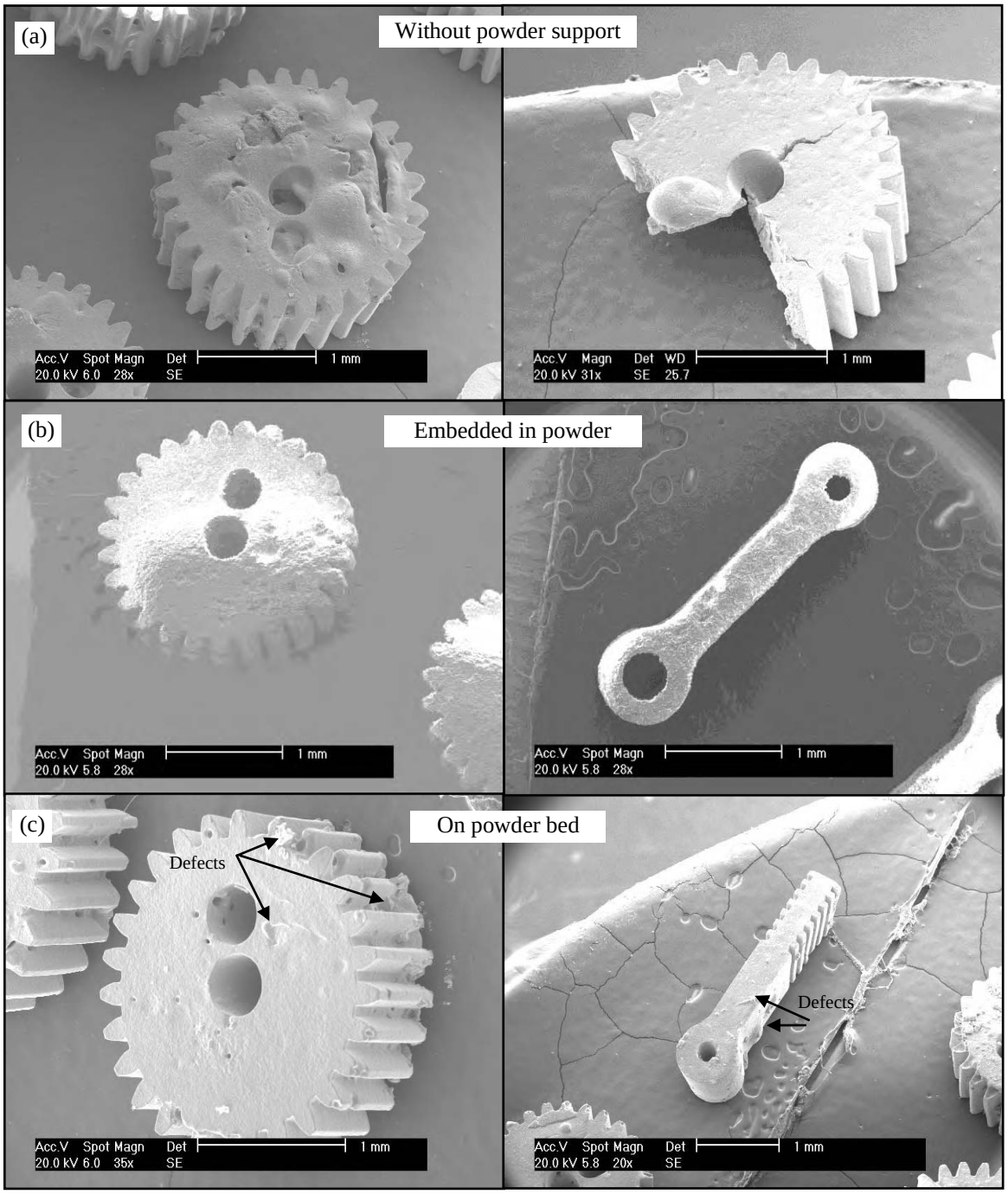

Figure 4.12. Sintered ceramic microcomponents fabricated using paraffin wax-based slurry and sintered (a) without powder support, (b) embedded in powder, and (c) on powder bed.

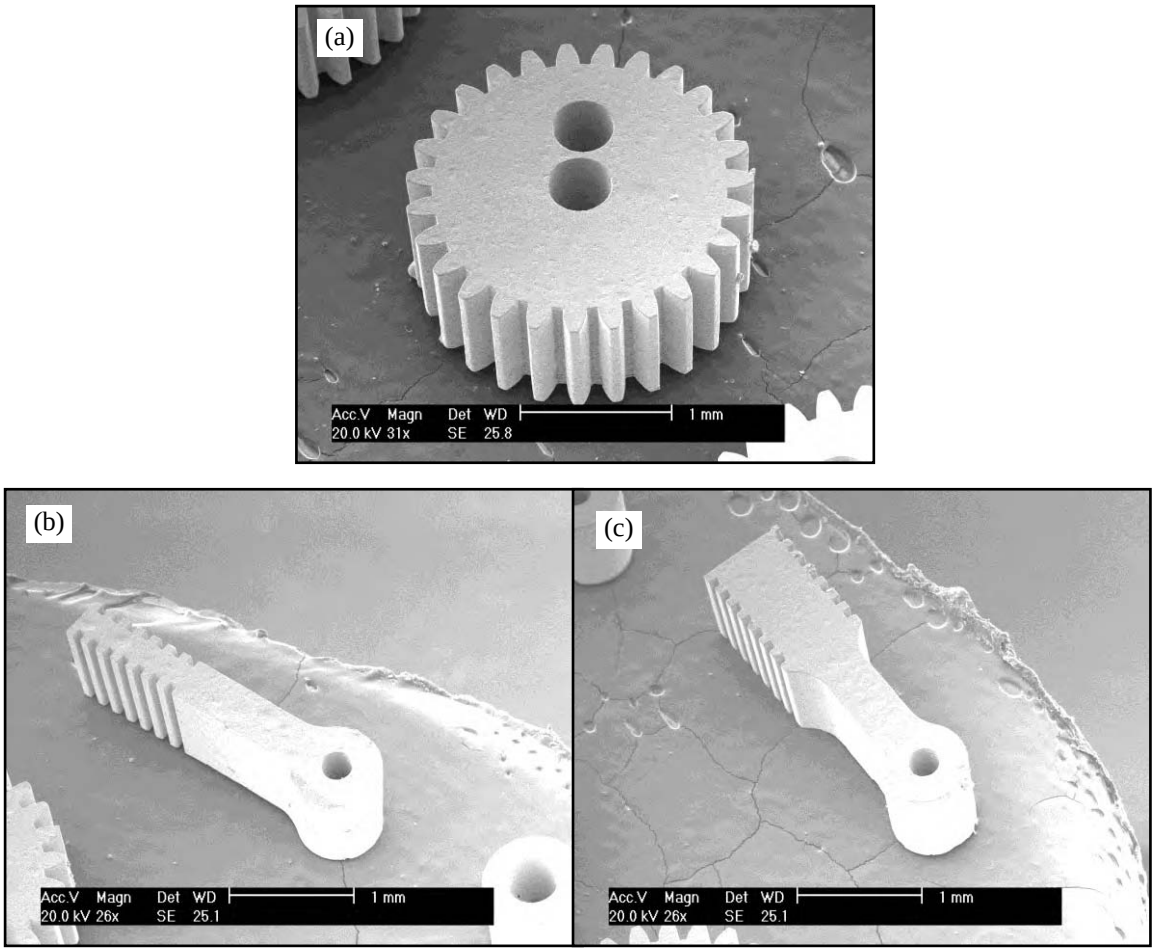

Figure 4.13. Sintered ceramic microcomponents fabricated using paraffin wax-based slurry and an optimum sintering process.

4.5 Discussion

In the performed experimental work and their results, three different slurry systems were used in the fabrication of Al_2O_3 and YSZ8 microcomponents. A comparison table summarizes their main properties in Table 4.5.

Table 4.5. Comparison between water, solvent and paraffin wax based slurries for the fabrication of Al_2O_3 and YSZ8 microcomponents.

Properties	**Water-based**	**Solvent-based**	**Paraffin wax-based**
Carrying medium	Water	Acetonitrile	Paraffin wax
Binder	B-1000+B-1007	HTA 1500	Paraffin wax
Dispersant	D-3005	Brij52	Stearic acid
Processing temperature	Room temperature	Room temperature	100:120 °C
Microengine green parts	All	Micropistons	All
Microengine sintered parts	All	Micropistons	All
Moulding	Excellent	Excellent	Good
Demoulding	Good	Poor	Excellent
Green parts curing duration	24 hours	5-8 hours	15 minutes
Total duration of the sintering	16 hours	15 hours	29 hours
Al_2O_3 & 2YSZ8 sintered densities	98.3 & 98.5%	57.6 & 55.3% in Air 72.2 & 69.9% in N_2	97.1 & 96.4%
Al_2O_3 & 2YSZ8 linear shrinkages	17.6% & 20.9%	10.5 & 11.4% in Air 15.2 & 18.4% in N_2	21.5 & 23.4%

As shown in the comparison table, it can be found that microcomponents fabricated using water-based slurry show distinctive advantages over solvent and paraffin wax-based

slurries in its high density and low shrinkage. In addition, the room temperature processing conditions and the use of water as carrying medium are more favourable in terms of safety, environmental and health benefits. However, water-based slurry has the longest processing time for obtaining the final components than the other slurries. On the other hand, green parts fabricated using water-based slurry are the weakest than the other green parts fabricated with the proposed slurries. Therefore, experience is necessary to keep it damage free during demoulding and handling. From all the above advantages and disadvantages, water-based slurry is chosen as the forming ceramic slurry for the fabrication of ceramic microengine parts. An extended experimental work is performed for detailed characterization of the slurry, green and sintered parts using different powder sizes of Al_2O_3 and YSZ8 in the chapter 5 and chapter 6.

4.6 Summary

The research in this chapter was aimed to identify a ceramic slurry system and its processing rout for the fabrication of Al_2O_3 and 8 mole% yttria stabilized zirconia microengine parts using soft lithography. To achieve this goal, water, solvent and paraffin wax-based slurries were proposed and their composition was optimized. Problems in preparation and fabrication of the introduced slurries were identified and possible solutions were proposed. Evaluation of each slurry system was performed to achieve a process of convenient moulding, demoulding, high quality shape retention, high green and sintered physical properties. Based on the assessments of the slurries given above, the water-based slurry seems to offer the greatest potential to realize suitable Al_2O_3 and YSZ8 microcomponents fabrication approach and produce near net shape ceramic microengine parts. Further characterization of this slurry is presented in the next chapter.

CHAPTER 5: CHARACTERISATION OF ALUMINA AND ZIRCONIA SLURRIES AND GREEN MICROCOMPONENTS

5.1 Introduction

This chapter deals with the principles and procedures of the preparation and characterisation of alumina and zirconia water-based slurries, which are performed for the fabrication of damage-free and dense green microengine components. Stable and well-dispersed suspensions with high solid loading were used and the effect of their composition together with the moulding and demoulding technique on the resulting structures were investigated. The chapter starts with a characterisation of ceramic slurries prepared using different Al_2O_3 and YSZ8 powder sizes, detailed in Section 5.2. Changing pH and dispersant concentration of the slurry alters the colloidal behaviour. To achieve highly stable suspensions zeta potential and sedimentation measurements were obtained to decide the optimal dispersant concentration and pH level. Based on the slurry results, and by optimizing dispersant and binder concentration, the resulting green microcomponents were characterised to ascertain the conditions that produce precise green parts with good physical properties. In Section 5.3, moulding and demoulding problems are defined and analysed so that possible causes can be identified and eliminated. Finally, the summary of the chapter is presented in Section 5.4.

5.2 Characterisation of Ceramic Slurry

In a ceramic colloid, ceramic particles are evenly distributed in a continuous phase with the aid of a proper dispersant. The resultant colloid can be a thick slurry or paste, or diluted as suspended particles. The ceramic particles are affected considerably by their surface chemistry. This allows the properties of the colloid to be controlled by changing the surface chemistry, therefore influencing subsequent fabrication processes. Colloidal processing has many advantages over other techniques, which is why it has been the focus of much recent research activity. It can overcome the problems of microstructural heterogeneity or flaws associated with dry powder processing. Heterogeneity arises from agglomerates and inclusions such as binders, dispersants and dissolved salts in the dry powder [149-151].

Various types of colloidal suspensions can be prepared by controlling the interparticle forces. The total interparticle potential energy that governs the colloidal stability can be expressed as:

$$V_{total} = V_{vdW} + V_{elect} + V_{steric} + V_{structral} \quad \text{Eq. 5.1}$$

where V_{vdW} is the energy associated with attractive long-range Van der Waals interactions between particles and V_{elect} is the energy associated with repulsive electrostatic interactions between particles that have same polarity. V_{steric} is the energy associated with repulsive steric interactions between particle surfaces coated with adsorbed polymeric species, and $V_{structural}$ is the potential energy resulting from the presence of nonadsorbed species in solution that may either increase or decrease suspension stability [152].

To improve ceramic suspension dispersion, the total interparticle energy described in equation 5.1 must be controlled. In this section, characterisation of ceramic suspensions with different powder sizes is performed using zeta potential and sedimentation measurement with respect to ceramic powder, pH and dispersant concentration.

5.2.1 Zeta Potential Measurement

5.2.1.1 Background

Zeta potential (electrophoretic mobility) indicates the degree of repulsion between similarly charged particles in dispersion. The importance of zeta potential is that its value can be related to colloidal dispersion stability. Highly stable suspensions can be obtained by generating strong repulsive forces between the particles to overcome the Van der Walls attraction and prevent aggregation. Achieving a high zeta potential is important in electro statically stabilizing the aqueous suspensions required for ceramic consolidation. Surface properties (and therefore zeta potential) of the suspended powders are determined by the adsorption of H^+ ions and OH^- ions onto the surface. Ion adsorption can be controlled by adjusting the pH value of the suspension. Alternatively, one can use dispersants to control particle surface charge by either introducing a steric barrier, electrostatic effects, or both. Any change in pH or dispersant concentration may significantly affect surface charge of particles and hence the stability condition [152-153].

5.2.1.2 Procedure

In the experiments described below, dilute aqueous ceramic suspensions with concentration of 0.05% wt. were prepared and the dispersant was added. The pH levels of the suspensions were adjusted to the desired level. The pH values were controlled by adding either hydrochloric acid or potassium hydroxide solutions. The suspension was

ultrasonically dispersed for 8 minutes prior to measurements to enhance dispersion and to eliminate tiny air bubbles, which may affect accuracy of the measurements. Afterwards, the suspensions zeta potential were measured using micro electrophoresis apparatus equipped with a Zetasizer (Malvern Instruments-School of chemical engineering-University of Birmingham) to determine the zeta potential. To understand the surface nature of the ceramic powder, initial zeta potential measurements were obtained without dispersant and final measurements in the presence of the dispersant for both Al_2O_3 and YSZ8 powders. Measurements were taken from aqueous colloidal ceramic suspensions consisting of 0.7 µm and 1.0 µm of Al_2O_3 powders, and 2.0 µm and 5.0 µm of YSZ8 powders, referred to as A0.7, A.10, 2YSZ8 and 5YSZ8 respectively, whereas sizes of 12.0 µm Al_2O_3 powder and 10.0 µm YSZ8 powder were excluded from the experiments, because of the difficulty of achieving a stable suspension using these values. Each zeta potential was measured three times and the average value was obtained.

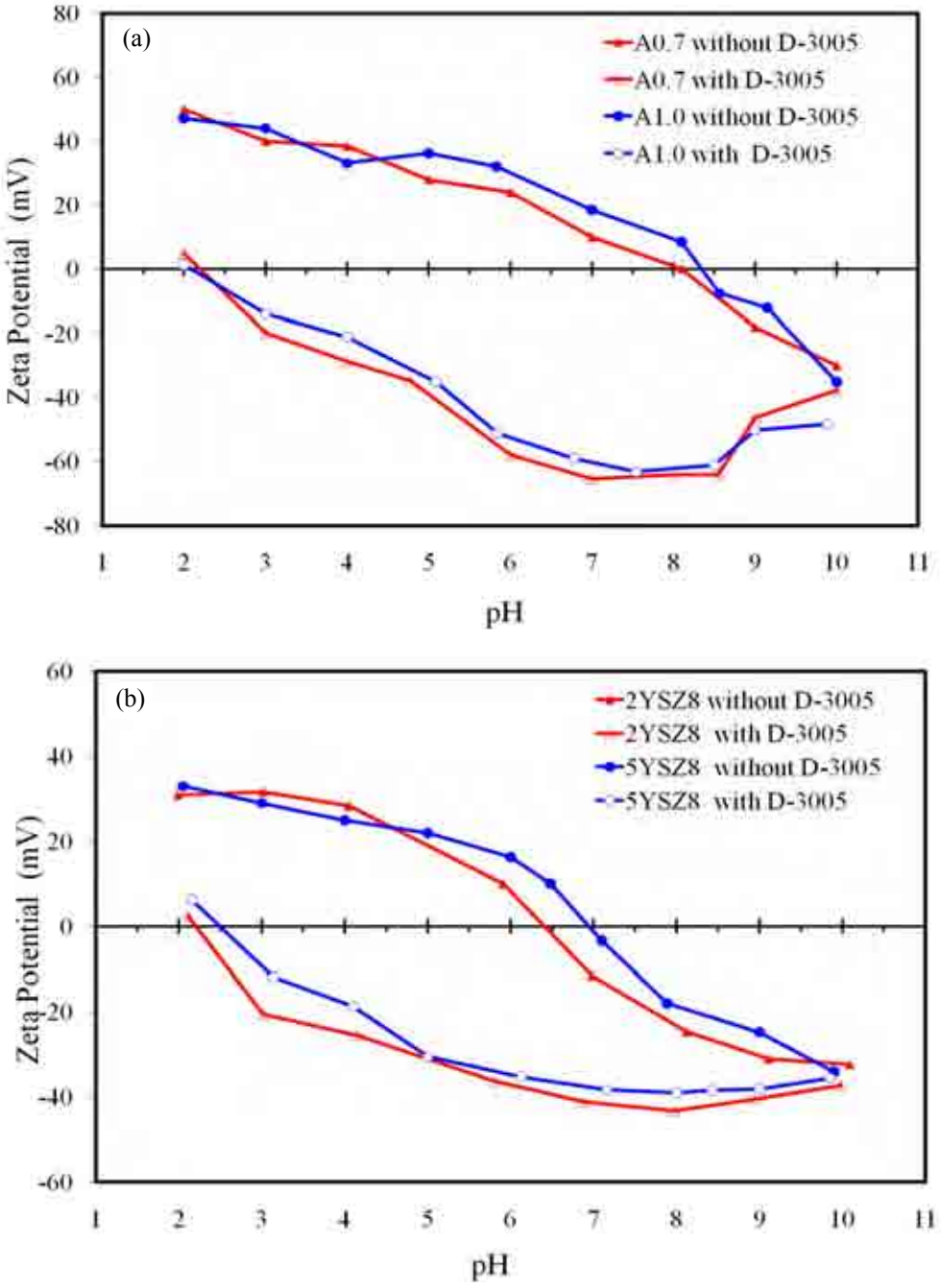

Figure 5.1. Zeta potential dependence on pH and the added dispersant for (a) Al_2O_3 and (b) YSZ8 powders.

5.2.1.3 Results and Discussions

In this section, results for both Al_2O_3 and YSZ8 powders of zeta potential as a function of pH value for bare ceramic powder and ceramic powder with the addition of D-3005 are presented.

Figure 5.1(a) shows results obtained from A0.7 and A1.0 alumina powders with a D-3005 concentration of 15 mg/g of ceramic powder. The isoelectrostatic point (IEP) for bare alumina is found in the basic regime at pHIEP = 8.1-8.3. Zeta potential was found to be positive in a wide range of pH values, particularly in the acidic regime. On the other hand, zeta potential is clearly negative at a pH higher than pHIEP and positive at a pH lower than pHIEP.

A significant increase in zeta potential was observed when D-3005 was added to the suspension, enlarging the pH region where the zeta potential value was negative and creating a high negative zeta potential of 63-65 mV. The highest values were located in a wide pH range, specifically from pH 7.0-8.5. The pHIEP moved towards the acidic region by about 6 units, to pHIEP = 2.

Results from similar experiments conducted on YSZ8 suspensions are shown in Figure 5.1(b). It is clearly seen from the figure that zeta potential is positive throughout the acidic regime while it is negative in the alkaline regime. Also, pHIEP is found to be near neutral at pHIEP = 6.5-7.0. Addition of D-3005 to the suspension induced a significant increase in suspension zeta potential, where the surface charge of YSZ8 particles is negative and is 39-43 mV over a wide pH range from pH=6.9-9. The pHIEP moved about 4-5 units towards the acidic pH region, at about pHIEP = 2.3-2.5.

From the above results, when no dispersant is added, the IEP points are in the range 8.1-8.3 and 6.5-7.0 for Al_2O_3 and YSZ8 powders respectively. These values confirm the basic nature of the Al_2O_3 surface and the slightly acidic-to-neutral nature of the YSZ8 surface. It was also found that Al_2O_3 had a high positive zeta potential in the acidic region because of the basic surface, which has a tendency to interact strongly with H^+ ions. As for YSZ8, there is no significant difference in the highest zeta potential values in both acidic and alkaline regimes. This is because of the slight acidic-to-neutral nature of the YSZ8 surface, which tends to interact similarly with both H^+ and OH^- ions. After adding D-3005, an increase was observed in the zeta potential from neutral to the basic region for both Al_2O_3 and YSZ8. An explanation of this behaviour is found by considering how the disassociation nature of the dispersant changes when the pH value is changed. The dissociated ratio of the polyelectrolyte dispersant D-3005 is high in the alkaline regime and decreases when the suspension pH shifts towards the acidic regime [154-156]. The small differences in zeta potential between the same types of powder may be because of the powder preparation methods, or the effect of impurities, as well as error in the measurements. Finally, the reason for a slightly reduced zeta potential for suspensions with pH> 8.5-9.0 after the addition of D-3005 could not identified.

In summary, for ceramic oxides such as Al_2O_3 or for YSZ8 suspensions, adsorption of the polyelectrolyte dispersant occurs readily in the neutral to basic regimes for pH range (7.0-9.0). This results in an increase in zeta potential values and hence implies stable suspensions.

5.2.2 Sedimentation Measurement

5.2.2.1 Background

Sedimentation is the tendency for particles to settle out of suspension after agitated fluid comes to rest. This is due to the response of the particles to forces acting on them, such as the gravity and the interparticle forces. Typically, aggregated particles will settle most rapidly, whilst dispersed particles will settle more slowly. The test is supplementary to the zeta potential measurements as it is a direct means to observe the dispersion of ceramic particles. The lower the sediment height, the more stable the suspension [157].

5.2.2.2 Procedure

Physical characterization of Al_2O_3 and YSZ8 aqueous suspension stabilities was carried out using the sedimentation technique. In these experiments, de-ionised water was mixed with 3 cc of each ceramic powder using a mechanical stirring system for 1 hour. This amount was chosen based on the tap density of each powder, ensuring that a convenient amount settles to produce a clear interface. Next, the mixture was poured into a graduated cylinder of 25 ml capacity. A rubber gasket was used to seal the cylinder. Next, the cylinder was held undisturbed in a vertical position. Thus, the suspension was allowed to settle under gravity until a sediment layer was formed, as shown in Figure 5.2. The interface separating the sediment layer at the bottom of the cylinder and the dispersed suspension at the top ascended slowly depending on the powder. The sediment heights were then read directly from the graduated cylinder. The initial height of the suspension, h_o, was noted followed by the final height h of settled alumina, recorded after 24 hours. Height ratio (h/h_o) of the suspension was calculated and analysed as a function of the dispersant and pH.

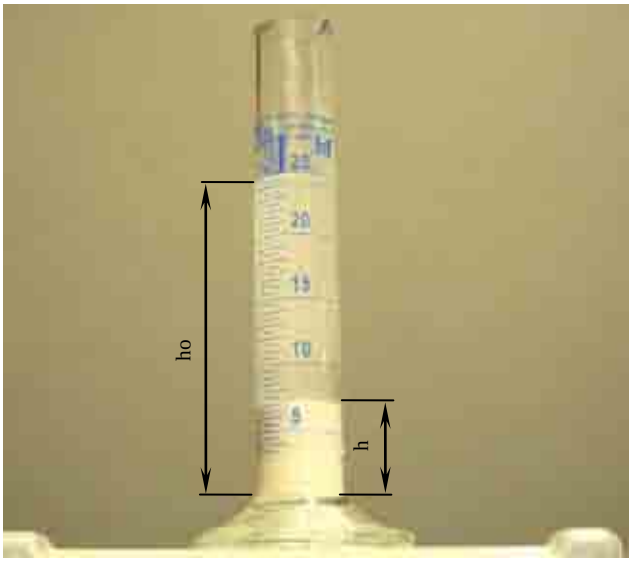

Figure 5.2. Sedimentation measurements setup.

5.2.2.3 Results and Discussions

The sedimentation behaviour of aqueous ceramic suspensions with different dispersant concentrations was studied to ascertain the conditions that provide maximum stability. With reference to zeta potential results, one suspension was set to pH = 7, for which the constituent particles have the maximum surface charge. In addition, to investigate the effectiveness of the dispersant in both acidic and alkaline mediums, two other suspensions were prepared, set to pH = 2 and pH = 10 respectively. Sedimentation results for both Al_2O_3 and YSZ8 powder are shown in Figure 5.3.

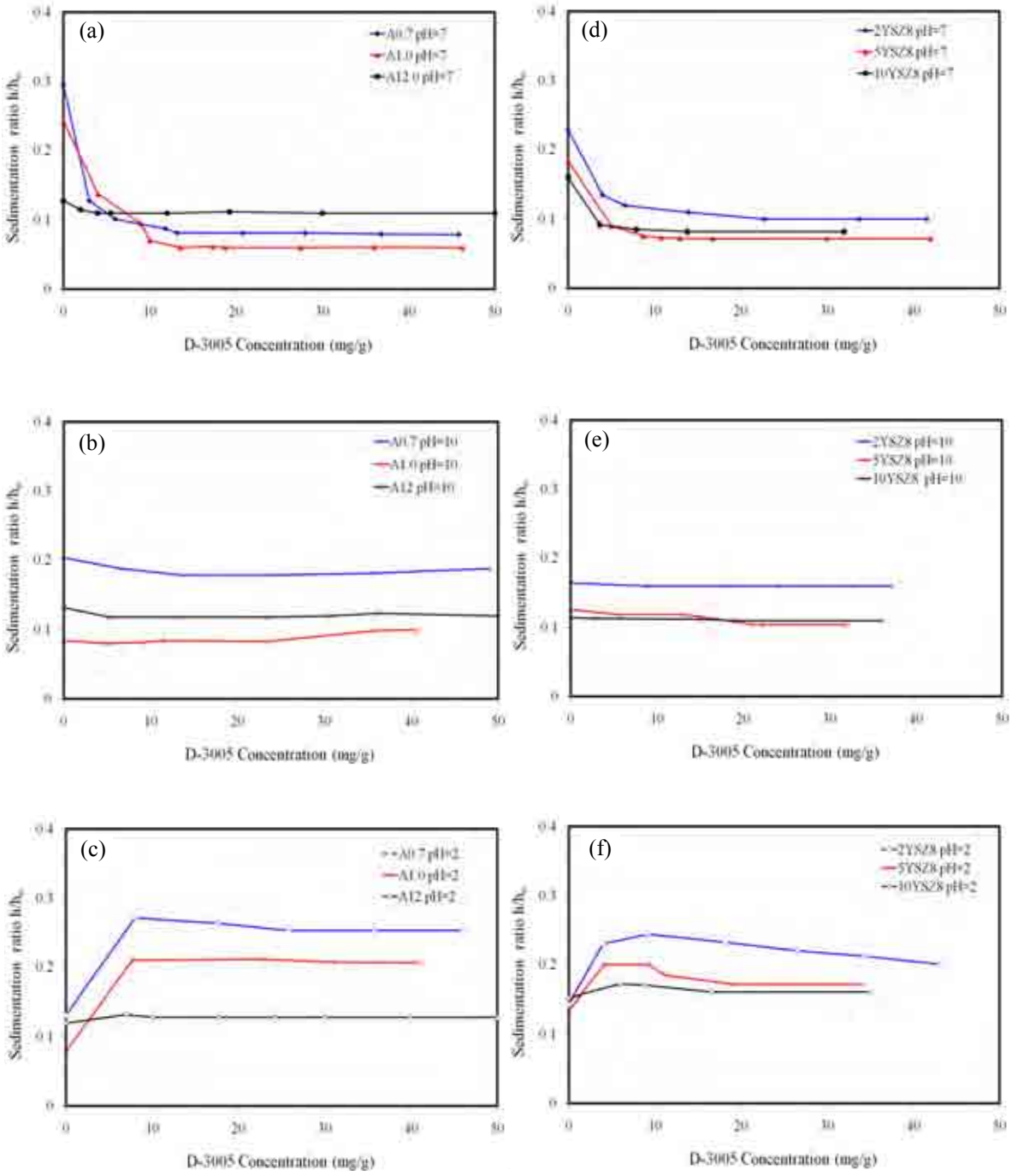

(a, b, c) Al_2O_3 measurements. (d, e, f) YSZ8 measurements.

Figure 5.3. Sedimentation behaviour of aqueous Al_2O_3 and YSZ8 suspensions of various powder sizes at pH=7, pH=10, and pH=2, as a function of D-3005 concentration.

In Figures 5.3(a)-(c), sedimentation heights were plotted against Al_2O_3 suspension with the addition of the D-3005 at pH = 7, 10 and 2, respectively. In the absence of dispersant, sedimentation height of A0.7, A1.0 and A12.0 suspensions was lowest at pH = 2, and higher at pH = 10, and was highest at pH = 7. These results clearly show that at pH = 2, the best dispersion occurs when no dispersant is used. An explanation of these results could be determined by comparing Figures 5.2(a) and 5.3(a)-(c). The suspension is considered well dispersed when the positive charge in the acidic range is sufficiently high. In a neutral environment at pH = 7, zeta potential approaches the IEP is therefore very low. A relatively low value of the zeta potential for aqueous alumina system supports the possibility of flocculation. Therefore, all particles have a natural tendency to settle fast, generating higher sedimentation heights. In the alkaline region at pH=10 alumina particles are negatively charged and zeta potential in the absence of dispersant is less than in the acidic range. As a result, the settled volume was low indicating that the suspension was dispersed.

As shown in Figure 5.3(a) for the neutral aqueous suspension at pH = 7, the dispersing ability was highly improved with the addition of D-3005 and reached the highest value at concentrations of 13.2, 13.5 and 5.5 mg/g for A0.7, A1.0 and A12.0 respectively. In this case, zeta potential was increased from nearly +10 mv to its maximum value of 63-65 mv, as shown in Figure 5.2(a). On increasing the D-3005 concentration further, stability of the suspension was decreased at a very low rate.

In alkaline suspensions, at pH=10, as shown in Figure 5.3(b), stability was slightly improved by increasing D-3005 concentration to about 13.6, 9.6 and 5.3 mg/g for A0.7, A1.0 and A12.0 respectively. The reason is because at pH=10, zeta potential is slightly

increased by the presence of D-3005, as shown in Figure 5.2(a). With further addition of D-3005, stability gradually decreased.

In the acidic environment at pH = 2, as shown in Figure 5.3(c), stability of the suspension was sharply degraded with the addition of the dispersant, reached the lowest value at concentrations of 8.0, 7.7 and 7.0 mg/g for A0.7, A1.0 and A12.0 respectively. This is due to the drastic decrease in the zeta potential after adding D-3005, Figure 5.2(a). On further addition of D-3005, the suspension showed a slight improvement in stability that may be due to the steric repulsive force.

Results from YSZ8 suspensions are shown in Figure 5.3(d)-(f) and indicate behaviour similar to Al_2O_3 suspensions. The sedimentation heights of 2YSZ8, 5YSZ8 and 10YSZ8 suspensions with and without D-3005 at pH = 2, 7 and 10 are plotted.

In the neutral suspension pH=7, Figure 5.3(d), the stability was highly improved with the addition of D-3005 and reached a maximum value at concentrations of 22.7, 16.7 and 13.8 mg/g for 2YSZ8, 5YSZ8 and 10YSZ8 respectively; with further increases of D-3005 concentration the settled height remained constant. In alkaline suspensions, as shown in Figure 5.3(e), sedimentation heights were slightly reduced by addition of D-3005 to about 32, 21 and 19 mg/g for 2YSZ8, 5YSZ8 and 10YSZ8, respectively. In the acidic suspension at pH=2, as shown in Figure 5.5(f), sedimentation was sharply increased with the addition of the D-3005, reaching its highest value at concentrations of 9.4, 9.2 and 6.0 mg/g for 2YSZ8, 5YSZ8 and 10YSZ8, respectively. On further addition of D-3005, the suspension shows a slight improvement in the stability behaviour.

In summary, for both Al_2O_3 and YSZ8, settled heights of ceramic suspensions with and without dispersant are highly related to the measured zeta potential of the suspension. The

highest stability obtained for Al_2O_3 was found when pH = 7 for concentrations of 13.2, 13.5 and 5.5 mg/g for A0.7, A1.0 and A12.0 respectively. The highest stability obtained for YSZ8 was when pH = 7 and for concentrations of 22.7, 16.7 and 13.8 mg/g for 2YSZ8, 5YSZ8 and 10YSZ8 respectively. In addition, it is notable that as tap powder density is increased, the dispersant amount required to affect suspension stability is reduced. Moreover, the addition of D-3005 has a limited effect on A12.0 suspension stability, due to coarse particle shapes, which tend to settle quickly, as shown in Figure 5.3. Uniformly dispersed powder is generally desirable for producing dense ceramics, because of its close packing during green compaction.

5.3 Characterisation of Green Microcomponents

The structure of the sintered parts is significantly affected by the quality of the green ceramic body. Density, strength and homogeneity are important aspects in assessing green ceramic bodies. It is important to ensure a high green density in the green ceramic body, retaining the high quality mould shape, the smoothness of the surfaces, and to achieve an even shrinkage during drying and sintering [151]. In this section, the effect of the powder size and slurry composition on the properties of the green microcomponents is introduced. Preliminary experiments were introduced in Chapter 4 that defined the shape retention and green density of the microengine parts using A0.7 and 2YSZ8 powders. Here, the work is extended to cover other powder sizes used in the thesis. The aim is to investigate the effect of the powder size, binder and dispersant amount on green shape retention, green density and drying shrinkage in order to decide on optimum dispersant and binder amount for each powder size.

5.3.1 Green Density and Drying Shrinkage

In the characterisation of Al_2O_3 and YSZ8 slurries, it was concluded that, addition of D-3005 to the prepared slurries at pH = 7 improves their stability significantly. Therefore, slurry pH values here were set to 7. The fabrication procedure remained the same as explained in Chapter 4. Solid loadings remained constant at 80% vol. for all slurries. In addition, the binder content used to prevent damage to the green parts during drying and demoulding was about 20-25 mg/g powder for all powders except for powder A12.0 which needed about 100 mg/g powder for a damage free green body. In this work, green parts fabricated using different powders are studied to characterise the green density and drying shrinkage with respect to the dispersant concentration, as shown in Figure 5.4.

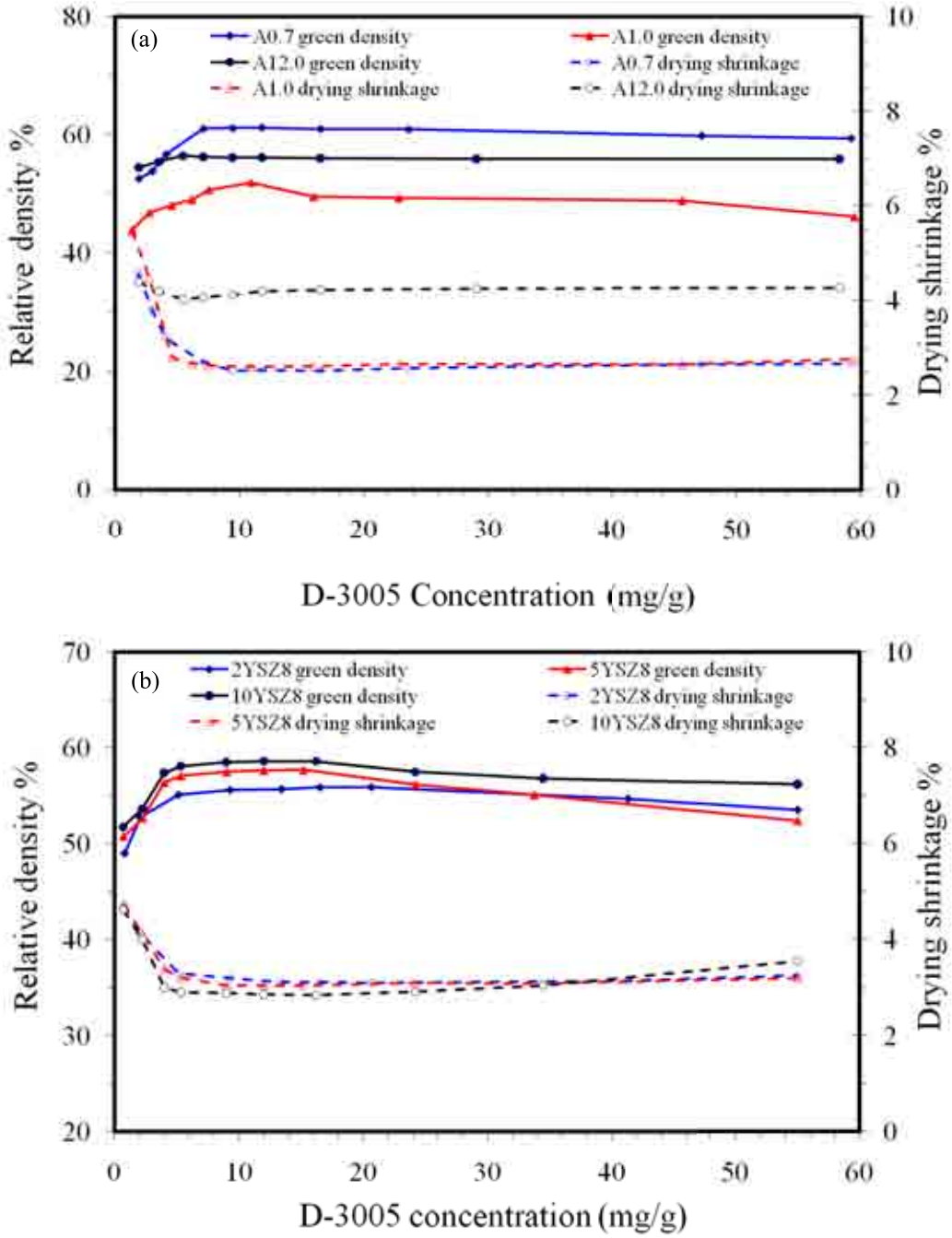

Figure 5.4. Green density and drying shrinkage as a function of D-3005 concentration for (a) Al_2O_3, and (b) YSZ8 powders.

As shown in both figures, the green density increased sharply with the addition of D-3005, and then reached its highest value when the dispersant concentration was almost the same as the concentration to achieve stable suspensions obtained from the sedimentation measurements. Here, the values were ~11.8, 10.9 and 5.5 mg/g for A0.7, A1.0 and A12.0 respectively. Increasing the concentration further caused the green density to slightly decrease. Similar behaviour was repeated for the drying shrinkage. Increasing the dispersant concentration decreased the shrinkage significantly until it reached its minimum value at nearly the same optimum concentration, and with the further addition of the dispersant, shrinkage was slightly increased.

By comparing the three alumina powders used in the experiments, the differences in powder size, morphology and tap density are clearly affecting the green properties. Powder A0.7 has a high tap powder density of 1.28 g/cc, which lead to a maximum green density of 61.2% with a lowest drying shrinkage of 2.5%. As for A1.0, it has a low tap powder density of 0.67 g/cc that is most likely due to its irregular particle shape and the presence of agglomerates as shown in Figure 4.1. Therefore, the highest green density obtained using the optimum dispersion was 51.9% with a lowest shrinkage of 2.6%. As for powder A12.0, the highest green density was 56.4% with a lowest drying shrinkage of 4%. Although A12.0 has the biggest powder size and highest tap density, it has a lower green density than powder A0.7. There are two reasons that may be involved in this result. The first reason, concluded from the sedimentation behaviour, was that the addition of D-3005 did not improve A12.0 suspension stability, unlike A0.7 suspension. The second reason is the high binder content in the slurry, which is about 4 times the amount of binder that was used with other powders.

The relative green density and the shrinkage of the green parts fabricated using 2YSZ8, 5YSZ8 and 10YSZ8 powders as a function of the dispersant concentration are shown in Figure 5.4(b). It can be seen that YSZ8 powders behave similarly to Al_2O_3. Briefly, the green density was improved significantly with the addition of dispersant, reaching its highest value at dispersant concentrations of 20.6, 15.2 and 12 mg/g. Similarly, increasing the dispersant concentration decreased the drying shrinkage significantly, reaching its minimum value, and then tending to increase with further addition of the dispersant. Differences in green densities between the three powder sizes are less notable due to the small differences between their tap powder densities. The maximum green densities obtained were 55.9%, 57.7% and 58.6% with drying shrinkage of 3.1%, 3% and 2.8% for 2YSZ8, 5YSZ8 and 10YSZ8 respectively.

In summary, both the dispersant, powder size, shape and the tap density strongly affect green properties of both Al_2O_3 and YSZ8.

5.3.2 Problems in Moulding and Demoulding

In the processing of Al_2O_3 and YSZ8 green parts using water-based slurry, structural defects such as cavities, distorted and broken parts in the green during moulding and demoulding can arise. These defects lead to unacceptable microengine parts when they are visible. In addition, they can reduce the mechanical properties of the components and affect the engine performance whether they are external or internal. The following presents these problems, causes and the adopted solutions.

5.3.2.1 Incomplete Moulding

An incomplete moulding defect means that the slurry could not fill the entire cavity of the PDMS micro mould. Figure 5.5 shows optical and SEM images of green microgears teeth missing due to incomplete moulding. The reason behind this kind of defect was confirmed by visual observation during moulding. The residual voids are caused by entrapped air bubbles formed on the bottom surface of the mould during casting of the ceramic slurry. The filled slurry was not able to fill the mould completely, especially at thin sections such as microgear teeth. As described in chapter 4, moulding of the PDMS was achieved by placing the filled mould inside a vacuum chamber. This method was very effective at filling the mould even in very fine sections. Air bubbles trapped at the thin sections of the mould, although initially microscopic in size, expanded to become large when a vacuum was applied. Bubbles then tended to rise to the surface of the material and, given enough time, would eventually release from the slurry. During experimentation, when the mould did not have the required time for degassing using vacuum, air bubbles became trapped on the bottom or inside of the mould, and hence the mould dried in this condition. Therefore, providing sufficient time for degassing to complete is essential for obtaining a complete mould. An advantage of the PDMS transparency is that the mould can be checked visually using an optical microscope. Another cause of this type of defect is the high solid loading. Although vacuum time may be long, due to the high solid loading, bubbles were unable to propagate to the surface of the mould. Therefore, solid loading must be tuned to allow proper moulding whilst retaining as high load as is possible to achieve a dense and strong green body. To compromise between these two requirements it was found experimentally that the highest possible solid loading to obtain complete green parts was in the range of 80-85% vol. based on the powder and its tap density.

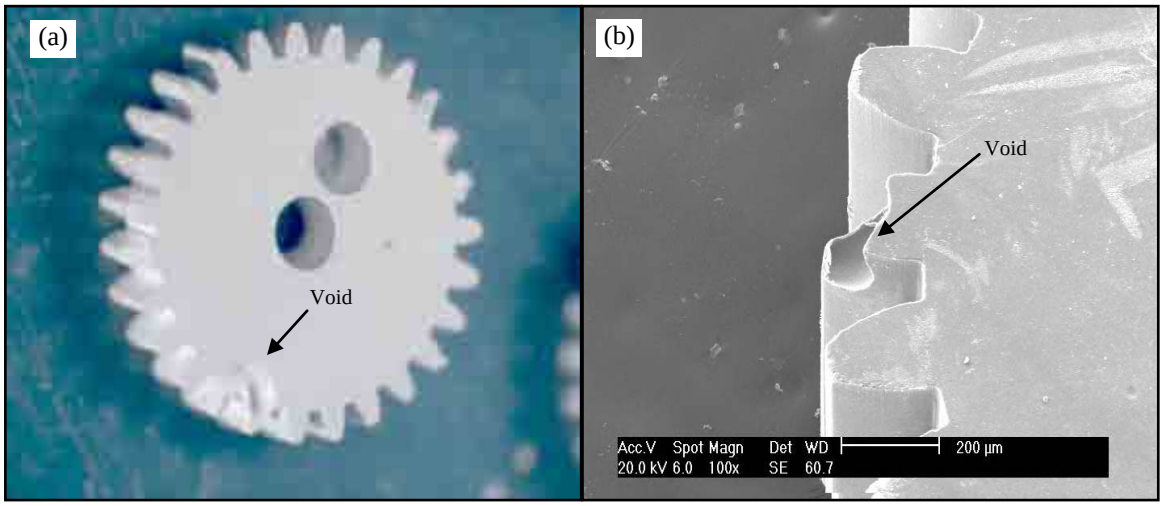

Figure 5.5. Optical and SEM images of defective green microgears due to incomplete moulding.

5.3.2.2 Damaged Green Structures

Preliminary experiments indicated that damage to the green parts occurred during demoulding. This suggests that the extraction stress is higher than the green body strength, which causing failure at the weak areas in the green parts, such as gear teeth or around micro holes, Figure 5.6. The main reason for this problem was the low binder content in the slurry. As mentioned, by using a binder content of 20-25 mg/g for most powders used in the experiments the majority of the green microcomponents were successfully obtained using a careful and practised demoulding technique. Powder A12.0 required a higher binding content of 100 mg/g powder.

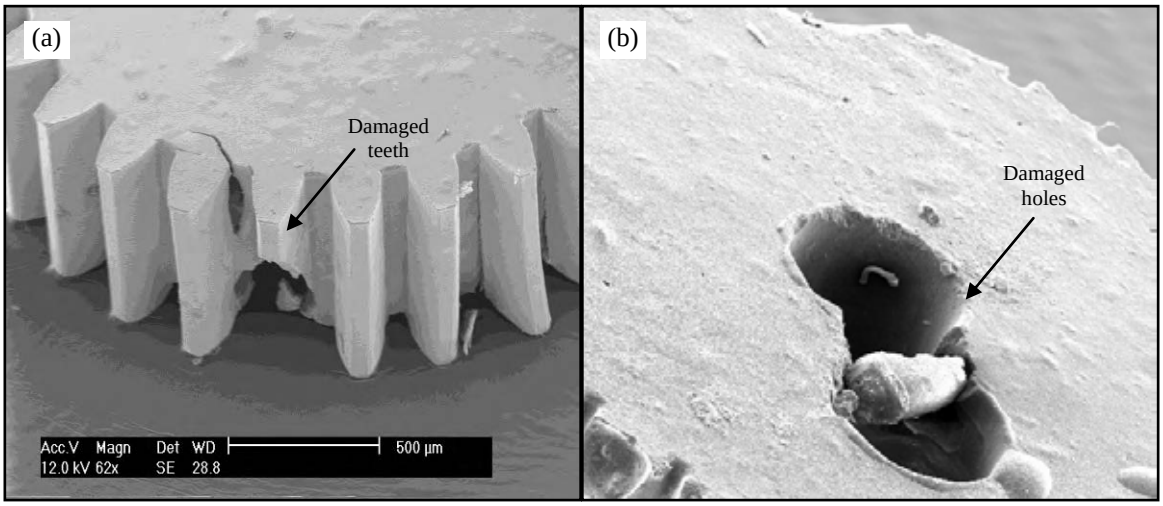

Figure 5.6. SEM images of (a) damaged microgear teeth, (b) damaged microgear holes.

5.3.3 Green Microcomponents Shape Retention

Green bodies fabricated using optimised results obtained from characterisation of the prepared slurries, green body properties and overcoming moulding and demoulding problems are presented here. The optimized processing recipe began by preparing ceramic slurries using dispersant concentrations of 11.8, 10.9 and 5.5 mg/g for A0.7, A1.0 and A12.0 respectively, and 20.6, 15.2 and 12 mg/g for 2YSZ8, 5YSZ8 and 10YSZ8 respectively. In addition, binder concentration was set to 20-25 mg/g for all powders except for A12.0, which was set to 100 mg/g. pH values of the prepared slurries were set to 7. In addition, solid loading of the slurries was in the range of 80-85% vol. Next, the moulding process was performed by vacuum casting to fill PDMS soft moulds. Afterwards, a slow drying rate was applied followed by careful demoulding to achieve the green microcomponents. The defect free green microengine parts fabricated using Al_2O_3 powders with average particle size of 0.7 µm, 1.0 µm and 12.0 µm are shown in Figure 5.7. On the other hand, green microengine parts fabricated using YSZ8 powders with

average particle of 2.0 µm, 5.0 µm and 10.0 µm are shown in Figure 5.8. In both figures, the whole microgear and a magnified tooth were examined. It can be seen that green microgears fabricated using different powder sizes were successfully obtained. From the micrographs, microgear teeth were kept in good shape and the structures were clearly defined. However, for alumina powder with particle size 12.0 µm, the microgear tooth has irregularities on the edge and a coarse surface, which would be expected to translate to a poor resolution and surface finish after sintering.

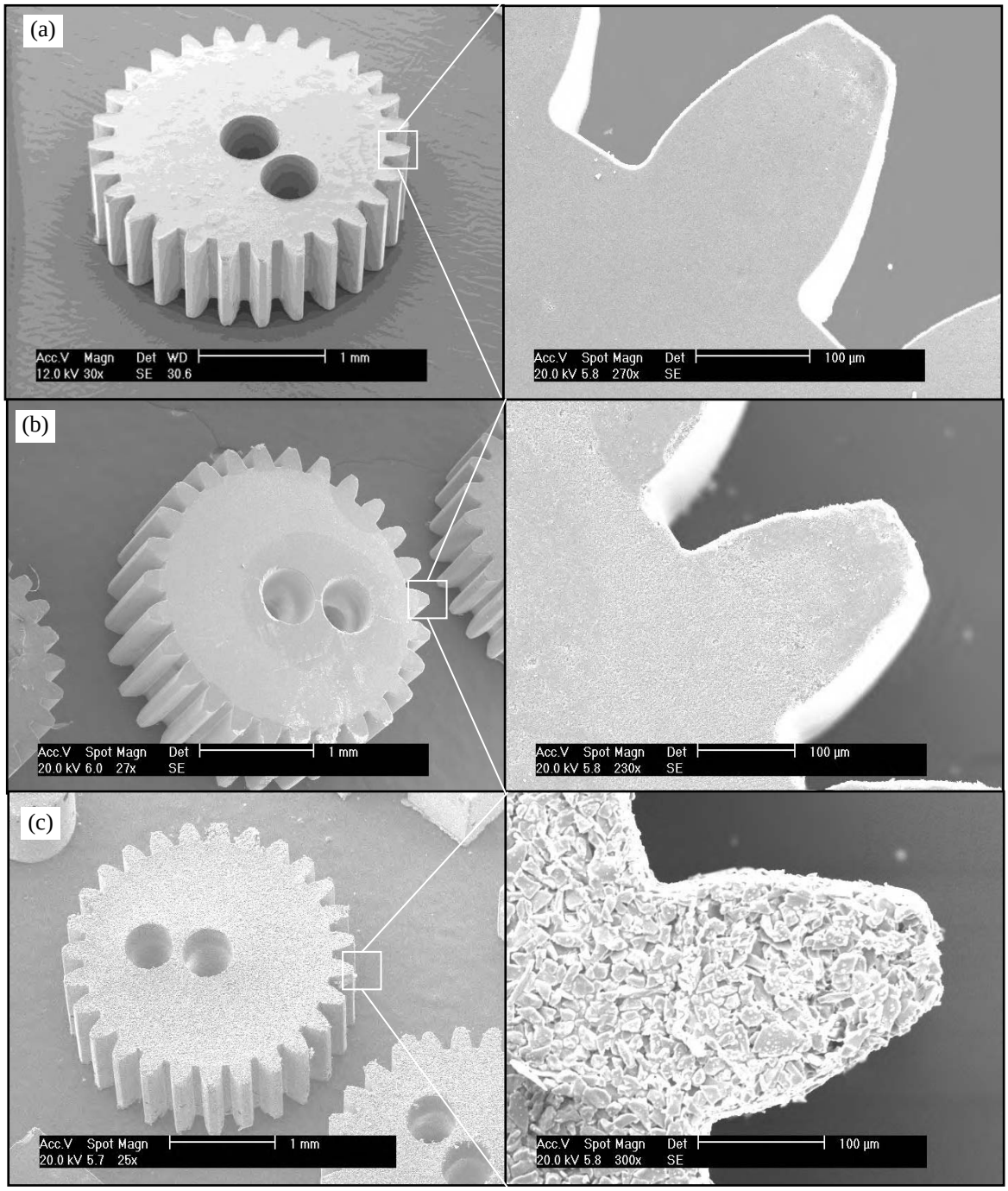

Figure 5.7. SEM images of Al_2O_3 green microgears fabricated using powder size of (a) 0.7 µm, (b) 1.0 µm, and (c) 12.0 µm.

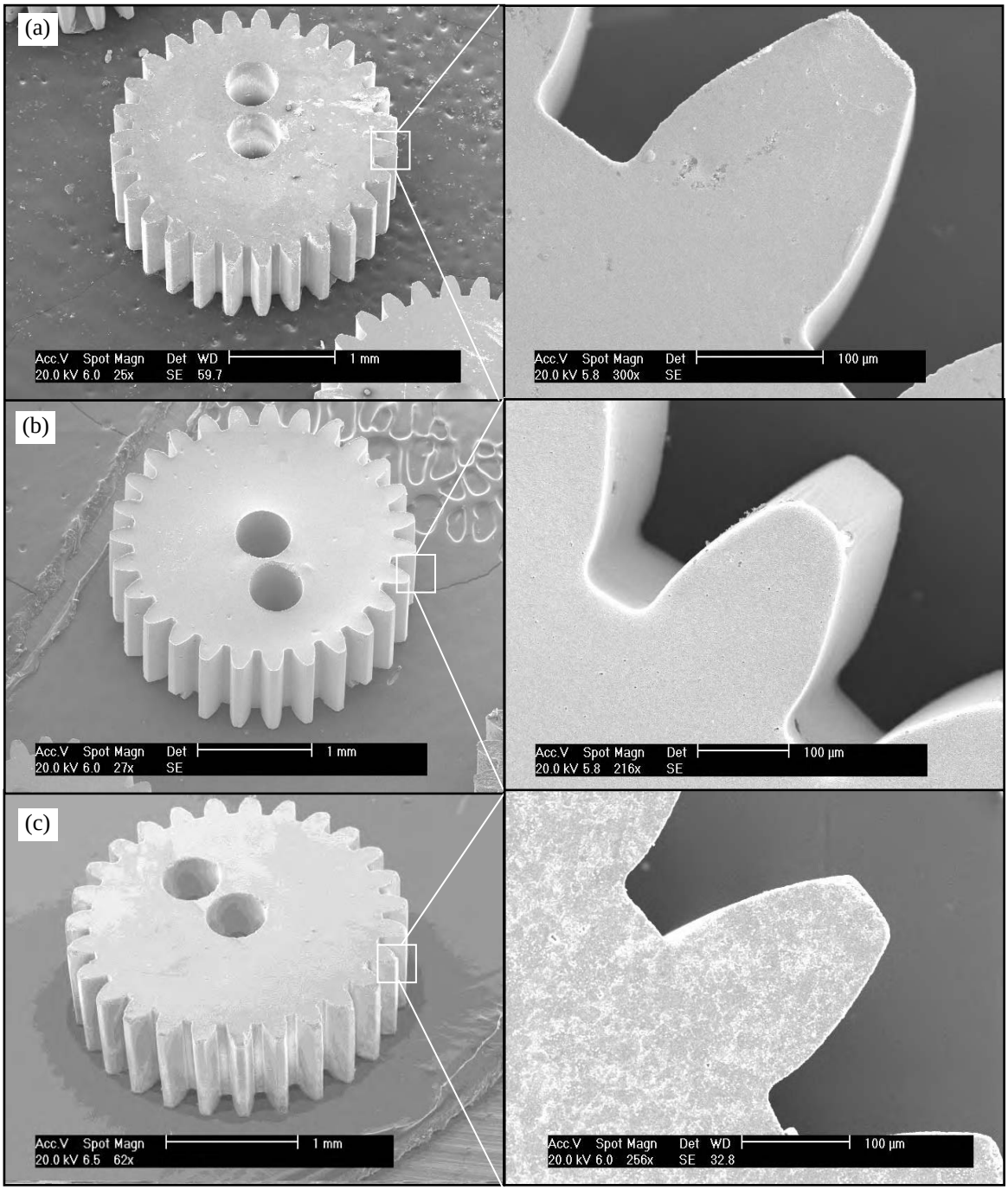

Figure 5.8. SEM images of YSZ8 green microgears fabricated using powder size of (a) 2.0 µm, (b) 5.0 µm, and (b) 10.0 µm.

5.4 Summary

In this chapter, characterisation of Al_2O_3 and YSZ8 slurries and green microcomponents were performed by altering colloidal behaviour with respect to powder size, suspension pH, concentration of the dispersant and binder in the slurry. The aim was to obtain the optimum pH value and dispersant concentration by examining zeta potential and sedimentation measurements to achieve highly stable suspension. A study on the microcomponents green density, linear shrinkage and shape retention was also investigated. It was found that using pH = 7 and the optimum dispersant concentration not only improves suspension stability but also improves green density and linear shrinkage significantly. Uniformly dispersed slurry is generally desirable for producing dense ceramics, because of its close packing during green compaction. Moulding and demoulding problems were discussed. It was found that using the optimum binder concentration, solid loading, vacuum casting and careful demoulding significantly diminished these problems. Finally, dense and net shape green microcomponents were obtained and were ready for sintering.

CHAPTER 6: CHARACTERISATION OF ALUMINA AND ZIRCONIA SINTERED MICROCOMPONENTS

6.1 Introduction

This chapter explains the characterisation details of sintered alumina and 8 mole% yttria stabilized zirconia green microcomponents. Alumina and zirconia sintered properties are examined for the purpose of net shape microcomponents with high physical and mechanical properties. High sintered density, low and uniform sintered shrinkage, high hardness and fracture strength are essential for microengine parts. The chapter begins with studying the effect of the dispersant on sintered density and linear shrinkage in Section 6.2. The effect of sintering temperature on sintered density, linear shrinkage, micro hardness, flexural strength is presented in Section 6.3. Shape retention of the sintered microcomponents is examined and discussed in Section 6.4. Surface morphology and porosity of the sintered microcomponents are presented in Section 6.5. Surface roughness measurements were performed and their results are discussed in Section 6.6. After characterisation of the sintered parts, the complete alumina and zirconia microengines are presented in Section 6.7. Finally, the chapter is summarized in Section 6.8.

6.2 The Effect of D-3005 on Sintered Density and Linear Shrinkage

Green microcomponents obtained using various dispersant concentration as shown in Chapter 5 were sintered at 1600 °C for 2 hours using the heating cycle presented in Chapter 4. Sintered density and linear shrinkage of these samples were measured, with

respect to dispersant concentration for Al_2O_3 and YSZ8 powders, and are shown in Figure 6.1.

For the given powders, by increasing D-3005 concentration to the optimum amount, densification behaviour was enhanced. Further addition of D-3005 caused sintering density to gradually decrease. Starting with YSZ8 powder, as shown in Figure 6.1(b), the maximum densities obtained were 98.4%, 98% and 95.1% with linear shrinkage of 21%, 18.9% and 18.1% for 2YSZ8, 5YSZ8 and 10YSZ8 based samples, respectively. It is clearly noted that, the smaller the powder size, the higher the sintered density, and hence the higher the linear shrinkage. Smaller powders have a higher surface energy, and hence a greater sintering rate and higher density is expected [158]. Back to Al_2O_3 sintered microcomponents as shown in Figure 6.1(a), the maximum densities obtained were 98.3%, 95.3% and 78.3% with linear shrinkage of 17.6%, 20.7% and 6.2% for A0.7, A1.0 and A12.0 based samples respectively. As mentioned, it was found that, the smaller powder size, the higher sintered density. However, for linear shrinkage, it can be seen that, the smaller the powder size, the higher the linear shrinkage, except for A0.7 powder. To understand this behaviour, several facts should be considered. First, the difference in the average particle size between A1.0 and A0.7 is small when compared to the difference in particle size between the other powders. Second, A0.7 has a tap powder density of 1.28 g/cc, which is almost twice when compared to A1.0 tap powder density of 0.67 g/cc. Third, A0.7 has a significant high green density of 61.2% when compared to A1.0 green density of 51.9%. From these facts, it can be concluded that, A0.7 has a smaller powder size when compared to A1.0, which has accelerating effect on sintering as previously explained. However, the starting porosity content in the A0.7 green part is much less than A1.0,

which leads to less shrinkage during densification. As a result, a higher sintering density with a lower linear shrinkage was achieved with A0.7 powder.

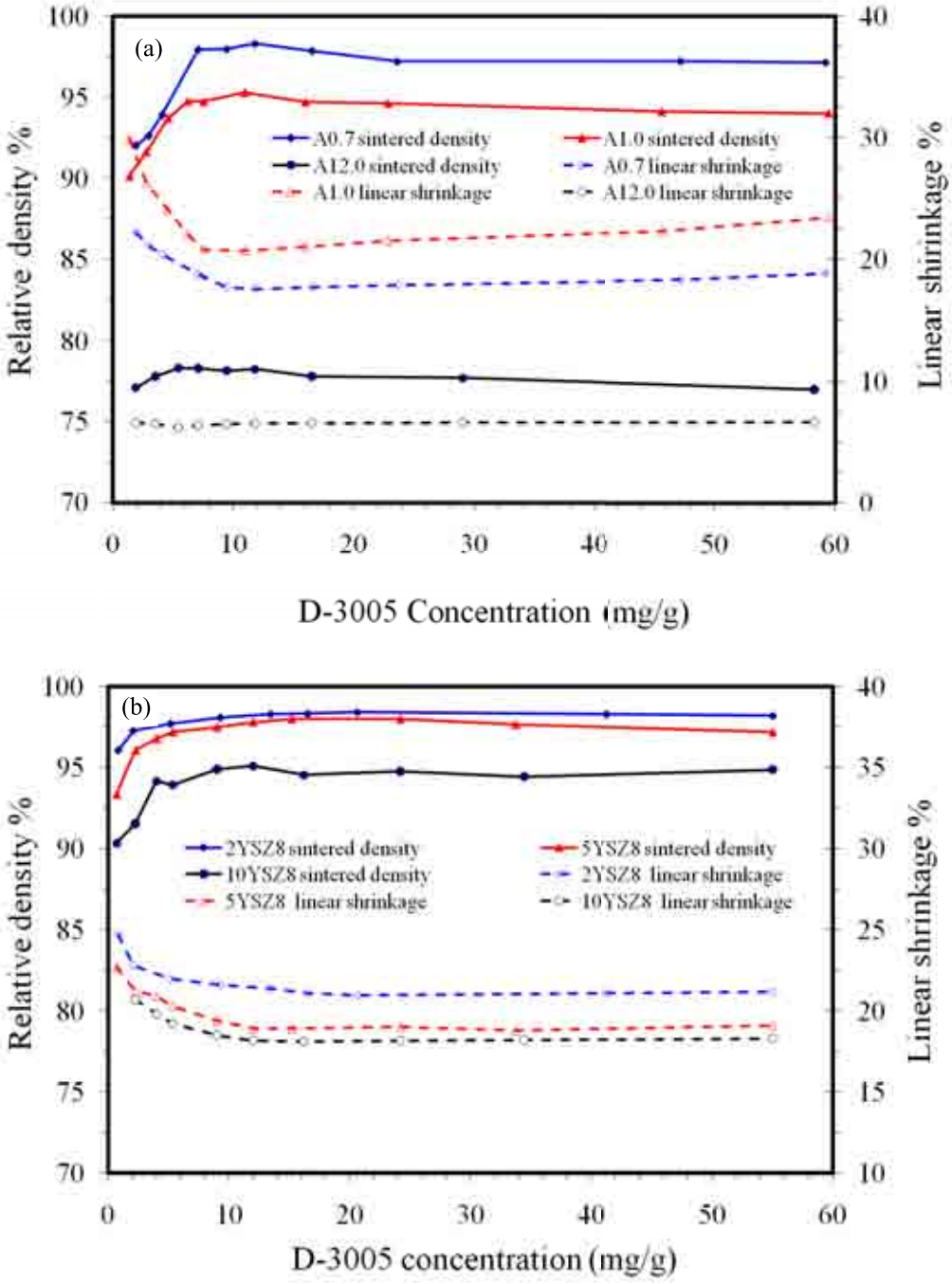

Figure 6.1. Sintered density and linear shrinkage as a function of D-3005 concentration for (a) Al_2O_3, and (b) YSZ8 powders.

6.3 The Effect of Sintering Temperature

To obtain the optimal sintering temperature, green microengine parts fabricated using Al_2O_3 and YSZ8 powders and optimal slurry composition were sintered at 1450 °C, 1550 °C and 1600 °C for two hours. Properties of the sintered microcomponents were measured in terms of density, shrinkage, hardness, flexural strength.

6.3.1 Sintered Density and Linear Shrinkage

The effect of sintering temperature on sintered density and linear shrinkage of Al_2O_3 and YSZ8 microcomponents fabricated using different powder sizes is shown in Figure 6.2. As shown in Figure 6.2(a), the relative density and linear shrinkage of Al_2O_3 samples increased gradually as the sintering temperature rose. The relative density of the sample reached a maximum of 98.3%, 95.3% and 78.3% with linear shrinkage of 17.6%, 20.7% and 6.4% for A0.7, A1.0 and A12.0 powders respectively at 1600 °C. The smaller powder size, the higher the sintered density and linear shrinkage was obtained when sintering temperature was increased. However, A0.7 has lower linear shrinkage when compared to A1.0 and A12.0 powders along with increasing of sintering temperature. The reason for this behaviour is discussed in Section 6.2. As for YSZ8 microcomponents, relative density and linear shrinkage increased as sintering temperature was raised except for 2YSZ8 where its relative density increased when sintering temperature rose from 1450 °C to 1550 °C. Then, relative density of 2YSZ8 based sample decreased slightly as sintering temperature rose further. The reason may be due to the increased volume of the trapped pores in grains or grain boundaries preventing further densification with the increase of sintering temperature [159]. Sintered densities of YSZ8 samples reached a maximum of 98.5%, 98% and 95.1% with linear shrinkage of 20.9%, 18.9% and 18.1% for 2YSZ8, 5YSZ8 and 10YSZ8 based samples and sintered at 1550 °C, 1600 °C and 1600 °C respectively. In

summary, it can be conclude that high densification was achieved for both Al_2O_3 and YSZ8 powders. The maximum sintered densities of 98.3% and 98.5% were achieved using A0.7 and 2YSZ8 powders and sintered at 1550 °C and 1600 °C, respectively.

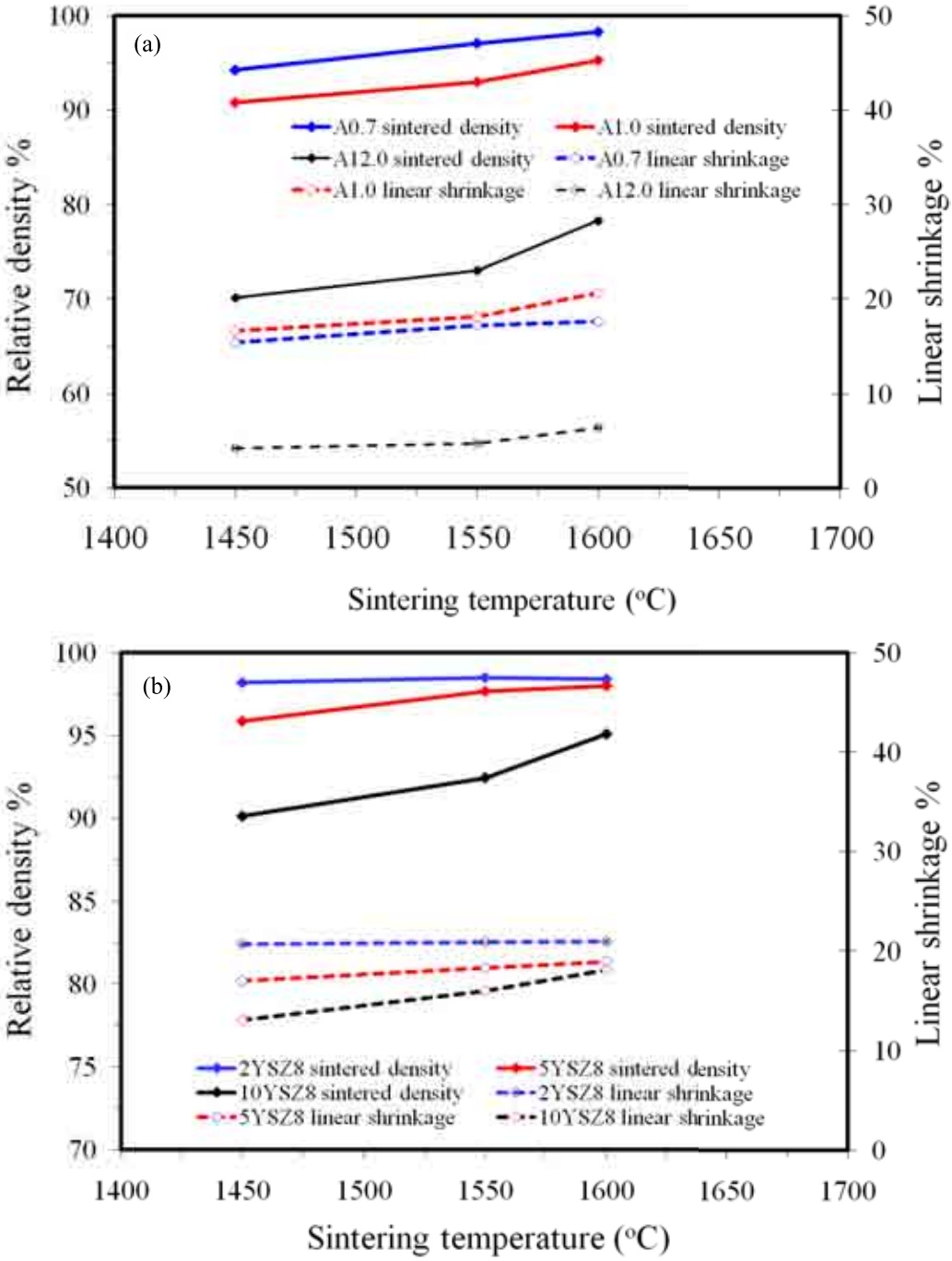

Figure 6.2. Sintered density and linear shrinkage as a function of sintering temperature for (a) Al_2O_3, and (b) YSZ8 powders.

6.3.2 Micro hardness Measurement

6.3.2.1 Background

Hardness is property of material that enables it to resist plastic deformation, usually by localized indentation. The higher the hardness, the more resistance it has to deform. Micro hardness measurements are similar to the hardness except that it is performed on a microscopic scale. In micro hardness tests, high quality surface finish, smaller load and high precision measurements are required. Measurements of micro hardness of materials are a quick and important method to obtain mechanical property data from the obtained sintered microcomponents.

6.3.2.2 Procedure

Vickers micro hardness of the sintered microcomponents was evaluated at ambient temperature with a Vickers pyramid indenter and an indent load of 9.8 N using five indents for each sample. In this measurement, Vickers micro hardness tests were performed on the sintered Al_2O_3 and YSZ8 microgears fabricated with various powders and sintering temperatures. Samples were directly measured without polishing as samples have a smooth surface roughness, as it is explained in Section 6.7. The measurements were realized with Buehler micro hardness equipment (MicroMet 5100 Series Microindentation). Vickers hardness was calculated by dividing the force applied to a Vickers indenter by the surface area of the permanent impression made by the pyramid indenter as shown in Figure 6.3.

$$Hv = \frac{1.8544\,P}{d^2} \qquad \text{Eq. 6.1}$$

Where P is the applied load (N) and d is the average diagonal length (m).

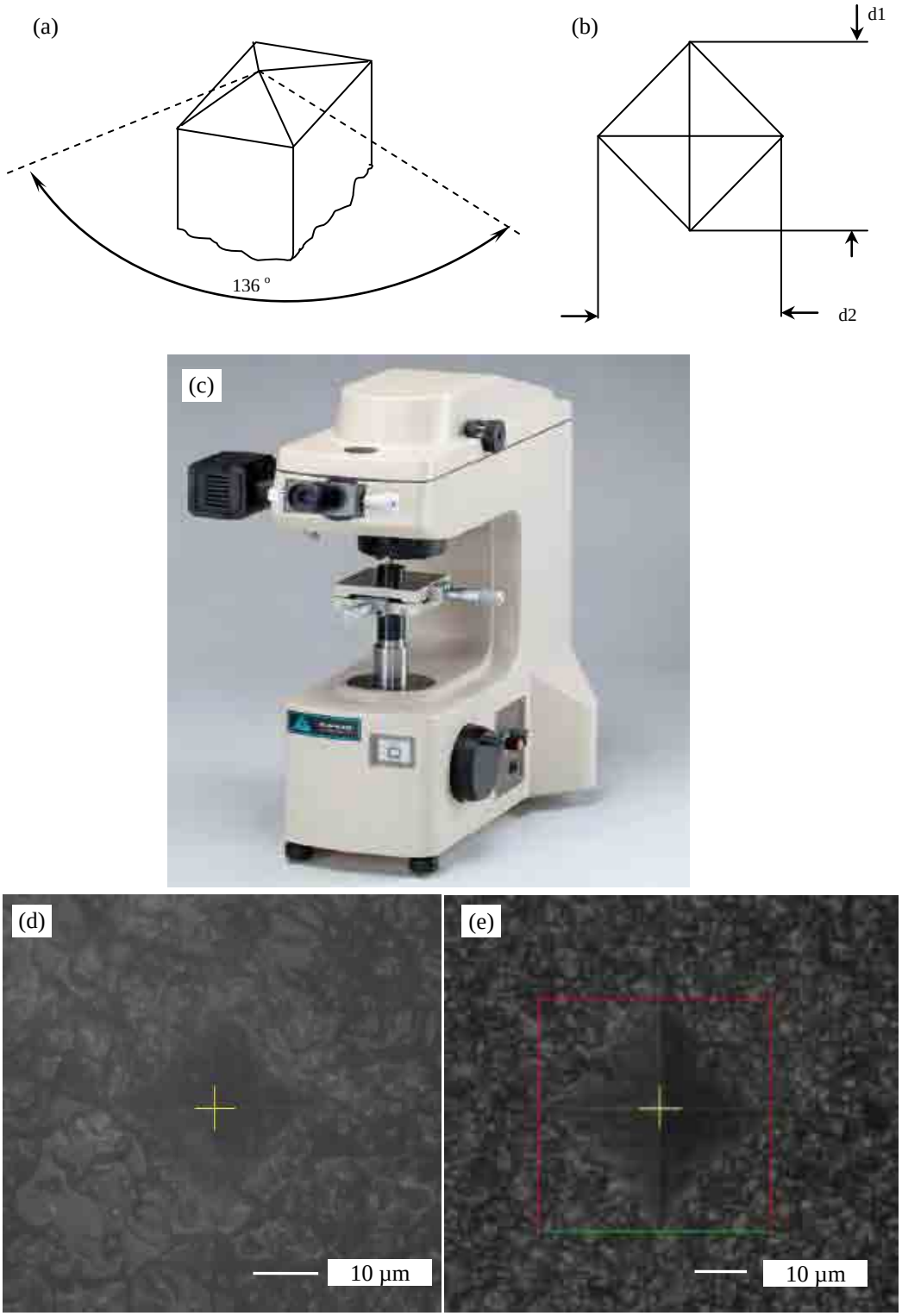

Figure 6.3. (a) Pyramid indenter, and (b) Indenter impression (c) Buehler microhardness equipment (MicroMet 5100 Series), (d) Al_2O_3 measured sample, (e) YSZ8 measured sample .

6.3.2.3 Results and Discussions

Vickers micro hardness of Al_2O_3 and YSZ8 microcomponents sintered at different sintering temperatures is shown in Figure 6.4. Figure 6.4(a) shows Vickers micro hardness for sintered microcomponents using A0.7 and A1.0 based samples. As for microcomponents fabricated using A12.0 powder, no indentation marks were observed in the sample surface in the Vickers micro hardness measurements. This is due to its low sintering density of 78.3%, which caused collapsing of the mark walls whenever indentation applied to the sample. As shown in the figure, Vickers micro hardness increased with the increase of sintering temperature. This is mainly because of the increase of sintered density when sintering temperature increased. High density means fewer pores and hence strengthens the material. In addition, it can be concluded that, the smaller the powder size, the higher hardness the sintered microcomponents will have. The highest Vickers values were 23.05 GPa and 22.1 GPa for A0.7 and A1.0 based samples when sintered at 1600 °C. As for YSZ8 microcomponents shown in Figure 6.4(b), it was found that, Vickers micro hardness also increased with the increase of sintering temperature for both 5YSZ8 and 10YSZ8 because of the increase in sintered density. As for 2YSZ8 microcomponents, Vickers micro hardness increased with the increase of sintering temperature from 1450 °C to 1550 °C, and then it remained almost constant when sintering temperature increased further from 1550 °C to 1600 °C. As explained, sintering density slightly reduced from 98.5% to about 98.4% by increasing sintering temperature from 1550 °C to 1600 °C. However, because of the small difference in sintered density at both 1550 °C and 1600 °C, the effect on the micro hardness on the 2YSZ samples was negligible. The highest Vickers values were 14.65 GPa, 14.5 GPa and 14.0 GPa for 2YSZ8, 5YSZ8 and 10YSZ8.

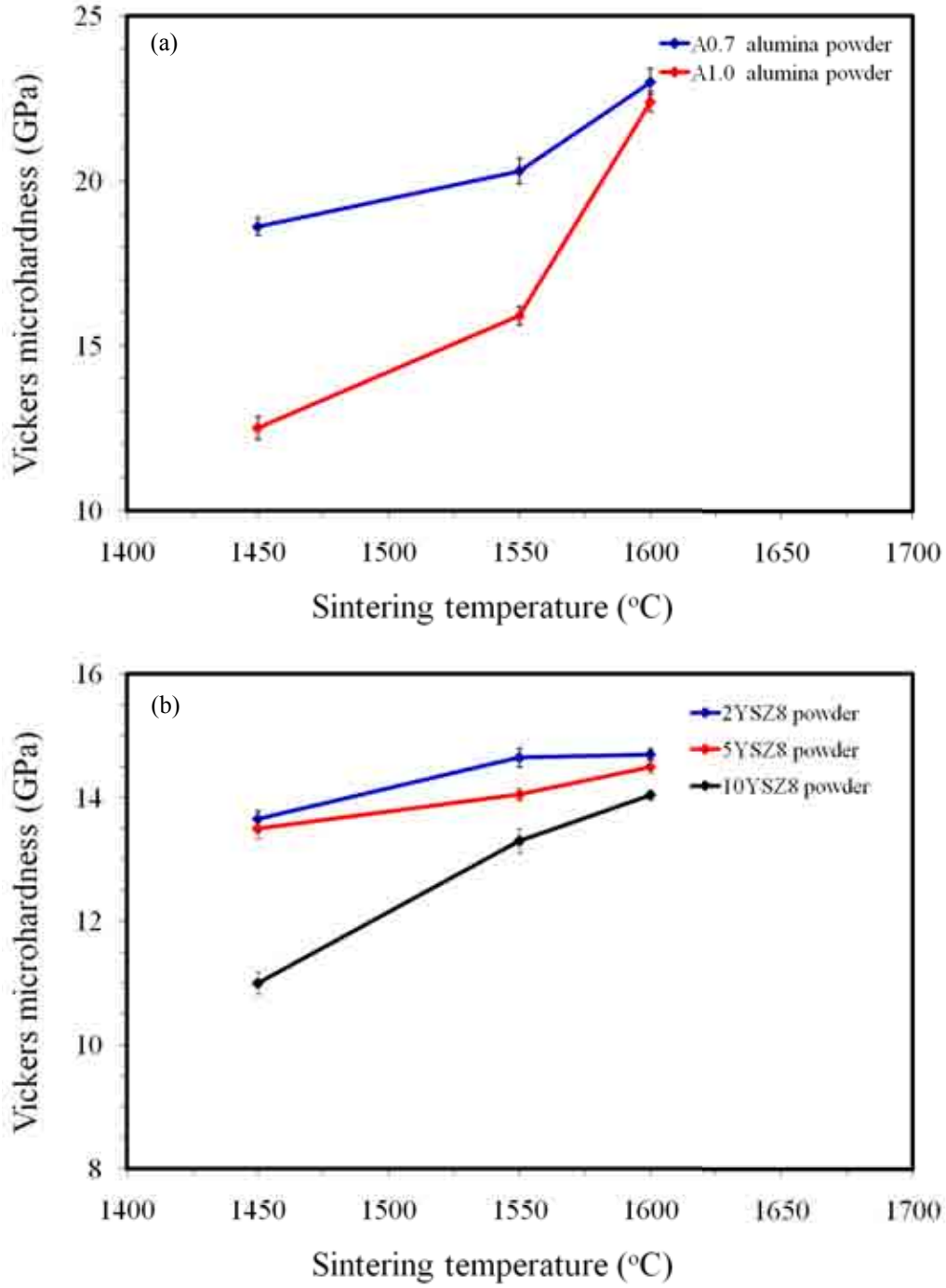

Figure 6.4. Vickers hardness as a function of sintering temperature for (a) Al_2O_3, (b) YSZ8 samples.

6.3.3 Flexural Strength

6.3.3.1 Background

Flexural strength, also known as bend strength or fracture strength is a mechanical property for brittle materials. Extremely low ductility materials does not allow the measurement of their strength property by conventional tensile test. This property is defined as a material's ability to resist deformation under bending load. Flexural strength in ceramic materials is usually measured by breaking test bars or rods in 3 or 4 point bending on a universal testing machine.

6.3.3.2 Procedure

The flexural strength of the sintered samples was measured using the three point bending method with INSTRON equipment, model 5848 Micro Tester (School of Chemical Engineering-University of Birmingham), as shown in Figure 6.5. The flexural strength was calculated by.

$$\sigma_f = \frac{3PL}{2bd^2} \qquad \text{Eq. 6.2}$$

where:

σ_f = Stress in outer surface at midpoint, (MPa).

P = Load at a given point on the load deflection curve, (N)

L = Support span, (mm)

b = Width of test beam, (mm)

d = Depth of tested beam, (mm).

As the measuring equipment used for this test cannot measure such small size samples of the microengine parts, special samples were fabricated using the same slurry and sintering conditions of the microengine parts. Sintered Al_2O_3 and YSZ8 bars with dimensions of $25\times2\times1.5$ mm^3 were used as the flexural samples [160]. Samples were fabricated using the same procedure used for fabrication of the microengine parts. After sintering at desired temperatures, the target dimensions were achieved with the aid of grinding and polishing.

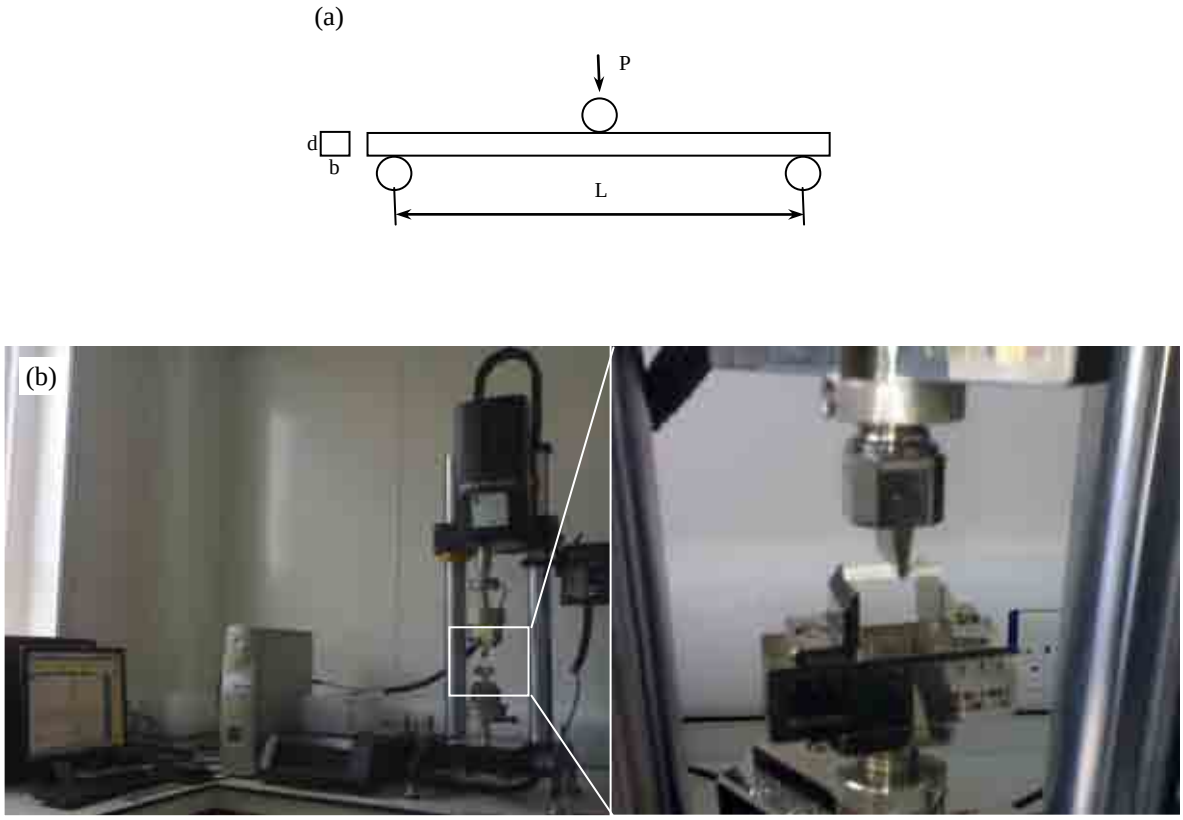

Figure 6.5. (a) Three-points fixture configuration, and (b) INSTRON model 5848 micro tester during sample measurement.

6.3.3.3 Results and Discussions

Figure 6.6 shows flexural strength of Al_2O_3 and YSZ8 samples as a function of sintered temperature. Flexural strength of Al_2O_3 increased with increasing sintering temperature, as shown in Figure 6.6(a). The samples reached to the highest flexural strength of 366 MPa when A0.7 powder components were sintered at 1600 °C. In addition, A0.7 based samples have higher flexural strength than A1.0 samples throughout the sintering temperatures. It is generally accepted that denser material has higher strength. As for A12.0 based samples, it was not possible to get results due its significantly low density. Applying the load caused immediate fracture of the samples. As for YSZ8 based samples, the same behaviour as alumina was repeated as shown in Figure 6.6(b). YSZ8 samples reached to the highest flexural strength of 508 MPa when 2YSZ8 powder components were sintered at 1550 °C. It can be clearly seen that, flexural strength increased with the increase of sintering temperature, except for 2YSZ based samples where it increased when sintered temperature increased from 1450 °C to 1550 °C. Further increase in sintering temperature reduced flexural strength, as the sintered density also decreased. In summary, for both Al_2O_3 and YSZ8 samples, flexural strength increased when denser samples were achieved during sintering process. It is also noted that, error bars are considered large. This mainly because, flexural strength is very sensitive to the surface condition and to minor flaws that may be inside the internal microstructure.

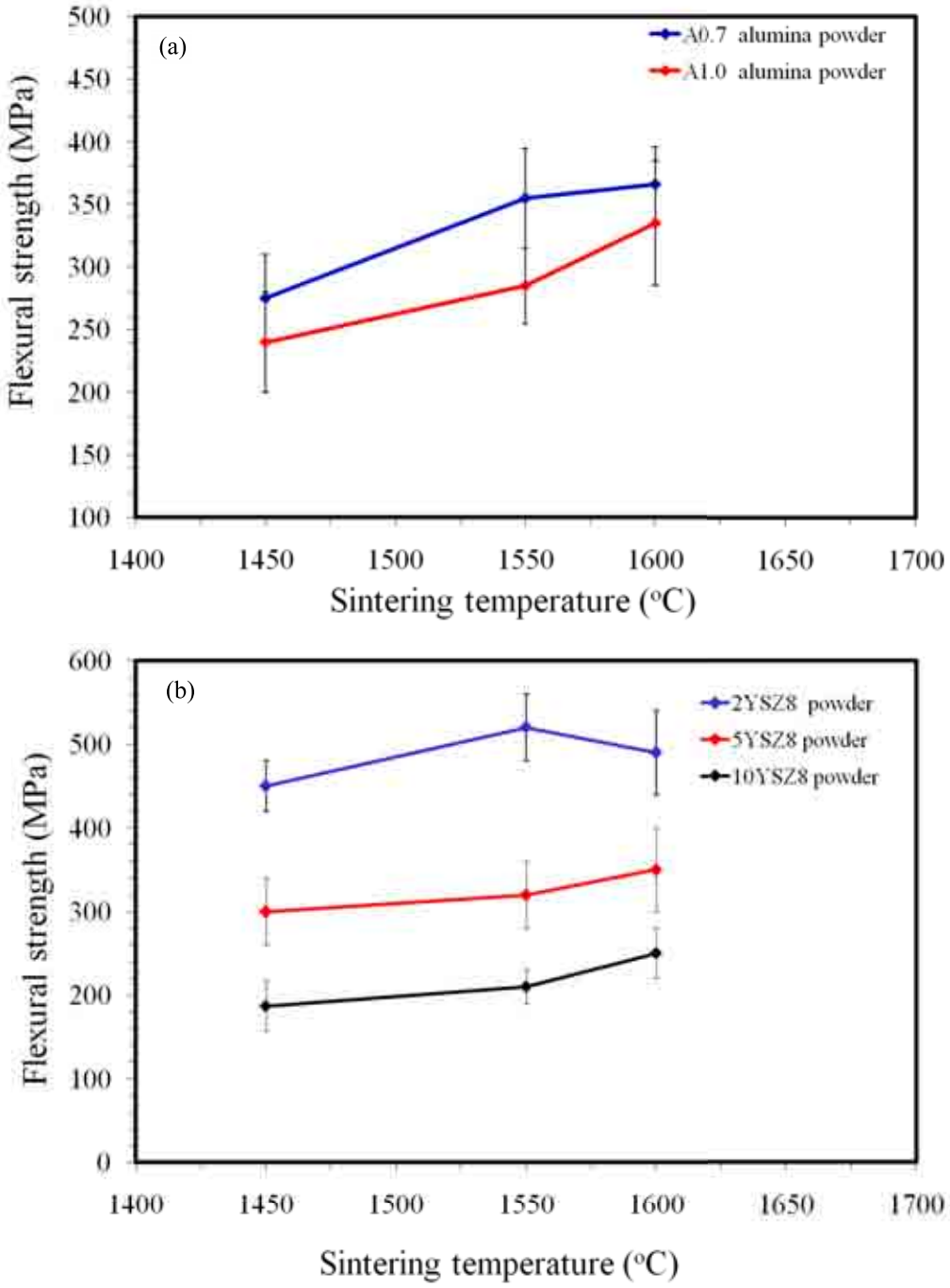

Figure 6.6. Flexural strength as a function of sintering temperature for (a) Al_2O_3, and (b) YSZ8 powders.

6.4 Shape Retention of Sintered Microcomponents

The fabricated microcomponents were inspected using SEM to investigate the effect of the powder size on the shape retention and edge resolution. Figure 6.7 shows SEM images of complete sintered microgears fabricated using Al_2O_3 powders with average particle size of 0.7 µm, 1.0 µm and 12.0 µm. It can be clearly seen that the Al_2O_3 microgears preserve their shapes completely after sintering. A close look to the magnified teeth from the top of the gears was performed for selected gears. The images demonstrate good edge profiles of the A0.7 and A1.0 based microgears. On the other hand, the A12.0 based microgear demonstrates irregular edge profile and poor resolution.

2YSZ8, 5YSZ8 and 10YSZ8 microgears are shown in Figure 6.8. The relevant SEM images show that the microgears preserve the original mould shapes completely after sintering using different powders. Similar to the Al_2O_3, the candidate YSZ8 samples can be examined further by looking at the teeth from the top. The figure demonstrates a good edge profile and dimensional accuracy for all presented microgears.

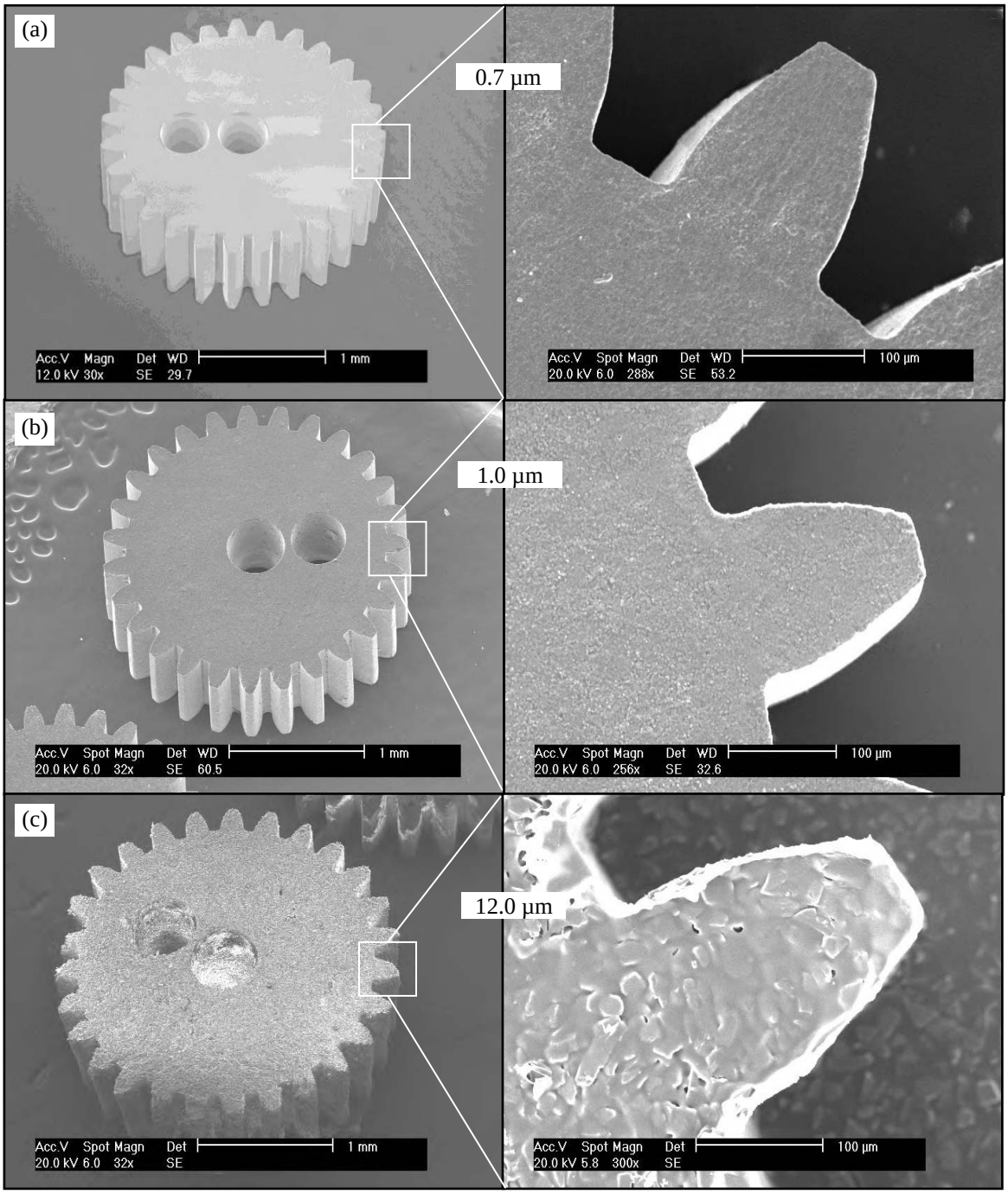

Figure 6.7. SEM images of Al_2O_3 sintered microgears fabricated using powder size of (a) 0.7 µm, (b) 1.0 µm, and (c) 12.0 µm.

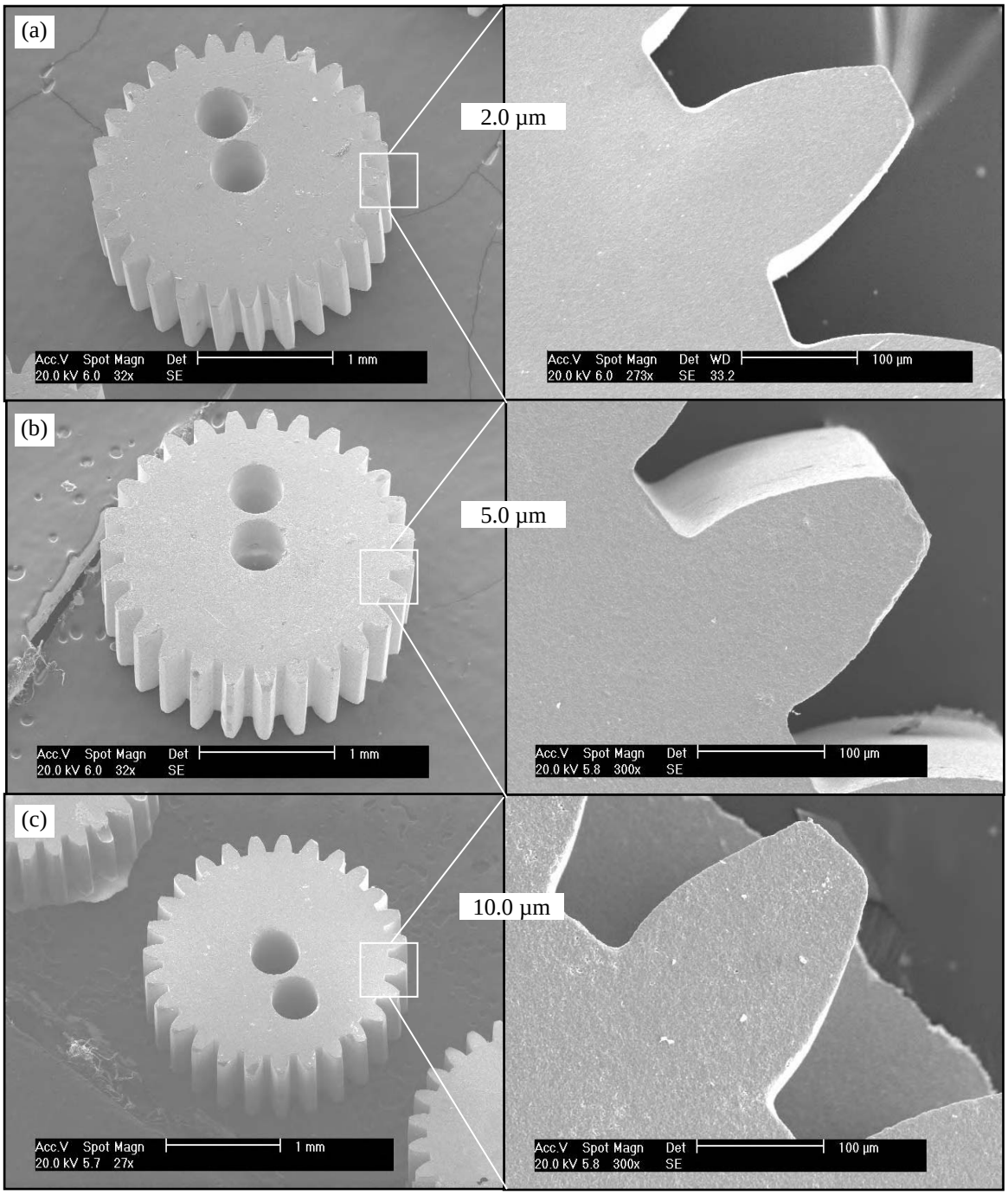

Figure 6.8. SEM images of YSZ8 sintered microgears fabricated using powder size of (a) 2.0 µm, (b) 5.0 µm, and (c) 10.0 µm.

6.5 Surface Morphology

Surface morphology of the sintered microgears were inspected using SEM images as shown in Figures 6.9. Well-defined ceramic grains are presented in high-resolution images without polishing, indicating a flat and smooth surface of the fabricated samples. Figures 6.9(a)-(c) show surface morphology of alumina samples prepared using 0.7 μm, 1.0 μm and 12.0 μm respectively. In the A0.7 and A1.0 based samples, surface appeared to have both small and coarse grains together. Small grains are about 1.0 μm in diameter and coarse grains are about 10 μm in diameter. Few pores were observed in the A0.7 based samples while more pores appear in 1.0 μm based samples. As for 12.0 μm based samples, many very large pores were observed. Figures 6.9(d)-(f) show surface morphology of YSZ8 samples prepared using 2.0 μm, 5.0 μm and 10.0 μm powder respectively. 2YSZ8, 5 YSZ8 and 10YSZ8 based samples exhibit relatively large grains as the construction blocks, while smaller grains are filled the joints where three or more large grains meet. The fine grains are about 1 μm in diameter and coarse grains are about 5 μm in diameter. It is clear that there is no much difference in the grain size between the three samples. In addition, there are no pores observed in the 2.0 μm based samples. A few pores exist in the 5YSZ8 based samples and more pores are found in the 10 YSZ8 based samples. In summary, for dense samples, such as A0.7 alumina and 2YSZ8 based samples, there are almost no or few pores observed. It can be clearly noted that dense samples have fewer pores while samples with low density have more pores. In addition, it is also noted that pore dimensions are related to powder particle sizes. The smaller the particle size, the smaller the pores.

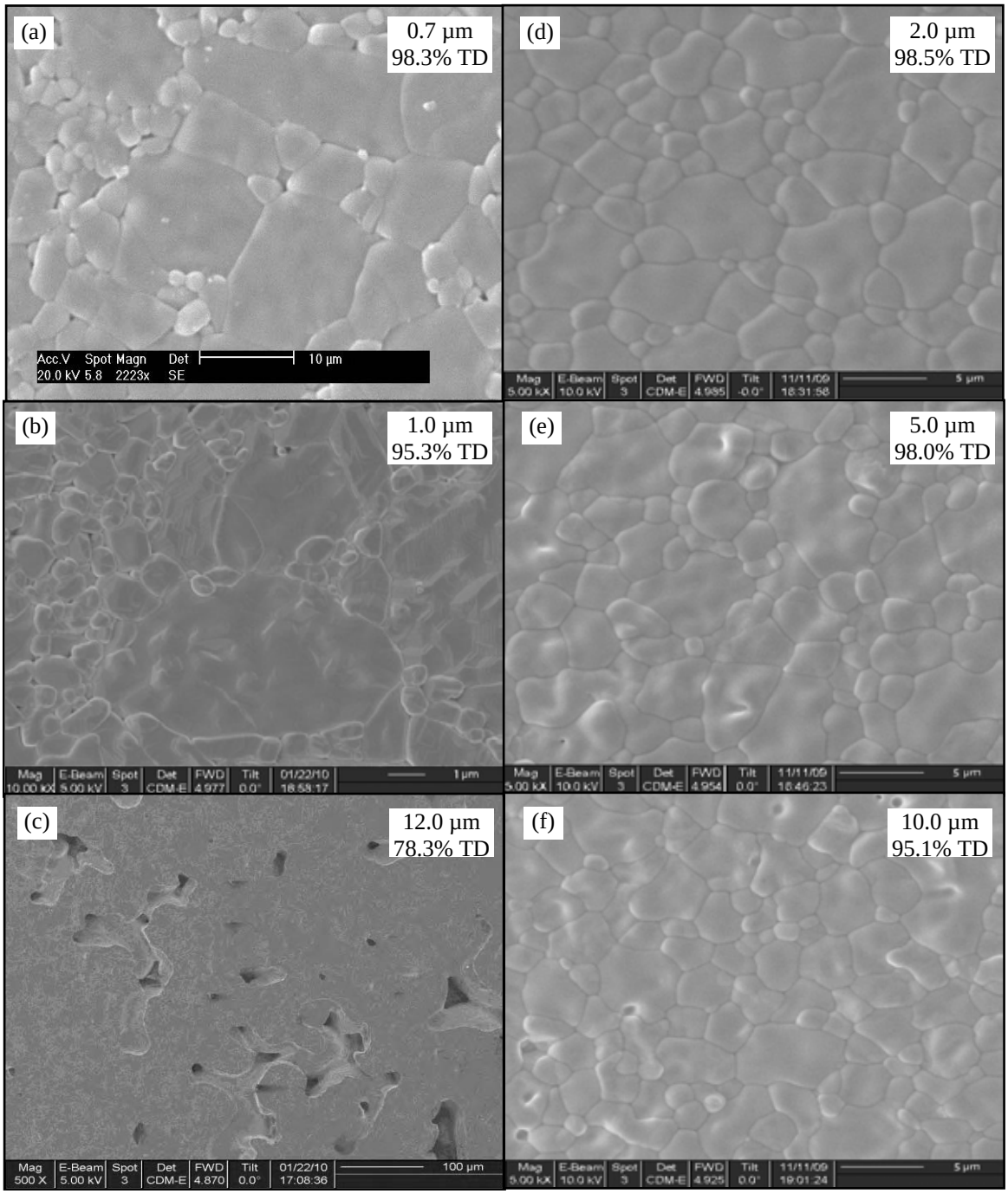

Figure 6.9. SEM images of sintered microgears surface morphology, fabricated using Al_2O_3 with powder size of (a) 0.7 µm, (b) 1.0 µm, and (c) 12.0 µm and YSZ8 with powder size of (d) 2.0 µm, (e) 5.0 µm, and (f) 10.0 µm.

6.6 Surface Roughness

A surface of the Al_2O_3 micro gear fabricated using the three powders sizes and sintered at 1600 °C are reconstructed in 3D and shown in Figure 6.10. The reconstruction of the surface is based on stereo SEM images, a technique existing in the research group. The presented 3D images clearly reveal the surfaces topography, demonstrating the capability of the stereo imaging technique for reconstructing a 3D surface of ceramic material. The computed surface roughness parameters are found to be R_a, R_q, R_p , R_v, R_{sk} and R_{ku}, as given in Table 6.1.

Alumina microcomponent results are given in both Figure 6.10 and Table 5.1. It can be generally noted that, the roughness parameters of the micro gear surface fabricated using A0.7 powder were less than A1.0 and A12.0 powder respectively. In roughness analysis of A12.0 based samples, large pores were clearly found on the surface due to the low sintering density. These large pores degrade the surface roughness quality. As a result, the measurement outputs are the highest when compared to both A0.7 and A1.0 based samples.

On the other hand, 3D reconstructed surface of the YSZ8 micro gears fabricated using the three powders sizes and sintered at 1550 °C, 1600 °C and 1600 °C respectively are shown in Figure 6.10. In addition, the computed surface roughness parameters are listed in Table 6.2. The surface roughness of YSZ8 is similar to the one concluded from the alumina components. 2YSZ8 based microgear has the smoothest surface when compared to 5YSZ8 and 10YSZ8 based components, respectively.

In summary, for both Al_2O_3 and YSZ8, the smaller powder size and denser the microcomponents, the smoother the surface is.

Table 6.1. Top surface parameters of the fabricated Al_2O_3 microgear.

Roughness parameters	**A0.7**	**A1.0**	**A12.0**
$\mathbf{R_a}$	54.77 nm	57.75 nm	3.26 µm
$\mathbf{R_q}$	71.04 nm	73.48 nm	5.33 µm
$\mathbf{R_p}$	329.92 nm	282.41 nm	23.76 µm
$\mathbf{R_v}$	332.34 nm	372.9 nm	72.65 µm
$\mathbf{R_{sk}}$	-0.097	-0.196	-2.17
$\mathbf{R_{ku}}$	3.73	3.36	14.07

Table 6.2. Top surface parameters of the fabricated YSZ8 microgear.

Roughness parameters	**2YSZ8**	**5YSZ8**	**10YSZ8**
$\mathbf{R_a}$	54.38 nm	70.122 nm	84.13 nm
$\mathbf{R_q}$	68.68 nm	88.68 nm	108.1 nm
$\mathbf{R_p}$	330.66 nm	388 nm	501.36 nm
$\mathbf{R_v}$	296.49 nm	523.36 nm	797.1 nm
$\mathbf{R_{sk}}$	0.1496	-0.1049	-0.2989
$\mathbf{R_{ku}}$	3.225	3.396	3.8658

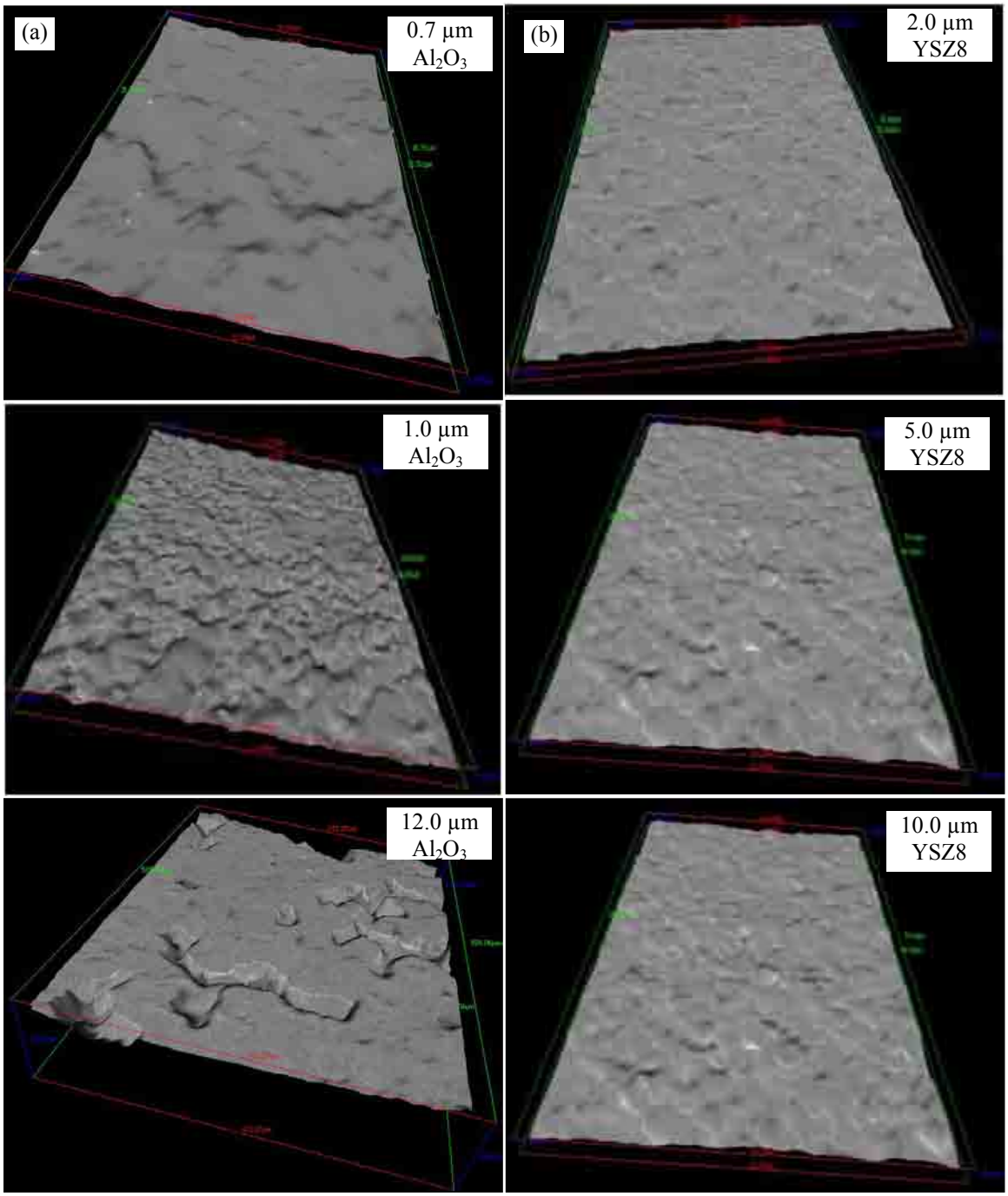

Figure 6.10. 3D reconstructed surface of the fabricated micro gear using (a) Al_2O_3, (b) YSZ8.

6.7 Complete Microengine

The above characterisation of the sintered microcomponents using different Al_2O_3 and YSZ8 powders clearly show that 0.7 µm alumina and 2.0 µm YSZ8 based samples exhibit excellent results in terms of good shape retention, high density, good mechanical properties and smooth surface roughness.

On the basis of the above characterization, 0.7 µm alumina and 2.0 µm YSZ8 were chosen for the fabrication of ceramic microengine parts. Several aspects have been taken into consideration before assembling microengine parts. Surfaces of the microcomponents should be flat and smooth to get desired contact between surfaces and to avoid leakage. Moreover, vertical sidewalls of the fabricated microcomponents are needed for two moving surfaces to be parallel. If the fabrication process leads to inhomogeneous shape retention and defected sidewalls, it will results in incomplete contact between moving parts and cause leakage and failure in bonding.

After fabrication of different microengine parts, further examination was performed to check critical areas in the microengine parts before assembling. Critical areas are identified as microgear teeth profile, sidewalls, micropiston teeth, sidewalls, and microholes in different parts. Examination of the above mentioned critical areas is shown in Figure 6.11. Figure 6.11(a-b) shows microgears sidewalls. The images illustrate vertical sidewalls with high magnification. Microgear sidewall is a very important area where it transfers the generated power from microengine to the output. Figure 6.11(c-d) shows two meshing gears. The gears are in smooth contact due their well-defined profile and precision teeth. Figure 6.11(e-f) shows micro piston sidewalls. The images also exhibit well-defined teeth with vertical sidewalls. High precision of this area is particularly important, as it will work

together with oil membrane to seal the combustion chamber. Figure 6.11(g-h) and show a microconnecting rod with a pin hole. The holes are in excellent geometry, which helps the engine in smooth movement. Complete alumina and zirconia microengines are assembled and shown in Figure 6.12. The pictures illustrate the high accuracy of the assembled Al_2O_3 and YSZ8 microengines, indicating consistent and uniform shrinkage between different microengine parts.

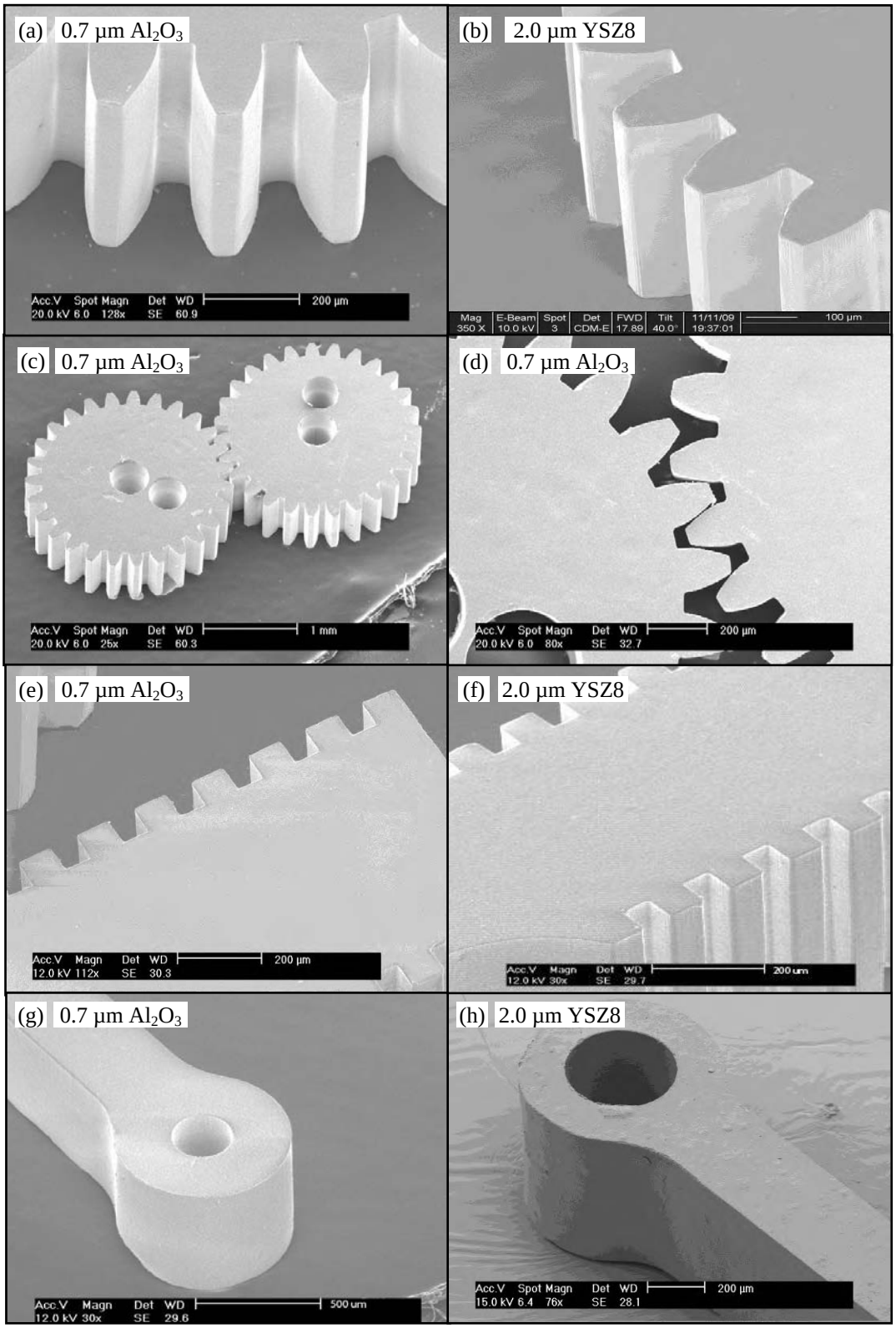

Figure 6.11. SEM images of critical areas of different microengine parts fabricated using 0.7 µm Al_2O_3 and 2.0 µm YSZ8 powders and they are (a,b) gear sidewalls, (c,d) Meshing gears, (e,f) micropiston sidewalls, (g,h) microconnecting rod holes.

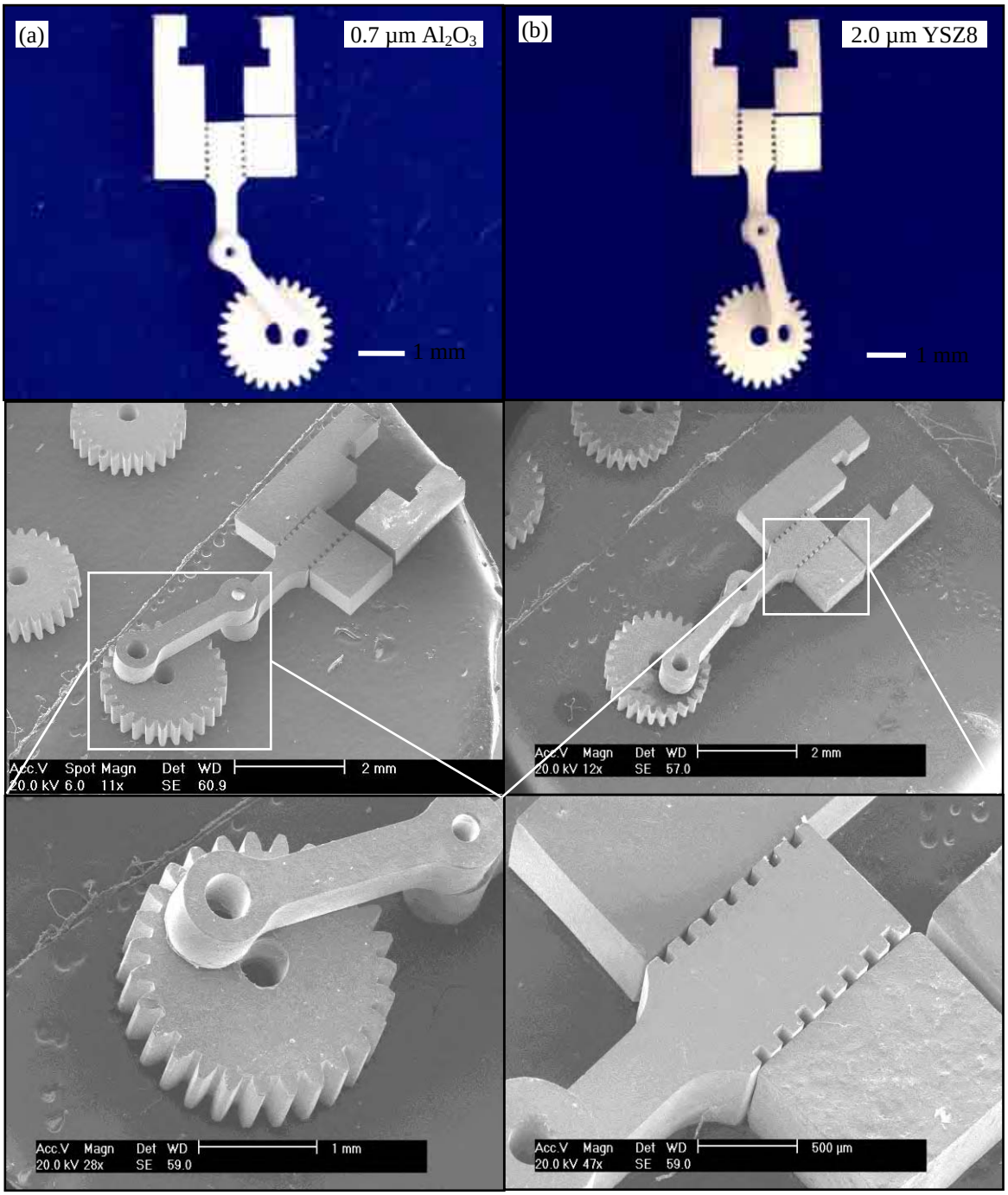

Figure 6.12. Optical and SEM images of (a) the assembled alumina microengine, (b) the assembled zirconia microengine.

6.8 Summary

In this chapter, characterisation of sintered Al_2O_3 and 8 mole% yttria stabilized zirconia microengine parts is explained. The effect of the dispersant on the sintered density was studied. It is concluded that, the optimum dispersant amount obtained to fabricate dense green parts is the same amount to fabricate dense sintered density. Furthermore, the effect of sintering temperature on the resultant sintered density, linear shrinkage, micro hardness, flexural strength was studied to find the optimum sintering temperature for both Al_2O_3 and 8 mole% yttria stabilized zirconia microengine parts. Moreover, shape retention, surface morphology and surface roughness of the sintered microcomponents were studied. It is concluded that, alumina microcomponents fabricated using particle size of 0.7 µm and sintered at 1600 °C has sintered density of 98.3%, linear shrinkage of 17.6%, Vickers hardness of 23.05 GPa, flexural strength of 366 MPa and surface roughness Ra= 54.77 nm. On the other hand, 8 mole% yttria stabilized zirconia microcomponents fabricated using particle size of 2.0 µm and sintered at 1550 °C produced sintered density of 98.5%, linear shrinkage of 20.9%, Vickers hardness of 14.65 GPa, flexural strength of 508 MPa and surface roughness Ra= 54.38 nm. The fabricated microcomponents were examined and showed excellent shape retention, which enabled the assembly of alumina and zirconia microengines.

CHAPTER 7: FABRICATION OF ZIRCONIA/ALUMINA COMPOSITE CERAMIC MICROCOMPONENTS

7.1 Introduction

This chapter presents fabrication of ceramic composite to obtain microcomponents of tailored properties. It introduces the experimental work to fabricate zirconia/alumina composite ceramic microcomponents in details and characterises the resultant properties accordingly. First, fabrication of zirconia matrix alumina nanocomposite microcomponents is introduced in Section 7.2. The research is intended to obtain homogenously dispersed alumina nano particles into 8 mole% yttria stabilized zirconia matrix. In this section, the fabrication procedure used in this experimental is introduced. The physical, microstructural and mechanical properties of the green and sintered nanocomposite microcomponents are analysed in details. Second, fabrication of functionally graded ceramic composite microcomponents is introduced in Section 7.3. The research is intended to obtain complete and crack free 8 mole% yttria stabilized zirconia/alumina graded composite with tuneable properties. The fabrication procedure to form graded layers used in experiments is introduced. Problems in the green and sintered microcomponents are discussed and solutions are proposed. Microstructural analysis is performed and results are discussed. Finally, the chapter is summarized in Section 7.4.

7.2 Zirconia Matrix Alumina Nanocomposite Microcomponents

8 mol% yttria stabilized zirconia (YSZ8) has excellent thermal, mechanical, and electrochemical properties, as detailed in the literature review, Chapter 2. However, it has been proven that addition of particles, platelet, whisker, or continuous fibre into yttria stabilized zirconia matrix could significantly improve many of its properties. Many researchers investigated the effects of alumina to yttria stabilized zirconia and found that incorporation of alumina particulate reinforcements into yttria stabilized zirconia matrix resulted in lighter, harder, stronger and stiffer composite by decreasing density and increasing strength and elastic modulus. Moreover, the addition of alumina improves high temperature strength of YSZ because the strength of alumina does not decrease as much as YSZ with increasing temperature [161-164]. Inspired by the experience with the reinforcement of YSZ, fabrication of YSZ8/Al_2O_3 ceramic nanocomposite microcomponents is studied in this chapter. The research was set up to study the influence of alumina nano particles on YSZ8/Al_2O_3 ceramic nanocomposite properties and explore the possibility of new composite material for net shaped ceramic microcomponents with improved properties.

The main challenges involved in the fabrication process in this part of the work include:

1. The composite materials should be homogenously dispersed with uniform size distribution.
2. Cracks and damages should be avoided on the green and sintered microcomponents.
3. Sintered properties of the yttria stabilized zirconia microcomponents should be improved with the incorporation of a small amount of alumina nano particles (0-5% vol.).

7.2.1 Fabrication Process

The fabrication process includes soft lithographic, water based slurry and vacuum casting processes, which was previously presented in this thesis.

7.2.1.1 Powders

8 mol% yttria stabilized zirconia powder with particle size of 2 μm was employed as the matrix material of the composite. Results obtained in Chapter 6 show that it produced better properties when compared to 5 μm and 10 μm powders. On the other hand, alumina powder used in this experiment is α-alumina with a particle size of 400 nm, properties of both powders are presented in Table 4.1 and Table 4.2.

7.2.1.2 Slurry Preparation, Moulding, Demoulding and Sintering

YSZ8/Al_2O_3 slurry preparation procedure is based on the proposed procedure presented in Chapter 4 and literature [4]. Six samples were used in the experiments with addition of 0-5 vol% alumina nano particles. The theoretical density value of the composite was calculated using the rule of mixture. In addition, the relevant mass percentages of each powder in the composite were also calculated and listed in Table 7.1.

Table 7.1. Characteristics of produced YSZ8/Al_2O_3 composite samples.

Sample	**Al_2O_3 (%vol.)**	**YSZ (%wt.)**	**Al_2O_3 (%wt.)**	**Theoretical Density (g/cc)**
YSZ8	0	100	0	5.953
0.2AYSZ8	0.2	99.866	0.134	5.949
0.5AYSZ8	0.5	99.665	0.335	5.943
1AYSZ8	1	99.331	0.669	5.933
3AYSZ8	3	97.979	2.021	5.894
5AYSZ8	5	96.609	3.391	5.854

Water-based slurry of YSZ8/Al_2O_3 nanocomposite was prepared with a solid loading of 80% vol. and pH=7. The preparation procedure is described in the following steps.

1. Dispersant D-3005 is added to deionised water and mixed with the aid of magnetic stirrer for 5 minutes.
2. Water mixture is divided into two portions of volume ratio approximately equal to YSZ8/Al_2O_3 volume ratio.
3. YSZ8 powder is added to its relevant water mixture and mixed using mechanical stirring for 30 minutes.
4. Al_2O_3 powder is added to its relevant water mixture and dispersed using ultrasonic processing for 16 minutes.
5. Al_2O_3 mixture is added to YSZ8 mixture and mixed using mechanical stirring for another 30 minutes.
6. Polymer based binders B-1000 and B-1007 are then added at a ratio of 1:4 and mixed for 30 minutes using a low speed stirring.
7. The prepared slurry is degassed using vacuum and then casted onto the PDMS to fill the mould cavities with the aid of stainless steel spatula and vacuum casting.
8. The excess slurry on the top of the mould is removed using a razor blade, and the mould is left to dry slowly for 24 hours.
9. Once the mould is dry, the green parts are achieved by carefully bending the soft PDMS mould and then are pulled out with the aid of a thin tweezer.

10. The green microcomponents are sintered to 1550 °C for 2 hours using heating cycle presented in Chapter 4.

7.2.2 Results

7.2.2.1 Green Density

In previous chapters, the effect of D-3005 concentration on dispersion of both alumina and yttria stabilized zirconia suspensions were shown. The highly dispersed suspensions resulted in high green densities for selected powders using pH=7 and optimum dispersant and binder concentration. Similarly, D-3005 was employed to deagglomerate ceramic powders and to disperse alumina nano particles to form homogenous composite in YSZ8 matrix. In these experiments, D-3005 concentration was varied and the green density of the composite was measured with respect to alumina content in the composite. The green density was measured using mass to volume ratio as described in Chapter 4. Six YSZ8/Al_2O_3 samples with alumina content at 0, 0.2, 0.5, 1, 3, and 5% vol. in YSZ8 matrix were prepared using dispersant concentration of 20.6, 15, and 10 mg/g powder. At each alumina content percentage, five samples were prepared and the average green density was recorded. The relative density is calculated with respect to the calculated theoretical densities listed in Table 7.1. The results are plotted in Figure 7.1.

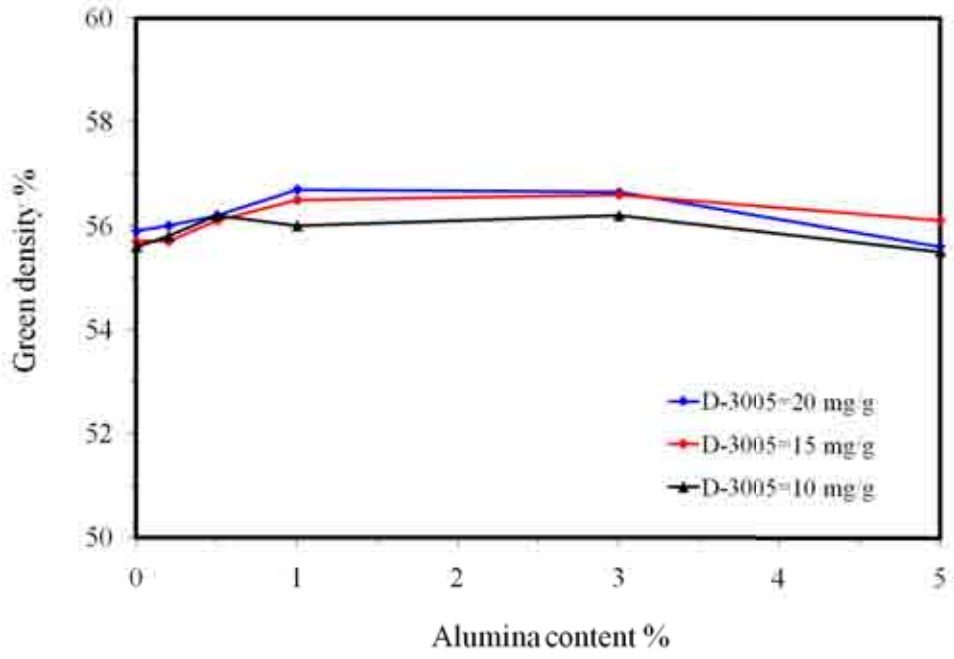

Figure 7.1. The green density of YSZ8/Al_2O_3 nanocomposite as a function of alumina content for different dispersant concentration.

As shown in the figure, when D-3005 concentration is 20 mg/g, addition of alumina nano particles has a small effect on the composite green density. A green density of only 55.9% was achieved with YSZ8 powders, compared to 56.7% for 1% vol. of alumina nano particles. The green density decreases gradually with further addition of alumina nano particles. It is also found that composite green density at D-3005 concentration = 20 mg/g is approximately the same as the composite green density when D-3005 concentration is at 15 mg/g. However, when D-3005 concentration is at 10 mg/g, composite green density is less than both green densities at 15 and 20 mg/g. After comparison, D-3005 concentration at 20 mg/g is chosen as the optimum concentration for fabrication of dense green composite microcomponents.

7.2.2.2 Green Shape Retention

YSZ8/Al_2O_3 green composite microcomponents were fabricated using the optimum dispersant rate 20 mg/g and binder concentration 20-25 mg/g. The help of vacuum system, dispersed slurry filled every detail of the moulds, resulting in intact YSZ8/Al_2O_3 nanocomposite green microcomponents with detailed features, as shown in Figure 7.2.

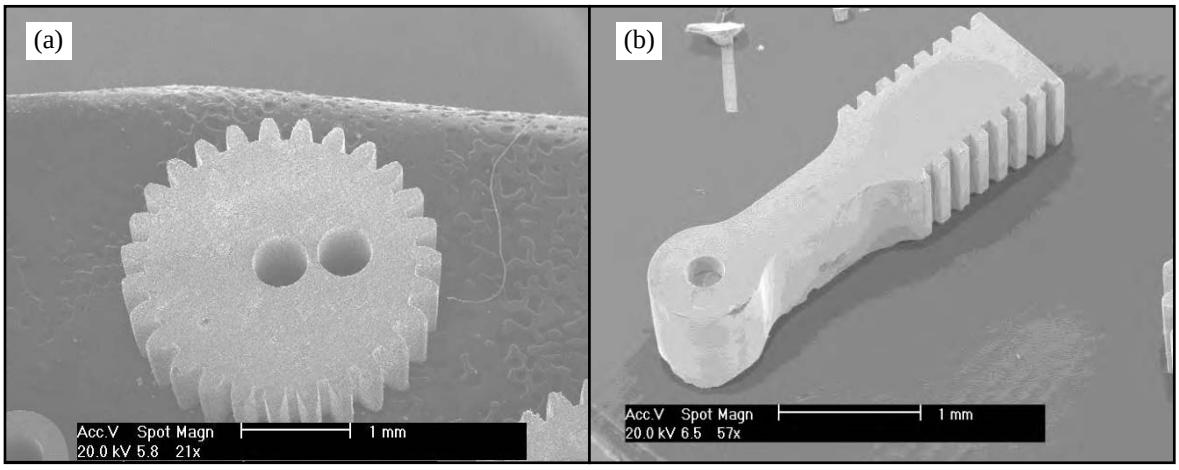

Figure 7.2. SEM images of 5% vol. Al_2O_3 green nanocomposite microcomponents.

7.2.2.3 Sintered Shape Retention

Green composite microparts were sintered at 1550 °C and the results were examined using SEM as shown in Figure 7.3. It is clear that the composite microcomponents retained their net shape quality. The obtained green microcomponents with their low dispersant and binder content granted subsequent easy debinding during heating cycle. Sintered parts were obtained with complete teeth, vertical sidewalls and without visible deformation or cracks.

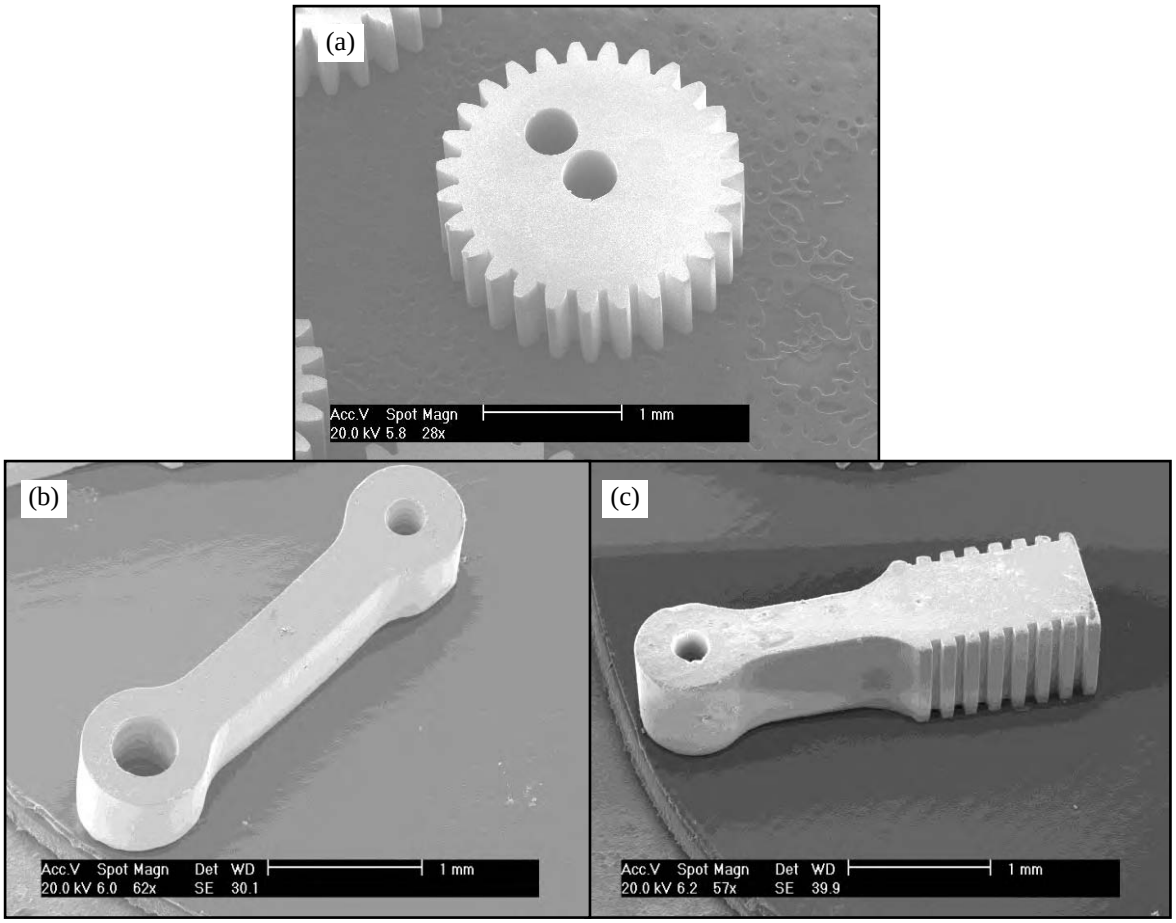

Figure 7.3. SEM images of YSZ8/Al_2O_3 nanocomposite microcomponents sintered at 1550 °C for (a) microgear, (b) micro connecting rod, (c) micro piston.

7.2.2.4 Sintered Density

The effect of adding Al_2O_3 nano particles on the sintered density of YSZ8/Al_2O_3 nanocomposite microcomponents was studies. A total of five specimens were used for a variation of alumina contents. The composite density was measured using Archimedes principal as used in Chapter 4. The relative density is calculated with respect to the calculated theoretical densities listed in Table 7.1. Figure 7.4 shows the relative density of the YSZ8/Al_2O_3 after sintering as a function of Al_2O_3 addition.

It can be seen that a small amount of Al_2O_3 nano particles in the YSZ8 matrix makes a clear increase in the sintered composite density. Sintered YSZ8/Al_2O_3 composite microcomponents with alumina nano particles content at 1% vol. exhibits the highest density of about 98.9%. With further addition of alumina, the sintered density decreases gradually. The enhanced density could be due to the improvement of the composite green density upon the addition of Al_2O_3 nano particles as explained in Section 7.2.2.1. In addition, it could be due the rearrangement of Al_2O_3 nano particles into YSZ8 matrix, which provides easy diffusion during densification. However, further increase in Al_2O_3 nano particles content leads to a gradual decrease in the sintered density. These results are in agreement with those in literature [165], whose microstructural analysis of YSZ/Al_2O_3 composite revealed very dense sintered samples and free from porosities in the grain interiors with the addition of small amount of alumina.

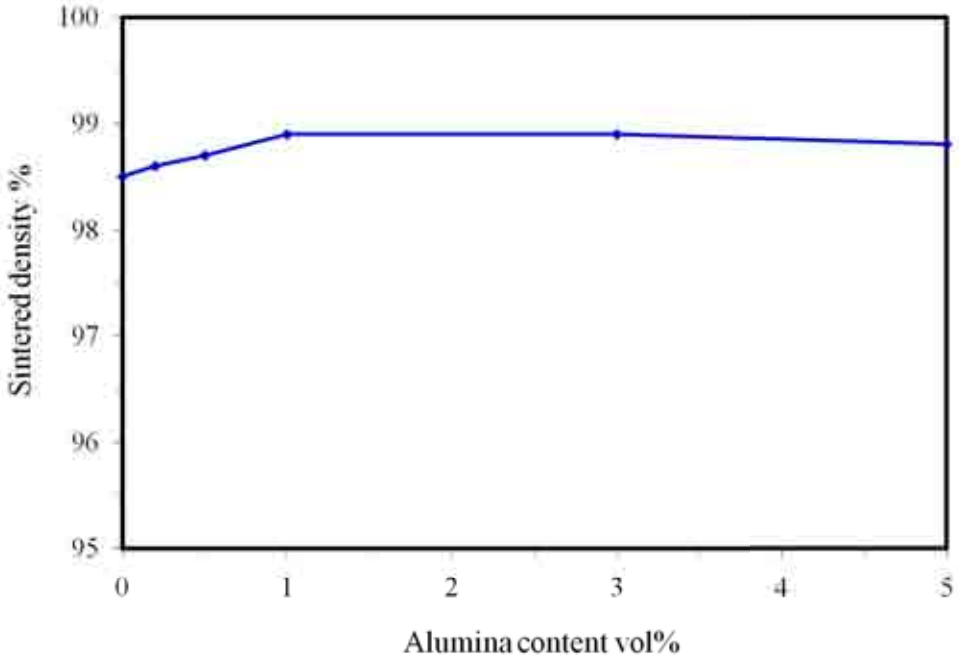

Figure 7.4. The sintered density of YSZ8/Al_2O_3 nanocomposite as a function of alumina content.

7.2.2.5 Linear Shrinkage

Linear shrinkage of sintered YSZ8/Al_2O_3 nanocomposite microcomponents was investigated with the addition of Al_2O_3 nano particles. Linear shrinkage measurements were performed using the same procedure described in Chapter 4 and based on the outer diameter of the YSZ8/Al_2O_3 with respect to SU-8 outer diameter, as detailed in Figure 7.5. Figure 7.6 shows the linear shrinkage of YSZ8/Al_2O_3 composite as a function of Al_2O_3 nano particles percentage. It can be seen that, the linear shrinkage gradually increases to its maximum of 21.2% when Al_2O_3 percentage increases to 0.3% vol. of Al_2O_3 nano particles. Afterwards, shrinkage gradually decreases with further addition of Al_2O_3 nano particles.

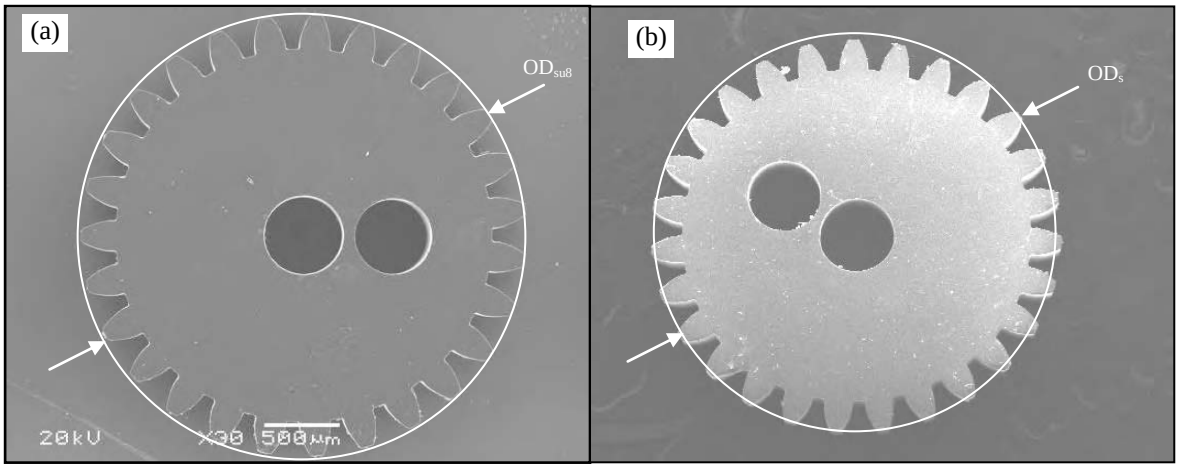

Figure 7.5. SEM images of (a) SU-8, (b) sintered YSZ8/ Al_2O_3 composite microgear for shrinkage measurements.

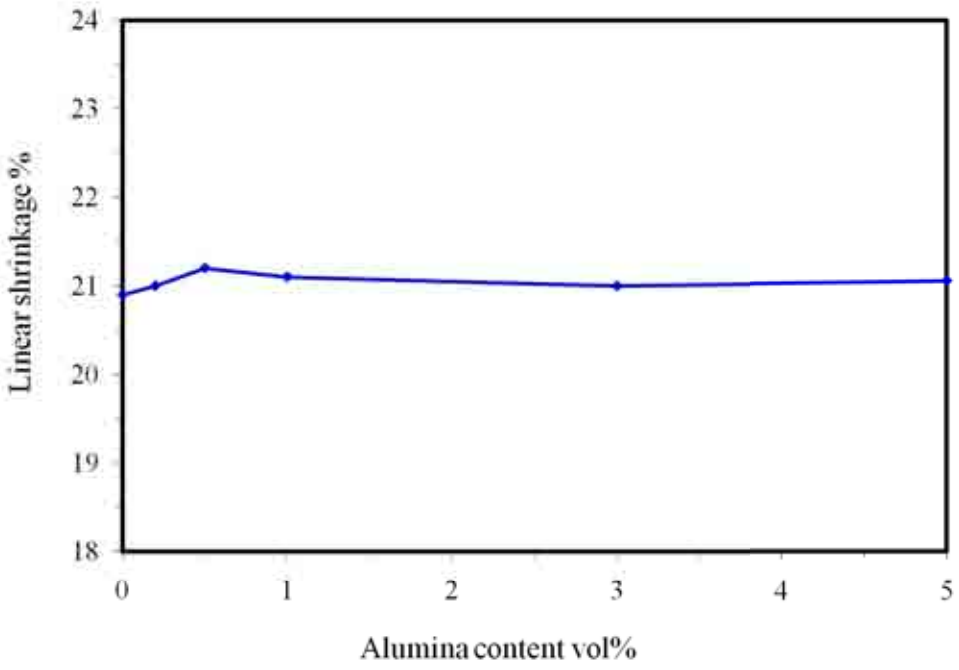

Figure 7.6. The linear shrinkage of YSZ8/Al_2O_3 nanocomposite as a function of alumina content.

7.2.2.6 Nanocomposite Surface Morphology

Alumina nano particles have a strong tendency of agglomeration due to their large specific surface area. Figure 4.1 shows an SEM image of the alumina nano powder used in this research in significant agglomeration. A good dispersion of such agglomerated particles in YSZ8 matrix is important, and the dispersion quality was investigated with surface morphological and microstructural examination. The sintered composite samples were directly inspected without polishing. Surface morphology of a sintered microgear fabricated using YSZ8/Al_2O_3 nanocomposite with 5% vol. alumina was examined using scanning electron microscopy at different magnifications, as shown in Figure 7.8. The SEM images at different magnifications provide detailed visions of the dispersion quality of alumina nano particles in both large and small scales. Figures 7.7 (a) and (b) show SEM views of YSZ8/Al_2O_3 composite microgear teeth and holes at about 160 times in magnification. The edges are sharp and the surface is homogenous, even in high resolution. At about 400 times in magnification, Figures 7.7 (c) and (d) show homogenous composite surface without visible flaws or agglomeration. Even higher magnification was used to inspect the composite grains and alumina particles dispersion. Images in Figures 7.7 (e) and (f) have a magnification of about 3000 times. It can be clearly seen that, there is no formation of alumina agglomerates inside YSZ matrix. The images show homogenous dispersion between the composite materials. It is noted that there are large and medium bright grey grains with a diameter size of 5μ and 1-2 μ respectively, which are expected to be YSZ grains. Moreover, there are smaller dark grey grains, which are expected to be alumina particles. As for porosity, it is not possible to visualize any pores within the composite. This is due to the high sintered density of the obtained composite.

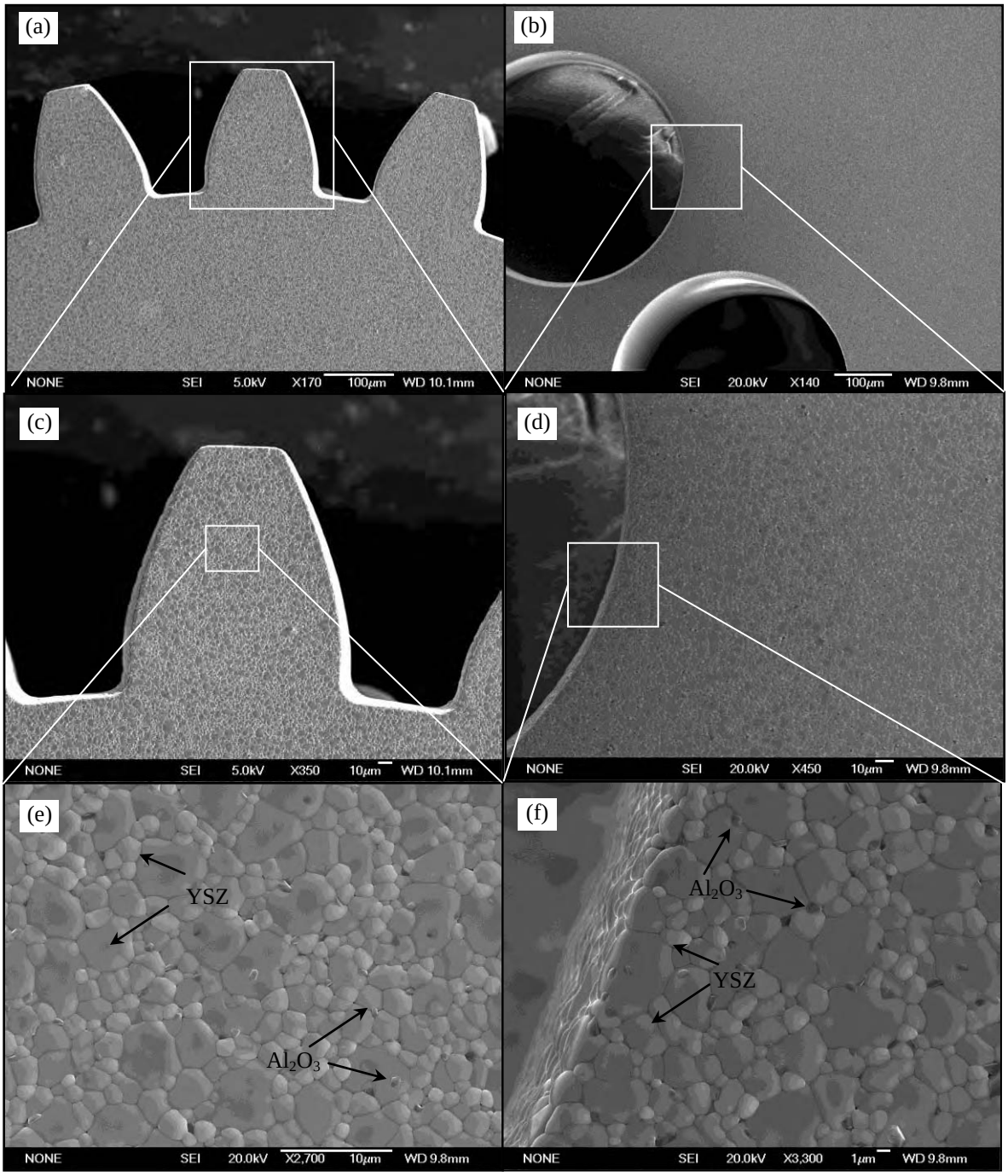

Figure 7.8. SEM images of sintered YSZ8/Al_2O_3 nanocomposite microgear with different magnification.

To distinguish between alumina and YSZ grains in the composite, back-scattered electrons (BSE) and energy dispersive X-ray spectroscopy (EDS) analysis were performed. EDS analysis was performed using Jeol 7000 scanning electron microscopy machine fitted with Oxford INCA Energy EDS software.

Figures 7.8 and 7.9 show back-scattered electrons images of YSZ8/Al_2O_3 nanocomposite with different Al_2O_3 nano particle contents. Figure 7.10 shows EDS analysis of both the dark and bright regions in the BSE images. The EDS analysis shown in Figure 7.11 proves that the dark grains are alumina and the bright grains are YSZ.

By examining Figures 7.8 and 7.9, it can be noted that when no alumina nano particles were added to the YSZ8 there is no dark grains found in the matrix, as shown in Figure 7.8(a). With addition of 0.2% alumina, the BSE image starts to show dark grains sparsely distributed, Figure 7.9 (b). With further addition of alumina at a concentration of 0.5%, the BSE images revealed more alumina grains in the YSZ matrix, Figure 7.9 (c). It is also noted that alumina particles are homogonously dispersed in YSZ8 matrix. Alumina particles are found in the YSZ8 matrix with a diameter size of 0.5-1.5 μm, which means that the proposed colloidal fabrication process were successful in deagglomerating alumina nano powder. In addition, it also helped the dispersion of alumina particle into YSZ8 matrix. It can be also seen that the majority of alumina particles are found at YSZ8 grain boundaries while few were found inside YSZ8 grains.

In summary, homogenous dispersion of alumina nano particles in YSZ matrix were successfully obtained. The proposed dispersion process of monolithic alumina and zirconia presented in Chapter 5 can be easily adopted to zirconia matrix alumina nanocomposite microfabrication process.

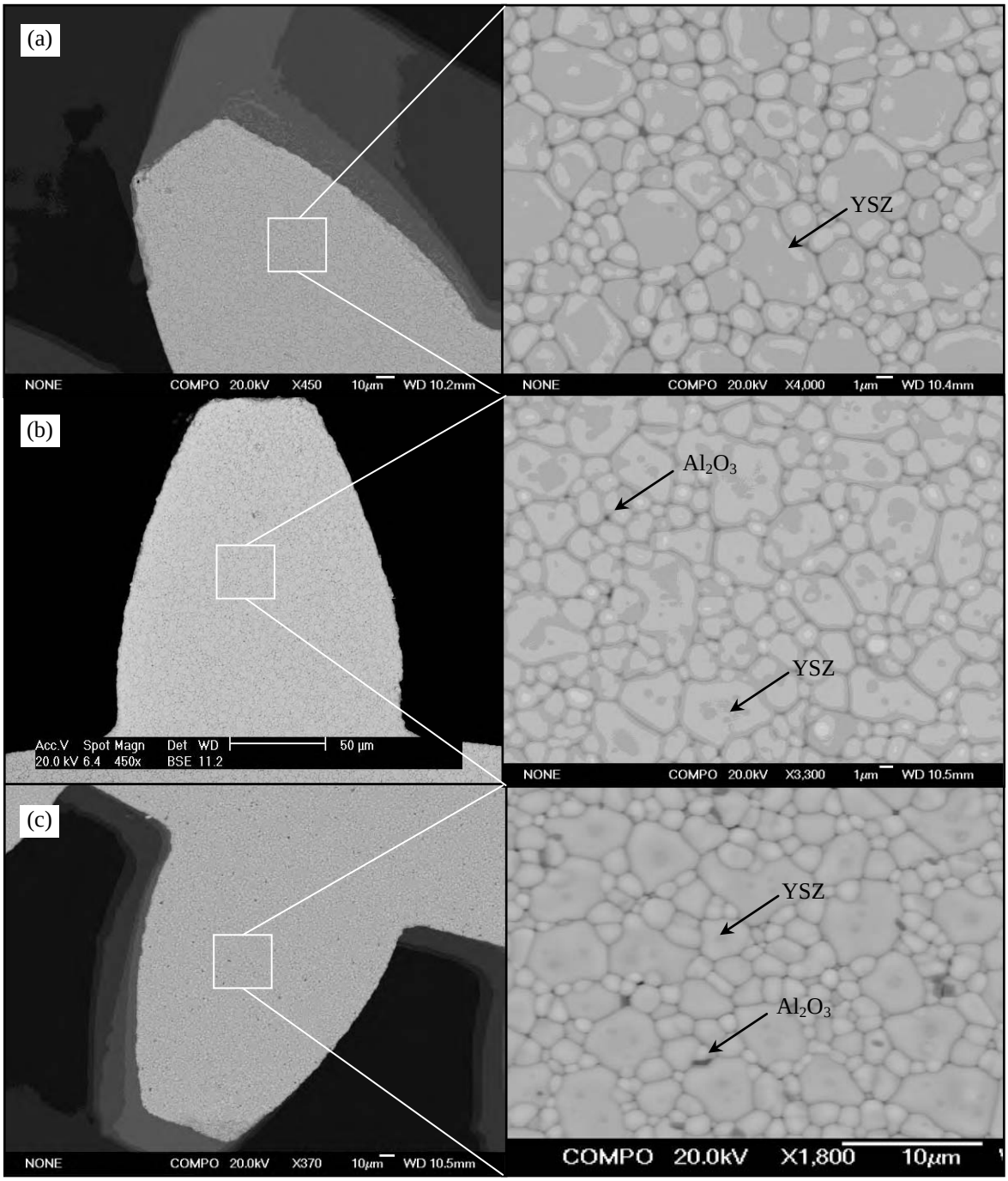

Figure 7.8. BSE images of sintered YSZ8/Al_2O_3 nanocomposite microgear with different alumina nano particles content (a) 0% vol., (b) 0.2% vol., (c) 0.5% vol.

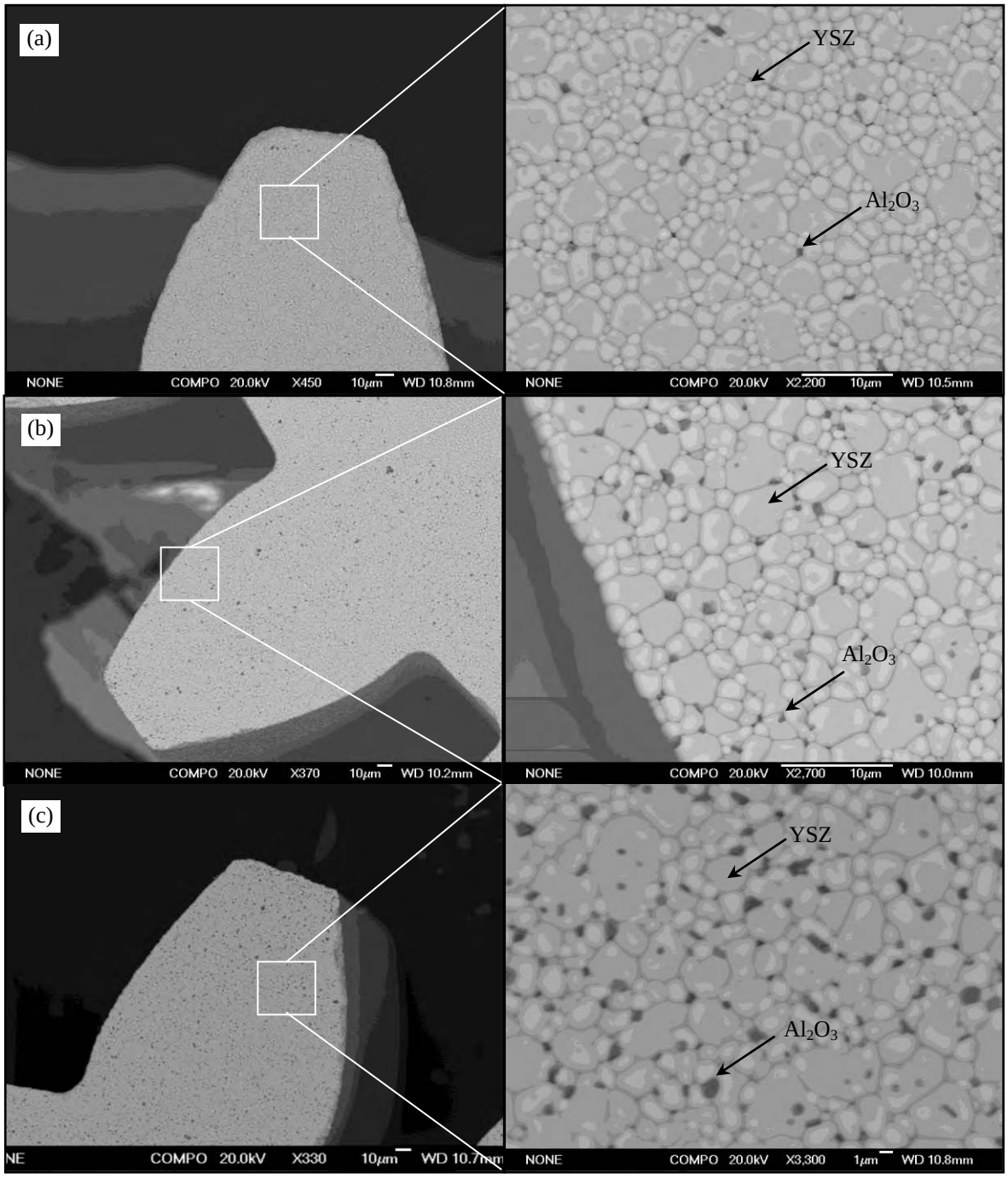

Figure 7.9. BSE images of sintered YSZ8/Al_2O_3 nanocomposite microgear with different alumina nano particles content (a) 1% vol., (b) 3% vol., (c) 5% vol.

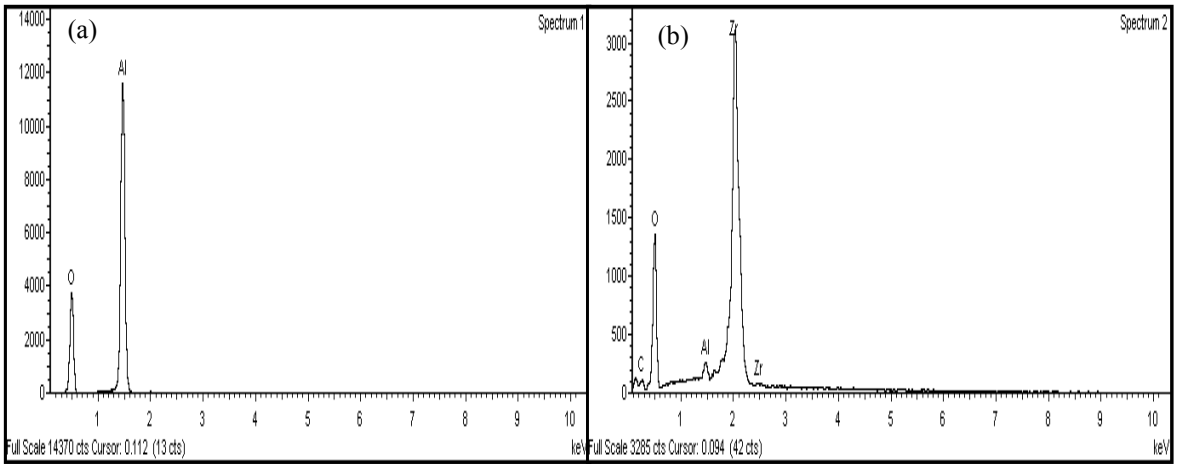

Figure 7.10. EDS analysis of YSZ8/Al_2O_3 nanocomposite microcomponents (a) dark regions, (b) bright region.

7.2.2.7 X-ray Diffraction Analysis

The crystalline phases of YSZ8/Al_2O_3 nanocomposite were identified by X-ray diffraction to investigate the effect of alumina nano particles on the YSZ8 phase transformation. The study was performed using X-ray diffractometry (Bruker D8 Autosampler- School of chemistry- University of Birmingham). X-ray diffraction patterns were collected at room temperature by scanning steps of 0.014^o (2θ) over a 24^o <2θ < 60^o angular range working with a Cu K_α radiation (λ = 1.5406 Å). In addition, EVA (Bruker-AXS) + 2009 (Powder Diffraction File, ICDD (International Centre for Diffraction Data) were used as phase ID software.

Figure 7.11(a) shows X-ray diffraction of sintered alumina samples. The figure depicts high intensity α alumina phase in the pattern. No other phases except α alumina are found in the pattern. Figure 7.11(b) shows X-ray diffraction of sintered YSZ samples. The figure shows a tetragonal phase, which is identified by the EVA software. In addition, a small intensity peak (z) is noticed besides a tetragonal phase, which may indicate a trace of

monoclinic phase. Monoclinic phase peaks with low intensity normally occurs beside tetragonal phase in sintered YSZ [166-167]. Further qualitative analysis is needed to confirm the phase of this trace as it is shifted closer to the tetragonal one.

As for 95% YSZ8/ 5% Al_2O_3 composite, Figure 7.11(c) shows the effect of alumina content on the composite phases. The figure demonstrates high intensities tetragonal phase with small α alumina peaks. No other phase is found in the pattern. A comparison between X-ray diffraction of both pure YSZ and YSZ/Al_2O_3 nanocomposite is shown in Figure 7.12. The peak intensities of the tetragonal reflections were dramatically improved compare with those of previous results for the pure YSZ8. These results are in agreement with those in literatures [167-168], whose X-ray analysis of YSZ/Al_2O_3 composite revealed pure tetragonal zirconia phase. Thus, it may be generalized that the addition of alumina can have a significant suppressive effect on the phase evolution in the emergence of other zirconia phases such as monoclinic phase.

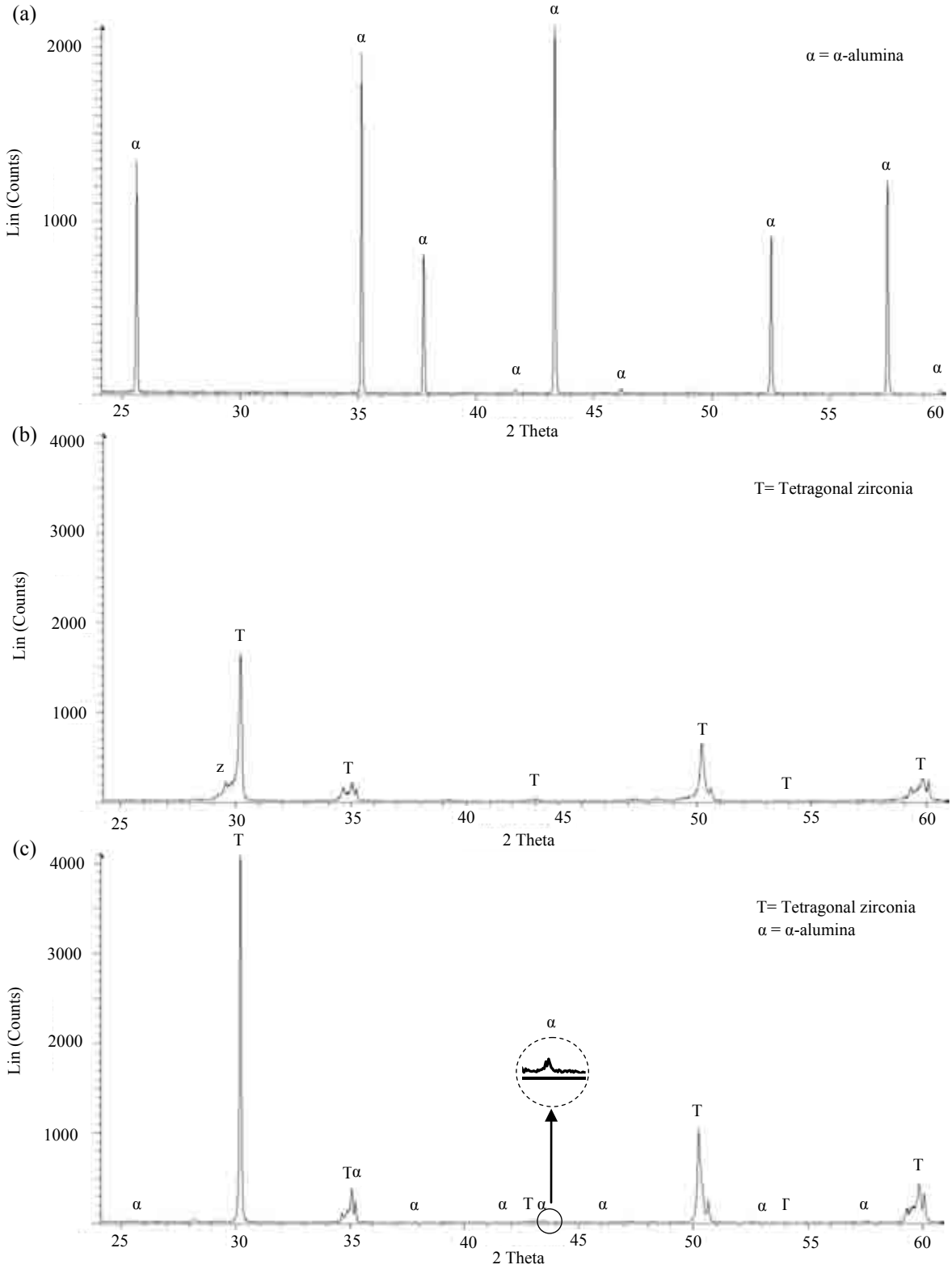

Figure 7.11. X-ray diffraction patterns of the sintered (a) Alumina, (b) YSZ8, and (c) 95 vol% YSZ8/ 5% vol. Al_2O_3.

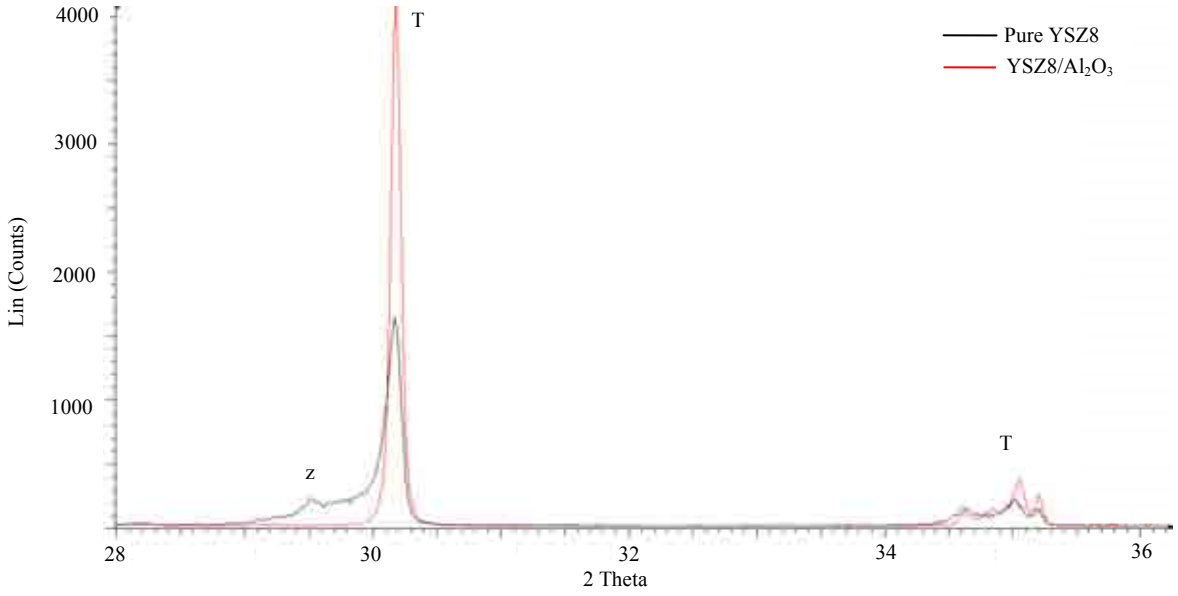

Figure 7.12. Comparison between X-ray diffraction patterns of the sintered pure YSZ8 and YSZ8/Al_2O_3 nanocomposite.

7.2.2.8 Nanoomposite Micro Hardness

The effect of adding alumina nano particles into YSZ8 matrix on the micro hardness of the composite was studied. Measurements of Vickers micro hardness were performed using the procedure described in Chapter 6 on MicroMet 5100 Series Microindentation with a loading of 9.8 N. A set of five readings were taken for each microgear sample and the averages were obtained.

Figure 7.13 is a plot of Vickers micro hardness as a function of alumina nano particles content. It can be clearly seen that, as alumina nano particles content increases in the composite, a significant increase in micro hardness is obtained. In particular, the micro hardness value increases from 14.65 GPa for pure YSZ8 sintered at 1550 °C to 17.1 GPa with the addition of 5% vol. of alumina nano particles. This behaviour can be attributed to both the improvement in the sintered density and the presence of the extraordinary

hardness properties of alumina nano particles. As a result, the harder the alumina nano particles, the more resistance to plastic deformation the components will be. Higher hardness values imply a good wear resistance, which is very important for microgears the surfaces of which are subject to contact loads.

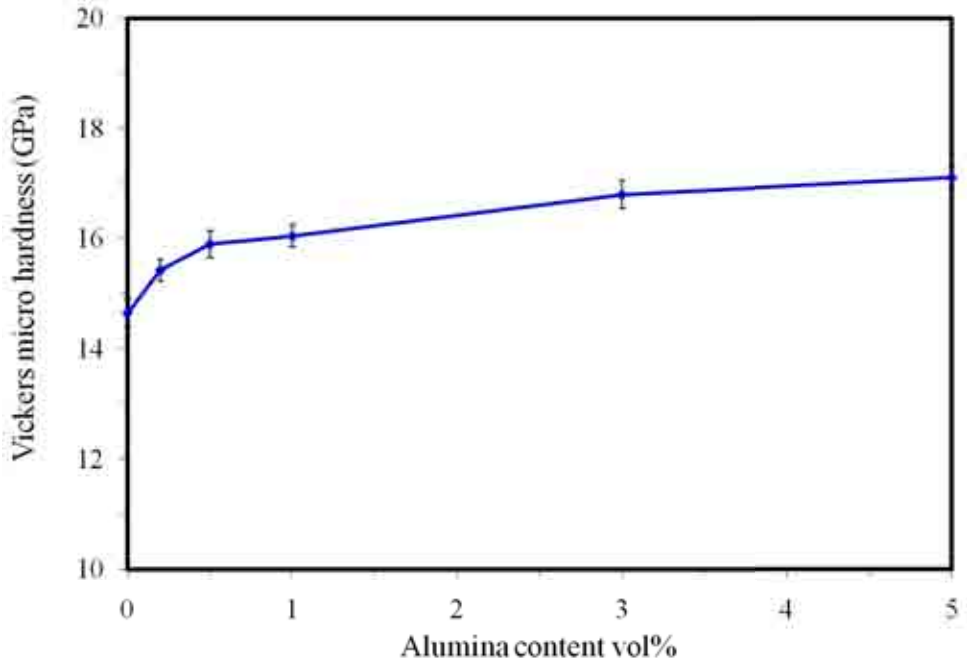

Figure 7.13. The relationship between Vickers micro hardness of YSZ8/Al_2O_3 nanocomposite and alumina content.

7.2.3 Discussion

The proposed fabrication process was successful obtaining net shaped YSZ8/Al_2O_3 nanocomposite microcomponents with good quality. The main challenges listed above were met successfully. It was found that dispersing the two powders separately with an optimum dispersant concentration was able to achieve well-dispersed composite. The effect of alumina nano particles on the composite microcomponents was investigated. X-ray diffraction of YSZ8/Al_2O_3 nanocomposite microcomponents reveals pure tetragonal

zirconia phase. In addition, the addition of alumina nano particles improves the composite in densities and micro hardness. The sintered YSZ8/Al_2O_3 nanocomposite microcomponents can achieve sintered density 0.4% and micro hardness 17% superior to the pure YSZ8 sintered microcomponents. The proposed composite seems to be an adequate material to be used in manufacture of ceramic microcomponents instead of pure ceramics previously presented in this project.

7.3 Functionally Graded Ceramic Composite Microcomponents

Functionally graded materials (FGM) are a new class of materials that exhibit a progressive compositional gradient change from one side to the other of a layer [168]. They are designed to take advantage of certain desirable phase or material, such as metals, ceramics, and polymers, resulting in desirable properties to suit a particular application. Required performance attributed to mechanical, thermal, electromagnetic or biochemical properties of the structures can be achieved by varying the composition, morphology and crystal structure gradually in volume [169]. Since the concept of FGM was introduced in Japan in 1984 during an aerospace plane project, growing efforts have been devoted to research in this field, especially to the fabrication techniques [170]. In this section, a novel approach is presented to design and process ceramic materials, and to combine irreconcilable properties, such as hardness and toughness, in one microcomponent. YSZ8/Al_2O_3 FGM is proposed in this project to obtain properties of both alumina and zirconia with a position dependant composition and related mechanical properties. The aim is to fabricate microgears with a hard alumina shell and tough zirconia core, as shown in Figure 7.14.

The main challenge involved in the fabrication process is to avoid cracks and delimitation in both green and sintered microcomponents due to the co-existence of two materials in one component.

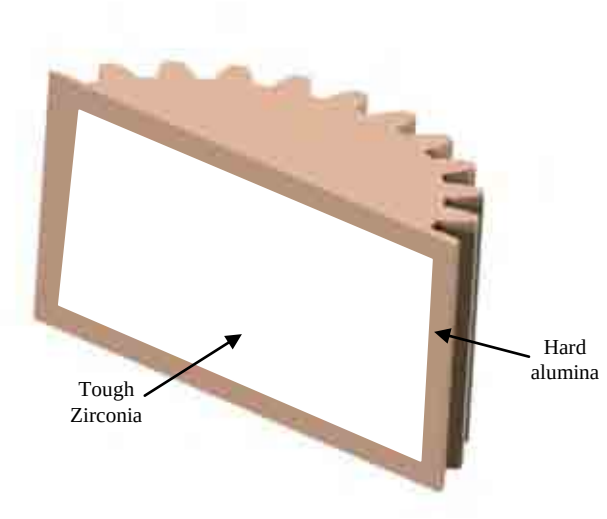

Figure 7.14. Schematic of YSZ8/Al_2O_3 functionally graded ceramic composite microgear.

7.3.1 Fabrication Process

7.3.1.1 Powders

8 mol% yttria stabilized zirconia powder of 2 µm in size was employed as the core material for the intended composite FGM microgear. In addition, α-alumina powder with a particle size of 0.7 µm was employed as the shell material. Both powders were proven in achieving high quality microcomponents in previous chapters.

7.3.1.2 Slurry Preparation

In preparation of the required slurry composition for producing both the shell and core layers, the mixing process was performed using the procedure explained in Section 7.2.1.2

7.3.1.3 Layer Formation, Drying, Demoulding and Sintering

The proposed filling process of highly stable suspensions plays a key role in determining integrated FGM green layers. First, it is important to understand the drying behaviour of ceramic suspension in PDMS moulds. Shrinkage is one of the consequences of the drying process. In a PDMS soft mould, evaporation of water contents in the moulded slurry takes place through its top surface, which is the only side open to atmosphere. Therefore, the top surface dries faster than the bottom of the moulded parts. On the other hand, it was observed that highly stable suspension with low solid loading tends to adhere to PDMS sidewalls. As a result, a concave top surface is produced when using highly stable and low solid loading suspension, as shown in Figure 7.15.

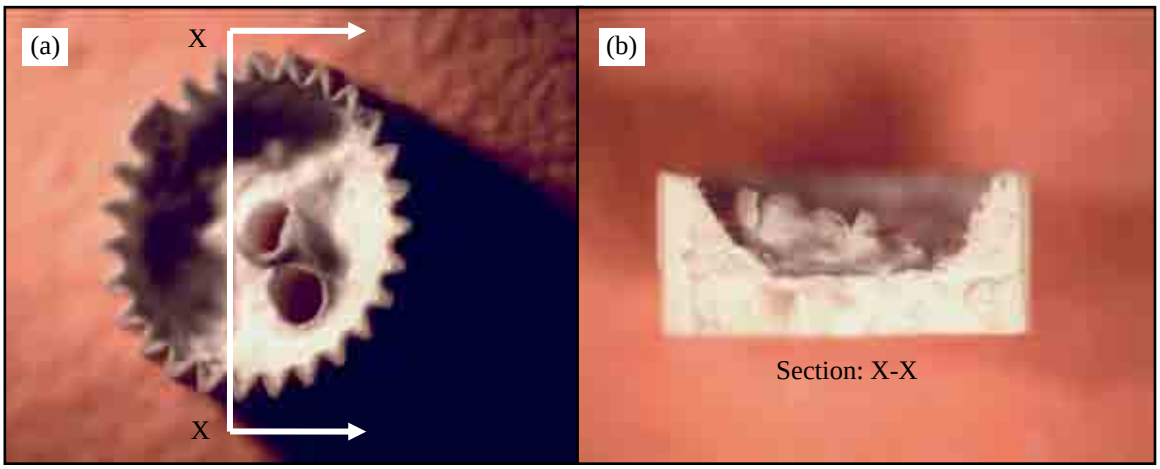

Figure 7.15. Optical images of green alumina microgear with concave top surface using low solid loading.

On the basis of the obvious shrinkage resulting a concave top surface, a new fabrication procedure was designed to form YSZ8/Al_2O_3 functionally graded layers as shown in Figure 7.16. The fabrication procedure is described in the following steps.

1. The first green layer is deposited by filling the PDMS cavities of the microcomponents with a low solid loading suspension.

2. The mould is left to dry, leaving the first semi dried green layer as the shell covering both the bottom and the sidewalls.

3. The core is formed by casting the second suspension over the first layer in the mould, followed by another drying process. It results in two semi dried materials in layers.

4. The outer layer is completed by casting the first suspension again with a high solid loading over the formed layers.

5. Once the mould is completely dry, the green parts are achieved by carefully bending the soft PDMS mould and then are peeled out with thin tweezers.

6. The green microcomponents are sintered using heating cycle presented in Chapter 4.

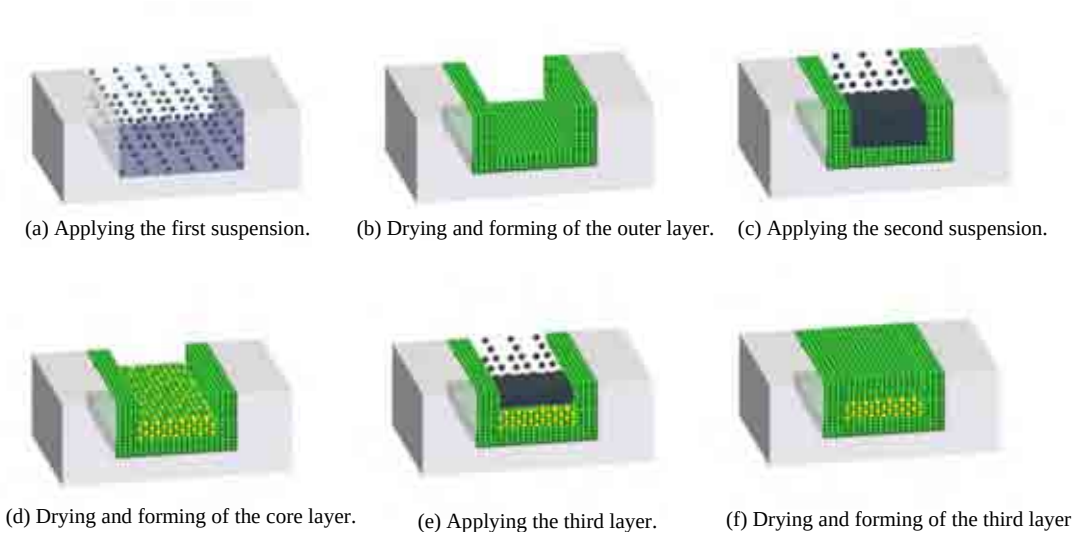

(a) Applying the first suspension. (b) Drying and forming of the outer layer. (c) Applying the second suspension.

(d) Drying and forming of the core layer. (e) Applying the third layer. (f) Drying and forming of the third layer

Figure 7.16. Schematic diagram of FGM microcomponents layers formation.

7.3.2 Results

7.3.2.1 Shrinkage Behaviour of the Green Layers

In the fabrication process, it is important to avoid differences in drying shrinkage between consecutive layers. A large difference in the linear shrinkage of two layers during drying induces residual stress, resulting in either cracks or distortion, as shown in Figure 7.17.

To reduce the effect of drying shrinkage between layers, the amount of dispersant that induces less difference in drying shrinkage between layers is chosen as the optimum amount. Drying shrinkage for both alumina and YSZ8 powders with particle size of 0.7 μm and 2.0 μm respectively was investigated in Chapter 5 and is analysed here again to obtain a new dispersant concentration suitable for formation of FGM layers.

Figure 7.18 shows the relationships between the drying shrinkages of both alumina with 0.7 μm particles and YSZ8 with 2 μm particles with respect to dispersant concentration. As

shown in the figure, the drying shrinkage of alumina initially decreases sharply as D-3005 concentration increases from 0 to ~ 7 mg/g and reaches the minimal value of 2.5% when D-3005 concentration is 11.8. The minimum shrinkage of YSZ8 can be found as 3.1% when D-3005 concentration is 20.6 mg/g. Any further addition of the dispersant does not affect the shrinkage with significant amount. The essential requirement for crack free green layers is that the linear shrinkage of each green layer after drying should remain at similar value. By optimizing the dispersant concentration in the suspension, it is found that at dispersant concentration of about 5.15 mg/g the difference in the drying shrinkage between layers is less than 0.5%. On the other hand, at this concentration, the green densities are 56.7% and 55.1% for alumina and zirconia, respectively. Cracks in the green microgears obtained after optimising dispersant concentration with respect to drying shrinkage were significantly reduced as shown in Figure 7.19.

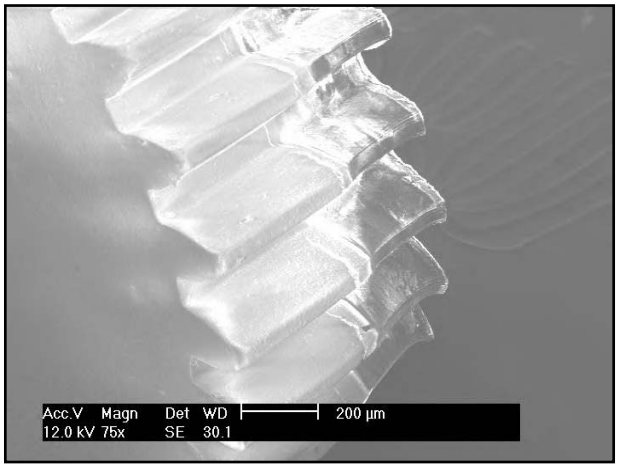

Figure 7.17. An SEM image of distorted green YSZ8/Al_2O_3 functionally graded ceramic composite microgear with visible cracks.

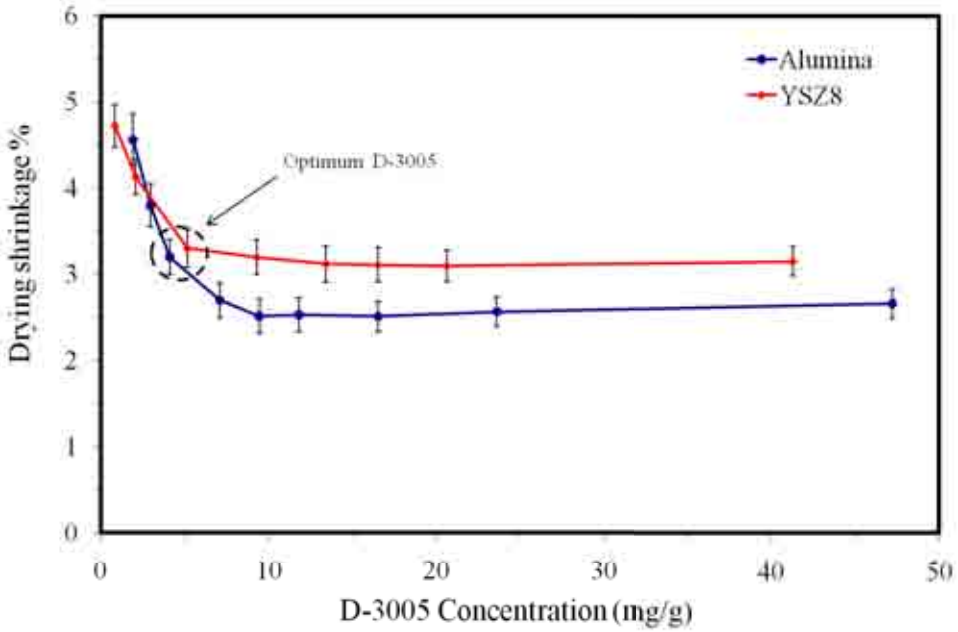

Figure 7.18. The dry shrinkage of different Al_2O_3/8YSZ composition as a function of the dispersant concentration.

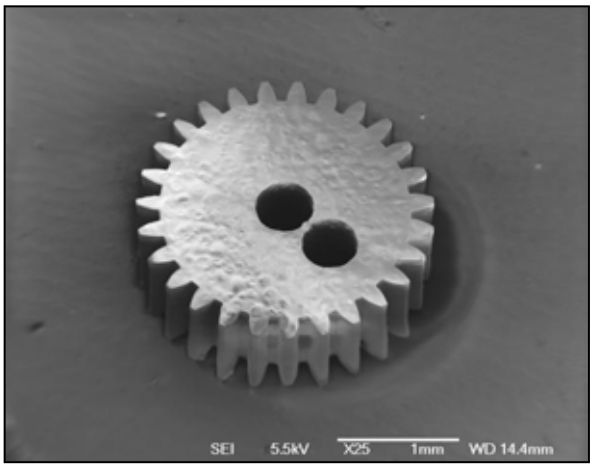

Figure 7.19. An SEM image of green YSZ8/Al_2O_3 functionally graded ceramic composite microgear without visible cracks.

7.3.2.2 Thermal Behaviour During Sintering

A fundamental principle for forming green FGM layers is to achieve nearly equal dimension changes between green layers. Apart from the shrinkage during the drying process, the change in the transient dimensions of different layers during sintering process should be also remaining in similar value.

To explain this, it is important to discuss the thermal behaviour of alumina and zirconia mentioned in the literature [171]. Figure 7.20 depicts the transient length changes of alumina and zirconia green bodies during sintering process. In the literature, alumina green body formed using alumina powder with an average size of 0.26 µm. In addition, zirconia green parts fabricated using zirconia powders with average sizes of 0.63 µm and 1.02 µm for type 1 and type 2 respectively. Thermal shrinkage of the chosen materials was determined using a dilatometer. The following can be concluded from the figure. First, sintering behaviour of each material has a unique densification start temperature, densification rate, and dimensional change owning to different thermal expansion coefficients, porosity content, particle sizes, shape and composition. Second, thermal expansion can be noticed below the starting densification temperature and it is considered low when compared to the shrinkage during densification. Third, shrinkage during cooling down of the specimens is small when compared to the total shrinkage.

Dimensional differences within the gradient result in the formation of undesired stresses, which lead to fracture or cracks at layer interfaces. To avoid complications associated with cracks between dissimilar layers, these undesirable stresses must be minimized by controlling the layers transient dimensions during sintering [170].

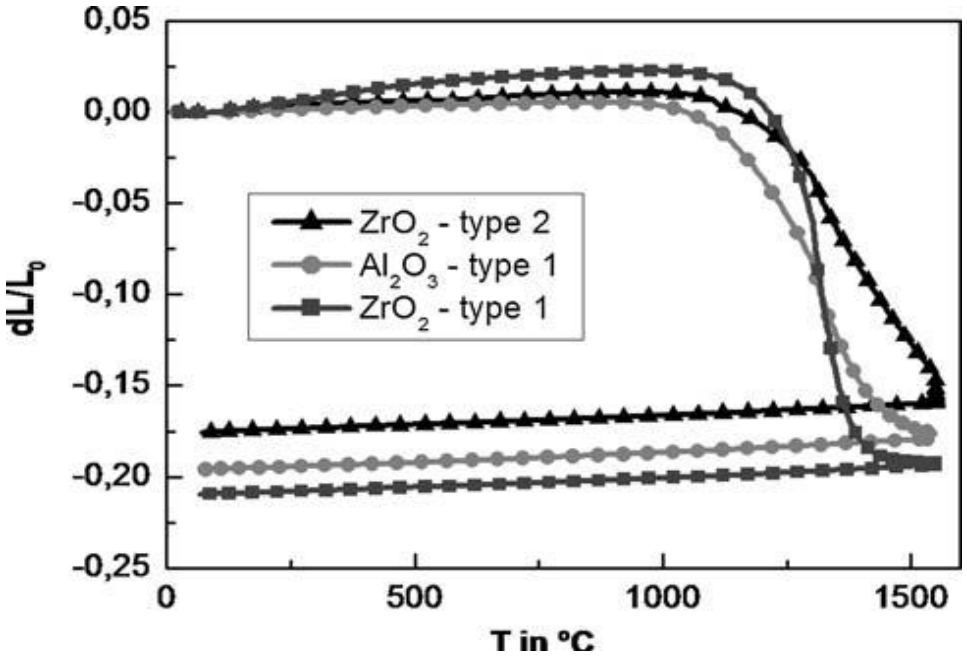

Figure 7.20. Relative length changes of alumina and zirconia during sintering [171].

In one experiment, a three layer microgear in Al_2O_3, 50% Al_2O_3/50% YSZ8, 100% YSZ8 FGM shows severe cracks between layers, as shown in Figure 7.21. The picture is an SEM image where cracks are clearly visible after sintering.

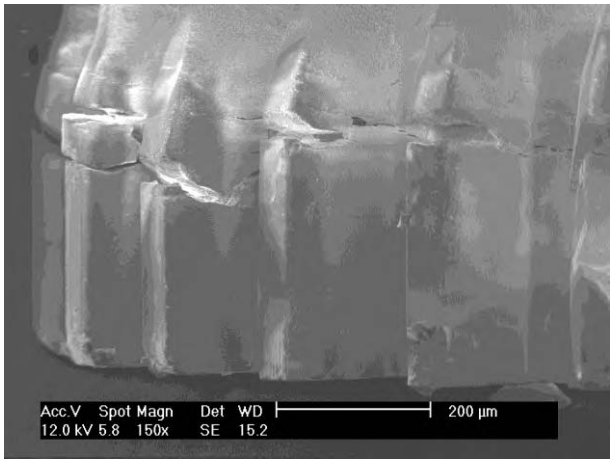

Figure 7.21. An SEM image of cracked sintered YSZ8/Al_2O_3 functionally graded ceramic composite microgear encountered during sintering.

To overcome sintering mismatch between layers, shrinkage properties of different YSZ8/Al_2O_3 compositions were studied.

Due to the unavailability of a dilatometer equipped with the sintering furnace, a manual technique was proposed to measure shrinkage behaviour of the samples in the sintering process. The proposed technique neglects dimensions change below 600 °C and during cooling down of the measured samples, as concluded from the literature [171]. The proposed technique was performed as the follows.

1. Green microcomponents were formed with five different alumina and zirconia compositions, with each composition, at least 10 green microgears were made for tests. The compositions of the samples prepared are 0 % A0.7/ 100% YSZ8, 20 % A0.7/ 80% YSZ8, 40 % A0.7/ 60% YSZ8 70 % A0.7/ 30% YSZ8, 100 % A0.7/ 0% YSZ8. Ten microgears were

2. The samples were placed in a chamber furnace as described in Chapter 4 for sintering. and heated up to the final temperature.

3. The temperature was increased from room temperature to 600 °C at rate of 1 °C /min. Next, it was increased to their respective final temperatures at a rate of 4 °C /min. Afterwards, the furnace was turned off and the samples were left to cool down naturally. The final temperatures were set from 600 °C to 1600 °C with a 100 °C step temperature.

4. The measurements were performed using fresh green samples at each sintering temperature.

5. The linear shrinkage was calculated based on the difference of the outer diameter of the microgears before and after sintering.

This study was done on the prepared samples where the diameter was measured using digital vernier caliper with a resolution of 0.01 mm. Sintered shrinkage was calculated from Equation 7.2 as follows.

$$\text{Sintering shrinkage } \% = \frac{OD_g - OD_s}{OD_g} \times 100 \qquad \text{Eq. 7.2}$$

where:

OD_g is the outer diameter of the green microgear.

OD_g is the outer diameter of the sintered microgear.

Figure 7.22 shows shrinkage behaviour during the sintering process of each group composite samples. It can be clearly seen that YSZ8/Al_2O_3 samples with different compositions have different shrinkage after sintering at different temperature. When sintering temperature was higher than 1000 °C, the differences in shrinkage increased sharply, and then the increase in shrinkage slows down from about 1400-1500 °C and upward. A the same time, it can be clearly seen that sintering shrinkage of YSZ8 is higher than of Al_2O_3.

From the analysis of sintering shrinkages of different YSZ8/Al_2O_3 composites, optimized compositions of different layers can be obtained in terms of the minimum sintering shrinkage difference between adjacent layers. It can be concluded that adjacent layers that exhibit less shrinkage difference are 100 % A0.7/ 0 % YSZ8 and 20 % A0.7/ 80 % YSZ8. As shown in Figure 7.22, the selected compositions begin the densification at about 1100

°C and then the rate of the change remains the same from that point and up to 1400 °C. The similarity of shrinkage rate for those chosen powder compositions ensures that no significant dimensional mismatch could occur during densification, thus reducing the possibility to form cracks. This approach has significantly reduced cracks during sintering and the sintered functionally graded ceramic composite microgears fabricated using the optimized dispersant concentration, optimum layers composition and sintered at 1500 °C were successfully obtained without visible cracks, as shown in Figure 7.23.

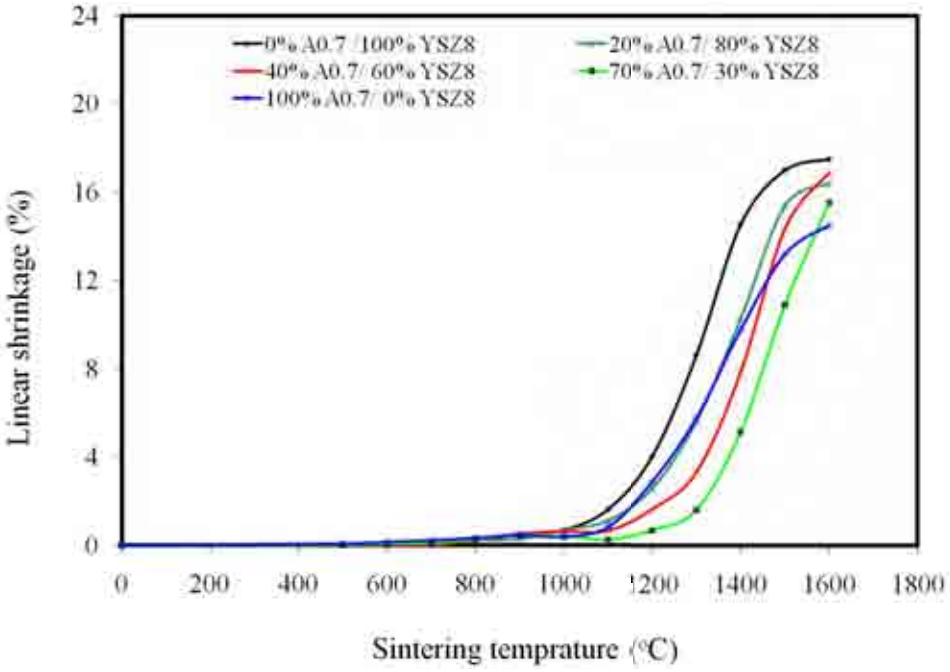

Figure 7.22. Linear shrinkage of Al_2O_3 and YSZ8 of different composition in relation with the sintering temperature.

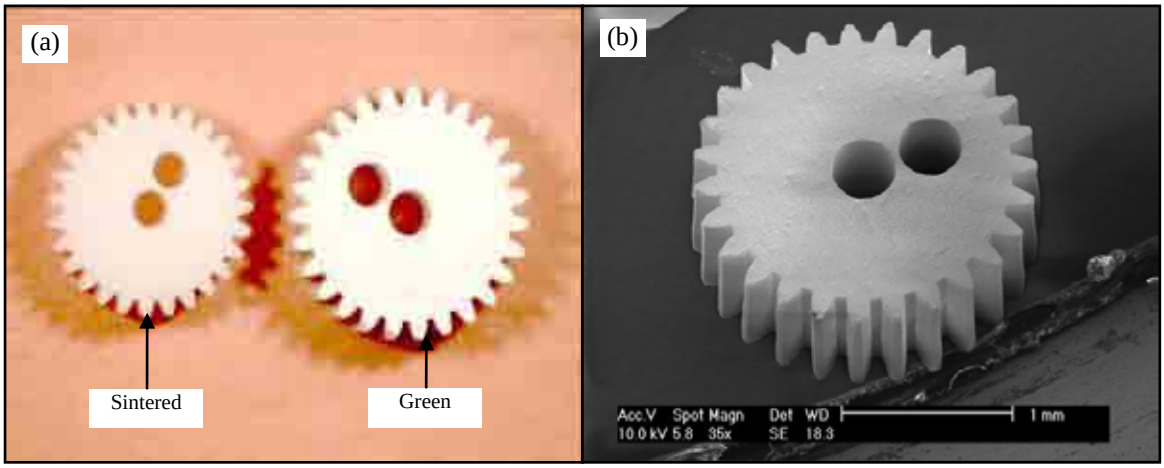

Figure 7.23. Optical and SEM images of green and sintered YSZ8/Al_2O_3 functionally graded ceramic composite microgears.

7.3.2.3 Microstructure of FGM Microcomponents

In the microstructure investigation of the fabricated FGM samples, sintered microgears were polished to remove the top alumina layer. Afterwards, the polished microgears were cleaned with acetone and then thermally etched at about 1250 °C. The samples were examined using backscattered scanning microscope to check the formation of different layers and internal cracks. Figure 7.24 presents a fabricated FGM microgear, while EDS analysis of the dark and bright grains are presented in Figure 7.25. The dark grains represent alumina while the bright grains zirconia. Figure 7.24 shows a BSE images of the polished FGM microgear sample. Generally, the cross section exhibits a dark Al_2O_3 shell and a brighter 20% Al_2O_3 - 80% 8YSZ core. It can be seen that there is no visible cracks found. Moreover, alumina dark shell can be clearly identified at all teeth of the microgear. However, small alumina spots were found inside the microgear YSZ8 core. In details, at magnifications of 141x and 380x, Figures 7.24(a) and (b) show gears with identified shell-core layers and no observed cracks were found. With further increase of magnifications to

1480x and 2000x, Figures 7.24(c)-(d) show clearly the shell-core interface at different position of the microgear tooth. Again, at these high magnifications, no cracks are identified between Al_2O_3 and 20% Al_2O_3 - 80% 8YSZ interface. It can also be seen that the shell thickness is not uniform through the circumference of the cross section. It is thick at concave features, such as gear teeth. This may be due to the capillary force of the suspension in thin features, which promotes the adhesion of the ceramic suspension in these parts of the mould.

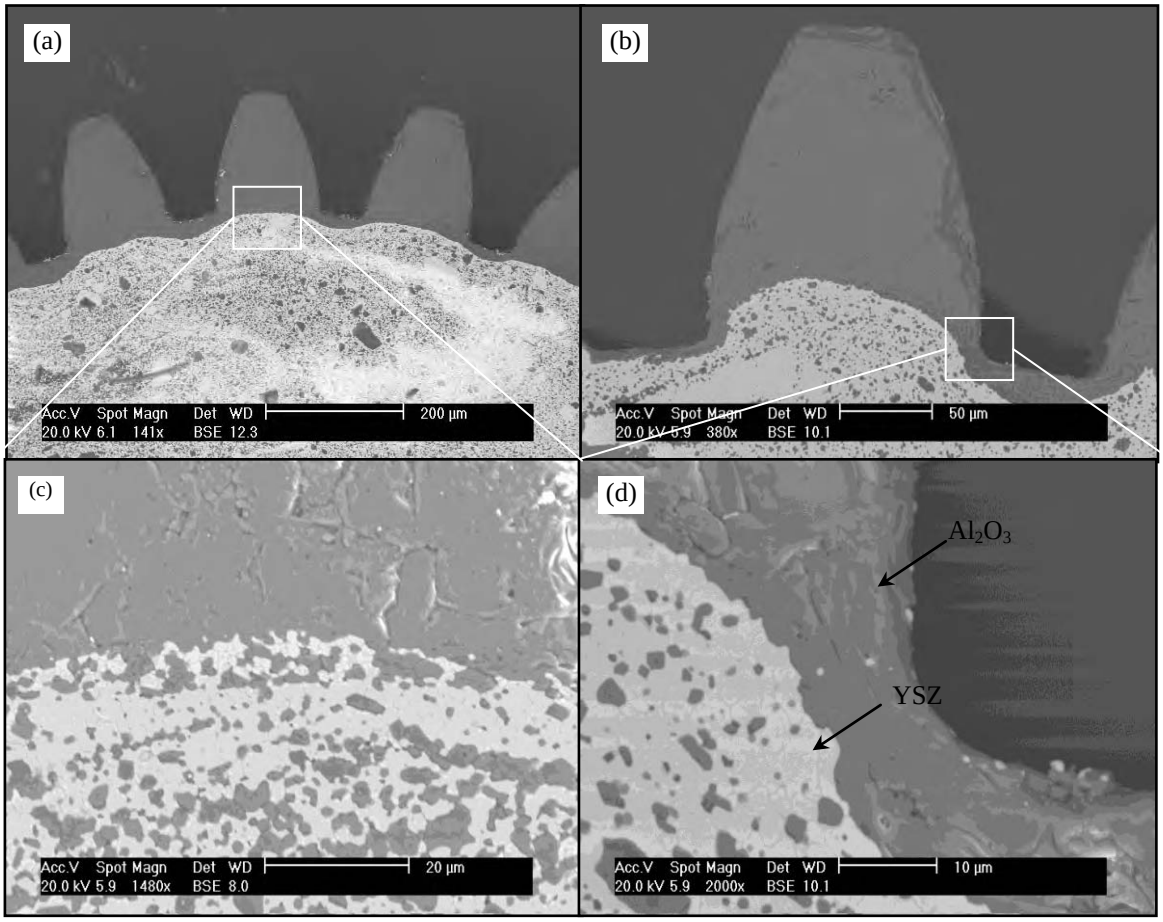

Figure 7.24. BSE images of FGM microgear cross section with different magnification.

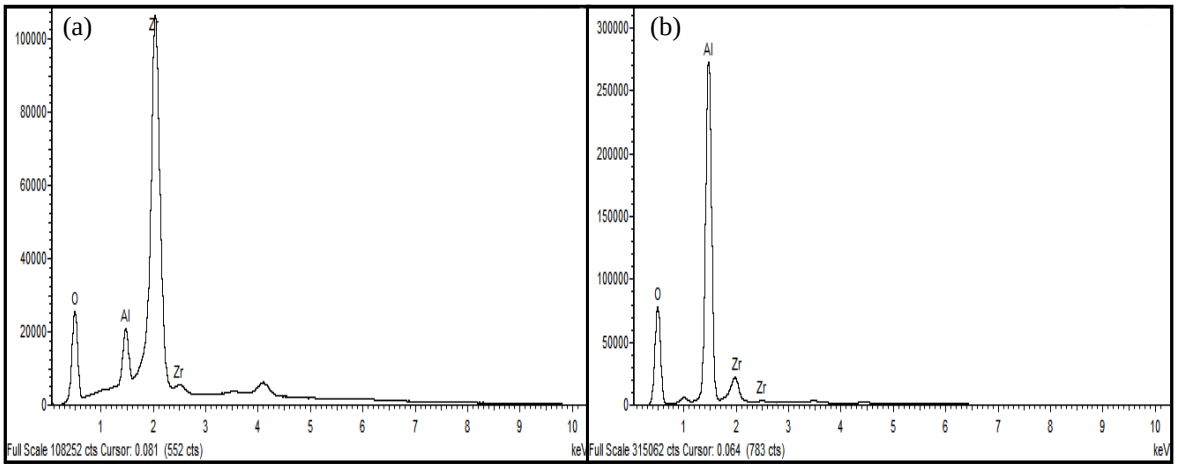

Figure 7.25. EDS analysis of Al_2O_3/YSZ8 FGM composite microcomponents (a) bright regions, (b) dark region.

7.3.3 Discussion

A novel technique is proposed to fabricate functionally graded ceramic composite microcomponents with alumina shell and YSZ8 composite core. During the experiments, cracks were observed between adjacent layers. The differences in drying shrinkage and sintered shrinkage between these layers are found to be responsible for the cracks. Altering the colloidal powder processing and manipulating powder characteristics by mixing powders with distinct properties are an effective approach to solve these problems. Consequently, various dispersant concentrations have yielded varying degrees of drying shrinkage. While, different powder mixtures were used to change sintering characteristics. Using optimum dispersant concentration significantly reduces cracks in the green parts. On the other hand, 100% A0.7/ 0% YSZ8 and 20% A0.7/ 80% YSZ8 layers were found to have similar sintering behaviour. The shrinkage curves of the chosen powder mixtures were found to be almost identical under the optimized sintering conditions and up to 1400 °C. The microstructural analysis of the optimum compositions showed clearly distinct shell-core layers with no apparent cracks and well-sintered interface. In addition, it was

observed that the YSZ8 composite core have few alumina spots. This is an indication of inhomogeneous core. As the dispersion technique were previously proven successful, it is expected that this spots were formed during the casting of different layers, which may be an indication of a less controllable casting technique at a micro scale level. However, these spots do not cause cracks. Therefore, crack free FGM microgears were successfully obtained with alumina shell and YSZ8 composite core. It is anticipated that microcomponents fabricated with the proposed functional microstructures will have applications where more than one property is needed in a microcomponent device.

7.4 Summary

In this chapter, research into net shaping YSZ8/Al_2O_3 composite microcomponents is introduced. Two different types of composites were proposed, fabricated and characterised. The first is zirconia matrix alumina nanocomposite microcomponents, where alumina nano particles are homogenously dispersed in nano scale into YSZ8 matrix. The second is functionally graded zirconia alumina composite microcomponents with alumina shell and YSZ8 composite core. In each type of composite, the fabrication process was proposed and adopted to overcome identified problems. Characterization of the resultant composite microcomponents was studied in terms of composite fabrication process, green and sintered properties. It can be concluded that, the proposed fabrication techniques are not only able to produce monolithic ceramic microcomponents with excellent properties, but also can be used to produce tuneable composite microcomponents after modification. Both types of composites proposed in this chapter are able to produce microcomponents with desired properties according to the application.

CHAPTER 8: CONCLUSIONS AND FUTURE WORK

8.1 Conclusions

This PhD project is aimed at filling the technical gap in precision fabrication by developing a novel approach of high precision ceramic fabrication processes suitable for mass production, and to meet the particular needs of microengine development. The research has involved fabrication of master and soft moulds, fabrication of alumina and zirconia microcomponents using different slurry systems, effect of colloidal processing on prepared slurry, green and sintered microcomponents and fabrication of zirconia/alumina composite microcomponents.

The significant contributions of the ceramic microfabrication research can be summarised as follows.

A. Fabrication of reinforced PDMS with a surfactant-treated surface as master mould.

PDMS replicas were successfully obtained by casting of PDMS onto reinforced PDMS surface treated with surfactant solutions used as release agents. Both the reinforced master and the replicas structure remained unharmed and the proposed PDMS master can be used repeatedly in several processes.

B. Fabrication of alumina and zirconia microcomponents using paraffin wax-based slurry in a PDMS mould.

A novel approach to fabricate dense net shape alumina and zirconia microcomponents successfully introduced by direct casting of low temperature paraffin wax-based slurry into a PDMS mould with the aid of manual and vacuum filling, demoulding, optimized debinding and sintering steps. This is in contrast with microinjection moulding method, where wax-based feedstock is injected into micro moulds either by high or low pressure injection moulding.

C. Fabrication of zirconia microcomponents using water-based slurry with optimum properties.

Water-based slurry was adopted to fabricate dense net shape zirconia microcomponents with good physical and mechanical properties.

D. Fabrication of nanocomposite microcomponents with zirconia matrix and alumina nanoparticles

Composite microcomponents with zirconia matrix and alumina nanoparticles have been successfully obtained with homogenous and dispersed alumina into zirconia matrix.

E. Fabrication of zirconia/alumina functionally graded composite microcomponents.

A novel approach to combine irreconcilable properties of zirconia and alumina in the same microcomponents has been developed. Microcomponents with zirconia core and alumina outer layer were successfully fabricated.

Through repeated fabrication cycles and vigorous characterization, all the project objectives have been met. The following conclusions can be drawn from the research.

1. SU-8 and reinforced PDMS master moulds and PDMS soft moulds prove successful in satisfying the fabrication requirements in terms of geometry control, sidewall profile and surface roughness.

2. Water based slurry is superior when compared to solvent and paraffin wax based slurries for fabrication of net shape ceramic and ceramic composite microcomponents with higher sintered properties.

3. Net shape ceramic and ceramic composite microcomponents can be fabricated by altering water based slurry colloidal properties. The process is successful in obtaining alumina and zirconia highly stable and dispersed slurries, dense green and sintered microcomponents. In addition, by applying the approach to ceramic composite, well dispersed and homogenous alumina nano particles in zirconia matrix are achieved.

4. 0.7 μm alumina powder and 2 μm yttria stabilised zirconia powder are preferred for their excellent physical and mechanical properties of the resultant microcomponents when compared to larger powders.

5. Sintering temperatures of 1600 °C and 1550 °C are found to be optimum for both alumina and yttria stabilised zirconia microcomponents respectively. Microcomponents sintered at these temperatures have optimum properties.

6. Addition of alumina nano particles into the YSZ microcomponents improves density and micro hardness of the resultant nanocomposite microcomponents. In addition, it improves YSZ sintered phases to a pure tetragonal.

7. Controlling green and sintered shrinkage plays a key role for achieving crack free functionally graded composite microcomponents.

Based on the experimental and analysis work presented in this thesis, the fabrication processes prove to be effective, repeatable and yield high quality ceramic microcomponents, both in shape retention and in material properties. Thus, project aims have been successfully met. The methodology and analysis adopted in the research adequate in leading to the projects aims. The fabrication processes developed in the research are applicable for other high strength power MEMS devices, such as micro turbines and micro pumps. In addition, they can be used in place of other materials such as metals, plastics and polymers. These processes can be further developed for bigger and more complicated shapes, and thus have wider applications.

8.2 Suggestions for Future Work

This thesis represents a comprehensive research efforts performed to explore ceramic and ceramic composite microfabrication options for microengines. As such, it should be viewed as a solid foundation for further work. Future research is needed either to expand more applications or to complete works initiated in this PhD project but has not been completed because they are well beyond the project scope.

The following is a list of further research topics, which are identified:

1. This thesis introduces the use of solvent based slurry with a preceramic polymer as a binder in a colloidal processing for the first time. The use of preceramic polymer as the binder and as the additive of ceramic inclusion within the sintered ceramic matrix is very promising in composite ceramics. The unavailability of high temperature tube furnace is one of the problems that limited the work within the proposed solvent based

slurry. Although the initial results have revealed low density when the sintering occurs at 1500 °C in nitrogen, it is expected that the density will improve if the samples are sintered at higher temperatures (1700 °C -1800 °C) to form crystalline $Si_xC_xN_x$ compounds within the alumina or zirconia matrix.

2. In this study, YSZ/Al_2O_3 composite microcomponents have shown enhanced properties. X-ray diffraction analysis shown the peak intensities of the tetragonal reflections were dramatically improved compared with those of previous results of pure YSZ8. Further examination is needed to detect the unconfirmed phase found in the YSZ8. This could be obtained by tracing phase change in both YSZ and YSZ/Al_2O_3 starting from the supplied powders and throughout different heating temperatures.

3. Adding metallic nano particles into ceramic matrix is not studied yet. It is expected to enhance flexural strength and modules of elasticity of the resultant microcomponents.

4. This thesis represents the first practice in FGM microcomponent fabrication. Further improvement on functionally graded composite microcomponents can be achieved by accurate control of thermal behaviour during sintering and by establishing more homogenous and controlled layers. Meanwhile, continues change in materials can be developed to reduce the stress between two materials and hence to eliminate cracking problems.

5. The proposed FGM microcomponents approach could be extended to cover joining and assembling techniques of MEMS parts fabricated from different materials.

6. This work could be extended to fabricate ceramics with nano features. The ceramic components with nano features can be used as master moulds in nanoimprinting and used in ceramic sensors.

7. The research group at University of Birmingham is developing a ceramic micro gas turbine engine with an indicating power of 1 kW. The microturbine of the engine will be able to withstand high stress and temperature and the fabrication processes presented in this thesis will be used and extended for making the turbine. The author has started the preliminary experiments in producing a 3D alumina ceramic compressor and good results have been achieved. The fabrication process was performed with modification in slurry, moulding and demoulding processes to overcome the difficulties of such complex 3D shape compressor and the result is shown in Figure 8.1.

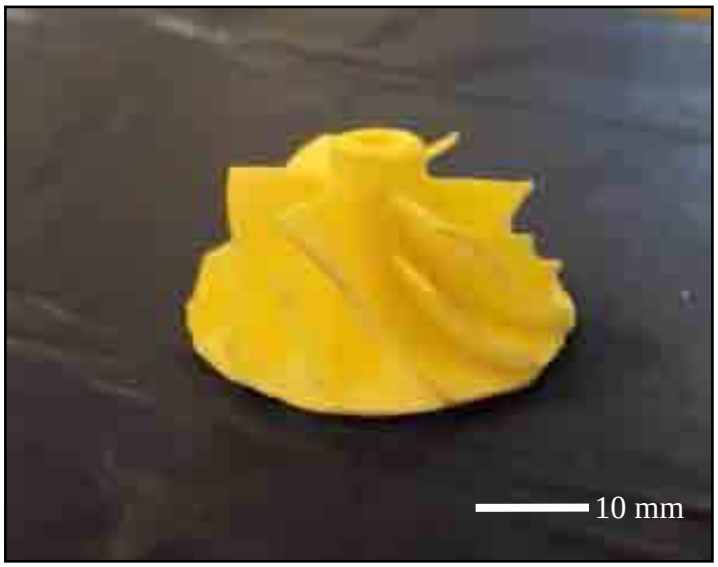

Figure 8.1. Optical image of alumina compressor fabricated using modified soft lithographic process.

REFERENCES

[1] Peng, J., Jiang, K. & Nianjun, S. Microfabrication of ultra-thick SU-8 photoresist for microengines. In Micromachining and Microfabrication Process Technology VII, 27-29 Jan. 2003, 105-110.

[2] Han Lee, C. Micro wankel engine and its metallic components fabrication. PhD thesis, University of Birmingham, 2008.

[3] Xueyong, W. Electroforming nanoparticulate strengthened microcomponents and metallic nanostructures. PhD thesis, University of Birmingham, 2009.

[4] Imbaby, M. Fabrication of 316-L stainless steel and composite micro machine components using softlithography and powder metallurgy process. PhD thesis, University of Birmingham, 2010.

[5] Moon, H. S., Anand, L. & Spearing, S. M. A constitutive model for the mechanical behavior of single crystal silicon at elevated temperature. In Materials Science of Microelectromechanical Systems (MEMS) Devices IV, November 25, 2001 - November 28, 2001, 279-284.

[6] Walters, D. Creep characterisation of single crystal silicon in support of the MIT micro-engine project. Masters of science thesis, Massachusetts institute of technology, 1995.

[7] Savoulides, N. Development of a MEMS turbocharger and a gas turbine engine. PhD thesis, Massachusetts institute of technology, 2000.

[8] Edirisinghe, M. J. Solid freeform fabrication of ceramics. In TMS Fall Meeting, 2001, 139-149.

[9] Tay, B. Y., Evans, J. R. G. & Edirisinghe, M. J. Solid freeform fabrication of ceramics. International Materials Reviews 48, 2003, 341-370.

[10] Heinrich, J. G. New developments in the solid freeform fabrication of ceramic components. CFI - Ceramic Forum International - Berichte der Deutschen Keramischen Gesellschaft 76, 1999, 29-35.

[11] Cawley, J. D. Solid freeform fabrication of ceramics. Current Opinion in Solid State and Materials Science 41, 999, 483-489.

[12] Bertsch, A., Jiguet, S. & Renaud, P. Microfabrication of ceramic components by microstereolithography. Journal of Micromechanics and Microengineering 14, 2004, 197-203.

[13] Licciulli, A., Corcione, C. E., Greco, A., Amicarelli, V. & Maffezzoli, A. Laser stereolithography of ZrO_2 toughened Al_2O_3. Journal of the European Ceramic Society 25, 2005, 1581-1589.

[14] Asberg, B. et al. Feasibility of design in stereolithography. Algorithmica 19, 1997, 61-83.

[15] Chu, G. T. M. et al. Ceramic SFF by direct and indirect stereolithography. Materials Research Society Symposium - Proceedings 542, 1999, 119-123.

[16] Chartier, T., Chaput, C., Doreau, F. & Loiseau, M. Stereolithography of structural complex ceramic parts. Journal of Materials Science 37, 2002, 3141-3147.

[17] Zhou, W., Li, D. & Wang, H. A novel aqueous ceramic suspension for ceramic stereolithography. Rapid Prototyping Journal 16, 2010, 29-35.

[18] Arif, K. & Murakami, T. Slant beam rotation UV scanning to eliminate stair-steps in stereolithography fabrications. International Journal of Advanced Manufacturing Technology 41, 2009, 527-537.

[19] Bertsch, A., Jiguet, S., Bernhard, P. & Renaud, P. Microstereolithography: a review. In Rapid Prototyping Technologies Symposium, 3-5 Dec. 2002, 3-15.

[20] Yoshinari, M., Weiwu, C. & Soshu, K. Smart processing of 3D micro ceramic devices by CAD/CAM micro-sterolithography and sintering. Transactions of JWRI 36, 2007, 57-60.

[21] Agarwala, M. K. et al. Structural quality of parts processed by fused deposition. Rapid Prototyping Journal 2, 1996, 4-19.

[22] Bellini, A. & Guceri, S. Mechanical characterization of parts fabricated using fused deposition modeling. Rapid Prototyping Journal 9, 2003, 252-264.

[23] Bellini, A., Shor, L. & Guceri, S. I. New developments in fused deposition modeling of ceramics. Rapid Prototyping Journal 11, 2005, 214-220.

[24] Kalita, S. J., Bose, S., Hosick, H. L. & Bandyopadhyay, A. Development of controlled porosity polymer-ceramic composite scaffolds via fused deposition modeling. Materials Science and Engineering C 23, 2003, 611-620.

[25] Bai, P.-K., Cheng, J. & Liu, B. Selective laser sintering of polymer-coated $Al_2O_3/ZrO_2/TiC$ ceramic powder. Transactions of Nonferrous Metals Society of China (English Edition) 15, 2005, 261-265.

[26] Shen, L. D., Huang, Y. H., Tian, Z. J. & Hua, G. R. Direct fabrication of bulk nanostructured ceramic from nano- Al_2O_3 powders by selective laser sintering. Key Engineering Materials 329, 2007, 613-618.

[27] Waetjen, A. M., Polsakiewicz, D. A., Kuhl, I., Telle, R. & Fischer, H. Slurry deposition by airbrush for selective laser sintering of ceramic components. Journal of the European Ceramic Society 29, 2009, 1-6.

[28] Exner, H. et al. Laser micro sintering: A new method to generate metal and ceramic parts of high resolution with sub-micrometer powder. Virtual and Physical Prototyping 3, 2008, 3-11.

[29] Bender, B. A., Rayne, R., Wu, C., Kim, C. & Bruce, R. W. Solid freeform fabrication of PZT ceramics via an automated tape laminated object manufacturing system. American Ceramic Society, 2004, 193-204.

[30] Zhang, Y., He, X., Han, J. & Du, S. Ceramic green tape extrusion for laminated object manufacturing. Materials Letters 40, 1999, 275-279.

[31] Weisensel, L., Travitzky, N., Sieber, H. & Greil, P. Laminated object manufacturing (LOM) of SiSiC composites. Advanced Engineering Materials 6, 2004, 899-903.

[32] Zhang, Y., He, X., Du, S. & Zhang, J. Al_2O_3 ceramics preparation by LOM (laminated object manufacturing). International Journal of Advanced Manufacturing Technology 17, 2001, 531-534.

[33] Windsheimer, H., Travitzky, N., Hofenauer, A. & Greil, P. Laminated object manufacturing of preceramic-paper-derived Si-SiC composites. Advanced Materials 19, 2007, 4515-4519.

[34] Klosterman, D., Chartoff, R., Osborne, N. & Graves, G. Laminated object manufacturing, a new process for the direct manufacture of monolithic ceramics and continuous fiber CMCs. Ceramic Engineering and Science Proceedings 18, 1997, 113-120.

[35] Seitz, H., Rieder, W., Irsen, S., Leukers, B. & Tille, C. Three-dimensional printing of porous ceramic scaffolds for bone tissue engineering. Journal of Biomedical Materials Research - Part B Applied Biomaterials 74, 2005, 782-788.

[36] Sachs, E. et al. CAD-casting: direct fabrication of ceramic shells and cores by three dimensional printing. Manufacturing Review 5, 1992, 117-126.

[37] Sachs, E., Cima, M. & Bredt, J. Three-dimensional printing of ceramic shells and cores for metal casting. ASME, 1991, 61-72.

[38] Hanafusa, A., Yamashita, Y. & Yasuda, M. Three-dimensional routing for multilayer ceramic printed circuit boards. IEEE Comput. Soc. Press, 1990, 386-389.

[39] Prakasan, K., Prasad, P. S. R. K., Reddy, A. V., Rajesh, P. K. & Ponnambalam, P. Studies on rheology of ceramic inks and spread of ink droplets for direct ceramic ink jet printing. Journal of Materials Processing Technology 176, 2006, 222-229.

[40] Somasundaram, R., Kanagaraj, R. & Kalakkath, P. Dynamic characteristics of drop-substrate interactions in direct ceramic ink-jet printing using high speed imaging system. Defence Science Journal 59, 2009, 675-682.

[41] Ponnambalam, P., Ramakrishnan, N., Rajesh, P. K. & Prakasan, K. Rheological behaviour of ceramic inks for direct ceramic ink jet printing. Defence Science Journal 56, 2006, 279-288.

[42] Teng, W. D. & Edirisinghe, M. J. Development of ceramic inks for jet printing: Effect of conductivity. Key Engineering Materials 132-136, 1997, 337-340.

[43] Hill, S. Micromoulding - a small injection of technology. Materials World 9, 2001, 24-25.

[44] Griffiths, C. A., Dimov, S. S., Brousseau, E. B. & Hoyle, R. T. The effects of tool surface quality in micro-injection moulding. Journal of Materials Processing Technology 189, 2007, 418-427.

[45] Stone, V. N. et al. Free flow isotachophoresis in an injection moulded miniaturised separation chamber with integrated electrodes. Journal of Chromatography A 1155, 2007, 199-205.

[46] Hill, S. D. J. et al. An investigation of computer modelling for micro-injection moulding. Comput. Mech. Publications, 1995, 275-283.

[47] Ju Hyun, Y. & Wei, G. Near-net ceramic micro-tubes fabricated by electrophoretic deposition process. International Journal of Modern Physics B 17, 2003, 1147-1151.

[48] Sarkar, P., Prakash, O., Wang, G. & Nicholson, P. S. Micro-laminate ceramic/ceramic composites (YSZ/ Al_2O_3) by electrophoretic deposition. Ceramic Engineering and Science Proceedings 15, 1994, 1019-1027.

[49] Von Both, H., Dauscher, M. & Hauelt, J. Fabrication of microstructured ceramics by electrophoretic deposition of optimized suspensions. American Ceramic Society 3, 2004, 135-140.

[50] Bonnas, S., Ritzhaupt-Kleissl, H.-J. & Hauelt, J. Electrophoretic deposition for fabrication of ceramic microparts. Journal of the European Ceramic Society 30, 2010, 1159-1162.

[51] Laubersheimer, J., Ritzhaupt-Kleissl, H. J., Hausselt, J. & Emig, G. Electrophoretic deposition of sol-gel ceramic microcomponents using UV-curable alkoxide precursors. Journal of the European Ceramic Society 18, 1998, 255-260.

[52] Van Hoy, C., Barda, A., Griffith, M. & Halloran, J. W. Microfabrication of ceramics by co-extrusion. Journal of the American Ceramic Society 81, 1998, 152-158.

[53] Kaya, C., Butler, E. G. & Lewis, M. H. Microfabrication of Al_2O_3/ZrO_2 bi-phase ceramics with continuous fibrillar microstructure by co-extrusion. Journal of Materials Science Letters 22, 2003, 357-361.

[54] Wert, J. A., Thomsen, C., Jensen, R. D. & Arentoft, M. Forming of bulk metallic glass microcomponents. Journal of Materials Processing Technology 209, 2009, 1570-1579.

[55] Brittain, S., Paul, K., Xiao-Mei, Z. & Whitesides, G. Soft lithography and microfabrication. Physics World 11, 1998, 31-36.

[56] Xia, Y. & Whitesides, G. M. Vol. 28 Annual Review of Materials Science, 1998, 153-184.

[57] Rogers, J. A. & Nuzzo, R. G. Recent progress in soft lithography. Materials Today 8, 2005, 50-5.

[58] Brehmer, M., Conrad, L. & Funk, L. New developments in soft lithography. Journal of Dispersion Science and Technology 24, 2003, 291-304.

[59] Heule, M., Schonholzer, U. P. & Gauckler, L. J. Patterning colloidal suspensions by selective wetting of microcontact-printed surfaces. Journal of the European Ceramic Society 24, 2004, 2733-2739.

[60] Lee, J.-H., Hon, M.-H., Chung, Y.-W. & Leu, I.-C. Microcontact printing of organic self-assembled monolayers for patterned growth of well-aligned zno nanorod arrays and their field-emission properties. Journal of the American Ceramic Society 92, 2009, 2192-2196.

[61] Nagata, H. et al. Microcontact printed BaTiO3 and $LaNiO_3$ thin films for capacitors. Journal of the American Ceramic Society 89, 2006, 2816-2821.

[62] Obreja, P., Cristea, D., Dinescu, A. & Gavrila, R. Replica molding of polymeric components for microsystems. IEEE, 2009, 4.

[63] Reinhardt, C., Passinger, S., Zorba, V., Chichkov, B. N. & Fotakis, C. Replica molding of picosecond laser fabricated Si microstructures. Applied Physics A (Materials Science Processing) A87, 2007, 673-677.

[64] Zhao, X. M., Xia, Y. & Whitesides, G. M. Fabrication of three-dimensional micro-structures: Microtransfer molding. Advanced Materials 8, 1996, 837-840.

[65] Dou, Z., Su, B. & Button, T. W. Preparation of concentrated aqueous alumina suspensions for soft-molding microfabrication. In 8th International Conference on Ceramic Processing, 2-5 Sept. 2002.2 231-237.

[66] Jooho, M., Chiwon, K. & Seughyun, C. Microtransfer molding of gelcasting suspensions to fabricate barrier ribs for plasma display panel. Journal of the American Ceramic Society 86, 2003, 1969-1972.

[67] Heule, M., Schell, J. & Gauckler, L. J. Powder-based tin oxide microcomponents on silicon substrates fabricated by micromolding in capillaries. Journal of the American Ceramic Society 86, 2003, 407-412.

[68] Heule, M. & Gauckler, L. J. Gas sensors fabricated from ceramic suspensions by micromolding in capillaries. Advanced Materials 13, 2001, 1790-1793.

[69] Weng Sing, B., Younan, X. & Dong, Q. Formation of patterned microstructures of polycrystalline ceramics from precursor polymers using micromolding in capillaries. Journal of Materials Research 14, 1999, 3995-4003.

[70] Mukherjee, R., Patil, G. K. & Sharma, A. Solvent Vapor-Assisted Imprinting of Polymer Films Coated on Curved Surfaces with Flexible PVA Stamps. Industrial and Engineering Chemistry Research 48, 2009, 8812-8818.

[71] Lawrence, J. R., Turnbull, G. A. & Samuel, I. D. W. Polymer laser fabricated by a simple micromolding process. Applied Physics Letters 82, 2003, 4023-4025.

[72] Rahaman, M. Ceramic Processing and Sintering. Second Edition, (Marcel Dekker, 2003).

[73] Ring, T. Fundamentals of Ceramic Powder Processing and Synthesis. First Edition, (Academic Press, 1996).

[74] Kang, S. Sintering Densification, Grain Growth, and Microstructure. First Edition, (Elsevier Butterworth-Heinemann, 2005).

[75] Rajendra, K. Advances in Sintering Science and Technology. First Edition, (John Wiley & Sons, Inc., 2010).

[76] Chaim, R., Levin, M., Shlayer, A. & Estournes, C. Sintering and densification of nanocrystalline ceramic oxide powders: A review. Advances in Applied Ceramics 107, 159-169 (2008).

[77] Kuang, X., Carotenuto, G. & Nicolais, L. Review of ceramic sintering and suggestions on reducing sintering temperatures. Advanced Performance Materials 4, 1997, 257-274.

[78] Shaw, N. J. Densification and coarsening during solid state sintering of ceramics. A review of the models. III. Coarsening. Powder Metallurgy International 21, 1989, 25-29.

[79] Shaw, N. J. Densification and coarsening during solid state sintering of ceramics: a review of the models. Powder Metallurgy International 21, 1989, 31-33.

[80] Shaw, N. J. Densification and coarsening during solid state sintering of ceramics: a review of the models - I. Densification. Powder Metallurgy International 21, 1989, 16-21.

[81] Shaw, N. J. Densification and coarsening during solid state sintering of ceramics: a review of the models. II. Grain growth. Powder Metallurgy International 21, 1989, 31-33.

[82] Gowri, S., Narayanasamy, K. & Krishnamurthy, R. Recent developments in ceramic-materials processing and applications. Journal of Materials Processing Technology 37, 1993, 571-582.

[83] Barsoum, M. Fundamentals of Ceramics. Second Edition, McGraw-Hill Inc, 1997.

[84] King, A. Ceramic Technology and Processing. First Edition, Noyes Publications, 2002.

[85] Munro, R. G. Evaluated material properties for a sintered -alumina. Journal of the American Ceramic Society 80, 1997, 1919-1928.

[86] Auerkari, P. Mechanical and physical properties of engineering alumina ceramics. VTT Tiedotteita - Valtion Teknillinen Tutkimuskeskus, X-26, 1996.

[87] Indra, Oh, S. W. & Kim, H. J. Sintering and mechanical properties of alumina ceramics prepared by nanosize alumina. Trans Tech Publications, 2007, 821-824.

[88] Rao, P., Iwasa, M. & Kondoh, I. Properties of low-temperature-sintered high purity -alumina ceramics. Journal of Materials Science Letters 19, 2000, 543-545.

[89] Schonholzer, U. P. & Gauckler, L. J. Ceramic parts patterned in the micrometer range. Advanced Materials 11, 1999, 630-632.

[90] Schonholzer, U. P., Hummel, R. & Gauckler, L. J. Microfabrication of ceramics by filling of photoresist molds. Advanced Materials 12, 2000, 1261-1263.

[91] Jin, P., Gao, Y.-L., Liu, N. & Jiang, K. Design and fabrication of alumina micro reciprocating engine. Journal of Harbin Institute of Technology, 15, 2008, 801-804.

[92] Zhigang, Z., Xueyong, W. & Kyle, J. A net-shape fabrication process of alumina micro-components using a soft lithography technique. Journal of Micromechanics and Microengineering 17, 2007, 193-198.

[93] Su, B., Zhang, D. & Button, T. W. Micropatterning of fine scale ceramic structures. Journal of Materials Science 37, 2002, 3123-3126.

[94] Zhang, D., Su, B. & Button, T. W. Microfabrication of three-dimensional, free-standing ceramic MEMS components by soft moulding. Advanced Engineering Materials 5, 2003, 924-927.

[95] Ghatee, M., Shariat, M. H. & Irvine, J. T. S. Investigation of electrical and mechanical properties of 3YSZ/8YSZ composite electrolytes. Solid State Ionics 180, 2009, 57-62.

[96] Capdevila, X. G. et al. High-density YSZ tapes fabricated via the multi-folding lamination process. Ceramics International 35, 2009, 1219-1226.

[97] Drings, H., Brossmann, U. & Schaefer, H. E. Preparation of crack-free nano-crystalline yttria-stabilized zirconia. Physica Status Solidi-Rapid Research Letters 1, 2007, 7-9.

[98] Jardiel, T., Sotomayor, M. E., Levenfeld, B. & Varez, A. Optimization of the processing of 8-YSZ powder by powder injection molding for SOFC electrolytes. International Journal of Applied Ceramic Technology 5, 2008, 574-581.

[99] Piotter, V., Beck, M. B., Ritzhaupt-Kleissl, H. J., Ruh, A. & Hausselt, J. Recent developments in micro ceramic injection molding. International Journal of Materials Research 99, 2008, 1157-1162.

[100] Rogner, J. et al. Relationships between process, microstructure and properties of molded zirconia micro specimens. Microsystem Technologies 14, 2008, 1831-1837.

[101] Kasanicka, B. et al. Correlations between production process, states and mechanical properties of microspecimens made of zirconia. Microsystem Technologies 12, 2006, 1133-1141.

[102] Yu, P. C., Li, Q. F., Fuh, J. Y. H., Li, T. & Ho, P. W. Micro injection molding of micro gear using nano-sized zirconia powder. Microsystem Technologies 15, 2009, 401-406.

[103] Narottam, P. Handbook of Ceramic Composites. Springer Science + Business Media, Inc., 2005.

[104] Walter, K. Ceramic Matrix Composites. WILEY-VCH Verlag GmbH & Co. KGaA, Weinheim, 2008.

[105] Imbaby, M. & Jiang, K. Net shape fabrication of stainless steel-alumina composite micro parts. Journal of Micromechanics and Microengineering, 2009, 19.

[106] Imbaby, M. F. & Jiang, K. Fabrication of free standing 316-L stainless steel-Al_2O_3 composite micro machine parts by soft moulding. Acta Materialia 57, 2009, 4751-4757.

[107] Muller, C., Hanemann, T., Wiche, G., Kumar, C. & Goettert, J. Fabrication of ceramic microcomponents using deep x-ray lithography. Microsystem Technologies 11, 2005, 271-277.

[108] Wei, X., Dong, H., Lee, C.-H. & Jiang, K. Determination of young's modulus of electrochemically co-deposited Ni-Al_2O_3 nanocomposite. Materials Letters 62, 2008, 1916-1918.

[109] Wei, X. & Jiang, K. Synthesis and characterization of nanoparticulate strengthened nickel microcomponents. In 3rd International Conference on Smart Materials, Structures and Systems - Smart Materials and Micro/Nanosystems, CIMTEC 2008, June 8, 2008 - June 13, 2008. 299-304.

[110] Wei, X., Prewett, P. D. & Jiang, K. Electrochemical co-deposition of Nickel-Alumina nanocomposite for microsystem applications. In 2007 7th IEEE International Conference on Nanotechnology - IEEE-NANO 2007, August 2, 2007 - August 5, 2007. 34-38.

[111] Zhao, B. et al. High strength Ni based composite reinforced by solid solution W(Al) obtained by powder metallurgy. Materials Science and Engineering A 456, 2007, 337-343.

[112] Imbaby, M. F. & Jiang, K. Stainless steel-titania composite micro gear fabricated by soft moulding and dispersing technique. Microelectronic Engineering 87, 2010, 1650-1654.

[113] Wei, X. Y., Zhu, Z. G., Prewett, P. D. & Jiang, K. Fabrication of Ni- Al_2O_3 composite microcomponent by electroforming. Microelectronic Engineering 84, 2007, 1256-1259.

[114] Zaman, A. C., Üstündag, C. B., Kuskonmaz, N., Kaya, F. & Kaya, C. 3-D micro-ceramic components from hydrothermally processed carbon nanotube-boehmite powders by electrophoretic deposition. Ceramics International 36, 2010, 1703-1710.

[115] Gadow, R. & Kern, F. Pressureless sintering of injection molded zirconia toughened alumina nanocomposites. Nippon Seramikkusu Kyokai Gakujutsu Ronbunshi/Journal of the Ceramic Society of Japan 114, 2006, 958-962.

[116] Chan, C. M. & Cao, G. Z. Sol-gel casting of ceramic microcomponents. in Materials Science of Microelectromechanical Systems (MEMS) Devices, 1-2 Dec. 1998. 171-176.

[117] Shin, H. Fabrication of functionally graded materials with internak channels in ceramics and ceramic composites. PhD thesis, Michigan State University, 2002.

[118] Takagi, K., Jing-Feng, L., Yokoyama, S. & Watanabe, R. Fabrication and evaluation of PZT/Pt piezoelectric composites and functionally graded actuators. Journal of the European Ceramic Society 23, 2003, 1577-1583.

[119] Imgrund, P., Rota, A. & Simchi, A. Microinjection moulding of 316L/17-4PH and 316L/Fe powders for fabrication of magnetic-nonmagnetic bimetals. Journal of Materials Processing Technology 200, 2008, 259-264.

[120] Imgrund, P., Rota, A., Petzoldt, F. & Simchi, A. Manufacturing of multi-functional micro parts by two-component metal injection moulding. International Journal of Advanced Manufacturing Technology 33, 2007, 176-186.

[121] Ostadi, H., Jiang, K. & Prewett, P. D. Characterisation of FIB milling yield of metals by SEM stereo imaging technique. Microelectronic Engineering 86, 2009, 1021-1024.

[122] Natarajan, S., Chang-Yen, D. A. & Gale, B. K. Large-area, high-aspect-ratio SU-8 molds for the fabrication of PDMS microfluidic devices. Journal of Micromechanics and Microengineering 18, 2008, 045021.

[123] Luo, Y. et al. Swelling of SU-8 structure in Ni mold fabrication by UV-LIGA technique. Microsystem Technologies 11, 2005, 1272-1275.

[124] SU-8 Permanent Epoxy Negative Photoresist: Micro Chem, USA. http://www.microchem.com/products/su_eight.htm. 2009.

[125] Jiang, K. & Jin, P. Lithographic Process. LOS ANGELES, CA US Patent, 2004.

[126] Zaifa, Z. et al. Contact UV lithography simulation for thick SU-8 photoresist. IEEE, 2007, 900-903.

[127] Sylgard 184 Silicon Elastomer Kit: Dow Corning, USA. http://www.dowcorning.com/applications/search/default.aspx?r=131en. 2010.

[128] Wei, X., Lee, C. H., Jiang, Z. & Jiang, K. Thick photoresists for electroforming metallic microcomponents. Journal of Mechanical Engineering Science 222, 2008, 37-42.

[129] Shipley BPR100 photoresist Data Sheet: Shipley EIF Advanced Packaging. http://www.chestech.co.uk/microelectronics.aspx/opendata/Microelectronics.aspx?CategoryID=134&Detail=true. 2010.

[130] Urban, A. & Laermer, F. Bosch-process - DRIE success story, new applications and products. Materials Research Society, 133-144.

[131] Koerner, T., Brown, L., Xie, R. & Oleschuk, R. D. Epoxy resins as stamps for hot embossing of microstructures and microfluidic channels. Sensors and Actuators, B: Chemical 107, 2005, 632-639.

[132] Lorenz, R. M. et al. Simultaneous generation of multiple aqueous droplets in a microfluidic device. Analytica Chimica Acta 630, 2008, 124-130.

[133] Seo, J. & Lee, L. P. Effects on wettability by surfactant accumulation/depletion in bulk polydimethylsiloxane (PDMS). Sensors and Actuators, B: Chemical 119, 192-2006, 198.

[134] Dragon Skin Series data sheet: Smooth On- USA. http://www.smooth-on.com/tb/files/DRAGON_SKIN_FX_PRO_TB.pdf, 2009.

[135] Solomon, M. J. et al. Effect of adsorbed surfactants on the rheology of colloidal zirconia suspensions. Langmuir 15, 1999, 20-26.

[136] Dang-Hyok, Y. & Lee, B. I. Processing of barium titanate tapes with different binders for MLCC applications-Part I: Optimization using design of experiments. Journal of the European Ceramic Society 24, 2004, 739-752.

[137] LeBeau, J. M. & Boonyongmaneerat, Y. Comparison study of aqueous binder systems for slurry-based processing. Materials Science and Engineering A 458, 2007, 17-24.

[138] Baklouti, S., Chartier, T., Gault, C. & Baumard, J. F. The Effect of Binders on the Strength and Young's Modulus of Dry Pressed Alumina. Journal of the European Ceramic Society 18, 1998, 323-328.

[139] Moon, H. & Lange, F. F. Strengthening with a uniform compressive layer produced by a dip-coating: A study of processing variables. Journal of the American Ceramic Society 93, 2010, 1264-1269.

[140] DURAMAX B-1000 Binder Data Sheet: Rohm and Haas, USA. http://www.dow.com/assets/attachments/business/pmat/duramax/duramax_b-1000/tds/duramax_b-1000.pdf, 2008.

[141] DURAMAX B-1007 Binder Data Sheet: Rohm and Haas, USA. http://www.dow.com/assets/attachments/business/pmat/duramax/duramax_b-1000/tds/duramax_b-1007.pdf, 2008.

[142] DURAMAX D-3005 Dispersant Data Sheet: Rohm and Haas, USA. http://www.dow.com/assets/attachments/business/pmat/duramax/duramax_d-3005/tds/duramax_d-3005.pdf, 2008.

[143] Stearns, L. C., Junhong, Z. & Harmer, M. P. Processing and microstructure development in Al_2O_3 -SiC `nanocomposites'. Journal of the European Ceramic Society 10, 1992, 473-477.

[144] Galusek, D., Sedlacek, J. & Riedel, R. Al_2O_3-SiC composites prepared by warm pressing and sintering of an organosilicon polymer-coated alumina powder. Journal of the European Ceramic Society 27, 2007, 2385-2392.

[145] HTA 1500 Slow Cure Data Sheet: KiON Speciality Polymer, USA. http://www.polysilazanes.com/europe-middle-east-africa/products/specialty materials/hta-1500-slow-cure/, 2000.

[146] Lee, J. N., Park, C. & Whitesides, G. M. Solvent Compatibility of Poly(dimethylsiloxane)-Based Microfluidic Devices. Analytical Chemistry 75, 2003, 6544-6554.

[147] Lee, D.-W., Kim, N.-H. & Chang, E.-G. Effect of nonionic surfactants on the stability of alumina slurry for Cu CMP. In EMRS 2004, Symposium D: Functional Oxides for Advanced Semiconductor Technologies.1-3 293-300.

[148] Moballegh, L., Morshedian, J. & Esfandeh, M. Copper injection molding using a thermoplastic binder based on paraffin wax. Materials Letters 59, 2005, 2832-2837.

[149] Singh, B. P., Menchavez, R., Takai, C., Fuji, M. & Takahashi, M. Stability of dispersions of colloidal alumina particles in aqueous suspensions. Journal of Colloid and Interface Science 291, 2005, 181-186.

[150] Tseng, W. J. & Wu, C. H. Sedimentation, rheology and particle-packing structure of aqueous Al2O3 suspensions. Ceramics International 29, 2003, 821-828.

[151] Tsetsekou, A., Agrafiotis, C. & Milias, A. Optimization of the rheological properties of alumina slurries for ceramic processing applications Part I: Slip-casting. Journal of the European Ceramic Society 21, 2001, 363-373.

[152] Lewis, J. A. Colloidal processing of ceramics. Journal of the American Ceramic Society 83, 2000, 2341-2359.

[153] Wasche, R., Naito, M. & Hackley, V. A. Experimental study on zeta potential and streaming potential of advanced ceramic powders. Powder Technology 123, 2002, 275-281.

[154] Degen, A. & Kosec, M. Influence of pH and ionic impurities on the adsorption of poly(acrylic) dispersant onto a zinc oxide surface. Journal of the American Ceramic Society 86, 2003, 2001-2010.

[155] Chibowski, S., Mazur, E. O. & Patkowski, J. Influence of the ionic strength on the adsorption properties of the system dispersed aluminium oxide-polyacrylic acid. Materials Chemistry and Physics 93, 2005, 262-271.

[156] Castro, R. H. R., Murad, B. B. S. & Gouvea, D. Influence of the acid-basic character of oxide surfaces in dispersants effectiveness. Ceramics International 30, 2215-2221 (2004).

[157] Vissers, J. P. C., Laven, J., Claessens, H. A., Cramers, C. A. & Agterof, W. G. M. Sedimentation behaviour and colloidal properties of porous, chemically modified silicas in non-aqueous solvents. Colloids and Surfaces A: Physicochemical and Engineering Aspects 126, 1997, 33-44.

[158] Kothari, N. C. The effect of particle size on sintering kinetics in alumina powder. Journal of Nuclear Materials 17, 1965, 43-53.

[159] Tianmin, H. et al. Characterization of YSZ electrolyte membrane tubes prepared by a vacuum casting method. Journal of Alloys and Compounds 337, 2002, 231-236.

[160] Kanchana, K. Marginal adaptation and flexural strength of a leucite reinforced dental glass ceramic. Journal of Matals, Materials and Minerals 11, 2001, 15.

[161] Mori, M. et al. Cubic-stabilized zirconia and alumina composites as electrolytes in planar type solid oxide fuel cells. Solid State Ionics 74, 1994, 157-164.

[162] Feighery, A. J. & Irvine, J. T. S. Effect of alumina additions upon electrical properties of 8 mol.% yttria-stabilised zirconia. in 11th International Conference on Solid State Ionics, 16-21 Nov. 1997.1-4 209-216.

[163] Ming, C., Ting-Lian, W. & Zhi-Yi, L. Microstructure and conductivity of alumina-fiber-doped YSZ membranes. Ionics 6, 2000, 403-407.

[164] Choi, S. R. & Bansal, N. P. Flexure strength, fracture toughness, and slow crack growth of YSZ/alumina composites at high temperatures. Journal of the American Ceramic Society 88, 2005, 1474-1480.

[165] Tekeli, S. The solid solubility limit of Al_2O_3 and its effect on densification and microstructural evolution in cubic-zirconia used as an electrolyte for solid oxide fuel cell. Materials & Design 28, 2007, 713-716.

[166] Chen, C., Hsiang, H. & Zhou, Z. Effects of the addition of minute amounts of alumina on the microstructure and sintering behavior of yttria stabilized tetragonal zirconia polycrystals ceramic via a co-precipitation process. Journal of Ceramic Processing Research 9, 2008, 234-23.

[167] Nazarpour, S., Lopez-Gandara, C., Ramos, F. M. & Cirera, A. Phase transformation studies on YSZ doped with alumina. Part 1: Metastable phases. Journal of Alloys and Compounds 505, 2010, 534-541.

[168] Jin, X., Wu, L., Sun, Y. & Guo, L. Microstructure and mechanical properties of ZrO2/NiCr functionally graded materials. Materials Science and Engineering A 509, 2009, 63-68.

[169] Kieback, B., Neubrand, A. & Riedel, H. Processing techniques for functionally graded materials. Materials Science & Engineering A (Structural Materials: Properties, Microstructure and Processing) A362, 2003, 81-105.

[170] Yeo, J., Jung, Y. & Choi, C. Zirconia-stainless steel functionally graded material by tape casting. Journal of the European Ceramic Society 18, 1998, 1281-1285.

[171] Ruh, A. et al. Production of two-material micro-assemblies by two-component powder injection molding and sinter-joining. Microsystem Technologies 14, 2008, 1805-1811.